Università degli Studi di Udine
Dipartimento Politecnico di Ingegneria e Architettura

PhD Thesis

Physics based modeling for 2D semiconductors as baseline materials for novel electron devices

Author:
Pedram Khakbaz

Supervisor:
David Esseni

Co-supervisor:
Francesco Driussi

PhD cycle XXXIV
2021

A Book of Verses underneath the Bough,
A Jug of Wine, a loaf of Bread—and Thou
Beside me singing in the Wilderness—
Oh, Wilderness were Paradise enow!

Omar Khayyam: The astronomer-poet of Persia (1048 – 1131)

Contents

Terminology iii

Abstract v

1 Introduction 1
- 1.1 2D materials and their applications . . . 1
  - 1.1.1 Graphene . . . 2
  - 1.1.2 Transition metal dichalcogenides . . . 3
- 1.2 Sensors . . . 4
  - 1.2.1 Strain Sensors . . . 5
  - 1.2.2 Temperature sensors . . . 6
  - 1.2.3 Gas sensors . . . 6
- 1.3 Contacts to 2D materials . . . 7

2 Contacts to 2D materials 9
- 2.1 Introduction . . . 9
  - 2.1.1 Schottky barrier . . . 9
  - 2.1.2 Fermi level pinning . . . 11
  - 2.1.3 Carrier injection mechanism . . . 13
- 2.2 Simulation methodology . . . 14
  - 2.2.1 Density functional theory . . . 15
  - 2.2.2 Interface modeling . . . 18
  - 2.2.3 Quantum Transport . . . 22
  - 2.2.4 Assessment of the simulation methodology . . . 23
- 2.3 Contacts between metal and graphene . . . 25
- 2.4 Contacts between (semi)metal and MoS_2 . . . 30
  - 2.4.1 Contact resistance in MoS_2 . . . 34
- 2.5 Conclusions . . . 40

3 Sensors based on 2D materials 43
- 3.1 Introduction . . . 43
- 3.2 Linear Resistance : Semiclassical methods . . . 43
  - 3.2.1 Linearized BTE . . . 44
  - 3.2.2 Carrier scattering . . . 47
- 3.3 Piezoresistance and strain Sensors . . . 53
  - 3.3.1 Experimental extraction of MoS_2 piezoresistance . . . 54
  - 3.3.2 Theoretical models of MoS_2 piezoresistance . . . 55
- 3.4 Temperature Sensors . . . 59
- 3.5 Gas Sensors . . . 65
  - 3.5.1 Titanium Carbide MXene as NH_3 Sensor . . . 65

3.5.2 Fluorinated Graphene-based resistive humidity sensor 77
3.6 Conclusion 85

4 Non linear transport based on MoS_2 87
4.1 Introduction 87
4.2 Description of the conduction band of monolayer MoS_2 88
4.3 The multi-valley Monte carlo transport simulator 89
4.4 Results 90
4.4.1 Mobility calculation: MC versus LBTE 90
4.4.2 Velocity-field curves in the presence of intrinsic phonons 91
4.4.3 Velocity-field curves including scattering with neutral defects and coulomb centers 92
4.4.4 Velocity-field curves including SO phonons 93
4.4.5 Effect of screening of SO phonons 95
4.4.6 I-V curves of a short channel FET 97
4.5 Conclusions 98

5 Conclusions 101

Bibliography 103

List of Publications i

Acknowledgements iii

Terminology

Abbreviations and acronyms

2D	2-Dimensional
3D	3-Dimensional
AIMD	*Ab-initio* Molecular Dynamics
BTE	Boltzmann Transport Equation
BZ	Brillouin Zone
CB	Conduction Band
CI	Coulomb Impurity
CMOS	Complementary Metal–Oxide–Semiconductor
COHP	Crystal Orbital Hamilton Population
CT	Charge Transfer
DFT	Density Functional Theory
DIGS	Defect-Induced Gap States
DoS	Density of States
EMA	Effective Mass Approximation
ESP	Electrostatic Surface Potential
FE	Field Emission
FET	Field-effect transistor
FG	Fluorinated Graphene
FLP	Fermi Level Pinning
G	Graphene
GF	Gauge factor
GGA	Generalized Gradient Approximation
GO	Graphene Oxide
HOMO	Highest Occupied Molecular Orbital
IC	Integrated Circuits
IGS	Interface Gap States
iPh	Intrinsic Phonon
IRDS	International Roadmap for Devices and Systems
ITRS	International Technology Roadmap for Semiconductors
LBTE	Linearized Boltzmann Transport Equation
LUMO	Lowest Unoccupied Molecular Orbital
MD	Minimum energy Distance
MIGS	Metal-Induced Gap States
MRT	Momentum Relaxation Time
ND	Neutral Defect
NEGF	Non Equilibrium Green's Functions
PAW	Projector Augmented-Wave
PBE	Perdew-Burke-Ernzerhof

PDoS	Projected Density of States
QTAIM	Quantum Theory of Atoms in Molecules
RH	Relative Humidity
SBH	Schottky Barrier Height
SC	Semiconductor
SF	Strain Fluctuation
SO	Surface Optical
TCR	Temperature Coefficient of Resistance
TE	Thermionic Emission
TEM	Transmission Electron Microscopes
TFE	Thermionic Field Emission
TMDC	Transition Metal Dichalcogenides
URBF	Unit-cell Restricted Bloch Functions
VASP	Vienna *Ab-initio* Simulation Package
VB	Valence Band
VdW	Van der Waals
VHJ	Vertical Hetero-Junction
WF	Work Function

Abstract

Scaling CMOS technology has been the cornerstone of the continued progress in the silicon-based semiconductor industry. Nowadays, the FinFETs and nanosheet transistors are the most advanced device architectures respectively in production and under development in the industry. However, due to the many constraints posed by short-channel effects and to the limitations due to extrinsic resistive and capacitive components, the scaling of transistors has become an increasingly challenging task. Two-dimensional semiconductors are attractive materials for nanosheet transistors and for many other prospective applications, thanks to their very good intrinsic transport properties compared to 3D semiconductors at the same layer thickness. The discovery of graphene and then the development of transition metal dichalcogenides raised high expectations for a new and wide family of two-dimensional crystalline materials with remarkable electronic, mechanical, and optical properties. However, there are still many concerns about the limitations of 2D materials and several hurdles to reach the industrial maturity. In order to overcome such limitations, a physical understanding of novel electron devices based on 2D crystals is vital.

After an introduction about 2D materials presented in chapter 1 of this thesis, in the second chapter we report a simulations based study of metallic contacts to 2D materials. In fact, one of the key challenges preventing the harnessing of good intrinsic transport properties of 2D crystals is the poor quality of the contacts between metals and 2D materials. First, we show that Cu and Ni largely dope graphene at the minimum energy distance, whereas a long-range interaction is predicted for Au-graphene contact. Then we discuss by using *ab-initio* simulations the Fermi level pinning in defects free metals to MoS_2 contacts. Then by using an *ab-initio* transport methodology, we investigate the contact resistance between several metals and MoS_2. Our results examine quantitatively the trade-off between Schottky barrier height and tunneling barrier in contacts with a buffer layer and confirmed by simulations the superior performance of the bismuth-MoS_2 n-type contact.

Chapter 3 is focused on sensors based on 2D materials. In this chapter, we first revisit the problem of the linearized Boltzmann transport equation for mobility calculations and the formulation of different scattering mechanisms. Then we use our mobility calculations to investigate piezo-resistance in MoS_2, and in particular for the interpretation of a giant intrinsic Gauge factor experimentally observed in monolayer MoS_2 This intrinsic piezoresistive can enable emerging applications in tactile sensing as well as improving the electronic transport in TMD electronics. The analysis in chapter 3 continues with the analysis and comparison with experiments for the temperature coefficient of resistance in MoS_2, with fast temperature sensors as a prospective application. In the last part of chapter 3, we address some possible options for gas sensors based on the 2D materials. First we investigate the 2D Mxene as a potential ammonia sensor employing a first-principles study. Then we focus on fluorinated graphene as a potential material for humidity sensing applications.

Finally in chapter 4, by utilizing a multi-valley Monte Carlo transport simulator, uniform field transport in 2D MoS_2 is analyzed. Our preliminary results for the high field uniform transport regime show that the electron's saturation velocity in monolayer MoS_2 is only slightly affected by scattering with Coulomb centers and neutral defects, while the effect of surface optical phonons is more subtle and it is, at the time of writing, still partly under investigation.

Chapter 1

Introduction

1.1 2D materials and their applications

ITRS [1] predicts that sustaining Moore's law is strongly chained to the discovery of new materials and to the design of new devices with modern architectures. The discovery and development of two-dimensional materials create the opportunity of designing new and ultra-thin devices.

The existence of 2D materials was debated for many years, even during the 1935-1937 period two physicists developed a theory which rejected the possibility of creating complete 2D materials due to the dynamic instability [2,3]. But the discovery of graphene, which is the mono layer of graphite by Andre Geim and Konstantin Novoselov in the year of 2004, put on end to the skepticism in the physic community and, moreover, the two researchers were awarded the Nobel prize [4].

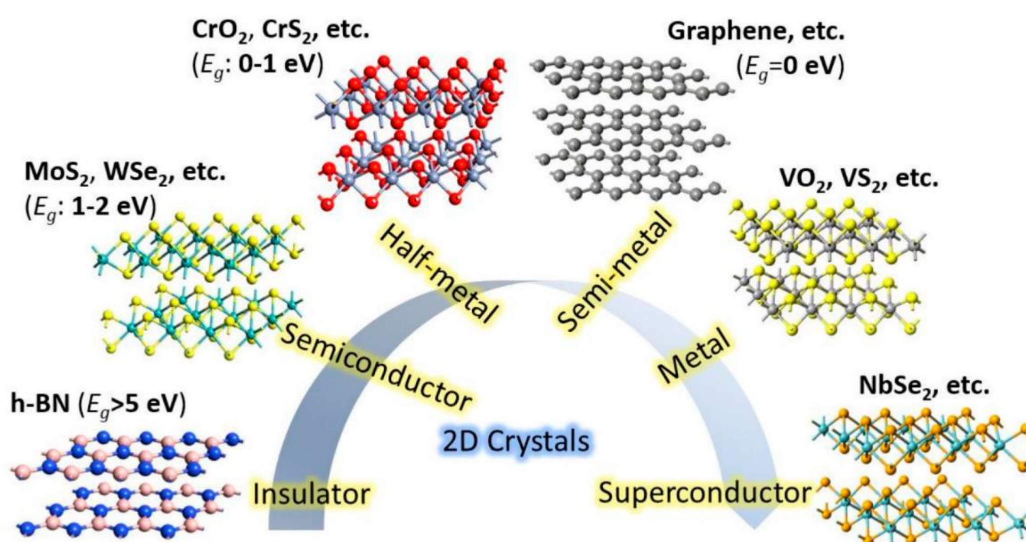

Figure 1.1: Different 2D crystals with diverse electrical properties. E_g is the band gap energy. This figure is taken from [5].

Two dimensional crystals are highly stable, and have a high quality structure. As an example in a graphene crystal, carriers can travel distances of several thousand times the distance between atoms without scattering [6,7]. These properties make the 2D materials an interesting research topic for scientists around the world. Unique behavior of the 2D

materials come from their unique crystal structure. 2D materials have covalent bonds, which hold the atoms together in the layer, that are very strong compared to the van der Waals (vdW) interaction. Moreover, when a material goes from bulk to a single layer (or few layers) arrangement, the periodicity does no longer obey in the out of plane direction, which leads to the modification of electronic band structure of the material. In the following, the most mature 2D materials are briefly reviewed.

1.1.1 Graphene

Graphene is an allotrope of carbon consisting of a single layer of atoms arranged in plane with honeycomb lattice (see Fig.1.2). Each atom in the graphene crystal connects to its three nearest neighbors and share one electron with them. This hexagonal structure can be directly recognized by using TEM.

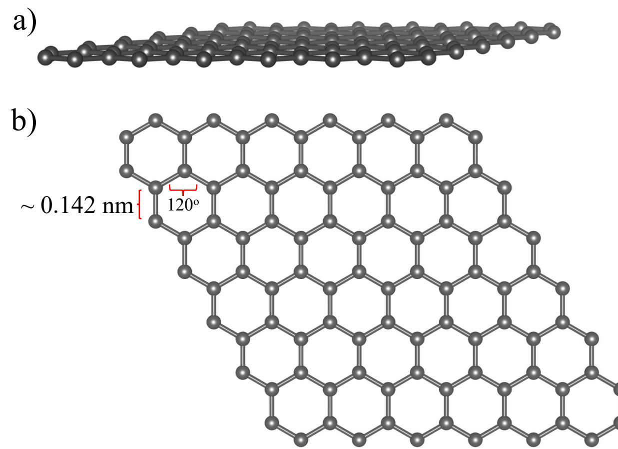

Figure 1.2: a) Side and **b)** top view of grapehene structure.

Graphene is a very efficient heat and electricity conductor; its hole and electron mobilities can reach 10^6cm^{-2}/(Vs) [8–10]. It is also the thinnest and lightest material ever fabricated with also unique electronic properties; in particular, the conduction band touches the valence band at six points (Dirac points) at the edge of Brillouin zone which can be grouped into two non-equivalent sets of three points, these two sets are labeled as K and K' points. Graphene has a linear dependence of the energy on the Bloch vector close to the Dirac point (see Fig.1.3), that can be best described by theories for massless relativistic particles [2]. Moreover, the conduction and valence bands close to the energy reference (in Fig.1.3 the energy reference is Fermi energy) are symmetric with respect to the Dirac point.

These properties can help us to understand the reason behind the interest towards graphene in the scientific society. In particular, graphene has been investigated for many applications such as gas sensors, solar cells, energy storage, etc., but it also has shortcomings for applications to electron devices. However one of the main drawbacks of graphene is its gapless nature. Also, a strong mobility degradation in graphene sheets has been reported due to its high sensitivity to the substrate material and fabrication process. For example SiO_2 substrates can decrease the graphene mobility down to 40000 cm^2/(Vs) [11–13]; the mobility can further degrade if the top gate dielectric is a high-k material [14].

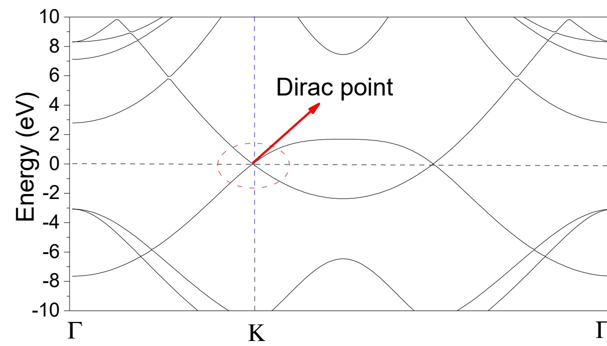

Figure 1.3: Electronic band structure of graphene, linear behavior is marked by dashed red circle.

1.1.2 Transition metal dichalcogenides

The discovery of graphene triggered a wide interest about other 2D materials. Recent studies show that monolayer Transition Metal Dichalcogenides (TMDCs), which can be easily exfoliated [15], have more promising properties than graphene for electron devices applications. These materials have 2D hexagonal structures with MX_2 as general chemical formula, where M stands for a transition metal arranged in a plane and sandwiched between two planes of X (chalcogen) atoms. Many of these 2D structures are semiconductors with direct or indirect band gap. Monolayer MoS_2, characterized by unique electrical and optical properties, is the most technologically mature material in this family; the high temperature stability up to 1100 C, the lack of dangling bonds and the quite large band gap in its electronic structure make it a very good candidate for electron devices applications [16]. Theoretical and experimental studies have shown that the electronic structure of MoS_2 is sensitive to the number of layers [17]: bulk MoS_2 has an indirect band gap of about 1.29 eV, which increases by decreasing the number of layers to about 1.8 eV direct band gap for monolayer MoS_2 (see Fig.1.4). In bulk crystals, while the maximum of the valence band is placed at Γ-point, the minimum of conduction band is located at a point between Γ-K. By decreasing the number of layers, both maximum of the valence band and minimum of the conduction band shift and move at the K-point.

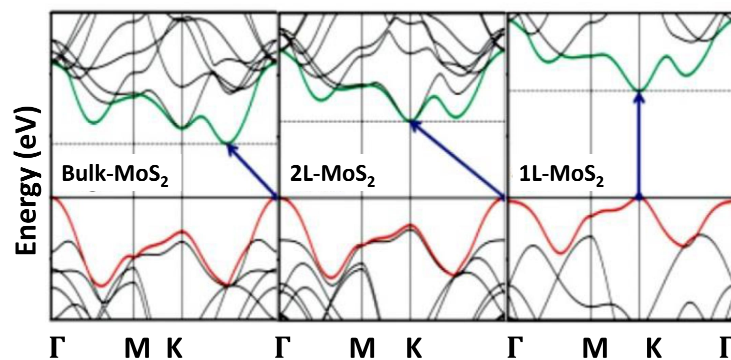

Figure 1.4: Band gap opening of MoS_2 by decreasing the number of layers. This figure is taken from [18].

External conditions such as strain, electric field and temperature can also influence the

electrical properties of TMDCs [19, 20]. The band structure of strained and unstrained MoS_2 is shown in Fig.1.5. By applying a small compressive biaxial strain, the energy distance between the K- and Q-valleys reduces. This leads to an increase in the inter-valley phonon scattering and consequently degradation of the mobility, whereas a tensile strain of about %1 can enhance the mobility.

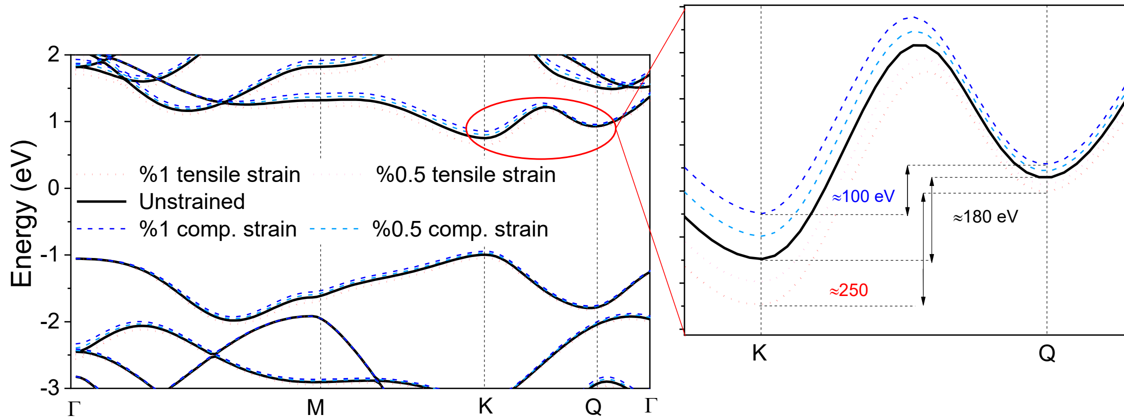

Figure 1.5: The band structure of a single layer MoS_2: dashed lines are under compressive strain, dotted lines are under tensile strain and solid line is the unstrained band structure. Applying %1 compressive strain reduces the $K - Q$ energy offset by about 80 meV, whereas same value of tensile strain increases it by 70 meV.

Two main approaches have been used to fabricate 2D TMDCs: either the exfoliation of bulk material into monolayers or the growth methods such as molecular epitaxy or chemical vapor deposition (CVD). The most powerful approaches to produce clean, highly crystalline, and thin nanosheets is mechanical exfoliation. In with this method, few TMDCs layers are first separated from the bulk crystal by means of adhesive tape, then the peeled crystals are placed on target substrate and cleaved again. By repeating this procedure and finally removing the tape, high quality crystals remain on substrate. But as Joshua Robinson, Associate Professor of Materials Science and Engineering at Penn State University says, “Industry is not going to accept mechanical exfoliation as a path forward for manufacturing these devices” [21]. Currently, CVD is the most promising way to produce large-area 2D TMDCs with a high quality crystal. Unlike the exfoliation approach, CVD method directly synthesize 2D TMDCs on a target substrate. Source materials can be pre-deposited on target substrates and then converted to TMDCs [22].

1.2 Sensors

A sensor is a system whose objective is to translate the variation of its environment parameters into an information readable by other devices. Sensors are used in almost every aspect of our daily life: chemical sensors, biosensors, neuromorphic sensors [24], image sensors and monitoring sensors [25] are few examples of widely used measurement devices. Recent technological advances yield to smaller sensors with faster measurement time and with, more importantly, higher sensitivity. Due to the high demand for more scaled and sharper sensors, scientists around the world are working on designing sensors

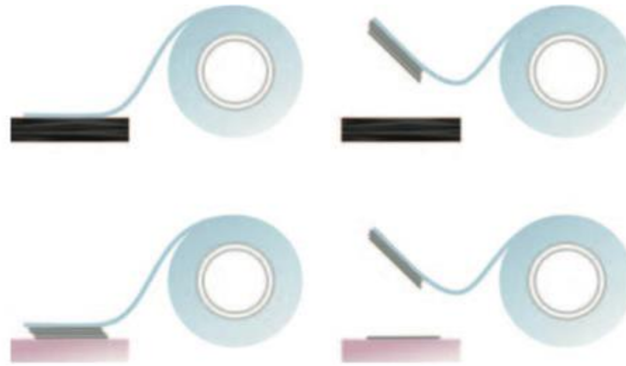

Figure 1.6: The exfoliation technique. Few layers TMDCs are first separated from the bulk crystal by means of adhesive tape, then the peeled crystals are placed on target substrate and cleaved again. This figure is taken from [23].

based on new materials. In the remainder of Sec.1.2 we briefly introduce a few examples of sensors that are linked to the work reported in the present manuscript. More detailed description can be found in the corresponding section in Chap.3.

1.2.1 Strain Sensors

For half a century, the intrinsic piezoresistive effect has remained the most straightforward means of translating physical interactions to electrical responses [26, 27]. Piezoresistance captures the relationship between strain, band structure, and the electrical resistance (R) of a material and it has been wildly disruptive to electronics, impacting both ICs and sensors [28, 29]. For example, tensile (compressive) strain is used in modern Si ICs to drastically enhance the electron (hole) mobility [28]. Regarding sensors, the natural application for piezoresistive devices is tactile sensing, which is the gateway for electronics to interact with the physical world. However, emerging applications in tactile sensing, like soft robotics [30], electronic skins [31], and haptics require extreme flexibility and sensitivity beyond the reach of conventional piezoresistive materials.

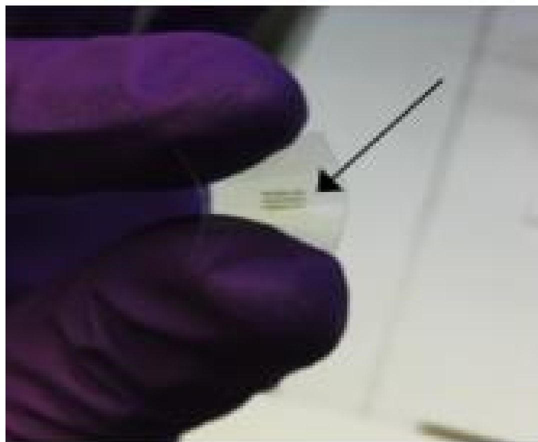

Figure 1.7: Flexible devices of 1L MoS_2 on polyethylene naphthalate .

Three-dimensional (3D) bulk materials like Si, Ge [27], InSb [32], and Ga-based

compound semiconductors exhibit intrinsic piezoresistive coefficients Π in the range of $100 - 300$, where $\Pi = (\Delta R/R)\Delta\varepsilon$ [33] and $\Delta\varepsilon$ is magnitude of the strain window. When dealing with strain sensors a broader term, the Gauge Factor (GF), often comes into play. A GF similarly captures the relative change in resistance per strain level, but also includes extrinsic geometrical [34,35], capacitive [36], contact [37], and surface effects [38]. As such, very large experimental GFs have been demonstrated, up to 5000 in a surface-modified Si nanowire [38]. However, extrinsic GFs have drawbacks. For example, capacitive sensors (like hollowed foams) suffer from hysteresis, while contact sensors (like meshes) can be unpredictable as they depend on thousands of underlying changes in contacts between internal mesh nodes [39,40]. In contrast, materials with a high intrinsic piezoresistance are simpler to implement for tactile sensing and offer a predictable and repeatable response within the elastic limit. Atomically thin 2D materials represent a potential departure from 3D materials in terms of both flexibility and piezoresistance [20, 41]. As the relationship between flexing a material and the imparted strain is thickness dependent, sub-nanometer thick 2D materials are capable of exceptionally tight bending radii and thus of stretching figures practically impossible for 3D materials [42]. In addition, 2D materials are strain-tunable through vdW interactions with substrates, encapsulation, or thermal cycling during fabrication [43,44]. Lastly, owing to their layered nature, 2D materials could have a low density defects and dangling bonds compared to artificially thinned 3D materials. As such, the onset of inelastic deformation is closer to the theoretical limits dictated by the elastic modulus and not by the defect-limited fracture observed in tailored materials [45–47].

1.2.2 Temperature sensors

Temperature sensing is critical for several applications including nanoscale thermometry [48, 49] thermal accelerometers [50, 51] bolometers [52], and suppression of thermal failures in integrated circuits [53, 54]. Traditional temperature sensors rely on thermocouples, platinum or polysilicon resistors, or circuit-based sensors [55, 56]. However, the former cannot be placed with microscale precision and most cannot respond to ultra-fast temperature transients [54, 56]. In fact, their relatively large thermal masses make them slow to recognize sharp temperature changes and limit their potential performance [57,58]. Fast thermal sensing requires a large Temperature Coefficient of Resistance (TCR) as well as low thermal capacitance [59], which can be obtained by thinning the sensor [51, 58]. However, when thinned below about 10 nm, the TCR of most metals drops sharply due to strong surface scattering and possible electron localization, thus limiting their use as fast thermal sensors [50, 51, 60] .

1.2.3 Gas sensors

The development of novel gas sensors with rapid and efficient gas concentration detection capabilities has been a major research focus for applications including air pollution monitoring [61], medical diagnostic [62], food and beverage quality control [63], and explosives detection [64]. Various materials, such as conductive polymer composites [65], carbon nanotubes [66, 67], metal oxide semiconductors [68], graphene [69], and metal-organic frameworks [70] have been used for the fabrication of gas sensors.

2D materials have received significant attention also in the context of gas sensing [72], biosensing [73], catalysis [74, 75], energy storage [76, 77], hydrogen generation [78], and water purification [79]. In fact the the large surface-to-volume ratio of 2D materials leads

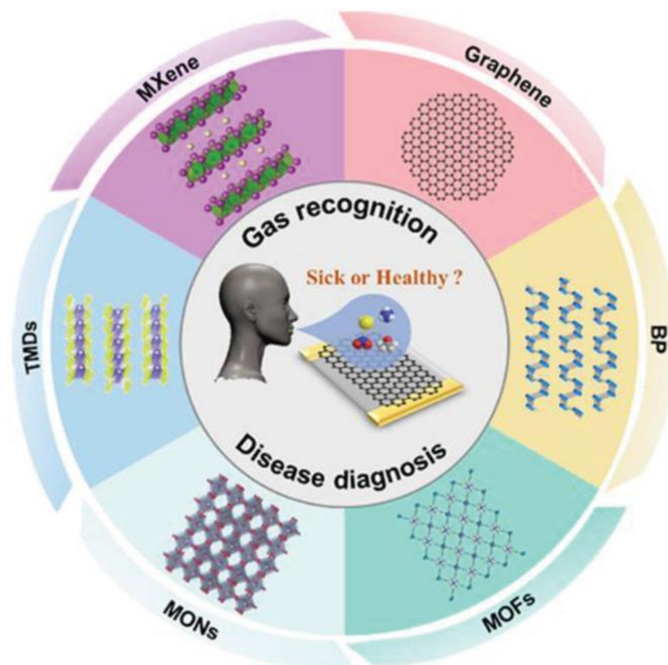

Figure 1.8: Different 2D materials based sensors for breath analysis. This figure is taken from [71].

to a larger adsorption of gas molecules and higher surface interactions [80]. Moreover some 2D materials usually have high carrier mobility and density (e.g. graphene), so a small amount of gas adsorption on the 2D sheet can appreciably change the resistance.

1.3 Contacts to 2D materials

Good control over the flow of charge carriers is crucial in electronic devices. The carriers are invariably injected into the semiconductor through electrical contacts. The quality of electrical contacts, usually measured in terms of contact resistance, is a main contributing factor to the device operation and performance, particularly for nanoscale transistors and integrated circuits [81].

As an example, Field-Effect Transistor (FET) is an electronic device widely used in the mainstream CMOS integrated circuits, and a low contact resistance is vital for the performance of FET. In particular, a high contact resistance between a 3D metal and the 2D semiconductor largely degrades the device current [82, 83]. Consequently, one of the main challenges for 2D materials based transistors is the engineering of high quality and low resistance contacts between 2D semiconductors and metal electrodes. The primary origin of such a high contact resistance is usually ascribed to the Schottky barrier between the 2D semiconductor and the metal contact. As typically done for 3D semiconductors, this energy barrier can in principle be engineered through the difference between metal work function and electron affinity of 2D semiconductor [84]. However the fairly large densities of gap states observed at the metal to semiconductor interface tend to effectively pin the Fermi level inside the gap of the 2D semiconductor, thus leading to a non-Ohmic contact. In 3D semiconductors the chemical, substitutional doping is widely used to decrease the contact resistance, but this approach does not seem to be similarly viable for 2D materials because of the fabrication process constrains.

At a carrier density of 10^{13}cm^{-2}, the quantum limit to the contact resistance to MoS_2 is about 30 $\Omega\mu$m [85]. However, to our best knowledge, this value is about one or two orders of magnitudes smaller than the typical resistance experimentally reported in metal to 2D materials contacts. In order to reduce the gap between the theoretical, minimum contact resistance values and the figures reported in actual devices, it is vital to study the detailed physics of contacts between metals and 2D semiconductors [81]. This topic will be discussed in detail in Chap.2.

Chapter 2

Contacts to 2D materials

2.1 Introduction

As mentioned in the previous chapter the discovery of 2D materials, because of their unique intrinsic properties, raised the expectations to overcome the Si-based devices limitations. Indeed since the discovery of graphene in 2004, 2D materials have been under extensive investigation. Although much progress has been made so far, there are still serious challenges that must be addressed. Low quality contacts between a 2D semiconductor (SC) and metal is one of the main issues hindering the outstanding properties of few-layer crystals. To gain a better understanding on this issue, Schottky barrier, Fermi Level Pining (FLP), carrier injection mechanism and the contact resistance value of the metal-2D SC system are addressed in this chapter.

2.1.1 Schottky barrier

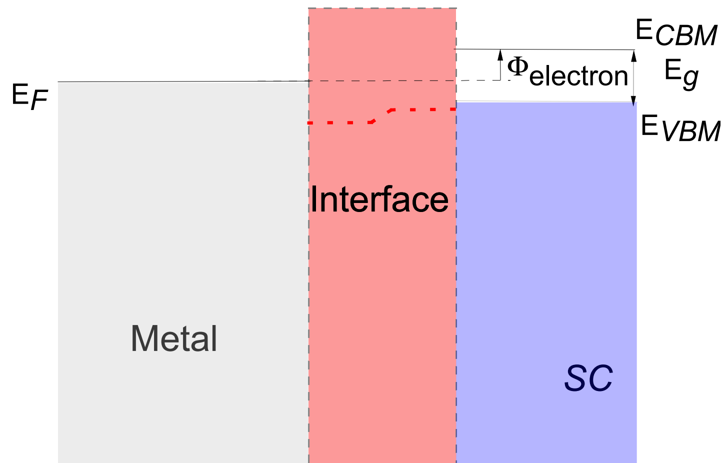

Figure 2.1: Band diagram at a metal-SC interface. The electrostatic potential energy is depicted in red.

Discontinuity on the energy scale of the states at the interface between a SC and a metal is responsible for the non-linear behavior of the current against applied bias voltage characteristics (see Fig. 2.1) [86]. For n-type (p-type) SCs, the electrons (holes) located at the minimum (maximum) of the conduction (valence) band are responsible for the current

flow. For instance, if the states at the minimum of conduction band are at an energy $\Phi_{electron}$ above the Fermi level (see Fig. 2.1), so there exists a potential step for electronic transport between metal and SC. This energy offset is called n-type Schottky barrier height (SBH) and it has a rectifying effect on the current versus voltage characteristic of a Schottky contact. The SBH has a great influence on the charge injection mechanism in 2D SCs, hence an accurate extraction and a possible tuning of its value are of vital importance for the evaluation and the eventual optimization of a metal-2D SC contact. According to Schottky-Mott rule [87], the work function of metal contact governs the SBH, and the value of this potential energy barrier for electrons can be defined as:

$$\Phi_{electron} = \phi_M - \chi_{SC} \tag{2.1}$$

and for holes:

$$\Phi_{hole} = \chi_{SC} + E_g - \phi_M \tag{2.2}$$

where ϕ_M stands for the metal work function, χ_{SC} and E_g are SC electron affinity and band gap energy respectively. The superposition principle of electrostatic potential is the fundamental concept behind the Schottky-Mott rule [88]. However, this simple model does not account for interface chemistry, therefore it will only hold when the charge redistribution during metal-SC interface formation is very small, namely when the band alignment over the final interface remains the same as in the case of isolated crystals [86].

Figure. 2.2 reports the experimentally extracted SBH for different metals on n-type Si versus their work function. It is clear that there is a weak sensitivity of SBH to the metal work function. This behavior originates from the fact that after the metal and SC have got in contact, the states of the newly formed system are hybrid overlapped and do not belong to either metal or SC, which corresponds to an hybridization of the metal-Sc system. This phenomenon where the band alignment of a SC in proximity of a metal weakly depends on the metal work function is called Fermi Level Pinning (FLP) (see Sec. 2.1.2).

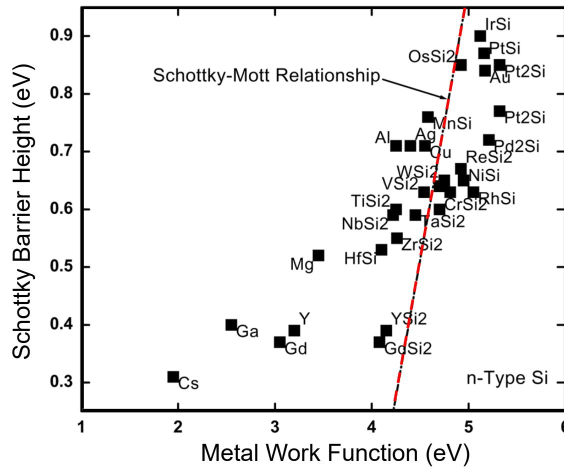

Figure 2.2: The experimentally extracted SBH for different metals on n-type Si. Dashed straight line is Schottky-Mott prediction. The figure is adapted from [89].

The lack of dangling bonds at the 2D surfaces may raise expectations for a weak FLP at the metal-2D interface and, thus, for a good control of the SBH with the metal work function. However, the slope of the SBH versus work function curves has been experimentally reported to be as small as 0.09 (Fig. 2.3) for the case of MoS_2 [81, 90]. Despite the fact that the measured FLP in the experiments may be mainly caused by

defects in the 2D structure [81], even for an ideal 2D layer several reports based on Density Functional Theory (DFT) calculations predicted large densities of gap states [90–92], that contribute to the measured FLP in actual test structures and, moreover, set a lower limit for the FLP in metal-2D systems. Although there are still some doubts or even contradictory theories about the origin of FLP in metal-2D SC interfaces, in the following we report some basics and recent advances about FLP and gap states.

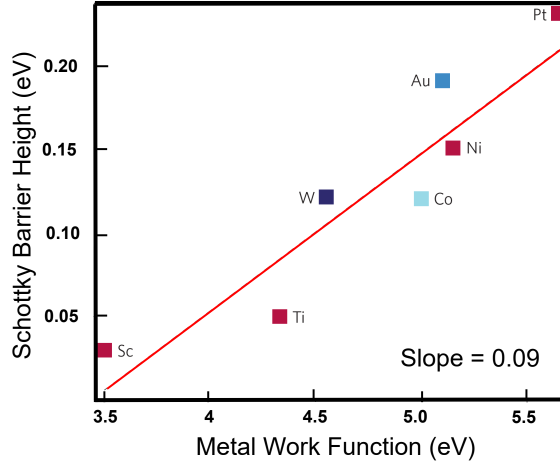

Figure 2.3: The extracted SBH of different metals in contact with multilayer MoS_2 . Adapted from [81]

2.1.2 Fermi level pinning

To achieve a high quality contact between metal and 2D SC, the ability to tune the SBH by metal work function is vital. However, as noted earlier, most often contacting a metal to 2D SC results in pinning of Fermi level inside the band gap of SC. The presence of available states at energy levels corresponding to the bandgap of the SC at the interface between metal and the 2D SC are responsible for FLP and for the resulting deviation of SBH from the Schottky-Mott rule. In this case, the SBH for the electron is characterized quantitatively as [93]:

$$\Phi_{electron} = S(\phi_M - \phi_S) + (\phi_S - \chi_{SC}) = S\phi_M + c \tag{2.3}$$

with ϕ_S defined as the charge neutrality level and S is the pinning factor. Both ϕ_S and ϕ_M are referred to the vacuum level. These parameters can be used as a characteristic of the interface where S is defined as the slope $(d\phi_{electron}/d\phi_M)$, ranging from $S = 0$ for a pinned interface (Bardeen limit) to $S = 1$ for an unpinned interface (Schottky limit). The hyper parameter c is related to the charge neutrality level, defined as the energy above which the states of a neutral surface are empty. In other words, the charge neutrality level is the energy at which the Fermi level of the metal is pinned. By using the following equation, ϕ_S can also be extracted [93]:

$$\phi_S = \frac{\chi_{SC} + c}{1 - S} \tag{2.4}$$

The alignment of the bands at a metal-SC interface depends on the charge transfer across the interface. Interface states in the SC band gap may be responsible for this charge transfer [93].

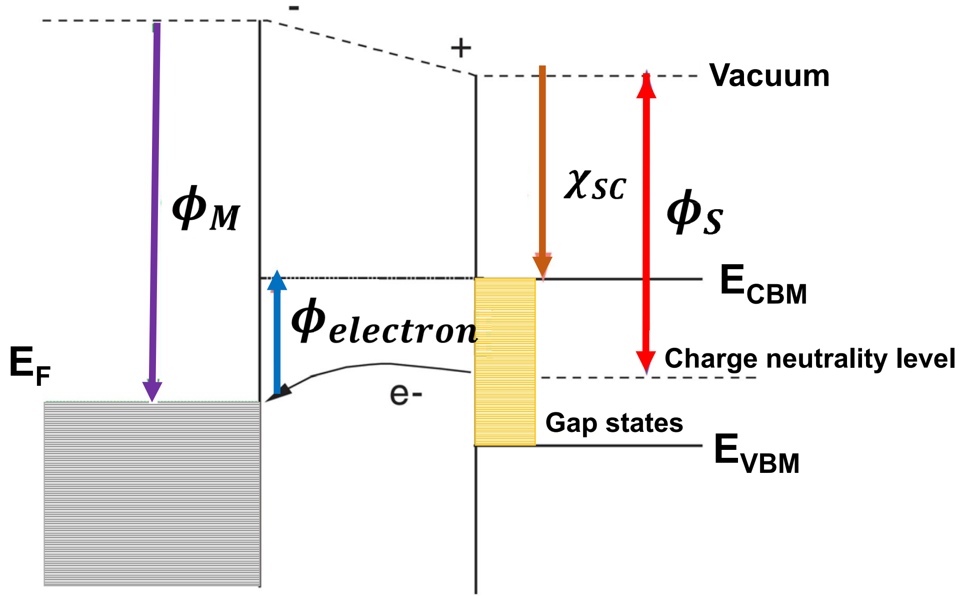

Figure 2.4: Charge transfer between the metal Fermi level and the 2D SC gap states. Adapted from [93]

In order to de-pin the Fermi level and to design the SBH through the choice of the proper metal contact, it is necessary to understand the physical mechanisms that govern this effect. Several models for explaining this phenomenon between 2D SCs and metals have been proposed, including the well-known metal-induced gap state model and the external disorders/defects induced gap state model, as well as those referring to interface dipoles and other impact variables [94]. There is a reasonable consensus that the gap states in the SCs can be considered the main origin of FLP.

2.1.2.1 Metal-induced gap states (MIGS) and defect-induced gap state (DIGS)

After contacting the metal electrode to the SC, intrinsic states inside the band gap of the SC appear, which are the virtual gap states generated owing to the exponential decay of the metallic wavefunction from the metal-SC interface into the SCs [95]. These states are called metal-induced gap states and are similar to the dangling bonds on the conventional 3D SCs [93, 96]. By knowing the density of interface states (N) and the interface state decay depth (λ), the pinning factor (S) can be extracted using the linear response model [93]:

$$S = \frac{1}{1 + (e^2 N \lambda / \epsilon \epsilon_0)} \tag{2.5}$$

where ϵ_0 is permittivity of vacuum, ϵ is SC dielectric constant in the interface, and e is the electronic charge. Experimentally, it can also be shown that [96, 97]:

$$S \propto \frac{1}{1 + 0.1(\epsilon_\infty - 1)^2} \tag{2.6}$$

which $\epsilon_\infty - 1$ is the electronic polarizability of the SC. For ideal and defect free surface of 2D crystals, the FLP is mainly caused by metal-induced gap states, however, regardless of fabrication process, it is hard to avoid the formation of defects on 2D SCs, so in order to have a dependable evaluation of FLP strength, an estimation of defects at the interface is indispensable [98]. In Eq. 2.5, the interface states can be both MIGS and DIGS.

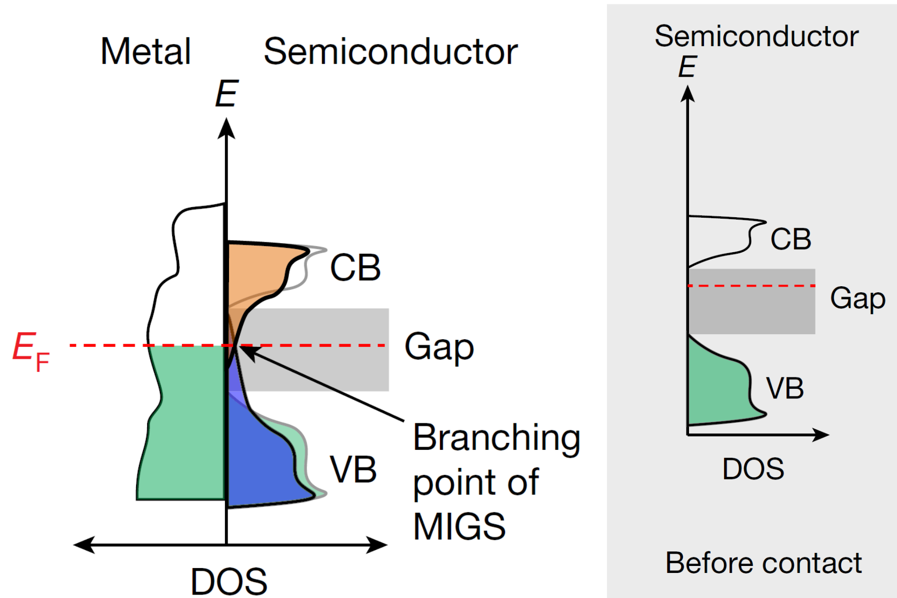

Figure 2.5: Left figure, the density of states at metal-SC interface. The conduction band and valence band contribute to the metal induced gap states and are as orange and blue areas, respectively. The Fermi level is pinned at around the branching point of the MIGS. Electron-occupied states are depicted as green area. Right figure is the density of states of SC before contacted to the metal. Adapted from [85].

The defects induced during the SC fabrication process can lead to the formation of dangling bonds. The superimposition and interaction of the dangling bond and metal states at the interface result in the formation of states in the SC band gap which are known as defect-induced gap state [98]. For instance, according to [93], in the case of MoS_2, the S vacancies, due to their lower formation energy are the responsible for DIGS and contribute to the FLP.

2.1.3 Carrier injection mechanism

There are three types of carrier injection mechanisms from metal electrodes into SCs: thermionic emission, field emission and thermionic field emission. Using n-type 2D SC as an example, the thermionic emission allows carriers to overcome the Schottky barrier, current based on thermionic emission can be described as follows [99]:

$$I_{2D} = WA^*_{2D}T^{3/2}exp(-\frac{e\phi_B}{k_BT})exp(\frac{eV}{\eta k_BT})[1 - exp(\frac{eV}{k_BT})] \tag{2.7}$$

where:

$$\phi_B = \phi_{eelctron} + e\Psi_S \tag{2.8}$$

A^*_{2D} is modified Richardson constant, W is the channel width, ϕ_B is the effective thermal injection barrier, η can be defined as the ideality factor, $e\Psi_S$ is the surface potential of SC and V is the applied voltage bias to the contact.

Concerning the current through the metal-2D SC contact, carriers can tunnel through the SC; based on the tunneling barrier height, this process can be divided into two different mechanisms (see Fig. 2.6). When the barrier is wide, the carrier injection mechanism can be modeled as a thermionic field emission (TFE), whereas tunneling through the

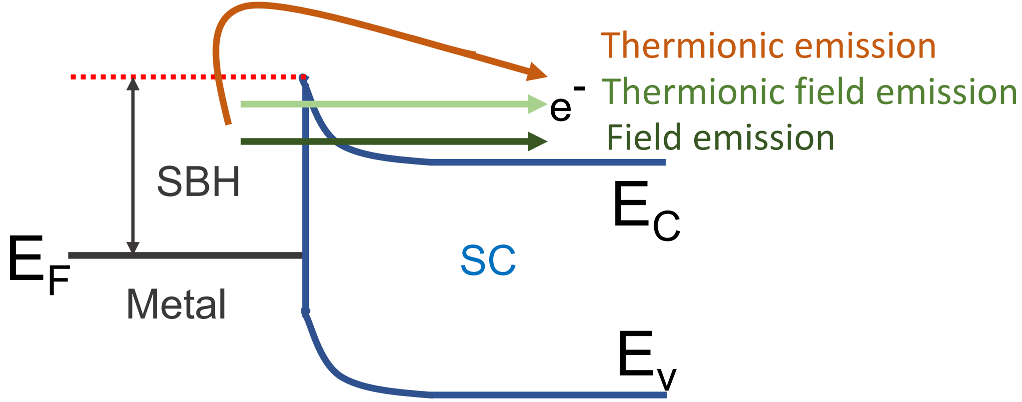

Figure 2.6: Various types of carrier injection mechanisms between metals and 2D SCs.

thin barrier is based on field emission (FE). The current based on TFE and FE can be respectively approximately expressed as:

$$I_{TFE} = \frac{A_{eff}e^3m_0V^2}{8\pi h_{SB}d^2m^*}exp\left(\frac{-8\pi d\sqrt{2m^*\phi^3_{electron}}}{3heV}\right) \tag{2.9}$$

$$I_{FE} = \frac{A_{eff}e^2V\sqrt{2m^*\phi_{electron}}}{h^2d}exp\left(\frac{-4\pi d\sqrt{2m^*\phi_{electron}}}{h}\right) \tag{2.10}$$

where A_{eff} is defined as an effective contact area, d as the Schottky barrier width, m_0 as the free electron mass and m^* is the electron effective mass inside the barrier. According to these equations, current-voltage relationship can help explain which mechanism dominates the carrier injection [94].

2.2 Simulation methodology

To describe the physical properties of a system at the atomic scale, in principle we need to solve the Schrodinger equation for many body systems. However, the exact solution of Schrodinger equation for a multi-particle system is practically impossible. In order to tackle this problem, instead of using the wave function of the many body system, we could make the problem smaller by using the spatially dependent electron density. Walter Kohn showed in 1964-65 that the ground state of a quantum-mechanical system is uniquely determined by its electron density. Kohn also provided a method which made it possible to set up equations whose solutions give the system's electron density and energy [100, 101]. This method is called Density Functional Theory (DFT); this name comes from the use of functionals of the electron density to describe the system. This

tool is among the most popular and versatile methods available in condensed-matter physics, computational physics, and computational chemistry.

2.2.1 Density functional theory

Since electron is much lighter than nuclei, with the same amount of kinetic energy, the velocity of electrons is much faster than that of nuclei. It can be assumed that electrons reach the lowest energy state much faster than nuclei so it is possible to treat the wave functions of atomic nuclei and electrons separately, therefore, the motion of electrons can be studied independently and their ground state will be estimated. This separation of electron and nucleus motion is known as the Born-Oppenheimer approximation:

$$\hat{H} = -\frac{1}{2}\sum_{i}\nabla_i^2 - \sum_{i}\sum_{\alpha}\frac{Z_\alpha}{|r_i - r_\alpha|} + \frac{1}{2}\sum_{i}\sum_{j\neq i}\frac{1}{|r_i - r_j|}, \tag{2.11}$$

where Z is the atomic number and the indexes α and i are related to the nucleus of atoms and electrons, respectively. The Hamiltonian is expressed in atomic units ($\hbar = m_{electron} = e = 4\pi\epsilon_0 = 1$) and for each state of the system, $|\Psi\rangle$, the minimum energy state $|\Psi_0\rangle$ is:

$$\frac{\langle\Psi_0|H|\Psi_0\rangle}{\langle\Psi_0|\Psi_0\rangle} \leq \frac{\langle\Psi|H|\Psi\rangle}{\langle\Psi|\Psi\rangle}. \tag{2.12}$$

This can be used to calculate the ground state of electrons; the many-electron Hamiltonian can be defined as:

$$\hat{H} = \hat{T} + \hat{V}_{ext} + \hat{U}, \tag{2.13}$$

where, for the N-electron system, $\hat{H}$ is the Hamiltonian, $\hat{T}$ is the kinetic energy and $\hat{V}_{ext}$ is the external potential. $\hat{V}_{ext}$ depends on the system under study. Therefore, by knowing N (number of electrons) and $\hat{V}_{ext}$, Hamilton as well as the ground state $|\Psi_0\rangle$ can be determined. The density of electrons for ground state can be written as:

$$n_0(r) = \langle\Psi_0|\hat{n}|\Psi_0\rangle = \int\prod_{i=2}^{N} dr_i|\Psi_0(r_1, r_2...r_N)|^2. \tag{2.14}$$

There are two important points that must be noticed [100]:

- $\hat{V}_{ext}$ can be identified uniquely from the density of ground state.
- For each electron density $n(r)$ in the potential V, the corresponding energy is not less than the energy of ground state:

$$E_V[n] \geq E_0, \tag{2.15}$$

and:

$$E_V[n] = \underbrace{\langle\Psi|\hat{T} + \hat{U}|\Psi\rangle}_{\hat{F}} + \int \hat{V}_{ext}n(r)d^2r. \tag{2.16}$$

Therefore, the ground state of a many-electron system can be turned into an optimization problem. Operator F is defined in terms of density function as follows:

$$F[n] = min\langle\Psi|\hat{F}|\Psi\rangle. \tag{2.17}$$

That is, the minimum expected value of $\hat{F}$ on the wave function Ψ, which is a functional of the density (n). An important result of DFT is the existence of a function that is

independent of the external potential ($\hat{V}_{ext}$). Instead of the wave function of entire system (a function of the 3N variable), the total density (a function of the 3 variables) is used, however, the exact form of $\hat{F}$ is unknown. Thomas-Fermi suggested the form of $\hat{F}$ as follows:

$$F_{TF}[n] = \frac{3}{10}(3\pi^2)^{\frac{2}{3}} \int n^{\frac{5}{3}}(r)dr + \frac{1}{2}\int\int \frac{n(r)n(r^{'})}{|r-r^{'}|}drdr^{'}. \tag{2.18}$$

2.2.1.1 Kohn-Sham equations

The Kohn-Sham equations can be written by adding the total number of electrons and minimizing the energy under the constraint with Lagrangian coefficients as follows:

$$\delta\left[F[n] + \int V_{ext}(r)n(r)dr - \underbrace{\mu\left(\int n(r)dr - N\right)}_{constraint}\right] = 0. \tag{2.19}$$

Kohn divides the $F[n]$ into three parts:

$$F[n] = T_s[n] + \frac{1}{2}\int \frac{n(r)n(r^{'})drdr^{'}}{|r-r^{'}|} + E_{XC}[n]. \tag{2.20}$$

T_s is the kinetic energy of a non-interacting electron system with the density of n, the second term is the classical electrostatic energy (Hartree), and the last term is exchange energy, and also the sum of the errors due to the difference of kinetic energy of non- and interacting electron system. The purpose of this separation is that the first two terms can be expressed simply and the difficult term E_{XC} is approximated as part of the total energy. Thus, the Kohn-Sham equation can be written as follows:

$$\frac{\delta T_s[n]}{\delta n(r)} + V_{KS}(r) = \mu, \tag{2.21}$$

and:

$$V_{KS}(r) = \int \frac{n(r^{'})}{|r-r^{'}|}dr^{'} + V_{XC}(r) + Vext(r), \tag{2.22}$$

$$V_{XC}(r) = \frac{\delta E_{XC}(n)}{\delta n(r)}, \tag{2.23}$$

Eq. 2.21 will has the same form for the state of non-interacting particles in the presence of the field $V_{KS}(r)$. To find the ground state of the non-interacting system, the Schrodinger equation must be solved:

$$[\frac{-1}{2}\nabla^2 + V_{KS}(r)]\psi_i(r) = e_i\psi_i(r), \tag{2.24}$$

where the density of electrons can be written as:

$$n(r) = \sum_i |\psi_i(r)|^2, \tag{2.25}$$

and the non-interacting kinetic energy:

$$T_s[n] = \frac{-1}{2}\sum_i \int \psi_i(r)\nabla^2\psi_i(r)dr. \tag{2.26}$$

Since the Kohn-Sham potential V_{KS} depends on the density, and on the other hand, the calculated density depends on V_{KS}, the Kohn-Sham equation must be solved iteratively. The summation of one-electron eigenvalues e_i:

$$\sum_i e_i = T_s[n] + \int n(r)V_{KS}(r)dr, \tag{2.27}$$

$$\sum_i e_i = T_s[n] + \int\int \frac{n(r)n(r')}{|r-r'|}drdr' + \int n(r)V_{XC}(r)dr + \int n(r)V_{ext}(r)dr \tag{2.28}$$

Where in comparison with the energy of system with interaction, the second term (Hartree energy) is two times larger and the third term must be replaced by $E_{XC}[n]$; then the energy of a system with interaction can be described as:

$$E = \sum_i e_i - \frac{1}{2}\int\int \frac{n(r)n(r')}{|r-r'|}drdr' - \int n(r)V_{XC}(r)dr + E_{XC}[n]. \tag{2.29}$$

Identifying E_{XC} is still under many doubts, however, there are some approximations such as local density approximation (LDA):

$$E_{XC}[n] = \int \epsilon_{xc}(n(r))n(r)dr. \tag{2.30}$$

In this approximation, for the exchange and correlation energy of each electron, at each point, it is assumed that it is a function of the density of the electrons at that point, whereas, in generalized gradient approximation (GGA), in addition to the electron density, the gradient of electron density is also included in the calculations.

2.2.1.2 Pseudopotential approximation

When all the electrons of the system are considered, the wave functions of the electrons in the VB oscillate fastly near the nuclei of the atoms. This is because:

- The core electrons (electrons inside the lower energy states) are populated near the nucleus.
- The wave functions of electrons are mutually orthogonal.

In order to maintain this orthogonality the electrons in VB must oscillate rapidly near the nucleus which results in a large kinetic energy. This large kinetic energy cancels the large potential energy due to the strong Coulomb potential. The rapid oscillations are problematic in numerical calculations. On the other hand these electrons, which are highly bound to the nucleus, usually have little effect on the chemical and electrical properties of the material. Therefore, it is convenient to try to replace the strong Coulomb potential and core electrons with a much weaker effective pseudopotential:

$$|\psi\rangle = |\psi_{ps}\rangle + \sum_n^{core} a_n|\phi_n\rangle, \tag{2.31}$$

where ψ is the wave functions of electrons in VB, ψ_{ps} and ϕ_n are pseudopotential and core electron wave functions respectively. As mentioned above, ψ is orthogonal to ϕ_n, so:

$$\langle\phi_m|\psi\rangle = 0 = \langle\phi_m|\psi_{ps}\rangle + a_m, \tag{2.32}$$

$$|\psi\rangle = |\psi_{ps}\rangle - \sum_n^{core} |\phi_n\rangle\langle\phi_n|\psi_{ps}\rangle. \tag{2.33}$$

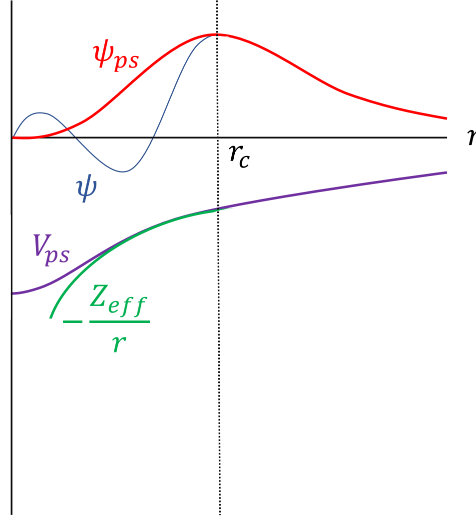

Figure 2.7: Schematic diagram of the relationship between all-electron and pseudopotentials and wavefunctions.

By using Schrodinger equation:

$$\hat{H}|\psi_{ps}\rangle - \sum_{n}^{core} E_n|\phi_n\rangle\langle\phi_n|\psi_{ps}\rangle = E|\psi_{ps}\rangle - E\sum_{n}^{core}|\phi_n\rangle\langle\phi_n|\psi_{ps}\rangle, \quad (2.34)$$

$$\hat{H}|\psi_{ps}\rangle + \sum_{n}^{core}(E - E_n)|\phi_n\rangle\langle\phi_n|\psi_{ps}\rangle = E|\psi_{ps}\rangle. \quad (2.35)$$

Eq. 2.35 is similar to Schrodinger equation plus a non-local potential term as follows:

$$V_{nl} = \sum_{n}^{core}(E - E_n)|\phi_n\rangle\langle\phi_n| \quad (2.36)$$

The energy of the pseudopotential wave function (ψ_{ps}) is equal to the all-electron wave function (ψ). If the energy difference between the VB state and the core state is large ($\delta E << E - E_n$), then E can be approximated and equal to the energy of the atomic VB state.

2.2.2 Interface modeling

In order to contact metal electrodes to 2D crystals, the first step is to model the interface between the constituent materials. Since the lattice constants of each material are often not identical, when constructing the atomic models great attention must be taken to ensure that strain is minimized [102], because the artificial strain might alter the electronic structure of the two materials. 2D crystals have high sensitivity to strain [20]; for example, altering the lattice parameter of 2D MoS_2 by %1 leads to the change of the band gap by almost 0.1 eV (see Fig. 1.5). However, it is also shown that a small modification of the in-plane lattice constant of the metal surface affects its electronic properties mildly [103]. Therefore, it is a wise choice to adapt the lattice of the metal to that of the 2D SC. To make this clear, here in the following, the procedure also used in [102] to build the

supercells based on 2D MoS_2 and metal lattices is described; this method can be also generalized to make other interfaces.

To build in-plane supercells, basis vector of a metal surface supercell and the MoS_2 surface are indicated as $\vec{T}_1'$ and $\vec{T}_1$, respectively.

$$\vec{T}_1 = n_1\vec{a}_1 + n_2\vec{a}_2 \qquad \vec{T}_1' = m_1\vec{b}_1 + m_2\vec{b}_2 \tag{2.37}$$

where $\vec{a}_1/\vec{b}_1$ and $\vec{a}_2/\vec{b}_2$ are the basis vectors of the primitive cell of the MoS_2 and metal, respectively, and n_1, n_2, m_1, and m_2 are integers. Then we look for sets of integers where the difference between basis vectors of MoS_2 and the metal supercell is smaller than a given target δ:

$$\frac{\left|\vec{T}_1\right| - \left|\vec{T}_1'\right|}{\left|\vec{T}_1\right|} \leq \delta. \tag{2.38}$$

To align the directions of the $\vec{T}_1$ and $\vec{T}_1'$, the MoS_2 lattice has to be rotated by an angle α. Since the lattice is symmetric, by rotating $\vec{T}_1$ by 120°, the second basis vector of the supercell can be obtained. The constructed suppercell is a $\sqrt{N} \times \sqrt{N}$ MoS_2 layer on top of a $\sqrt{M} \times \sqrt{M}$ metal lattice [91], where:

$$N = n_1^2 + n_2^2 + n_1 n_2 \qquad M = m_1^2 + m_2^2 + m_1 m_2 \tag{2.39}$$

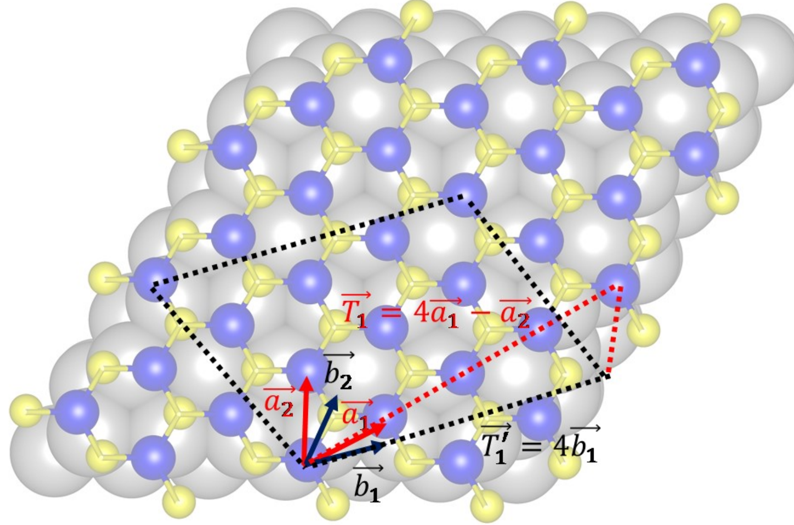

Figure 2.8: The supercell (dotted black lines) in top view of the MoS_2-Al(111) interface, the primitive basis vectors $\vec{a}_1$, $\vec{a}_2$ and $\vec{b}_1$, $\vec{b}_2$ belongs to the MoS_2 and Al(111) lattices, respectively.

It is worth mentioning that in order to choose the parameter δ properly, which is a trade off between size of the supercell and the applied strain, it is necessary to have an estimation about available computational power. In fact it is obvious that larger systems leads to less lattice mismatch and consequently smaller artificial strain, but to a higher computational cost. On the other hand, a small system with a large artificial strain may affect the electronic structure of the heterostructure. Here in Table 3.7, required parameters (Eq. 2.38) for constructing a heterostructre based on MoS_2 and several metals are listed. The mismatch parameter (δ) is chosen to be smaller than 1%.

Table 2.1: Supercell defined by the MoS_2 lattice vector $R(\alpha)\vec{T}_1$. The Table is taken from [91]

Metal	n_1, n_2	m_1, m_2	α	δ(%)
Ag	$4, -1$	$4, 0$	13.9^o	0.15
Al	$4, -1$	$4, 0$	13.9^o	0.5
Au	$4, -1$	$4, 0$	13.9^o	0.15
Co	$5, -4$	$4, -3$	3°	0.01
Cu	$4, 0$	$5, 0$	0°	0.3
Mg	$1, 0$	$1, 0$	0°	0.6
Ni	$5, -4$	$4, -3$	3°	0.8
Pd	$1, 1$	$2, 0$	30°	0.3
Pt	$1, 1$	$2, 0$	30°	0.3
Ti	$5, -2$	$4, 0$	23.4^o	0.7

2.2.2.1 Band unfolding

One of the foremost widely applied analysis tools in the study of electronic structure of crystals, is undoubtedly the electronic band structure. All the basic ingredients to describe the crystal properties (e.g., optical, electrical and magnetic properties, transport) can be extracted from the electronic band structure.

However, in many studies such as the contacts analysis or the evaluation of the effects related to the or introduction of impurities or lattice distortion [104], instead of a primitive unit cell it is necessary to use large supercells. By enlarging the primitive cell and constructing the supercell, the first Brillouin Zone (BZ) of the corresponding supercell shrinks, and the bands of the first BZ of the primitive cell get folded into the first BZ of the supercell (see Fig. 2.9). Generally, it is not trivial to extract information from folded bands, so unfolding the band structure from the shrunk BZ is crucial. For the studies

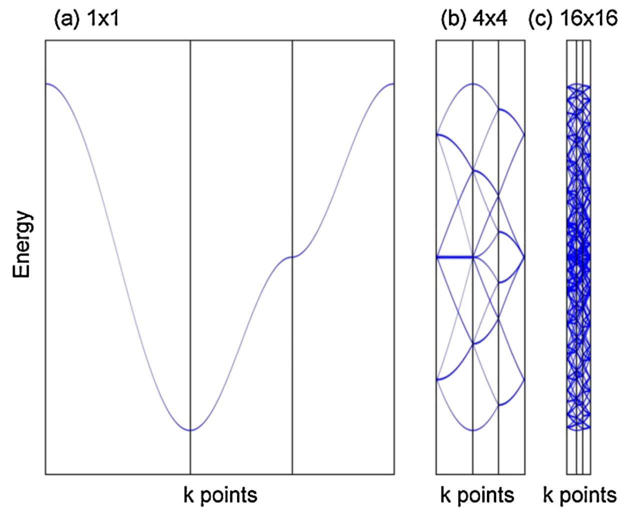

Figure 2.9: Illustration of band folding in the supercell calculations: (a) band structure of primitive cell, (b) the same obtained from a 4×4 supercell calculation, and (c) the same obtained from a 16×16 supercell calculation. This figure is taken form [104].

reported in this thesis, only the positions of Conduction Band Minimum (CBM) and Valence Band Maximum (VBM) in the first BZ of supercell are required, and the unfolding the bands can be a way simpler problem if one considers only the band extremum. In the

following, as an example, the procedure for finding the position of the band extremum of a $\sqrt{3} \times \sqrt{3}$ monolayer MoS_2 is described.

The direct lattice vectors of primitive unit cell of monolayer MoS_2 (Fig. 2.10.a) are:

$$\vec{a_1} = a\hat{x} + b\hat{y} \quad , \quad \vec{a_2} = a\hat{x} - b\hat{y}, \tag{2.40}$$

where:

$$a = \frac{\sqrt{3}a_0}{2} \quad , \quad b = \frac{a_0}{2}, \tag{2.41}$$

the lattice constant of monolayer MoS_2 a_0 is 3.16 angstrom. Hence it is possible to calculate the reciprocal space lattice vectors $\vec{A}_1$ and $\vec{A}_2$ and the first BZ of primitive unit cell (red hexagon shown in Fig. 2.10.b). $\vec{A}_1$ and $\vec{A}_2$ can be calculated as :

$$\vec{A}_1 = \frac{2\pi\,(\vec{a_2} \times \hat{z})}{\vec{a_1} \cdot (\vec{a_2} \times \hat{z})} = \frac{\pi}{a}\hat{k_x} + \frac{\pi}{b}\hat{k_y} \tag{2.42a}$$

$$\vec{A}_2 = \frac{2\pi\,(\hat{z} \times \vec{a_1})}{\vec{a_2} \cdot (\hat{z} \times \vec{a_1})} = \frac{\pi}{a}\hat{k_x} - \frac{\pi}{b}\hat{k_y} \tag{2.42b}$$

$\hat{z}$ is the direction perpendicular to the plane ($\hat{x}$, $\hat{y}$) and ($\hat{k_x}$, $\hat{k_y}$) is the reciprocal space.

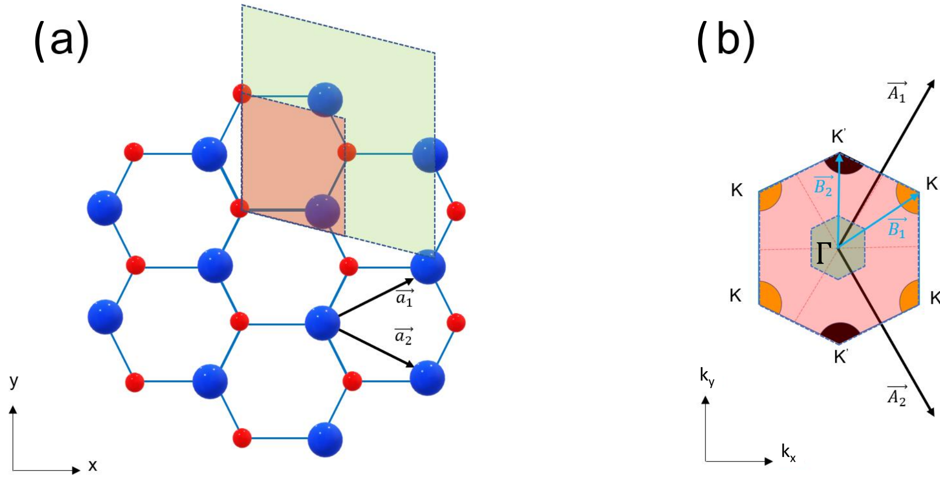

Figure 2.10: (a) Primitive unit cell (red) and $\sqrt{3} \times \sqrt{3}$ (green) of monolayer MoS_2. The real space lattice vectors $\vec{a_1}$ and $\vec{a_2}$ of primitive unit cell are shown. (b) hexagonal first BZ of monolayer MoS_2 and the related reciprocal space lattice vectors. K and $K^{'}$ are the six high symmetry points of monolayer MoS_2 in the primitive unit cell, which are folded into Γ point in shrunk BZ of the monolayer MoS_2 in larger supercell.

The hexagonal first BZ is identified by the following vertices (called K and $K^{'}$ points):

$$\left(0, \pm\frac{2\pi}{3b}\right) \quad , \quad \left(\pm\frac{\pi}{a}, \pm\frac{\pi}{3b}\right).$$

The direct lattice vectors of the supercell ($\sqrt{3} \times \sqrt{3}$ monolayer MoS_2) can be as (see Sec. 2.2.2):

$$\vec{T_1} = \vec{a_1} + \vec{a_2} = \begin{bmatrix} 2a \\ 0 \end{bmatrix} \quad , \quad \vec{T_2} = \begin{bmatrix} \cos\theta & -\sin\theta \\ \sin\theta & \cos\theta \end{bmatrix} \begin{bmatrix} 2a \\ 0 \end{bmatrix} \tag{2.43}$$

where $\theta = \frac{2\pi}{3}$. The reciprocal space lattice vectors $\vec{B}_1$ and $\vec{B}_2$ are:

$$\vec{B}_1 = \frac{\pi}{a}\hat{k_x} + \frac{\pi}{3b}\hat{k_y}, \tag{2.44a}$$

$$\vec{B}_2 = \frac{2\pi}{3b}\hat{k_y}. \tag{2.44b}$$

The first BZ of the supercell is shown in Fig. 2.10.b (green hexagon).

As shown in Fig. 2.10, the K and K' (at the edge of first BZ of the primitive unit cell) are located outside of first BZ of the supercell. More precisely the K and K' points of the primitive unit cell coincide with the reciprocal space vectors $\vec{B}_1$ and $\vec{B}_2$, consequently the K and K' are folded at the center (Γ point) of the BZ of the $\sqrt{3} \times \sqrt{3}$ supercell. Therefore, by this folding, the VBM and the CBM are located at Γ point (Fig. 2.11.b).

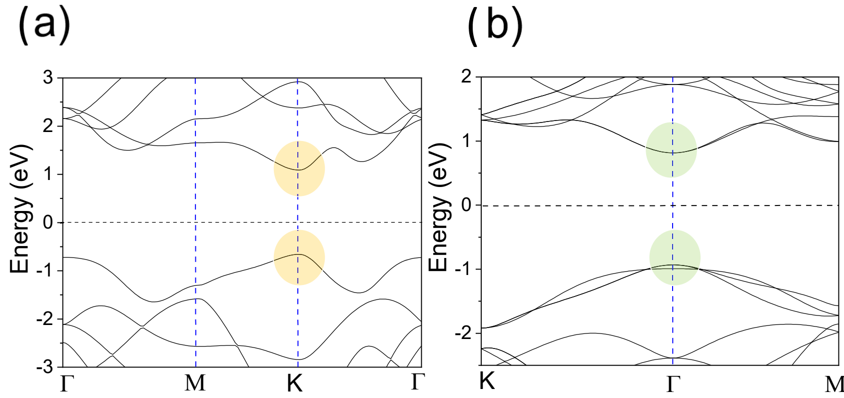

Figure 2.11: (a) Band structure of a free-standing MoS_2 monolayer in primitive unit cell, where the direct band gap is located in K; (b) band structure of a free-standing MoS_2 monolayer in a $\sqrt{3} \times \sqrt{3}$ cell, where the direct band gap is located in Γ.

2.2.3 Quantum Transport

In order to extend the rigour of the DFT method to transport calculations, we obtained the conductance across the heterostructures in Fig. 2.12 by employing the *ab-initio* quantum transport methodology based on the Non Equilibrium Green's Functions (NEGF) approach presented in [105].

The method starts from the plane-wave DFT Hamiltonian in Quantum ESPRESSO, and reduces the size of the Hamiltonian blocks by transforming first to the hybrid basis xK_{yz} space (consisting of real-space along the transport direction x and plane waves in the (y,z) directions [106]), and then to a basis set consisting of unit-cell restricted Bloch functions (URBF). Originally conceived for homogeneous systems, the method in [105] has been extended to deal with the heterostructures in Fig. 2.12, consisting of the (semi)metal, the vertical heterojunction (VHJ), and finally the 2D semiconductor. In order to efficiently simulate such heterostructures we used the following methodology. First the Hamiltonian blocks $[\mathbf{H}_{00}^{(i)}]_\Phi$, $[\mathbf{H}_{01}^{(i)}]_\Phi$ in the URBF basis were extracted for each sub-system ($i = 1, 2, 3$) as described in [105]. Then the Hamiltonian blocks $[\tilde{\mathbf{H}}_{01}^{(i,i+1)}]_\Phi$ describing the coupling between two adjacent sub-system i and $(i+1)$ (see Fig. 2.12.b) are approximated as $[\tilde{\mathbf{H}}_{01}^{(i,i+1)}]_\Phi \approx [\mathbf{U}_i]_\Phi^\dagger [\mathbf{H}_{01}^{(i+1)}]_{xK_{yz}} [\mathbf{U}_{i+1}]_\Phi$, where $[\mathbf{U}_i]_\Phi$ is a unitary matrix

whose columns are given by the URBF of the i-th material [105]. Here we notice that $[\tilde{\mathbf{H}}_{01}^{(i,i+1)}]_\Phi$ may also be calculated by using the $[\mathbf{H}_{01}^{(i)}]_{xK_{yz}}$ of the sub-system i, namely as $[\tilde{\mathbf{H}}_{01}^{(i,i+1)}]_\Phi[\mathbf{U}_i]_\Phi[\mathbf{H}_{01}^{(i)}]_{xK_{yz}}[\mathbf{U}_{i+1}]_\Phi$. We verified that, for the systems studied in this work, the current obtained for such two definitions of $[\tilde{\mathbf{H}}_{01}^{(i,i+1)}]_\Phi$ is very similar, because the coupling between the atoms present in both sub-systems and actually carrying the current is similar in both cases. Once the blocks of the Hamiltonian matrix in the reduced URBF basis have been determined, the transmission and the current, I_C, across the (semi)metal-MoS_2 contacts were calculated by using standard NEGF algorithms. We verified that a dependable I_C value can be obtained by sampling the Bloch vector k_y in the periodic direction with a $0.1\,[2\pi/b]$ step.

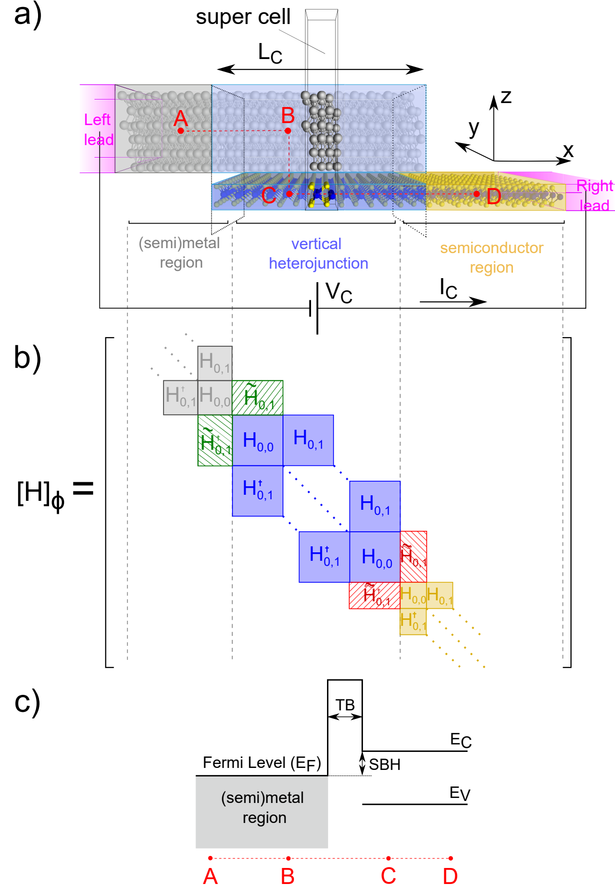

Figure 2.12: Metal- or semimetal-MoS_2 heterostructures analysed in this work, where x, y and z denote respectively the transport direction, the periodic or contact width direction, and the direction of the VHJ. (a) Sketch of the simulated structures consisting of the (semi)metal region at the left, the MoS_2 region at the right, and the actual (semi)metal-MoS_2 heterostructure in the center. (b) Sketch of the block tridiagonal Hamiltonian matrix along the (semi)metal-MoS_2 heterostructure, where $[\tilde{\mathbf{H}}_{01}^{(i,i+1)}]_\Phi$ are the Hamiltonian blocks describing the coupling between two adjacent sub-systems. (c) Simplified sketch of the band diagram along the A-B-C-D path.

2.2.4 Assessment of the simulation methodology

Quantum ESPRESSO was used to study the contact properties between a metal and graphene/MoS_2 by means of DFT. We first started our analysis of metal-2D contacts from heterostructures based on graphene, three-layer-thick clusters for Ni, Cu and Au contacts have been built and the 111 metal surface has been matched with the graphene lattice, which primitive cell has an in-plane lattice constant of $a = 0.246$ nm [107] (Fig. 2.14). We

verified that the three metal layers are sufficient to develop a band structure consistent with the bulk metallic material (not shown).

Then we moved to the study of the most mature 2D semiconductor, by building some heterostructures based on MoS_2 and either metals or semimetals [108]. For these case studies, for each heterostructure we selected the proper surface of a six-layer metal crystal to be matched to the MoS_2 monolayer supercell (x-y plane, Fig. 2.13) so as to minimize strain [91].

The supercells also include a vacuum region along z and dipole correction is applied to minimize the spurious coupling with periodic replicas of the supercell [108].

In general we employed Projector augmented-wave (PAW) pseudopotentials to describe the electron-ion interactions and the PBE (Perdew-Burke-Ernzerhof) exchange-correlation functional with Grimme vdW dispersion corrections. We added to the simulated systems also a back-gate in order to apply an electric field to the heterostructure along the z direction (Fig. 2.13.b) [109–111].

We applied relaxation to all the analyzed heterostructures in order to reduce residual forces on atoms [112]. In this respect, when considering the metal-MoS_2 systems featuring 6 layers of metal,Simulations fixing the position of the top metal layers have been reported in literature [91,92] where only few metal layers close to the MoS_2 are relaxed (Fig. 2.13.a). However, this may lead to artifacts in the dipole analysis. In fact, the dipole correction procedure uses an energy step (ΔV) to zero the field in vacuum [108]. Such (ΔV) value is often considered a measure of the charging of MoS_2 and it is also used to calculate the SBH [91]. But in the setup of Fig. 2.13.a, the metal slab alone (MoS_2 is removed) has a sizeable ΔV in vacuum (black line, Fig. 2.15.a), because of the redistribution of charges due to the mixture between fixed and relaxed atomic positions. The spurious ΔV of metal alone affects the ΔV and the SBH of the entire MoS_2-metal stack (red line), which has sometimes led to artifacts in the SBH extraction [91, 92]. A more dependable

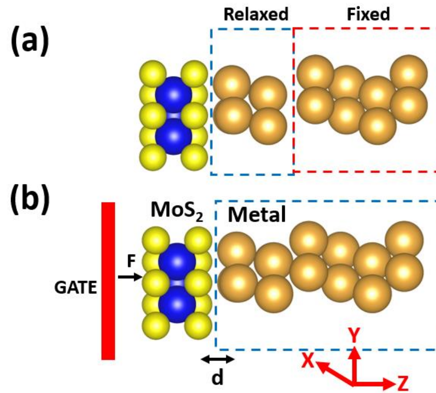

Figure 2.13: Simulation methods: (a) as in [91, 92] four metal layers are fixed and the two metal layers adjacent to MoS_2 are relaxed. (b) This thesis: fully relaxed stack. Here d is the metal-MoS_2 distance. A back gate is included to bias the system.

simulation procedure consists in relaxing the position of all atoms (Fig. 2.13.b), and it has been used throughout this work. The metal slab alone now shows $\Delta V = 0$ in vacuum (black, Fig. 2.15.b). Thus the ΔV value of the entire MoS_2-metal stack (red) is a genuine signature of the dipole in the contact.

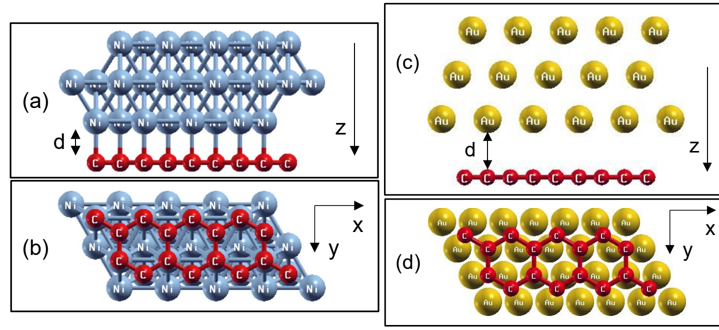

Figure 2.14: (a) Lateral and (b) bottom view of the simulated Ni-G structure. A 1×1 graphene cell with a lattice constant of $a = 0.246$ nm is considered. For the Cu-G stack, we used the same cell. (c) Lateral and (d) bottom (view of the simulated Au-G structure. The Au lattice is matched with a 2×2 graphene supercell [107].

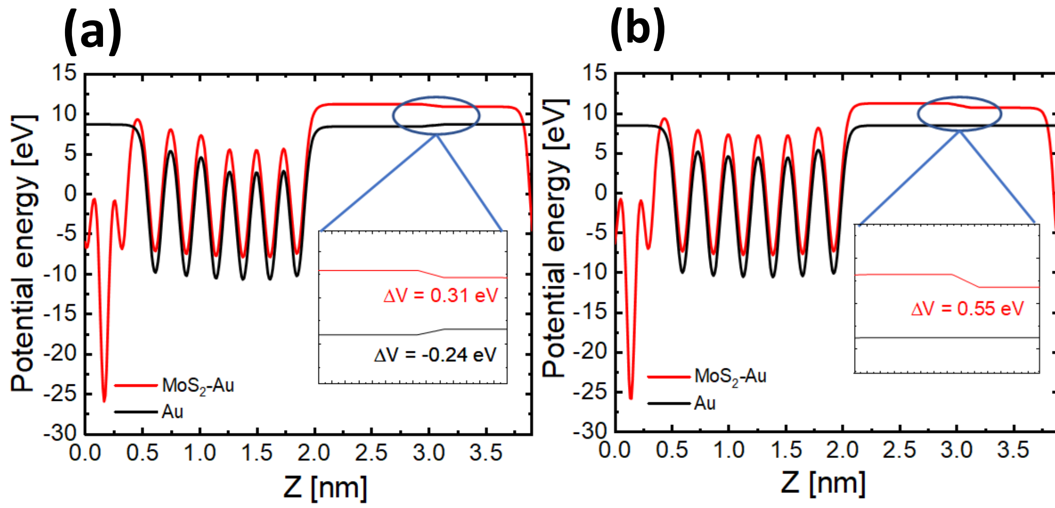

Figure 2.15: Potential energy profiles of either Au alone or the MoS_2 stack. Steps in vacuum are used to zero the electric field due to dipoles in the stack. (a) Simulations as in Fig. 2.13.a, where the non-homogeneous Au alone displays dipole effects (black line), affecting also the MoS_2-Au result (red line). (b) Results from the simulations as in Fig. 2.13.b. Au alone does not display any dipole effect.

2.3 Contacts between metal and graphene

For a proper contact engineering, the physics underlying the conduction through the M-G contacts needs to be completely understood. Therefore, we made use of the DFT simulations described above to interpret the experimental R_C values obtained for graphene in contact with different metal materials [113]. Figure. 2.16 reports the contact resistance values measured on back-gated TLM structures with contacts to graphene fabricated with nickel, copper and gold. Details concerning the measured devices and the exploited characterization technique can be found in [114,115]. As it can be seen, R_C largely depends on the applied back-gate voltage V_{BG}. Furthermore, despite the similar graphene quality between the different samples (not shown) [109], the R_C values do depend on the metal contact, with larger R_C values for Ni and smaller R_C values for Au. This indicates that the M-G interactions influence the electrical properties of the M-G contact, which is not a surprising result also in the view of the discussions reported in the previous sections [116].

The energy bands of the (a) Cu-G and (b) Au-G stacks at Minimum energy Distance (MD) are shown in Fig. 2.17, these bands are simply the superimposition of metal and graphene bands (not shown) and no hybridization of the metal and graphene orbitals is expected [107]. Here, the typical Dirac cone of graphene at the K point is clearly visible. Furthermore, opposite spin states are degenerate, because Cu, Au and graphene are diamagnetic. Figure. 2.18 shows instead the energy bands of the Ni-G structure at two Ni-G distances: (a) MD $d = 0.21$ nm and (b) $d = 0.3$ nm. Spin degeneracy is here lifted, because Ni is ferromagnetic. The Ni-G interaction is very strong and the hybridization of graphene and Ni orbitals changes the bands compared to isolated materials. Indeed, at the K point, it is no longer possible to identify the Dirac cone of graphene for any of the distances in Fig. 2.18 [107].

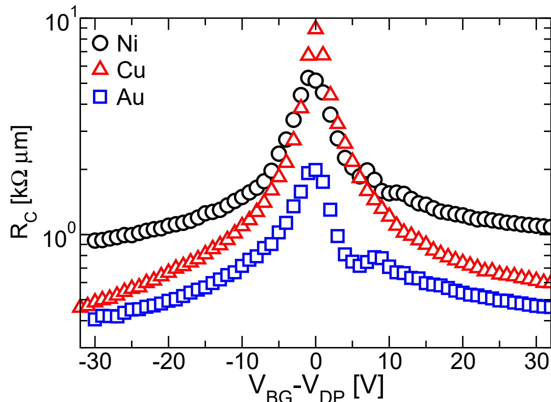

Figure 2.16: Experimental contact resistance R_C as a function of V_{BG} for samples with Ni, Cu and Au contacts. V_{DP} is the V_{BG} corresponding to the Dirac Point, at which the graphene resistance is maximum.

The potential energy calculated along the z direction of the Ni-G stack (perpendicular to graphene, Fig. 2.14) and averaged over the x-y plane (see Fig. 2.19). The energy profiles are reported for different Ni-G distances (d) and they describe the variation of the energy of the two materials when they are approaching. The lower peaks are located at the atom positions and, by reducing d, the graphene peak lowers with respect to the Ni peaks (see Fig. 2.19.b), indicating the charging of the two materials.

The charge transfer due to the chemical interaction between metal and graphene has been extracted (Fig. 2.20) and averaged over the graphene plane for the Cu-G stack (at $d = 0.51$ nm). The interaction between the metal and graphene results in a large charge transfer and consequently, the charge in the graphene underneath the contact affects the R_C values [107]. Thus, there is the need of estimating the graphene doping due to the metal proximity. Since it is not straightforward to distinguish between the charge belonging either to graphene or to the Cu contact [109] it is not possible to evaluate the metal-induced G doping.

To extract a dependable value for the graphene doping, also avoiding spurious contributions by the charge redistribution due to Pauli repulsion [117], we made used of the so-called Bader analysis to calculate the charge variation of each C atom induced by the presence of the metal contact [118]. In particular, Richard Bader from McMaster University developed an intuitive method for dividing molecules into atoms, the Quantum Theory of Atoms in Molecules (QTAIM). His definition of an atom is based solely on the 3D electronic charge density profile. Bader uses zero flux surfaces to subdivide the real space in volumes labeled as the atoms. A zero-flux surface is a 2D surface on which the charge density is minimum. Actually, the charge density usually reaches a minimum

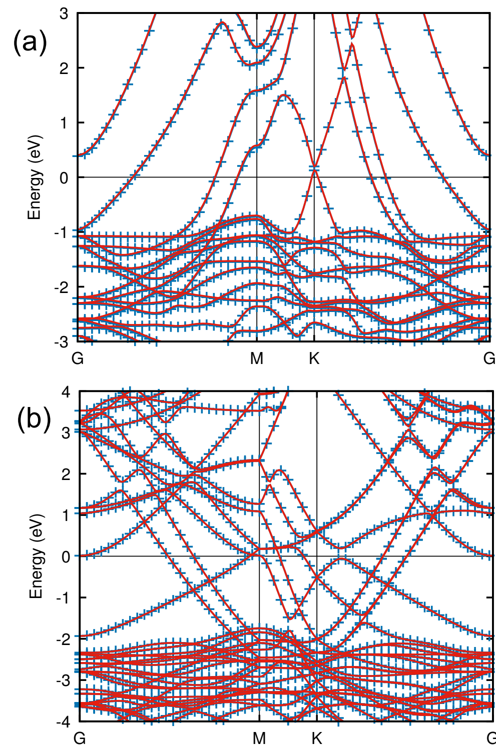

Figure 2.17: Energy bands of (a) Cu-G and (b) Au-G stacks at minimum energy distance ($d = 0.31$ nm). For both cases bands are the superimposion of metal and graphene bands and the Dirac cone is visible at the K point. Note that the Au-G supercell is based on a 2×2 graphene cell, resulting in the folding of graphene bands. Blue crosses/lines are for spin up, red lines are for spin down.

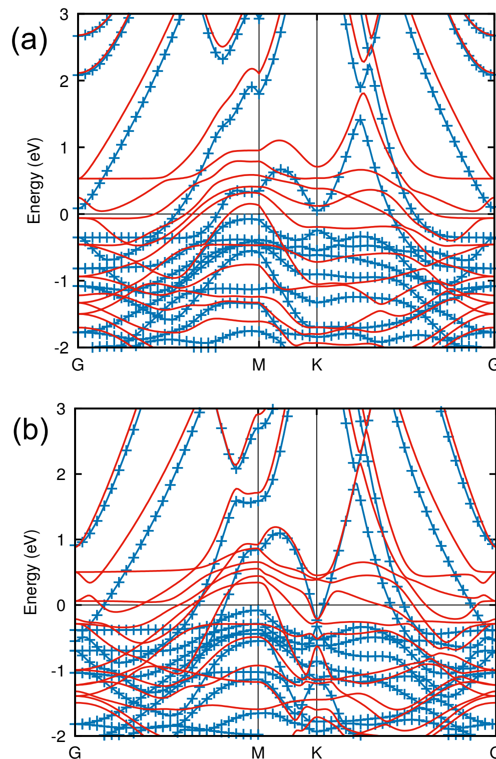

Figure 2.18: Energy bands of Ni-G stack for two d values: (a) MD, $d = 0.21$ nm; (b) $d = 0.3$ nm. Ni induces gaps in graphene and the Dirac cone at the K point vanishes. Blue crosses/lines are for spin up, while red lines are for spin down.

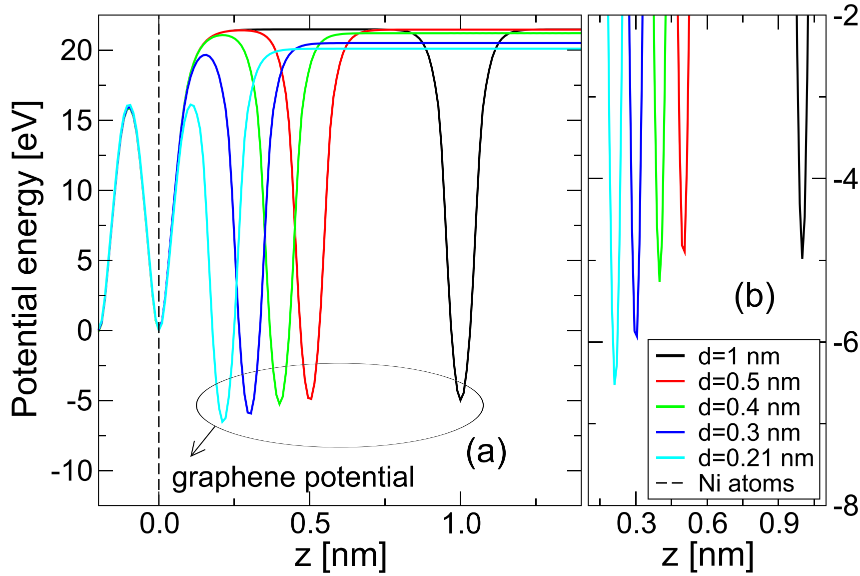

Figure 2.19: (a) d along z (perpendicular to graphene) of the Ni-G stack for different d values. The energy reference has been taken at the Ni atoms position. (b) Zoom in the graphene region. The graphene relative energy with respect to Ni atoms changes when the layers are approaching, indicating the charging of the two materials.

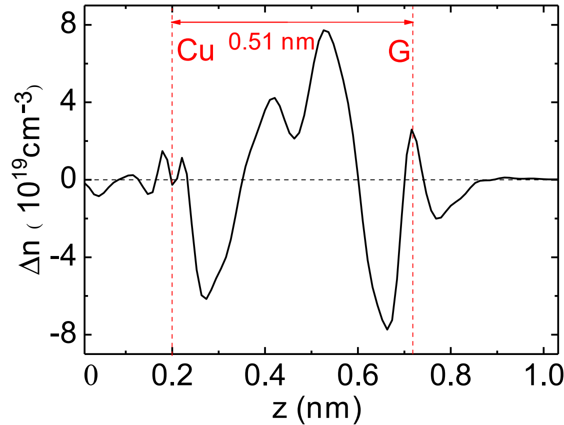

Figure 2.20: Induced net charge along z (perpendicular to graphene) for the Cu-G stack at d = 0.51 nm. Vertical dashed lines are the positions of graphene and of the closest Cu layer.

between atoms in molecular systems, and this is a natural place to be considered as the limit of the volume occupied by atoms [119]. Therefore we used this technique to attribute different portions of space, and the charge contained into such volumes, to the different atoms. Fig. 2.21 shows the calculated doping for the different M-G contacts and for several d values down to the MD of each structure. Cu and Ni induce n-type doping in graphene, while, for the Au contact, graphene becomes p-type [117]. It is evident that, at small d, the metals largely dope the graphene, with a huge doping value in the case of the Ni-G stack at MD. However, under these circumstances, it becomes difficult to interpret the Ni-G stack in terms of a Ni and a graphene sub-systems, because of the strong hybridization of the two materials already discussed in Fig. 2.18.

Fig. 2.21 demonstrates the very different dependence on d of the induced graphene doping for the different metals, with a very long range interaction between Au and graphene. For Ni and Cu, instead, the interaction with graphene has a much shorter range. This trend for distances larger than the MD is consistent with the experimental results of

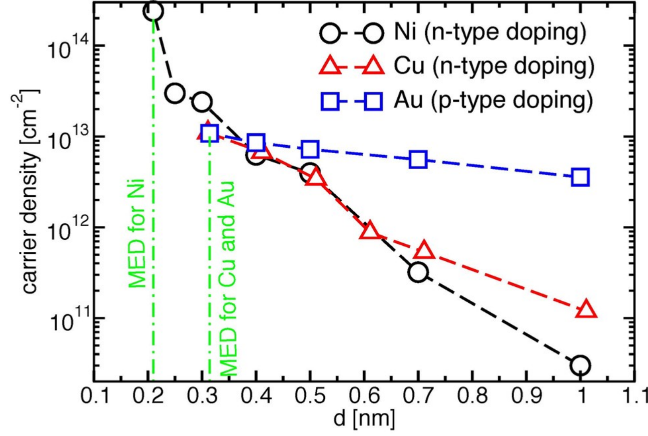

Figure 2.21: Graphene doping as a function of the distance d, calculated through Bader analysis. Au-G contact shows long range interaction, while Ni-G and Cu-G stacks show shorter range interactions. MD values are highlighted for the three M-G contacts.

Fig. 2.16. Indeed, the Au-G stack shows the lowest R_C values suggesting a significant doping of graphene, while the Ni-G system has the worst R_C, thus indicating a weak Ni-G interaction. The comparison between the experimental R_C behavior and the simulations in Fig. 2.21 suggests that the actual M-G distance in the fabricated contacts is larger than 0.5 nm, thus leading to an inefficient doping of graphene by the Ni (with the worst R_C). Au instead is still effective in doping the underlying graphene (with the best R_C), even at a non optimal Au-G distance. In order to interpret the experimentally observed

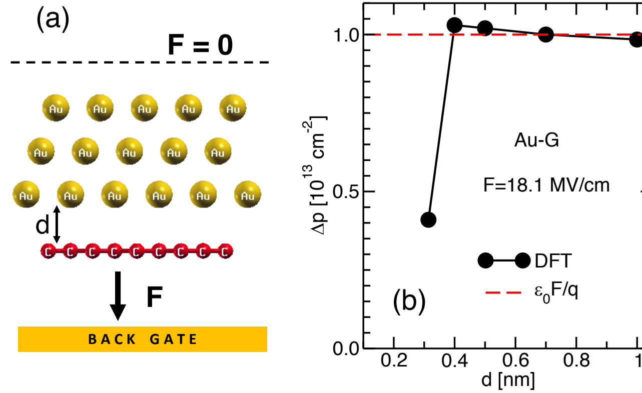

Figure 2.22: Back gated Au-G stack: (a) Sketch of the applied electric field F inducing a total charge $\varepsilon_0 F/q$ in the stack; (b) graphene hole density variation Δp determined via Bader analysis and compared to the total charge $\varepsilon_0 F/q$.

R_C dependence on V_{BG}, we used DFT simulations and Bader analysis to study also the influence on the graphene doping of a back-gate induced electric field F. In particular, as sketched in Fig. 2.22.a, we repeated the analysis in Fig. 2.21 on M-G stacks undergoing the electrostatic effect of gate plate, inducing F along the z direction perpendicular the graphene sheet. The dipole correction option in the Quantum Espresso suite allowed us to apply a non null F only at the graphene side of the M-G stack, thus reproducing an electrostatic configuration similar to that in the experiments [109]. Fig. 2.22(b) reports the F induced variation of the graphene doping (Δp), calculated as the difference between the charge configuration in the Au-G stack subject to the field F and that for the unperturbed stack (with $F = 0$, thus without the gate plate). The results show that,

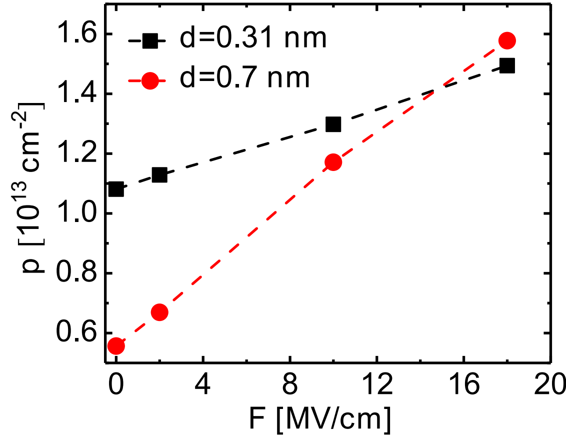

Figure 2.23: Back gated Au-G stack: graphene doping density p determined via Bader analysis at different back-gate electric fields F for two Au-G distances. At MD, the gold contact is more effective in defining the doping of the underlying graphene, also reducing the p dependence on F.

for $d \geq 0.4$ nm, the Δp accounts for the entire charge $\varepsilon_0 F/q$ induced in the Au-G stack, whereas at the MD $d = 0.31$ nm only about the 40% of $\varepsilon_0 F/q$ is induced in the graphene.

Fig. 2.23 compares the dependence of the graphene doping p on the applied F value, for Au-G stacks at the MD and at $d = 0.7$ nm. At MD, the gold contact is more effective in defining the doping of the underlying graphene, also reducing the p dependence on F, that is more pronounced for $d = 0.7$ nm. Therefore, the large R_C dependence on the V_{BG} bias in the experiments of Fig. 2.16 is consistent with a distance $d \geq 0.4$ nm, such that V_{BG} can still modulate the graphene charge to a large extent.

2.4 Contacts between (semi)metal and MoS$_2$

MoS$_2$ is the most technologically mature 2D semiconductor [120]. Unique properties of 2D MoS$_2$ make it a potential candidate for crossing the limitations in numerous applications [121, 122]. However, as discussed previously, for most applications the quality of the metal-MoS$_2$ contact is critical, with best reported values being in the range $1K\Omega\mu$m [123], which sharply contrasts with the projections of the IRDS roadmap [124], targeting tens of $\Omega\mu$m for nanoscale FETs. The lack of dangling bonds at the MoS$_2$ surface may raise expectations for a weak FLP at the metal-MoS$_2$ interface and, thus, for a good control of the SBH with the metal WF. However, as already discussed in Sec. 2.1.1, the slope of the SBH versus WF curves is small. In this section, we report new DFT results for FLP and SBH in defect free metal-MoS$_2$ contacts. The conditions for Fermi level depinning are also discussed, which is a prerequisite for the engineering of the SBH and the attainment of an Ohmic behavior of the metal-MoS$_2$ contacts. Al, Sc, Ni, Pd, Cr, and Au are commonly used as contact metals due to their fundamental chemical and physical properties (e.g., stability, thermal and electrical conductances). However, to form an Ohmic n-type (p-type) contact to MoS$_2$, the selected bulk metal should have low WF (high WF) to make SBH small enough. Because of the significant lattice mismatch with MoS$_2$, Cr and Ni have been excluded from this analysis. For the others (Al, Au, Pd) the 111-surface of a six-layer 2×2 cell is matched to $\sqrt{3} \times \sqrt{3}$ MoS$_2$ monolayer supercell (Fig. 2.24). After a complete relaxation of the heterostructure, the Minimum energy Distance (MD) between MoS$_2$ and metal has been extracted (see Table.2.2). The charge transfer due to the chemical interaction between metal and MoS$_2$ has been extracted by

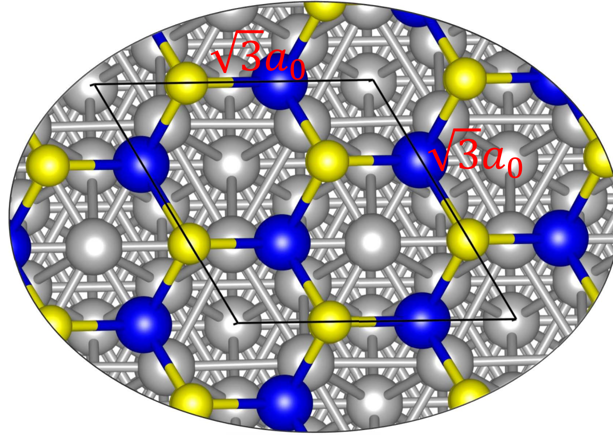

Figure 2.24: 2×2 supercell of Al(111) has been matched to $\sqrt{3} \times \sqrt{3}$ supercell of MoS_2. a_0 is the lattice constant of the MoS_2 primitive unit cell.

Table 2.2: Properties of various metal-MoS_2 contacts.

Metal	Lattice constant (nm)	Calculated WF (eV)	MD (nm)
Sc(0001)	0.33	3.5	0.18
Al(111)	0.29	4.0	0.27
Au(111)	0.29	5.5	0.30
Pd(111)	0.89	5.3	0.25

calculating the difference (Δn) between the valence electron density of the metal-MoS_2 stacks and the isolated metal and MoS_2 layers. The interaction between the metal and MoS_2 induces a non-negligible charge transfer (Fig. 2.25), with the building up of dipoles along the direction perpendicular to the stack ($\Delta n > 0$ corresponds to negative charge, $\Delta n < 0$ indicates positive charge). In this respect, contact properties are expected to be largely impacted by the charge transferred between metal and MoS_2 [107]. So we tried to estimate the MoS_2 doping due to the metal proximity.

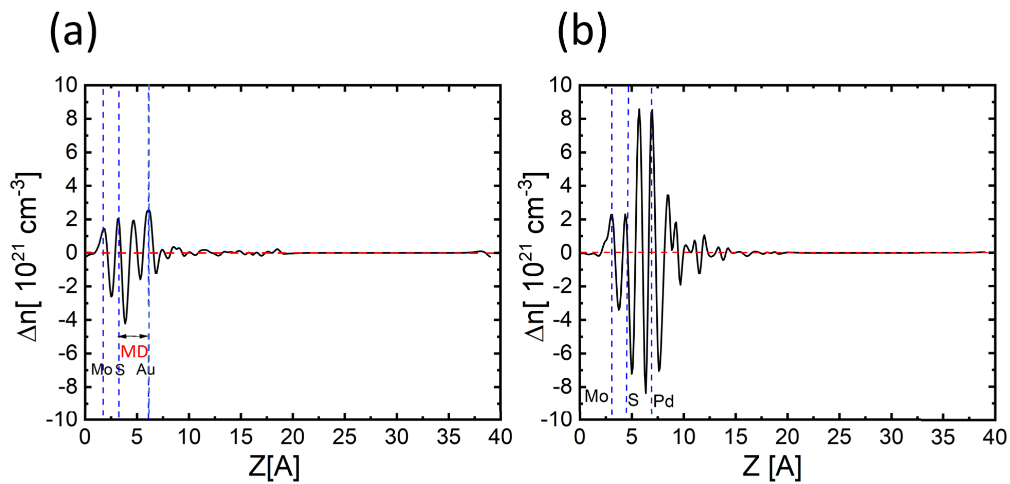

Figure 2.25: Induced net charge along z (perpendicular to the heterostructure) for the (a) Au–MoS_2 ,and (b) Pd-MoS_2 heterostructures at MD. Vertical dashed lines are the positions of atoms.

However, from Fig. 2.25 it is not possible to evaluate the metal–induced MoS_2 doping since it is not straightforward to distinguish between the charge belonging either to MoS_2 or to the metal contact [109]. To make the picture more clear, the Bader analysis was used to calculate the charge variation of each atom induced by the proximity of metal and MoS_2 [118], then we converted this charge into an areal doping density of each structure (Table.2.3).

Table 2.3: Doping of MoS_2 by metal at MD.

	Pd-MoS_2	Au-MoS_2
MoS_2 charge variation [10^{13} cm^{-2}]	7.16	0.80

The Bader analysis indicates that Pd can dope MoS_2 more than Au; this might be the result of a smaller lattice mismatch, and consequently a larger overlap between d orbitals in Pd-MoS_2 heterostructure leading to a better electron injection. However, it also shows that both metals largely n-doped MoS_2 at MD, which is not completely consistent with the results of the PDoS analysis in the following. Figure. 2.26 shows the projected density of states of MoS_2 in Pd–MoS_2 and Au-MoS_2. It is clear that the large density of IGS, especially for the case of Pd, pins the Fermi level well inside the gap of MoS_2, so this should prevent the charging of the MoS_2 layer. So an interpretation of the results in Tab. 2.3 is required. Since Bader analysis spatially partitions the space and attributes these pieces to each atom, the presence of large IGS (which belong to both metal and MoS_2) in such small distances (0.25 nm in Pd–MoS_2) leads to an overestimation of the doping of the MoS_2 layer. Figure. 2.27 shows that by increasing the distance, the charges at the interface drastically decrease due to the reduction of gap states inside the interface. To evaluate the SBH and FLP, the partial density of states (PDoS) of MoS_2 is extracted

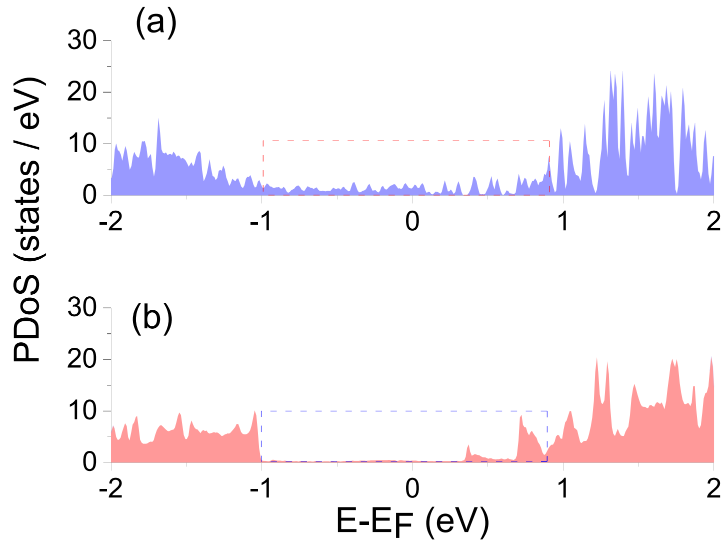

Figure 2.26: PDoS of MoS_2 in (a) Pd–MoS_2 and (b) Au-MoS_2 stack at MD. The Fermi energy set to zero. The dashed boxes indicate the expected bandgap of MoS_2. Gap states (e.g. the peaks inside the dashed boxes) are responsible for charge exchanging with metal.

for different distances. d (Fig. 2.13), between MoS_2 and the metal. Figure. 2.28 shows the PDoS of MoS_2 in Au-MoS_2 stack at two different distance. For $d = 0.8$ nm (Fig. 2.28.a), the PDoS of the MoS_2 layer is consistent with the isolated material ($E_{gap} \simeq 1.8$ eV), with no Interface Gap States (IGS). Moreover, by defining the SBH for electrons/holes

($\phi_{electron}/\phi_{hole}$) as the difference between the conduction/valence band (CB/VB) edge and the Fermi level (E_F), the extracted SBH agrees well with the Schottky–Mott rule with a work function $\phi_m = 5.5$ eV for Au and a MoS_2 affinity of 4.2 eV. For shorter d values (Fig. 2.28.b), instead, the IGS density increases considerably, thus pinning E_F and affecting the SBH.

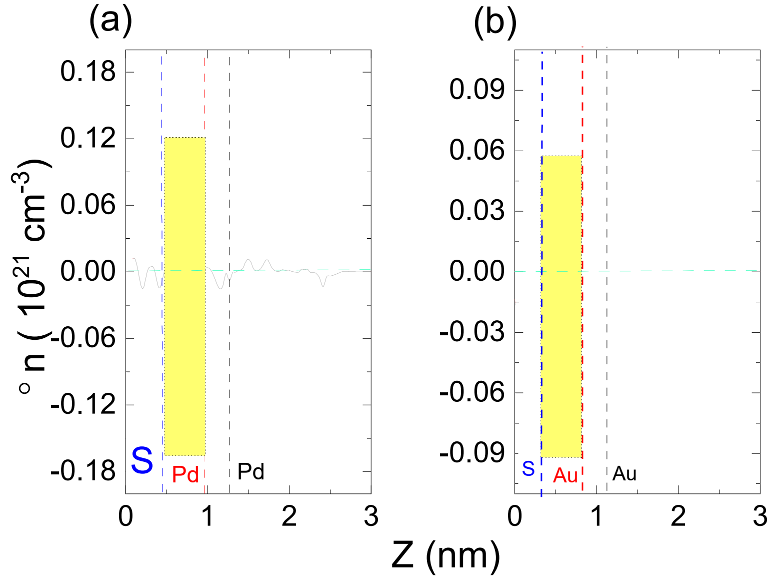

Figure 2.27: Induced net charge along z (perpendicular to the heterostructure) in (a) Pd–MoS_2 and (b) Au–MoS_2 heterostructures at different distances, the red and black solid lines are the net charge for $d = 0.5$ nm and $d = 0.8$ nm respectively. Remaining charge at metal-MoS_2 interface is highlighted in yellow box. The vertical dashed lines are the positions of atoms.

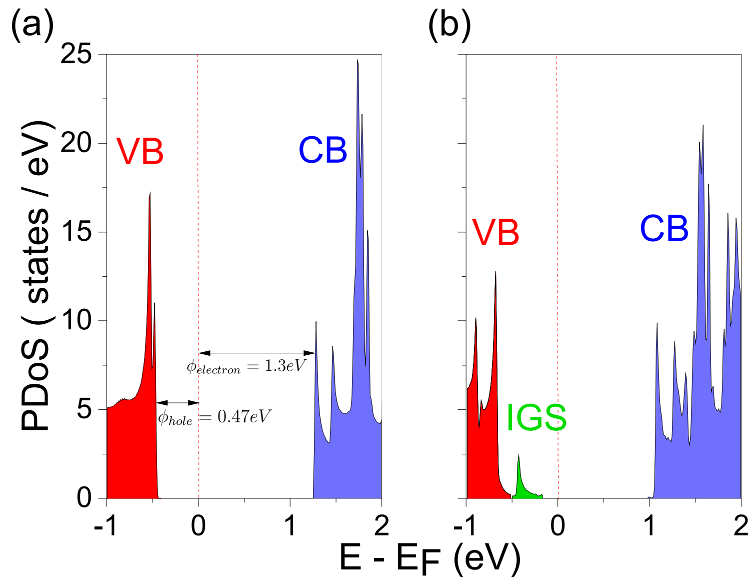

Figure 2.28: PDoS of MoS_2 in the MoS_2-Au stack for (a) $d = 0.8$ nm and (b) $d = 0.4$ nm. At short distances and we see the onset of IGS (e.g. the large green peak) that pin the Fermi level E_F inside the bandgap.

Similar results are observed for the MoS_2-Al stack (Fig. 2.29), with a large PDoS increase in the MoS_2 gap at small d, that pins E_F. For $d = 0.8$ nm, instead, the SBH is about zero, consistently with $\phi_m = 4$ eV for the Al slab.

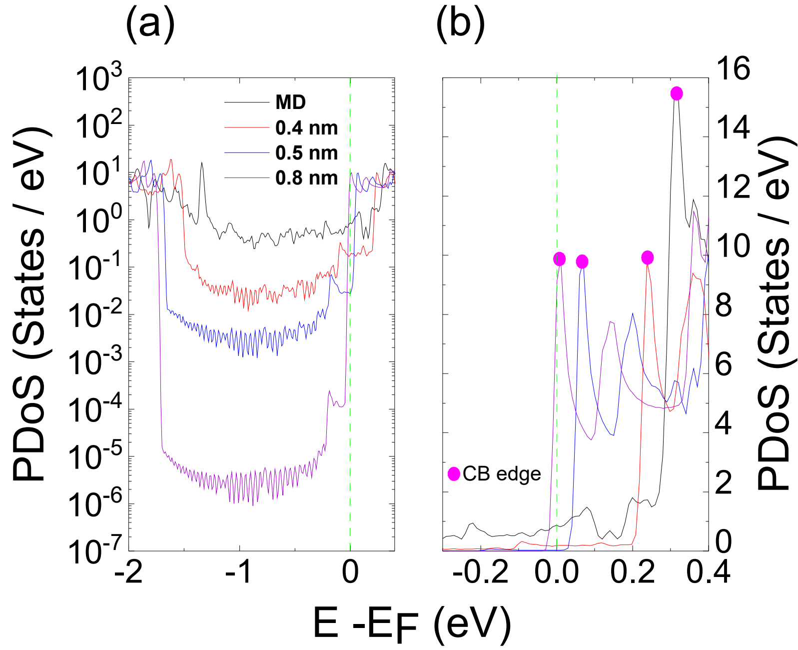

Figure 2.29: PDoS of MoS_2 in MoS_2-Al stack for different d values in (a) logarithmic, and (b) linear scales (zoomed around E_F). For MD, E_F is pinned in the MoS_2 bandgap due to IGS (black). By increasing d, the IGS density is suppressed, so that E_F gets de-pinned and reaches the MoS_2 CB for $d = 0.8$ nm.

The back-gate in Fig. 2.13.b allows the biasing of MoS_2 through an external electric field (F). However, the strong FLP for small d values precludes any SBH modulation (Fig. 2.30). For $d = 0.8nm$, instead, due to the E_F de-pinning, the field can shift E_F with respect to the CB edge (Fig. 2.31), hence $\Phi_{electron}$ reduces for $F > 0$ and increases for $F < 0$. To gain a better physical insight, we extracted the F induced charge in MoS_2 by using either the Bader analysis [109,110] or simply the Gauss law; in fact, for $d = 0.8nm$, a dependable F value can be determined at both sides of MoS_2 from the potential energy profile (Fig. 2.33). The charges extracted from Bader analysis or Gauss law agree well for MoS_2-Al (Fig. 2.34.a) and MoS_2-Au (b). An electric field $F > 0$ increases the electron density in MoS_2 and eases the contact to the CB in the MoS_2-Al system, while a negative field eases a contact to the VB in the MoS_2-Au stack. It is worth mentioning that the apparently large F values needed to induce n-type or p-type contacts are partly due to the use of vacuum as a spacer between MoS_2 and the back-gate. By exploiting the dielectrics typically available in CMOS technologies, the required field can be reduced by a factor equal to the corresponding permittivity, namely of about 4 for SiO_2 and 30 for HfO_2.

2.4.1 Contact resistance in MoS_2

The insertion of a proper buffer layer (e.g. graphene or h-BN) between the metal and the TMD has been recently explored to de-pin the Fermi level in metal-MoS_2 contacts [125–127]. This approach is completely consistent with the analysis performed so far. Indeed the buffer layer may allow a different positioning of metal w.r.t MoS_2, enlarging the distance between the materials. However the reduction of FLP comes at the cost of a larger tunneling barrier (TB) in the vdW gap (see Fig. 2.12.c), so that the trade-off between spacing between metal and MoS_2 and FLP must be addressed. Recent results have shown that the semimetallic bismuth can effectively suppress IGS and lead to an

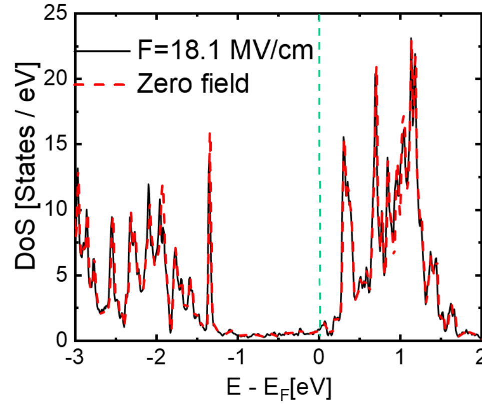

Figure 2.30: PDoS of MoS_2 in the back gated MoS_2-Al stack at MD for $F = 0$ and $+18.1$ MV/cm. Due to the large density of IGS, E_F is strongly pinned and the electric field imposed by the back gate cannot influence E_F.

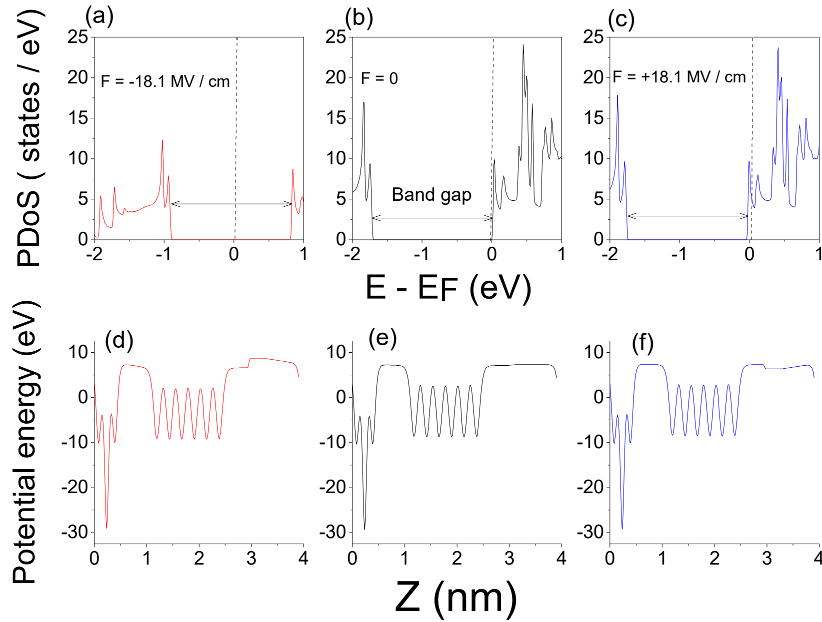

Figure 2.31: PDoS and potential energy of MoS_2 in back gated MoS_2-Al at $d = 0.8$ nm with (a, d) $F = -18.1$ MV/cm , (b, e) $F = 0$, and, (c, f) $F = +18.1$ MV/cm . E_F is de-pinned: the field shifts E_F with respect to CB and VB of MoS_2 (n-type contact for $F > 0$).

ultra low resistance n-type Ohmic contact to several TMDs [85]. So, We applied the *ab initio* quantum transport methodology recently presented in [105] to evaluate the contact resistance of MoS_2 contact featuring semi-metal and/or buffer layers. We present an effort to examine quantitatively: a) the trade off between SBH and the TB in metal-MoS_2 contacts with different buffer layer options; b) the *ab-initio* calculation of resistance in bismuth-MoS_2 [85]; c) the Au-NbS_2-MoS_2 system as an attainable option for a p-type contact to MoS_2. The effectiveness of our simulation approach allowed us to simulate relatively large overlap regions between (semi)metal and TMDs, so as to bridge the gap between the atomistic description and the technologically relevant figures of merit. Figure. 2.35 shows the projected electronic structure (left) and projected MoS_2 Density of States (DoS, right) for the Al-MoS_2 system with $d = 0.35$ nm, where a SBH of about 0.2 eV is still observed. Figure. 2.36(left) shows that for $d = 0.71$ nm, instead, the Fermi

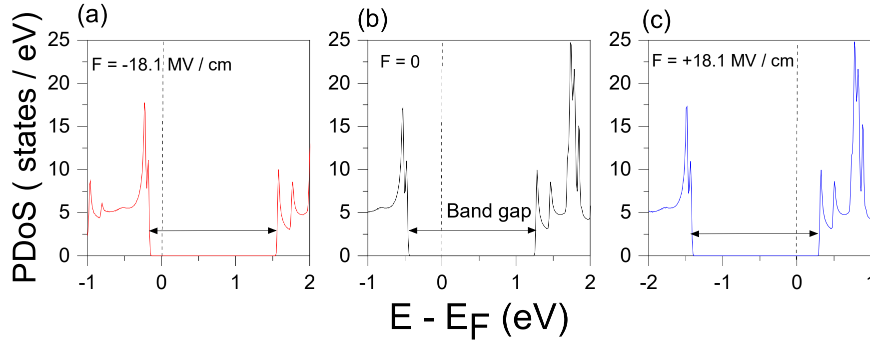

Figure 2.32: PDoS of MoS_2 in back gated MoS_2-Au at $d = 0.8$ nm with (a) $F = -18.1$ MV/cm , (b) $F = 0$, and, (c) $F = +18.1$ MV/cm . E_F is not pinned anymore : the field shifts E_F with respect to CB and VB of MoS_2.

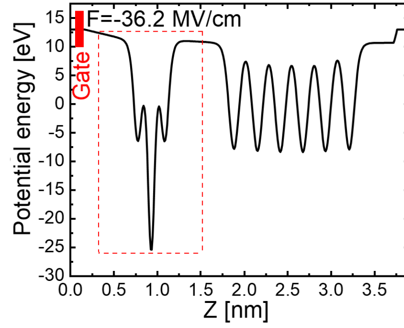

Figure 2.33: Back gated MoS_2-Au stack. $d = 0.8$ nm is large enough to calculate the field at both sides of MoS_2 (red dashed box).

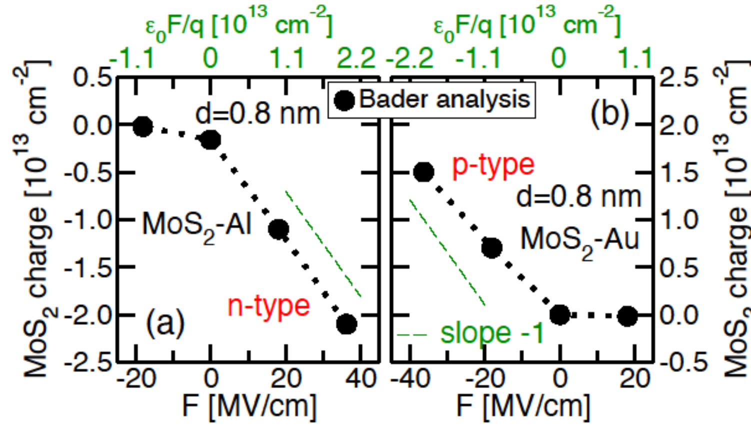

Figure 2.34: MoS_2 charge vs. F extracted with Bader analysis or through the Gauss law for MoS_2-Al (a) and MoS_2-Au (b) stacks. The back gate field induces either a n-type (a) or a p-type contact (b).

level E_F touches the projected MoS_2 conduction band (CB) minimum, namely the SBH is zero. This is in agreement with the Schottky–Mott rule considering an Al work function $WF = 4$ eV and a MoS_2 affinity of 4.2 eV. The Al-hBN-MoS_2 also exhibits a negligible SBH (Fig. 2.36(right)), however both the options in Fig. 2.36 imply a wider TB region compared to, for example, the Al-MoS_2 contact with a minimum energy distance. This latter aspect is best illustrated in Fig. 2.37, reporting the transmission across the Al-

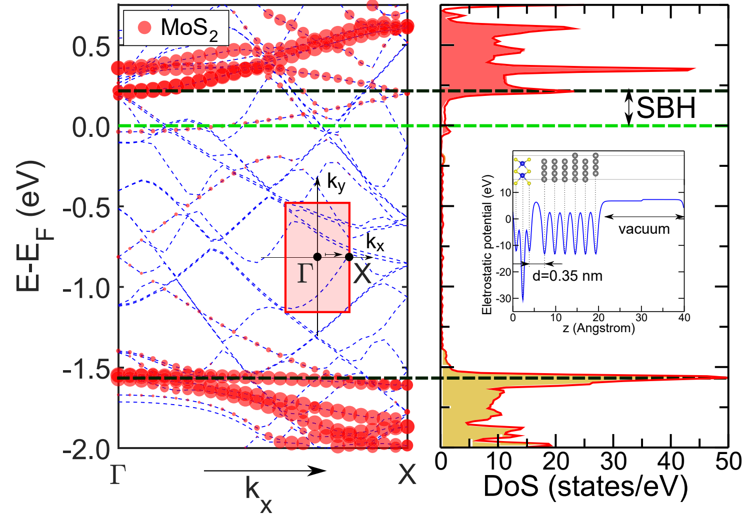

Figure 2.35: Electronic structure (left) and Density of States (DoS, right) for a vertical Al-MoS_2 heterostructure with a 0.35 nm vacuum region between Al and MoS_2. Left: Electronic structure projected on MoS_2 orbitals and for a transverse Bloch vector $k_y = 0$. The size of circles is proportional to the weight of the states projection. Dashed lines show the bands of the whole VHJ. Right: projected DoS for MoS_2 showing a Schottky barrier hight of about 0.2 eV. The inset shows that, thanks to the dipole correction placed at $z = 30$ $\AA$, the potential is flat in the vacuum region.

MoS_2 and the Al-hBN-MoS_2 structure calculated with our *ab-initio* transport approach described in Sec. 2.2.3. The Al-MoS_2 system with $d = 0.35$ nm has the largest transmission at the CB minimum (see vertical dashed lines), but the transmission is negligible at $E = E_F$ due to the SBH of ~ 0.2 eV . The Al-MoS_2 system with $d = 0.71$ nm and the Al-hBN-MoS_2 system, instead, exhibit a negligible SBH, but the transmission at the CB minimum is largely degraded by the TB compared to the transmission at the CB minimum of the $d = 0.35$ nm system. Fig. 2.38 reports I_C versus V_C (see Fig. 2.12.a) curves

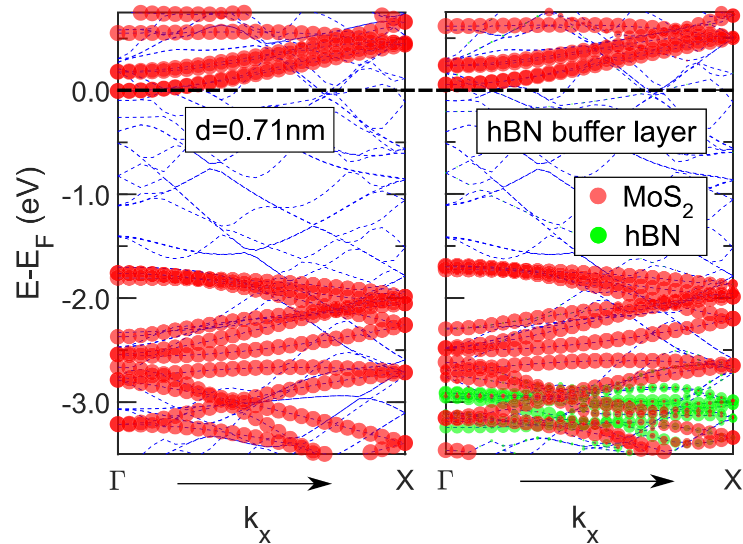

Figure 2.36: Projected electronic structure for: (left) the Al-MoS_2 vertical heterostructure with an Al-MoS_2 distance $d = 0.71$ nm; (right) the Al-hBN-MoS_2 heterostructure, having a calculated minimum energy distance that is also $d = 0.71$ nm. Bands are reported for a transverse Bloch vector $k_y = 0$.

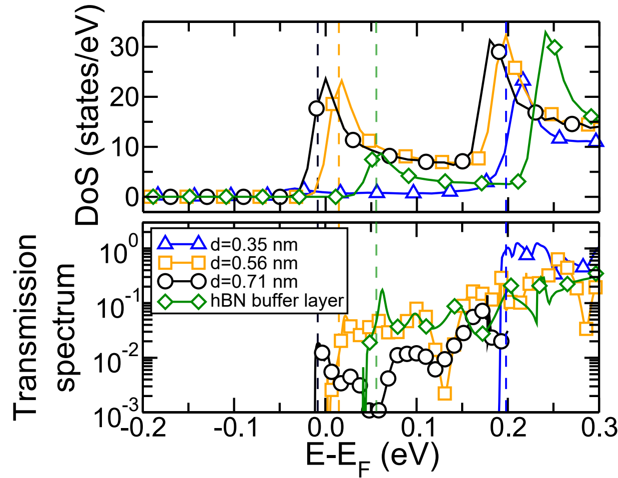

Figure 2.37: Top: MoS_2 Projected DoS in the Al-MoS_2 VHJ for different Al-MoS_2 distances. Bottom: Corresponding transmission spectrum versus the energy (referred to the equilibrium Fermi level E_F) calculated with the *ab-initio* quantum transport methodology described in Sec. 2.2.3. Results are shown for $k_y = 0$. Vertical dashed lines identify approximately the minimum of the MoS_2 conduction band in each system.

at small V_C for the Al-MoS_2 system at different distances d and for the Al-hBN-MoS_2 contact. For $d = 0.8$ and 0.7 nm the I_C - V_C plot of the Al-MoS_2 system is fairly linear in the explored V_C range. Namely these contacts exhibit an Ohmic behavior that eases the extraction of the contact resistance R_C, which has been here defined as $R_C = V_C/I_C$ at $V_C = 25$ mV. For the $d = 0.35$ nm system, instead, the ~ 0.2 eV SBH results in a Schottky behavior of the I_C - V_C plot, such that the I_C has a super-linear increase with V_C for V_C larger than about 50 mV. The R_C extracted from the I_C - V_C plots are reported in Fig. 2.39 for different contact options and versus the inverse of the contact length. The contact resistivity ρ_c inferred from the slope of the R_C versus $1/L_C$ curves are also indicated. As expected, the ρ_c of the Al-MoS_2 contacts substantial degrades by increasing the thickness d of the vdw gap.

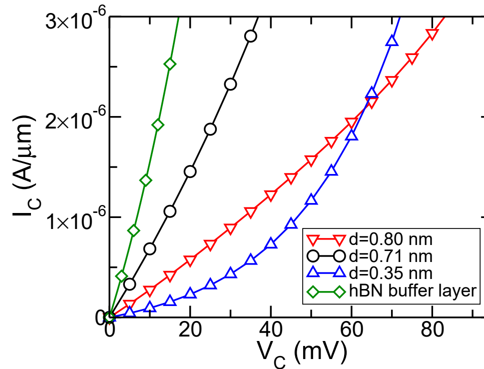

Figure 2.38: Numerically calculated current, I_C, versus voltage, I_C, through the Al-MoS_2 contact for different Al-MoS_2 distances (see Fig. 2.12.a). The contact resistance is here defined as $R_C = V_C/I_C$ at $V_C = 25$ mV. The length of the Al-MoS_2 heterostructure is $L_C = 9.49$ nm (corresponding to 10 orthorhombic unit cells) (see Fig. 2.12.c). The R_C dependence on L_C is analyzed in Fig. 2.39.

It was experimentally shown that the semimetal bismuth can provide an essentially Ohmic, n-type contact to MoS_2 [85]. For the first time we here report *ab-initio* simulations of the resistance in a bismuth-MoS_2 system (see Fig. 2.40). For simulations with the

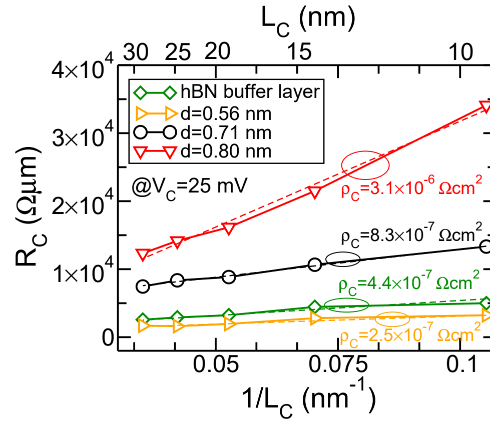

Figure 2.39: Contact resistance R_C versus the inverse $1/L_C$ of the contact length (see Fig. 2.12.c) for either the Al-MoS_2 or the Al-hBN-MoS_2 contact. From the slope of the linear regression the contact resistivity ρ_c can be readily extracted.

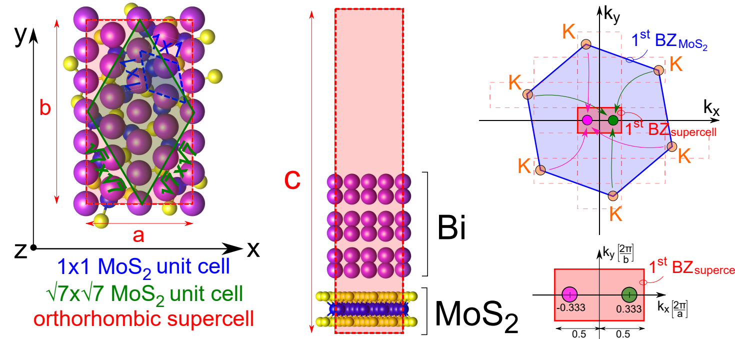

Figure 2.40: Top and side view of the orthorhombic supercell used for the simulations of the Bi-MoS_2 heterostructures. First BZ for the primitive MoS_2 unit cell (blue hexagon), and first BZ for the orthorhombic supercell (red rectangle). Arrows show that the K, K' points of the primitive BZ of MoS_2 are backfolded at points $[\mp\frac{1}{3}(\frac{2\pi}{a}), 0]$ in the BZ of the orthorhombic supercell.

semimetal bismuth (Bi), a 2×2 supercell of three Bi layers (0001) has been matched to a $\sqrt{7} \times \sqrt{7}$ unstrained MoS_2 cell (see Fig. 2.40). The lattice mismatch is about 3.6% (compressive strain on Bi atoms), and our simulations show that this strain has a limited influence on the Bi electronic structure near the Fermi level (not shown). Furthermore, after a complete geometry optimization, the extracted distance between Bi and S atoms is $d = 0.326$ nm, in good agreement with [85]. Figure. 2.41(left) reports the projected electronic structure for the Bi-MoS_2 VHJ close to the CB minimum. The green line identifies a branch with the expected CB minimum in $[0.33(2\pi/a), 0]$ (see Fig. 2.40), while the blue line marks a branch due to the hybridization between bismuth and MoS_2 orbitals. In virtue of such an uncertainty about the SBH in this system, Fig. 2.41(right) reports the calculated R_C for the SBH values ranging in the shaded area of Fig. 2.41(left). For the small SBH values the calculated R_C approaches the experimental value reported in [85]. Moreover the calculated R_C for the bismuth-MoS_2 system is more than ten times smaller than the counterpart for the Al-hBN-MoS_2 contact (see Fig. 2.39). Since monolayer MoS_2 has a high ionization energy of about 5.95 eV, contacting the MoS_2 valence band (VB) is a very challenging problem. We here propose to use an interlayer consisting of a metallic monolayer NbS_2. In fact the high NbS_2 workfunction of about 6.2 eV is expected to push the E_F of the system down to the VB edge of MoS_2 [125]. In order to investigate

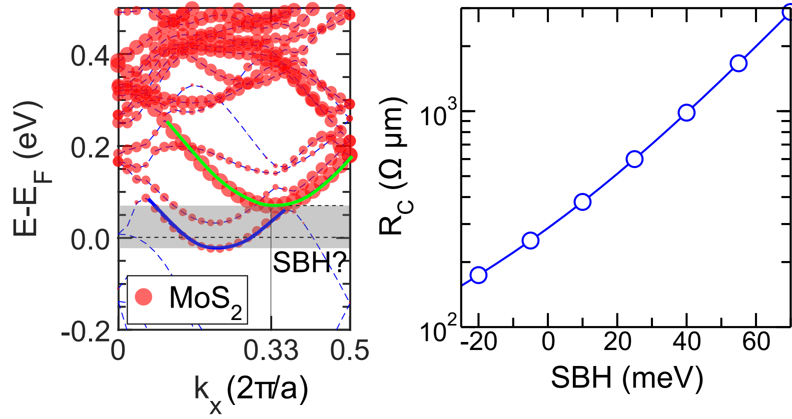

Figure 2.41: Left: Electronic structure for the Bi-MoS_2 VHJ zoomed in an energy range close to the projected MoS_2 CB minimum. The size of the red circles is proportional to the weight of the states projection on MoS_2 (see Fig. 2.35). The green line identifies the CB branch with the minimum in $k_x = 0.33$ $[2\pi/a]$ corresponding to free-standing MoS_2. The blue line marks a branch due to Bi- MoS_2 hybridization (as implied by the smaller projection on MoS_2), whose minimum lies about 20 meV below the Fermi level. The shaded area indicates the uncertainty in the SBH value. Right: Contact resistance R_C versus the SBH for a contact length $L_C = 8.37$ nm (i.e 10 orthorhombic unit cells) and for the SBH values of shaded area in the left figure. R_C from [85] : 123 $\Omega\mu$m.

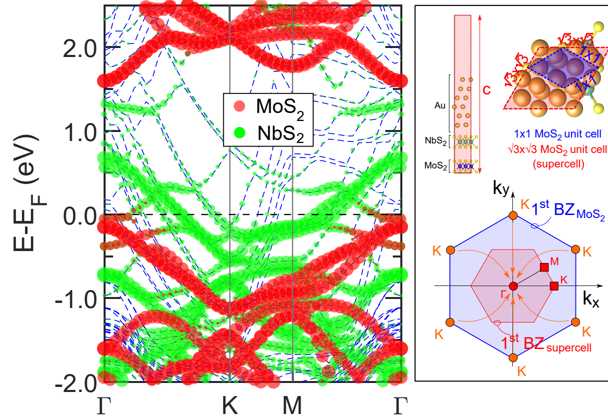

Figure 2.42: Top and side view of the simulated supercell for the Au-NbS_2-MoS_2 vertical heterostructure and corresponding first BZ. Electronic structure at $k_y = 0$ projected either on MoS_2 or on NbS_2 orbitals.

this hypothesis we studied in details the Au-NbS_2-MoS_2 system. Figure. 2.42 shows the supercell of the system, and the electronic structure projected either on MoS_2 or on NbS_2. As it can be seen, the E_F can reach the top of the MoS_2 VB and, moreover, it crosses a few branches of the NbS_2 VB. Because of its clearly metallic behaviour, the NbS_2 does not introduce a TB in the Au-NbS_2-MoS_2 heterostructure, which is a key advantage compared to an Al-hBN-MoS_2 system.

2.5 Conclusions

In this chapter, first we have showed that Ni and Cu largely dope graphene at MD, but at larger distance they fail to dope graphene. In this respect, the experiments for Ni-G and Cu-G contacts report a large R_C (especially at $V_{BG} = 0$), thus suggesting

$d > 0.5$ nm. This increased distance may be the result of wrinkles, roughness and/or impurities impacting the quality of the M-G interface. For the Au-G contact, a longer range interaction and significant G doping are predicted for d up to 1 nm, explaining the lower experimental R_C compared to Ni-G and Cu-G. Furthermore, the simulations predict a large R_C dependence on V_{BG} at $d > 0.4$ nm. This result seems to grasp the experimental behavior, thus supporting the picture of a M-G distance larger than the minimum distance.

Then we have also showed that for a defect-free MoS_2 layer, the control of the metal-MoS_2 distance d is crucial in order to enable a modulation of the SBH, that can be further adjusted by an effective back-gating of the structure. This may be achieved thanks to the insertion of a proper buffer layer such as graphene or h-BN between the metal and MoS_2. Moreover, we have used an in house developed, *ab-initio* transport methodology to investigate several options for a metal contact to monolayer MoS_2. Our results examined quantitatively the trade off between SBH and TB in contacts with a buffer layer, and confirmed by simulations the superior performance of the bismuth-MoS_2 n-type contact. We also showed that the Au-NbS_2-MoS_2 system provides a pathway to an Ohmic p-type contact. These results can be naturally extended to TMDs other than MoS_2.

Chapter 3

Sensors based on 2D materials

3.1 Introduction

As already mentioned in Chap. 1, the discovery of 2D materials has increased the world-wide efforts to develop novel sensors for different applications. Due to the high carrier mobility and surface-to-volume ratio, fast sensors with high sensitivity based on 2D materials have been developed [19, 128–130]. First, this chapter revisits the problem of the Linearized Boltzmann Transport Equation (LBTE) and scattering mechanisms that have been accounted for in this thesis. Then in the Secs. 3.3 and 3.4 we discuss the preformed analysis based on the method described in Sec.3.2. Finally, Sec. 3.5 presents different gas sensors based on 2D materials. Since the material in Sec.3.5 stems from the continuation of my previous studies carried out at the University of Tehran, the context of this part is different from other sections in the current chapter.

3.2 Linear Resistance : Semiclassical methods

Low field mobility is a critical parameter for many electronic devices, especially MOS transistors. The reason behind this importance is that there is a correlation and connection between low field mobility and drain current in MOSFET transistors [131–133].

Quantum transport models for electrons accounting for scattering mechanisms are computationally costly, so various methods such as Effective Mass Approximation (EMA) or k.p theory have been proposed to reduce the computational costs. However, these methods have their limitation, for example, in EMA only one of the CBM can be considered. In order to cross these limitations, the Boltzmann Transport Equation (BTE) for all energy bands must be solved. The BTE can be solved by general methods (e.g., the Monte Carlo method), but a Linearized BTE (LBTE) is also sufficient to calculate low field mobility accurately, provided that both the formulation and the solution of the LBTE do not involve simplifying assumptions. This approach has a high accuracy in low field conditions with smaller computational burden compared to other methods. Here in the following, the linearaztion of the BTE will be revisited [134]. In this thesis, we have used a previously developed simulator based on this model [20], by adding some extensions concerning scattering mechanisms.

3.2.1 Linearized BTE

The distribution function for electron $f_v(\vec{k})$ in valley ν in the presence of an electric field F_x can be written as:

$$f_\nu(\vec{k}) = f_0\left(E_\nu(\vec{k})\right) - eF_x g_\nu(\vec{k}), \tag{3.1}$$

where $f_0(E)$ is the Fermi-Dirac distribution function, x is one of the longitudinal (l) or transverse (t) directions of the valley, and $\vec{k} = (\vec{k_l}, \vec{k_t})$ is the wavevector in the the valley coordinate system. Eq.3.1 is a definition for $g_\nu(\vec{k})$ which are the unknown functions in the linearized Boltzmann equation. We make the *ansatz* that $g_\nu(\vec{k})$ can be written as:

$$g_\nu(\vec{k}) = -\tau_\nu(\vec{k})v_x^\nu(\vec{k})\frac{\partial f_0(E_\nu(\vec{k}))}{\partial E} \tag{3.2}$$

where τ_v and v_x^ν are the $\overline{k}$ dependent Momentum Relaxation Time (MRT) and the group velocity (x component) of valley ν, respectively. According to the the Fermi-Dirac distribution function Eq.3.2 can be re-write as follows:

$$g_\nu(\vec{k}) = \frac{\tau_\nu(\vec{k})v_x^\nu(\vec{k})}{K_B T} f_0(E_\nu(\vec{k}))\left[1 - f_0(E_\nu(\vec{k}))\right], \tag{3.3}$$

where K_B is the Boltzmann constant and T is the temperature. From this equation we can write the MRT as:

$$\tau_\nu(\vec{k}) = \frac{g_\nu(\vec{k})}{v_x^\nu(\vec{k})} \times \frac{K_B T}{f_0(E_\nu(\vec{k}))[1 - f_0(E_\nu(\vec{k}))]}. \tag{3.4}$$

In order to avoid numerical problems in the numerical solution of the LBTE, we calculate $g_\nu(\vec{k})$, then we extract the MRT using Eq.3.4. LBTE for 2D materials is defined as [135]:

$$\begin{gathered} v_x^\nu(\vec{k}) f_0\left(E_\nu(\vec{k})\right)\left[1 - f_0(E_\nu(\vec{k}))\right] = \\ K_B T \Sigma_{\omega,\vec{k'}} S_{\nu,\omega}(\vec{k},\vec{k'})\left[g_\nu(\vec{k})\frac{1 - f_0(E_\omega(\vec{k'}))}{1 - f_0(E_\nu(\vec{k}))} - g_\omega(\vec{k'})\frac{f_0(E_\nu(\vec{k}))}{f_0(E_\omega(\vec{k'}))}\right], \end{gathered} \tag{3.5}$$

where $S_{\nu,\omega}(\vec{k},\vec{k'})$ is the scattering rate from the wavevector $\vec{k}$ in the valley ν to the wavevector $\vec{k'}$ in the valley ω. According to the Fermi's golden rule, an in-elastic scattering rate can be written as:

$$S_{\nu,\omega}(\vec{k},\vec{k'}) = \frac{2\pi}{\hbar}\left|M_{\nu,\omega}(\vec{k},\vec{k'})\right|^2\left[n_{op} + \frac{1}{2} \mp \frac{1}{2}\right]\delta\left[E_\omega(\vec{k'}) - E_\nu(\vec{k}) \mp E_{ph}(q)\right], \tag{3.6}$$

where $E_{ph}(q) = \hbar\omega(q)$ is the phonon energy and $q = \pm(\vec{k'} - \vec{k})$ is the wavenumber, and n_{op} is the phonon occupation number obtained according to the Bose-Einstein distribution. Upper and lower signs are for the absorption and emission of phonons, respectively. Eq.3.6 is related to a single scattering mechanism, we will discuss about multiple scattering mechanisms later in this section.

If we convert the summation in Eq.3.5 to the integral and write the $S_{\nu,\omega}(\vec{k},\vec{k'})$ by using Eq.3.6, then Eq.3.5 can be re-written as:

$$\frac{g_\nu(\vec{k})K_BT}{f_0\left(E_\nu(\vec{k})\right)\left[1-f_0\left(E_\nu(\vec{k})\right)\right]}\left[\frac{1}{2\pi\hbar}\sum_\omega\int_{\vec{k}'}\Lambda_{\nu,\omega}(\vec{k},\vec{k}')\delta[E_\omega(\vec{k}')-E_\nu(\vec{k})\mp E_{ph}(q)]d\vec{k}'\right]$$
$$-\frac{1}{2\pi\hbar}\sum_\omega\int_{\vec{k}'}\Lambda_{\nu,\omega}(\vec{k},\vec{k}')\frac{g_\omega(\vec{k})K_BT}{f_0\left(E_\omega(\vec{k}')\right)\left[1-f_0(E_\omega(\vec{k}')\right]}\delta\left[E_\omega(\vec{k}')-E_\nu(\vec{k})\mp\right.$$
$$\left.E_{ph}(q)\right]d\vec{k}'=v_x^\nu(\vec{k}), \tag{3.7}$$

where:

$$\Lambda_{\nu,\omega}(\vec{k},\vec{k}')=\left|M_{\nu,\omega}(\vec{k},\vec{k}')\right|^2\left[\frac{1-f_0(E_\omega(\vec{k}')}{1-f_0(E_\nu(\vec{k})}\right]. \tag{3.8}$$

By changing the integration variables and using the polar coordinates $\vec{k}=(k,\beta)$ for each valley ν and direction β, the integration variable changes from magnitude of wavenumber (k) to the energy $E_\nu(k,\beta)$:

$$\frac{g_\nu(\vec{k})K_BT}{f_0\left(E_\nu(\vec{k})\right)\left[1-f_0\left(E_\nu(\vec{k})\right)\right]}\left[\frac{1}{2\pi\hbar}\sum_\omega\int_{-\pi}^{\pi}d\beta'\int_{-\infty}^{+\infty}dE_\omega\Theta_{\nu,\omega}(\vec{k},\vec{k}')\delta[E_\omega-E_\nu(\vec{k})\mp E_{ph}(q)]\right]$$
$$-\frac{1}{2\pi\hbar}\sum_\omega\int_{-\pi}^{\pi}d\beta'\int_{-\infty}^{+\infty}dE_\omega\Theta_{\nu,\omega}(\vec{k},\vec{k}')\frac{g_\omega(\vec{k})K_BT}{f_0\left(E_\omega(\vec{k}')\right)\left[1-f_0(E_\omega(\vec{k}')\right]}\delta\left[E_\omega(\vec{k}')-E_\nu(\vec{k})\mp\right.$$
$$\left.E_{ph}(q)\right]=v_x^\nu(\vec{k}). \tag{3.9}$$

In the above equation, the symbol $\Theta_{\nu,\omega}(\vec{k},\vec{k}')$ is defined as:

$$\Theta_{\nu,\omega}(\vec{k},\vec{k}')=\vec{k}'(E_j,\beta')\left[\frac{dE_\omega(\vec{k}',\vec{\beta}')}{dk}\right]^{-1}\left|M_{\nu,\omega}(\vec{k},\vec{k}')\right|^2\left[\frac{1-f_0(E_\omega(\vec{k}')}{1-f_0(E_\nu(\vec{k})}\right]. \tag{3.10}$$

The Dirac function in Eq.3.7 limits integration in the k space to $E_\omega(\vec{k}')=E_\nu(\vec{k})\pm E_{ph}(q)$. To numerically solve this equation, the energy driven discretization of the electron wavevector is utilized guarantying that all the discrete wavevectors correspond to energies differing by a multiple of the energy step ΔE. The same discretization method is used for the phonon energy that is equal to $p\Delta E$, where p is a positive integer.

According to the method of discretization mentioned above and by considering $\vec{k}_{\nu,r,d}=(k_{\nu,r,d},d\Delta\beta)$, the positive integer number $n_{\nu,r,d}$ is defined as follows:

$$E_\nu(k_\nu,r,d)=E_{min}+n_{\nu,r,d}\Delta E. \tag{3.11}$$

The difference between the initial wavevector $\vec{k}_{\nu,r,d}$ and the final wavevector $\vec{k}_{\omega,r',d'}$ is equal to:

$$q=|\vec{k}_{\omega,r',d'}-\vec{k}_{\nu,r,d}|, \tag{3.12}$$

where $q\in\Delta q_p$ and will correspond to the phonon discrete energy ($p\Delta E$). According to the above information about discretization, the energy conservation for a phonon assisted

transition between an initial state and final state can be expressed as follows:

$$[n_{\omega,r',d'} - n_{\nu,r,d}] = 0. \tag{3.13}$$

Then we can re-write the Eq.3.9:

$$\begin{gathered} g\left(k_\nu, r, d\right)\left[\frac{\Delta\beta}{2\pi\hbar}\Sigma_{\omega,r',d'} A_{\nu,r,d}^{\omega,r',d'} \delta_{\nu,r,d}^{\omega,r',d'}\right] - \\ \frac{\Delta\beta}{2\pi\hbar}\Sigma_{\omega,r',d'} B_{\nu,r,d}^{\omega,r',d'} g\left(k_{\omega,r',d'}\right)\delta_{\nu,r,d}^{\omega,r',d'} = \frac{v_x(k_\nu, r, d) f_0\left(E(k_{\nu,r,d})\right)\left[1 - f_0\left(E(k_{\nu,r,d})\right)\right]}{K_B T}, \end{gathered} \tag{3.14}$$

where:

$$A_{\nu,r,d}^{\omega,r',d'} = k_{\omega,r',d'}\left[\frac{dE(k_{\omega,r',d'})}{dk}\right]^{-1} |M_{\nu,\omega}(k_{\nu,r,d}, k_{\omega,r',d'})|^2 \left[\frac{1 - f_0\left(E(k_{\omega,r',d'})\right)}{1 - f_0\left(E(k_{\nu,r,d})\right)}\right], \tag{3.15}$$

$$B_{\nu,r,d}^{\omega,r',d'} = k_{\omega,r',d'}\left[\frac{dE(k_{\omega,r',d'})}{dk}\right]^{-1} |M_{\nu,\omega}(k_{\nu,r,d}, k_{\omega,r',d'})|^2 \left[\frac{f_0\left(E(k_{\nu,r,d})\right)}{1 - f_0\left(E(k_{\omega,r',d'})\right)}\right]. \tag{3.16}$$

The Kronecker symbol defined as follows:

$$\delta_{\nu,r,d}^{\omega,r',d'} = \begin{cases} 1 & for \quad [n_{\omega.r',d'} - n_{\nu,r,d} \mp p] \\ 0 & otherwise \end{cases} \tag{3.17}$$

Finally the relaxation time can be extracted by solving the Eq.3.14.

It is worth mentioning that the Eq.3.14 is for an anisotropic energy relation and scattering mechanism (most general case), resulting in a computationally demanding numerical solution. For the case of 2D MoS_2, although the energy relation of K-valley is considered isotropic, in addition to the anisotropic energy relation of Q-valley, some scattering mechanisms (e.g., Coulomb Impurities) must be also treated as an anisotropic mechanism. So simplifying methods are a prerequisite to make this problem computationally affordable. In order to reduce computational effort, a non-parabolic description of the band structure based on the EMA close to the K and Q conduction band minima has been used. By defining the θ as an angle between armchair and longitudinal direction in real space, we have:

$$E\left(1 + \alpha E\right) = \hbar^2 k_l^2/(2m_l^*) + \hbar^2 k_t^2/(2m_t^*), \tag{3.18}$$

where $\vec{k} = (k_t, k_l) = (\overline{k}sin(\theta), \overline{k}cos(\theta))$, m_l and m_t respectively denote the longitudinal and transverse effective mass, and α is the non-parabolicity factor [135]. The θ dependent mass m_{tl} can be introduced as follows:

$$m_{tl}(\theta) = \left[\frac{cos^2(\theta)}{m_l} + \frac{sin^2(\theta)}{m_t}\right]^{-1}. \tag{3.19}$$

Now we can calculate the k and its derivative with respect to the energy as:

$$k(E, \theta) = \frac{\sqrt{2m_{tl}(\theta)E(1 + \alpha E)}}{\hbar}, \tag{3.20a}$$

$$\frac{\partial k(E, \theta)}{\partial E} = \frac{m_{tl}(\theta)E(1 + 2\alpha E)}{\hbar\sqrt{2m_{tl}(\theta)E(1 + \alpha E)}}. \tag{3.20b}$$

After discretization of $m_{tl}(\theta)$ and introducing the Eq.3.20 in Eqs.3.15, 3.16:

$$A_{\nu,r,d}^{\omega,r',d'} = \frac{m_{tl,d}^{\omega}}{\hbar^2}(1 + 2\alpha_\omega E\left(k_{\omega,r',d'}\right)) |M_{\nu,\omega}(k_{\nu,r,d}, k_{\omega,r',d'})|^2 \left[\frac{1 - f_0\left(E(k_{\omega,r',d'})\right)}{1 - f_0\left(E(k_{\nu,r,d})\right)}\right], \tag{3.21}$$

$$B_{\nu,r,d}^{\omega,r',d'} = \frac{m_{tl,d}^{\omega}}{\hbar^2}(1+2\alpha_\omega E(k_{\omega,r',d'}))\left|M_{\nu,\omega}(k_{\nu,r,d},k_{\omega,r',d'})\right|^2\left[\frac{f_0(E(k_{\nu,r,d}))}{1-f_0(E(k_{\omega,r',d'}))}\right]. \quad (3.22)$$

Using this method slightly reduces the volume of calculations and also prevents some numerical problems in solving the equation.

Eq.3.14 only considers a single inelastic scattering mechanism. In order to consider all scattering mechanisms, the mentioned method in [136] is used. To do so, Eq.3.14 is re-written as $\bar{\bar{M}}^s\bar{g} = \bar{G}$ where $\bar{\bar{M}}^s$ is a matrix for scattering s, $\bar{g}$ is the same unknown function defined in Eq.3.3 and $\bar{G}$ is the r.h.s vector. Then the unknown function $\bar{g}$ for all scattering mechanisms can be extracted by means of a linear equation:

$$\Sigma_{s=1}^{N_{sc}}\bar{\bar{M}}^s\bar{g} = \bar{G}, \quad (3.23)$$

where N_{sc} is the number of scattering mechanisms. By using Eqs.3.14, 3.16, corresponding matrices of the above equation can be determined.

After solving the LBTE and extracting the g or τ, the calculation of mobility will be straightforward. The mobility matrix of each valley must be defined according to the following:

$$\begin{bmatrix} J_l^\nu \\ J_t^\nu \end{bmatrix} = eN_i\begin{bmatrix} \mu_{ll}^v & \mu_{lt}^v \\ \mu_{tl}^v & \mu_{tt}^v \end{bmatrix}\begin{bmatrix} F_l \\ F_t \end{bmatrix}. \quad (3.24)$$

Each matrix element of the mobility must be calculated separately. The current per unit width can be finally written as:

$$J_l^\nu = \mp\frac{e}{A}\Sigma_k v_l^\nu(\vec{k})f_\nu(\vec{k}) = \frac{e^2F_t}{A}\Sigma_k v_l^\nu(\vec{k})v_t^\nu(\vec{k})\tau_t^\nu(\vec{k})\left|\frac{df_0(E_\nu(\vec{k}))}{dE}\right|. \quad (3.25)$$

In the above equation, A is the normalization area factor, and $f^v(\vec{k})$ is defined in the Eq.3.1. The mobility matrix elements can be extracted by the following equations:

$$\mu_{ll}^\nu = \frac{J_l^\nu}{eN_iF_l} = \frac{e}{AN_i}\Sigma_k v_l^\nu(\vec{k})v_l^\nu(\vec{k})\tau_l^\nu(\vec{k})\left|\frac{df_0(E^\nu(\vec{k}))}{dE}\right|, \quad (3.26a)$$

$$\mu_{tt}^\nu = \frac{J_t^\nu}{eN_iF_t} = \frac{e}{AN_i}\Sigma_k v_t^\nu(\vec{k})v_t^\nu(\vec{k})\tau_t^\nu(\vec{k})\left|\frac{df_0(E^\nu(\vec{k}))}{dE}\right|, \quad (3.26b)$$

$$\mu_{lt}^\nu = \frac{J_l^\nu}{eN_iF_t} = \frac{e}{AN_i}\Sigma_k v_l^\nu(\vec{k})v_t^\nu(\vec{k})\tau_t^\nu(\vec{k})\left|\frac{df_0(E^\nu(\vec{k}))}{dE}\right|, \quad (3.26c)$$

$$\mu_{tl}^\nu = \frac{J_t^\nu}{eN_iF_l} = \frac{e}{AN_i}\Sigma_k v_t^\nu(\vec{k})v_l^\nu(\vec{k})\tau_l^\nu(\vec{k})\left|\frac{df_0(E^\nu(\vec{k}))}{dE}\right|. \quad (3.26d)$$

It should be noted that in the symmetric energy bandstructures, such as circular and elliptical, the elements μ_{tl}^ν and μ_{lt}^ν will be equal to zero.

3.2.2 Carrier scattering

In this section, we revisit the scattering sources of carriers in a single-layer MoS_2. Intrinsic Phonons (iPh) (including acoustic phonons, optical phonons and optical-polar phonons), Remote or surface optical Phonons (SO Ph), Coulomb Impurities (CIs), Neutral Defects (NDs) and Strain Fluctuations (SFs) will be discussed in following section.

To calculate the scattering rates, it is assumed that the dielectrics surrounding 2D MoS_2 create a large energy barrier that confines electrons in the 2D layer. We assume that the envelope wavefunction Ψ for the 2D electron gas in monolayer MoS_2 can be approximately written as [20, 137]:

$$\Psi_{\vec{k}}(\vec{r}, z) = \chi(z)\, exp\left(i\vec{k}.\vec{r}\right)/\sqrt{(A)}\,, \qquad \chi(z) \;= \sqrt{(2/a_z)}sin\left(\pi z/a_z\right) \tag{3.27}$$

where $\vec{r} = (x, y)$ is the position in the transport plane, A is the normalization area, and $a_z = 0.615$ nm is the thickness of monolayer MoS_2.

3.2.2.1 Intrinsic phonon scattering

The Ph scattering mechanisms have considered are acoustic and optical phonons and the piezoelectric coupling with acoustic phonons is not considered, because this coupling has been shown to be relevant at temperatures below 100 K which is beyond our scope [138]. As mentioned earlier, according to the Fermi's golden rule, an inelastic scattering rate can be defined as Eq.3.6. iPh scatterings are divided into these categories :

- intra-valley elastic scattering;
- intra-valley in-elastic scattering;
- inter-valley in-elastic scattering;

The rate of intra-valley scattering ($\nu = \omega$) of accoustic phonons approximated as elastic scattering can be calculated as:

$$S_{ac}(\vec{k}, \vec{k'}) = \frac{2\pi K_B T D_{ac}^2}{\rho A \hbar v_s^2}\delta[E(\vec{k'}) - E(\vec{k})], \tag{3.28}$$

where K_B is the Boltzmann constant, T is the absolute temperature, D_{ac} is the acoustic deformation potential(taken from [20]), $\rho = 3.1 \times 10^{-7}$ gr/cm^2 is the mass density and v_s is the sound velocity in 2D MoS_2. The rate of other scattering mechanisms including the intra- and inter-valley in-elastic mechanisms can be formulated as:

$$S_{ac/op}^{\nu,\omega}(\vec{k}, \vec{k'}) = \frac{\pi(D_{ac/op}^{\nu,\omega})^2}{\omega_{ac/op}\rho A}\left[n_{op} + \frac{1}{2} \mp \frac{1}{2}\right]\delta[E_\omega(\vec{k'}) - E_\nu(\vec{k}) \mp \hbar\omega_{ac/op}(q)], \tag{3.29}$$

where $D_{ac/op}^{\nu,\omega}$ is the acoustic/optical deformation potential for scattering from ν to ω valley and $\hbar_{ac/op}(q)$ is the phonon energy. In our calculations, we employed the deformation potentials and phonon energies described in [139] that are reported in Tab. 3.1 and Tab. 3.2.

3.2.2.2 Scattering with Surface Optical Phonons

Another scattering mechanism considered in our analysis is the remote or surface-optical phonon. The source of this scattering is in the surrounding dielectrics (Fig. 3.1). The energy dispersion $\hbar\omega(q)$ of surface phonons versus the phonon wavevector q can be obtained by solving the secular equation [140]:

$$\begin{aligned} &\epsilon_{box}(\omega) + \epsilon_{2D}][\epsilon_{tox}(\omega) \times coth(qt_{ox}) + \epsilon_{2D}] \\ &- [\epsilon_{box}(\omega) - \epsilon_{2D}][\epsilon_{tox}(\omega) \times coth(qt_{ox}) - \epsilon_{2D}]\exp^{-2qa_z} = 0 \end{aligned} \tag{3.30}$$

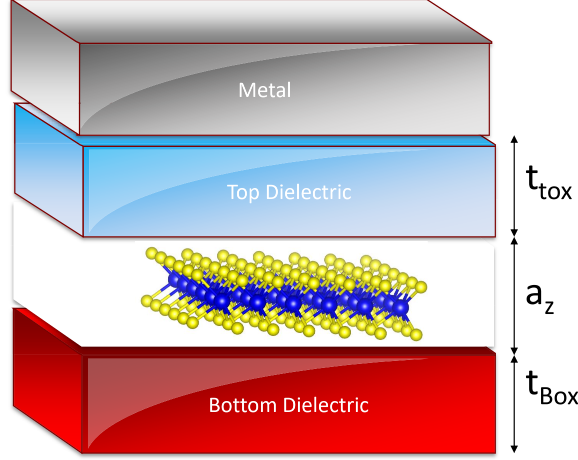

Figure 3.1: Physical structure of the surrounding dielectrics for 2D MoS_2.

where ϵ_{box} and ϵ_{tox} are the frequency dependent dielectric constant of the lower and upper dielectric, respectively, ϵ_{2D} and a_z are the dielectric constant and thickness of 2D material, and t_{ox} is the thickness of upper dielectric (thickness of lower dielectric assumed to be semi-infinite). Studies show that even the thickness of upper dielectric (entering Eq.3.30 in $coth(qt_{ox})$) does not have a large effect on the SO scattering, so by assuming the semi-infinite thickness for upper dielectric:

$$[\epsilon_{box}(\omega) + \epsilon_{2D}][\epsilon_{tox}(\omega) + \epsilon_{2D}] - [\epsilon_{box}(\omega) - \epsilon_{2D}][\epsilon_{tox}(\omega) - \epsilon_{2D}] \exp^{-2qa_z} = 0. \tag{3.31}$$

Numerical calculations show that the sub-nanometric thickness of MoS_2 causes a very weak dependence of the remote phonon frequency on $q = \left|\vec{k} - \vec{k'}\right|$. This dependence has been neglected by taking $\exp^{-2qa_z} \simeq 1$, which simplifies Eq.3.31 as:

$$\epsilon_{box}(\omega) + \epsilon_{tox}(\omega) = 0. \tag{3.32}$$

Eq.3.32 can be solved analytically by taking a single polar phonon expression for the $\epsilon_{ox}(\omega)$:

$$\epsilon_{ox}(\omega) = \epsilon_{ox}^i + \frac{\epsilon_{ox}^0 - \epsilon_{ox}^i}{1 - \omega^2/\omega_{TO}^2}, \tag{3.33}$$

where ϵ_{ox}^0 and ϵ_{ox}^i are the low and intermediate frequency permittivities of the considered oxide, and ω_{TO} is the transverse optical phonon frequency. The parameters of dielectric materials are reported in Tab. 3.3. The solution of Eq.3.33 yields the surface optical polar phonon frequencies $\omega_{SO}(q)$:

$$\omega_{SO/box}^2 = \left(-B + \sqrt{B^2 - 4AC}\right)/(2A), \tag{3.34a}$$

$$\omega_{SO/tox}^2 = \left(-B - \sqrt{B^2 - 4AC}\right)/(2A), \tag{3.34b}$$

where $A = (\epsilon_{tox}^i + \epsilon_{box}^i)$, $B = -(\epsilon_{tox}^0 + \epsilon_{box}^i +) \times \omega_{TO,tox}^2 - (\epsilon_{box}^0 + \epsilon_{tox}^i +) \times \omega_{TO,box}^2$ and $C = (\epsilon_{tox}^0 + \epsilon_{box}^0) \times \omega_{TO,tox}^2 \omega_{TO,box}^2$. In this chapter, we have assumed that surface

Table 3.1: Deformation potentials for inelastic phonon assisted transitions in single-layer MoS_2.

Phonon momentum	Electron transition	Deformation potential
Γ	$K \to K'$	$D_{ac} = 4.5$ eV
Γ	$K \to K$	$D_{op} = 5.8 \times 10^8$ eV cm^{-1}
K	$K \to K'$	$D_{ac} = 1.4 \times 10^8$ eV cm^{-1}
K	$K \to K'$	$D_{op} = 2.0 \times 10^8$ eV cm^{-1}
Q	$K \to Q$	$D_{ac} = 9.3 \times 10^7$ eV cm^{-1}
Q	$K \to Q$	$D_{op} = 1.9 \times 10^8$ eV cm^{-1}
M	$K \to Q$	$D_{ac} = 4.4 \times 10^8$ eV cm^{-1}
M	$K \to Q$	$D_{op} = 5.6 \times 10^8$ eV cm^{-1}
Γ	$Q \to Q$	$D_{ac} = 2.8$ eV
Γ	$Q \to Q$	$D_{op} = 7.1 \times 10^8$ eV cm^{-1}
Q	$Q \to Q$	$D_{ac} = 2.1 \times 10^8$ eV cm^{-1}
Q	$Q \to Q$	$D_{op} = 4.8 \times 10^8$ eV cm^{-1}
M	$Q \to Q$	$D_{ac} = 2.0 \times 10^8$ eV cm^{-1}
M	$Q \to Q$	$D_{op} = 4.0 \times 10^8$ eV cm^{-1}
K	$Q \to Q$	$D_{ac} = 4.8 \times 10^8$ eV cm^{-1}
K	$Q \to Q$	$D_{op} = 6.5 \times 10^8$ eV cm^{-1}
Q	$Q \to K or K'$	$D_{ac} = 1.5 \times 10^8$ eV cm^{-1}
Q	$Q \to K or K'$	$D_{op} = 2.4 \times 10^8$ eV cm^{-1}
M	$Q \to K or K'$	$D_{ac} = 4.4 \times 10^8$ eV cm^{-1}
M	$Q \to K or K'$	$D_{op} = 6.6 \times 10^8$ eV cm^{-1}

optical phonons are responsible only for intra-valley transitions, hence we can write the un-screened matrix elements as:

$$|M^{\nu,\nu}_{SO,tox}(\vec{k},\vec{k'})|^2 = \frac{\hbar\omega_{SO,tox}}{2Aq}\left[\frac{1}{\epsilon^i_{tox}+\epsilon_{box}(\omega_{SO,tox})} - \frac{1}{\epsilon^0_{tox}+\epsilon_{box}(\omega_{SO,tox})}\right]. \quad (3.35)$$

Finally, the scattering rate due to surface optical phonons is:

$$S^{\nu,\nu}_{SO}(\vec{k},\vec{k'}) = \frac{2\pi}{\hbar}|M_{SO}(\vec{k},\vec{k'})|^2\left[n_{SO}+\frac{1}{2}\mp\frac{1}{2}\right]\delta[E^\nu(\vec{k'})-E^\nu(\vec{k})\mp\hbar\omega_{SO}]. \quad (3.36)$$

3.2.2.3 Scattering with Coulomb centers

To study the scattering of carriers due to the Coulomb impurities and the effect of surrounding dielectrics on this mechanism, the Fourier transform of the scattering potential due to the charged impurity located at $(\vec{r}, z) = (0, z_0)$ can be written as [135]:

$$\phi(q,z) = \frac{e^2}{2q\epsilon_{2D}}\left[e^{-q|z-z_0|} + C_1\exp^{qz} + C_2\exp^{-qz}\right], \quad (3.37)$$

where $0 < z < a_z$, e is the elementary charge, $\epsilon_{2D} = 7.6\epsilon_0$ is the static permittivity of monolayer MoS_2, and the q dependent constants C_1, C_2 are given by:

$$C_1 = \frac{\left[(\epsilon_{2D}-\epsilon^0_{box})(\epsilon_{2D}-\epsilon^0_{tox})\exp^{-q|z_0|} + (\epsilon_{2D}+\epsilon^0_{box})(\epsilon_{2D}-\epsilon^0_{tox})\exp^{-q|a_z-z_0|-a_z}\right]}{(\epsilon^0_{box}+\epsilon_{2D})(\epsilon^0_{tox}+\epsilon_{2D})\exp^{2qa_z} - (\epsilon_{2D}-\epsilon^0_{box})(\epsilon_{2D}-\epsilon^0_{tox})}, \quad (3.38)$$

$$C_2 = \frac{(\epsilon_{2D}-\epsilon^0_{box})(C_1+\exp^{-q|z_0|})}{\epsilon_{2D}+\epsilon^0_{box}}. \quad (3.39)$$

Table 3.2: The phonon energy for intra-valley and inter-valley transitions at the K, M, and Q points of single-layer MoS_2 as reported in [139].

Phonon mode	Γ	K	M	Q
Acoustic [meV]	0	26.1	24.2	20.7
Optical [meV]	49.5	46.8	47.5	48.1

Table 3.3: Parameters for the polar phonons in some high-κ materials. Data from [141]

Material	SiO_2	$ZrSiO_4$	AlN	Al_2O_3	HfO_2	ZrO_2
$\epsilon^0_{tox}(\epsilon_0)$	3.9	11.75	9.14	12.53	22	24
$\epsilon^i_{tox}(\epsilon_0)$	3.05	9.73	7.35	7.27	6.58	7.75

If we assume that the wavefunctions are expressed by Eq.3.27 and scattering with coulomb centers is responsible only for intra-valley transitions, then the un-screened matrix element will be given by:

$$\begin{aligned} M^{v,v}_{CI}(\vec{k},\vec{k'}) = \frac{e^2}{2qa_z\epsilon_{2D}}\left(\frac{1}{q} - \frac{q}{q^2+(2\pi/a_z)^2}\right) \times \\ \left[C_1(\exp^{qa_z} - 1) + C_2(1 - \exp^{-qa_z}) - \exp^{-qz_0} - \exp^{-q(a_z-z_0)}\right] + \\ \frac{e^2}{qa_z\epsilon_{2D}}\left(\frac{1}{q} - \frac{q}{q^2+(2\pi/a_z)^2} \times cos(2\pi z_0/a_z)\right). \end{aligned} \tag{3.40}$$

We have assumed that the scattering with Coulomb centers is elastic, therefore the rate can be written as:

$$S^{\nu,\nu}_{CI}(\vec{k},\vec{k'}) = \frac{2\pi}{\hbar}\frac{N_{imp}}{A}|M^{v,v}_{CI}(\vec{k},\vec{k'})|^2\delta[E^\nu(\vec{k'}) - E^\nu(\vec{k})] \tag{3.41}$$

where N_{imp} is the defects' concentration per unit area. It is worth mentioning that in the developed simulator in [137], the charge impurities were assumed to be located at the center of SC (half of the thickness), while in this thesis we generalized the formulation of potential for an arbitrary position z_0 of the Coulomb centers.

3.2.2.4 Neutral Defects scattering

Monolayer TMDs can have a fairly large density of NDs, and S and Mo vacancies in monolayer MoS_2 have been previously analyzed [142, 143]. Here, we have developed a phenomenological model for scattering by NDs, similar in nature to models for alloy scattering in 3D semiconductors [144]. We assume that a ND located in $(\vec{r}, z) = (\vec{0}, z)$ produces a strongly localized scattering and constant scattering potential according to the hard-cube model:

$$U_S = \Delta U \text{ for } 0 < z < a_z,\ |x|, |y| < a_d/2 \tag{3.42}$$

Based on Eqs.3.42, 3.27 the un-screened transition matrix element for scattering with neutral defects can be written as:

$$|M^{\nu,\nu}_{ND}(\vec{k'},\vec{k})|^2 = \frac{\Delta U^2 a_d^4}{A}\left[sinc\left(\frac{q_x a_d}{2\pi}\right) sinc\left(\frac{q_y a_d}{2\pi}\right)\right]^2, \tag{3.43}$$

where a_d^2 is the effective defect area and ΔU is an effective scattering potential. The ΔU is estimated as the difference between the energy at the peak of the density of states of the

defect and the conduction band minimum [143], which is similar in spirit to the effective scattering potential for alloy scattering estimated from the conduction band discontinuity between the two constituent semiconductors [143]. q_x and q_y are the x and y component of the wavevector $\vec{q} = \vec{k'} - \vec{k}$. By treating the scattering with neutral defects as elastic, the rate for a defects' concentration equal to N_D becomes:

$$S^{\nu,\nu}_{ND}(\vec{k},\vec{k'}) = \frac{2\pi}{\hbar}\frac{N_D}{A}|M^{\nu,\nu}_{ND}(\vec{k},\vec{k'})|^2\delta[E_\nu(\vec{k'}) - E_\nu(\vec{k})]. \tag{3.44}$$

3.2.2.5 Scattering due to strain fluctuations

The scattering due to strain fluctuations (SF) has been claimed to be a dominant source of scattering in high-quality graphene layers [145], motivating us to develop a model accounting for their effect on electron scattering in monolayer MoS_2. If we let $\Delta\varepsilon(\vec{r})$ denote the random deviation from the average strain value, then the scattering potential $U_{\Delta\varepsilon}(\vec{r})$ is identified with the random fluctuation of the valley energy minima and it can be written as $U_{\Delta\varepsilon}(\vec{r}) = D_{\Delta\varepsilon}\Delta\varepsilon(\vec{r})$, where $D_{\Delta\varepsilon}$ is the effective deformation potential for SFs scattering. As the strain-induced variation of the effective masses is small [146], we neglected its influence on SFs scattering. By using the wavefunction in Eq.3.27, the matrix element M_{SF} for SFs scattering can be written as:

$$M_{SF}(\vec{k},\vec{k'}) = (D_{\Delta\varepsilon}/A)\int_A \Delta\varepsilon(\vec{r})\exp^{-i\vec{q}r}\,dr \tag{3.45}$$

where $q = \left|\vec{k'} - \vec{k}\right|$ is the electron wavevector redirection. The squared magnitude of the matrix element is thus readily given by:

$$\left|M_{SF}(\vec{k'},\vec{k})\right|^2 = {D_{\Delta\varepsilon}}^2 S_{\Delta\varepsilon}(q) \qquad S_{\Delta\varepsilon}(q) = \pi\left(\Delta\varepsilon L_c\right)^2\left(1+(qL_c)^2/2\right)^{-3/2} \tag{3.46}$$

and it is proportional to the power spectrum $S_{\Delta\varepsilon}(q)$ of $\Delta\varepsilon(\vec{r})$. In this work we used the form of the SF spectrum reported in Eq.3.46, which corresponds to an exponential auto-correlation function of $\Delta\varepsilon(\vec{r})$, where $\Delta\varepsilon(\vec{r})$ and L_C are the root mean square (r.m.s.) value and the correlation length of $D_{\Delta\varepsilon}(\vec{r})$, respectively. Such a spectrum has been frequently employed to describe the random variations in the position of the semiconductor-oxide interface in CMOS transistors [135].

3.2.2.6 Screening

This section revisits the effect of screening of CB electrons on the carriers scattering. Screenong is accounted for only intra-valley transitions; inter-valley transitions are left un-screened [135]. The static screening method described in this section is called the dielectric function approach [135]:

$$M^\nu(\vec{k},\vec{k'}) = \Sigma_\omega \epsilon_{\nu,\omega} M^\omega_{scr}(\vec{k},\vec{k'}), \tag{3.47}$$

where $M^\omega_{scr}(\vec{k},\vec{k'})$ is the screened scattering matrix element for $\vec{k},\vec{k'}$ states of valley ω and $M^\nu(\vec{k},\vec{k'})$ is an un-screened scattering matrix element of valley ν. The $\epsilon_{\nu,\omega}$ denotes an entry of the dielectric matrix:

$$\epsilon_{\nu,\omega}(q) = \delta_{\nu,\omega} - \frac{e^2}{q(\epsilon_{2D}+\epsilon_{box})}\Pi_\omega(q)F_{\nu,\omega}(q), \tag{3.48}$$

where $q = \left|\vec{k} - \vec{k'}\right|$, $\delta_{\nu,\omega}$ is the Kronecker function , $\Pi_\omega(q)$ and $F_{\nu,\omega}(q)$ are the polarization factor and Form factor, respectively. The polarization factor is defined as:

$$\Pi_\omega(q) = \frac{1}{A}\Sigma_k \frac{f_0[E_\omega(k+q)] - f_0[E_\omega(k)]}{E_\omega(k+q) - E_\omega(k)}, \tag{3.49}$$

where f_ν is the Fermi Dirac occupation function in valley ν. The form factor can be expressed as:

$$F_{\nu,\omega}(q) = \int dz \chi_\nu(z)(\chi_\nu(z))^\dagger \int dz_0 (\chi_\omega(z_0))^\dagger \chi_\omega(z_0)\phi_N(q, z, z_0), \tag{3.50}$$

where ϕ_N is the normalized Fourier transform of the scattering potential due to the charged impurities located at $z = z_0$:

$$\phi_N(q, z, z_0) = \frac{q(\epsilon_{2D} + \epsilon_{box})}{e^2}\phi(q, z, z_0), \tag{3.51}$$

and $\phi(q, z, z_0)$ is defined in Eq.3.37. To calculate the screened matrix elements, inverse matrix of dielectric function must be extracted and then we have:

$$M^\omega_{scr}(\vec{k}, \vec{k'}) = \Sigma_\omega [\epsilon^{-1}]_{\nu,\omega} M^\nu(\vec{k}, \vec{k'}). \tag{3.52}$$

Because in the case of study the dielectric matrix is two by two, the dielectric matrix can be analytically inverted to evaluate screened matrix elements as:

$$M^\omega_{scr}(\vec{k}, \vec{k'}) = \frac{(1 - \Sigma_{\omega\neq\nu}\epsilon_{\nu,\omega})M^\nu(\vec{k}, \vec{k'}) + \Sigma_{\omega\neq\nu}\epsilon_{\nu,\omega}M^\omega_{scr}(\vec{k}, \vec{k'})}{2 - \Sigma_\omega \epsilon_{\nu,\omega}}. \tag{3.53}$$

3.3 Piezoresistance and strain Sensors

As mentioned earlier, monolayers of 2D transition metal dichalcogenides (TMDs) consist of a plane of transition metal atoms sandwiched between two planes of chalcogen atoms via covalent bonds [147]. In the semiconducting phase, monolayer TMDs of the form MX_2 (where $M = Mo$, W; $X = S$, Se) have a similar energy band structure with a conduction band minimum at the K-point, and a satellite minimum between the K- and Γ-point, often labelled as the Q-point. This $K - Q$ energy separation ΔE_{KQ} strongly influences the intrinsic electron mobility through inter-valley phonon scattering [148]. Under the influence of strain, ΔE_{KQ} is tunable [149, 150], which is predicted to give rise to a giant intrinsic piezoresistive coefficients Π on the order of 3000 [20, 146], where $\Pi = (\Delta R/R)\Delta\varepsilon$ [33] and $\Delta\varepsilon$ is magnitude of the strain window. This contrasts with the weaker Π of 3D materials that is mostly driven by changes in effective mass [27, 32, 33]. To date, no experiments have probed the appropriate window of strain and/or taken care to isolate the Π of TMDs from extrinsic limiters like contacts and surface effects. As such, reported experimental values have been below 300, rendering them comparable to 3D materials [151–153].

As an outcome of a collaboration with Stanford University (simulation parts have been done in our laboratory), we demonstrate a giant piezoresistance $\Pi \approx 724$ in monolayer MoS_2 under uniaxial strain, which is the highest intrinsic value yet reported for a material at room temperature. We optically map both the global strain and short-range strain variation using Raman spectroscopy and photoluminescence (PL), and extract sheet resistance using the Transmission Line Method (TLM) under vacuum [154]. A rigorous transport model and analysis of several scattering mechanisms is used to investigate the physical origin of this giant intrinsic piezoresistive effect.

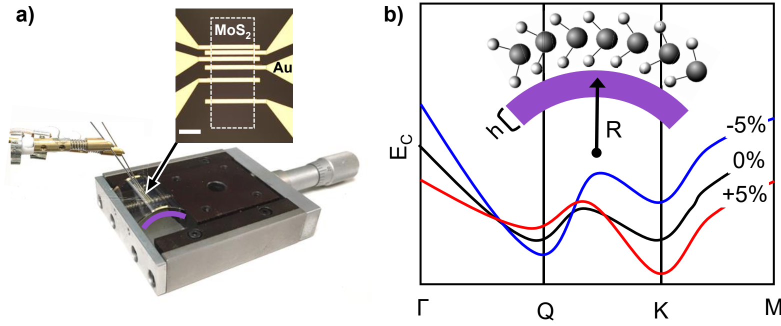

Figure 3.2: The flexible device used to probe piezoresistance in our 2D materials and an illustration of the strain-induced tuning of the band structure in monolayer MoS_2. (a), TLMs are fabricated on flexible substrates and controlled uniaxial strain is applied using a two-point bending method. The inset shows the metal contacts and the outline of the etched 2D material. (b), an illustration of changes to the $K - Q$ valley separation under strain, which drive the piezoresistive effect in monolayer MoS_2. The inset shows monolayer MoS_2 under strain dictated by the height (h) and bending radius (R) of the substrate.

3.3.1 Experimental extraction of MoS_2 piezoresistance

Piezoresistance of 2D MoS_2 was experimentally extracted in Stanford using the flexible device shown in Fig. 3.2.a. 2D MoS_2 is transferred onto polyethylene naphthalate (PEN) substrates and TLM structures are fabricated with Au contacts for MoS_2. Uniaxial surface strain of $\varepsilon = 2h/R$ is applied by two-point bending, where h is the substrate thickness and R is the bending radius. The strain dependence on the band structure of monolayer MoS_2, which drives the piezoresistive effect, is qualitatively illustrated in Fig. 3.2.b. Our devices are limited to 1% externally applied strain to avoid slipping at the vdW interface of the 2D material and substrate. TLMs are used to deembed the contacts and extract the sheet resistance of the 2D material under strain. Double sweeps (forward and backward) of the voltage are used to reveal any signs of hysteresis and slow charge traps. All testing is carried out under vacuum (10^{-5} torr) to stabilize the carrier density and avoid chemi- or physisorption during or between testing. We note that the MoS_2 used here is un-gated and un-intentionally doped, and is expected to have an as-grown electron density of $n \approx 2 \times 10^{11}$ cm^{-2} [155].

The TLM data used to extract Π for MoS_2 are shown in Fig. 3.3. Channel lengths of 5, 10, 20, and 40 μm are used and an optical image is shown in the Fig. 3.3.a inset. The MoS_2 strain is also verified through optical techniques discussed in subsequent paragraphs. While we exert $\sim 1\%$ of externally applied tensile strain, our devices have $\sim 0.5\%$ of built-in compressive strain from the fabrication process. This built-in strain is essential to probing the appropriate compressive-to-tensile window of strain where the piezoresistive effect is observable [20, 146]. The MoS_2 is transitioned from about -0.5 (compressed) to $+0.5$ (tensile) strain, a $\Delta\varepsilon$ of $1 \pm 0.15\%$, giving sheet resistances of 27.2 MΩ sq^{-1} and 3.3 MΩ sq^{-1}, respectively (Fig. 3.3.a). This corresponds to a Π of 724 ± 108. We report Π as an isotropic value as we likely have mixed crystallographic orientations within our channel given the MoS_2 grain size [155]. Moreover, our simulations show armchair and zigzag orientations have similar piezoresistive effects. The current-voltage (I-V) data from the TLM under compressive and tensile strain are shown Fig. 3.3.b,c, respectively.

Experimentally, strain can be verified in MoS_2 using optical techniques such as Raman and PL. Monolayer MoS_2 (1H semiconducting phase) is of the D_{3h} point group symmetry and has nine vibrational modes, three of which are Raman-active [156]. These three

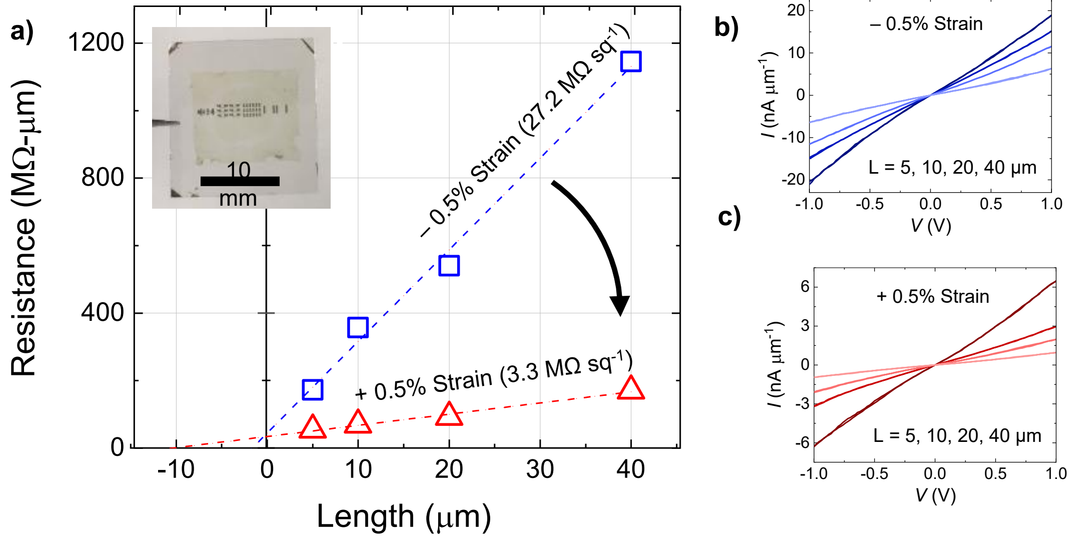

Figure 3.3: Extractions of MoS_2 sheet resistance when cycled between -0.5% and $+0.5\%$ strain. (a), the first cycle reveals a change in sheet resistance from 27.2 MΩ sq^{-1} to 3.3 MΩ sq^{-1}, respectively, giving a Π of 724. The inset shows an array of fabricated TLMs on a PEN substrate. (b), two-terminal I-V data for the compressed TLM. The lines correspond to measurements for each channel length (L), with the longest channel having the lowest current. (c), two-terminal I-V data for the tensile TLM.

Raman-active modes are denoted as the E″, E′, and A_{1g}, and reside near wavenumbers of $\sim$ 286, $\sim$ 384.3, and $\sim$ 404.3 cm^{-1}, respectively, for unstrained intrinsic material at room temperature [157]. The in-plane E′ mode shows a strong dependence of peak position (ΔE′) with strain [158], shifting $\sim$ 1.9 cm^{-1} per percent of strain. Similarly, the E′ full-width-half-maximum ($\Gamma_{E'}$) captures short range strain variation that is buried within the Raman spot size ($\sim$ 500 nm) [145, 159].

3.3.2 Theoretical models of MoS_2 piezoresistance

We assume that the envelope wavefunction Ψ for the 2D electron gas in monolayer MoS_2 can be written as Eq.3.27, where the thickness of monolayer MoS_2 is $a_z = 0.615$ nm. For energies close to the K- and Q-valley minima, we use the non-parabolic effective mass energy relation (Eq.3.18). For the unstrained MoS_2 we used $\alpha = 0.94$ eV^{-1}, $m_l = m_t = 0.47m0$ for the isotropic K-valleys, and $\alpha = 1.16$ eV^{-1}, $m_l = 1.14m0$ and $m_t = 0.54m0$ for Q-valleys. All transport calculations account for the strain-dependence of α, m_l, m_t, as determined from *ab-initio* DFT calculations [137]. In order to ensure a sound, microscopic transport model of monolayer MoS_2, we utilized the numerical solution of the LBTE (see Sec.3.2.1). The formalism for scattering mechanisms have been revisited in Sec.3.2.2 and the corresponding deformation potentials and phonon energies are described in [20].

Fig. 3.4.a shows the calculated phonon-limited mobility versus strain at a carrier density of $n = 2 \times 10^{11}$ cm^{-2}, which is the experimentally estimated value for the un-gated and unintentionally doped samples [155]. It can be seen that mobility grows quite sharply with increasing tensile strain (black squares) in the -0.5% to $+0.5\%$ range that was experimentally explored. The first BZ for the single-layer MoS_2 is shown in Fig. 3.4.b. The six K-valleys are degenerate in all the strain conditions considered in this work, while the six Q-valleys split into four Q_A- and 2 Q_B-valleys with different effective masses and energy minima when a uniaxial strain is introduced. The physical interpretation of strain-induced

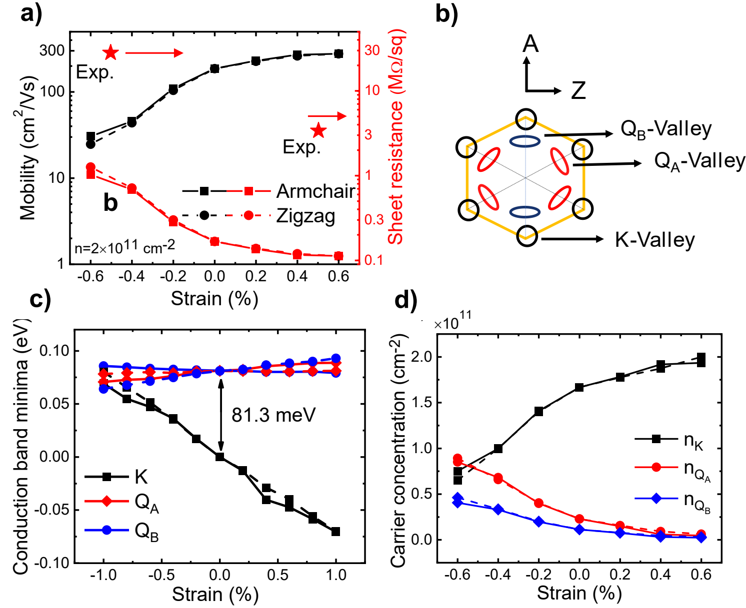

Figure 3.4: Simulated intrinsic electron piezoresistance and strain-induced valley re-population. (a), intrinsic phonon-limited electron mobility (black lines, left y-axis) and sheet resistance (red lines, right y-axis) versus uniaxial strain for a carrier density $n = 2 \times 10^{11}$ cm^{-2}. Transport and strain direction are either armchair (solid lines) or zigzag (dashed lines); red stars are experimental sheet resistance values (b), the first BZ for the single-layer MoS_2. The six K valleys are degenerate in all the strain conditions considered in this work, while the six Q-valleys split into four Q_A- and two Q_B-valleys with different effective masses and energy minima when a uniaxial strain is introduced. (c), K-, Q_A- and Q_B-valley minimum energy for MoS_2 versus strain obtained from *ab-initio* DFT calculations [135]. (d), calculated carrier density n_K, n_{Q_A}, n_{Q_B} in the K and $Q_{A/B}$-valley for an overall carrier density (i.e. K- plus $Q_{A/B}$-valley density) of $n = 2 \times 10^{11}$ cm^{-2}, which is the estimated value in experiments.

mobility modulation is illustrated in Fig. 3.4.c,d, which report the K- and Q-valley energy minima and corresponding carrier density, respectively. In fact, for compressive strain the mobility is small at first because the Q-valley, which has a lower mobility compared to the K-valley [137], has a relatively large population, and also because ΔE_{KQ} is small enough that inter-valley phonon scattering degrades the mobility.

While the behavior of the phonon-limited mobility in Fig. 3.4.a is qualitatively consistent with the giant piezoresistance observed in experiments, Fig. 3.4.a also reveals that the correspondingly sheet resistance, calculated as $R_s = 1/(e\mu n)$, is much smaller than measured because mobility is overestimated. Hence, we now continue our analysis by adding other sources of scattering, starting with the short-range strain fluctuations (SFs) observed in the Raman map (not shown). The effective deformation potential for SFs scattering $D_{\Delta\varepsilon}$ is extracted directly from Fig. 3.4.c as ~ 0.7 eV for the K-valley as ~ 0.3 eV for the Q-valley. In this analysis we used the form of the SF spectrum reported in Eq.3.46 and, we also account for the effect of the static screening produced by the electrons in the MoS_2 conduction band, however the effect of screening is practically negligible due to the small carrier density $n = 2 \times 10^{11}$ cm^{-2}.

Fig. 3.5.a shows the calculated mobility and sheet resistance including both phonons and SFs scattering, for $\Delta\varepsilon = 1.0\%$ and consistent with the Raman maps (not shown). Due to the Raman spot size (~ 500 nm), it is difficult to estimate the nanoscale length,

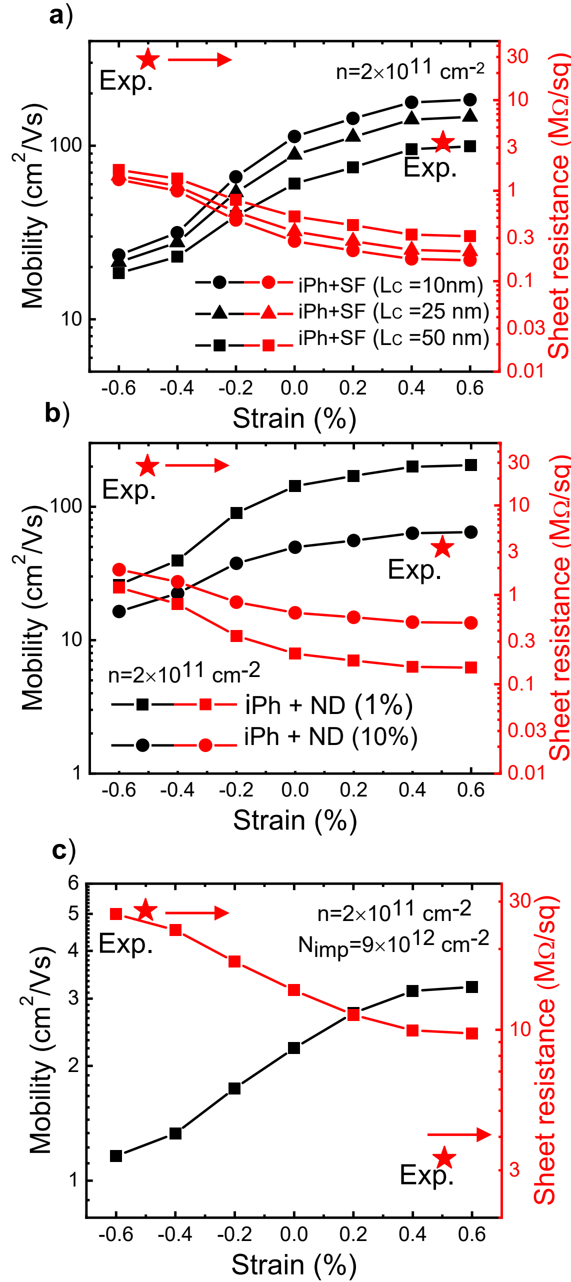

Figure 3.5: Simulated electron piezoresistance with various sources of scattering. (a), mobility and sheet resistance versus strain for a carrier density of $n = 2 \times 10^{11}$ cm^{-2} for scattering due to: (a), intrinsic Phonon (iPh) and Strain Fluctuations (SFs) at various correlation lengths L_c. (b), Phonon and Neutral Defects (NDs) with various levels areal densities N_D expressed in percentage of the sulfur atoms areal density. (c), iPh and Coulomb Impurities (CIs) for a density $N_{imp} = 9 \times 10^{12}$ cm^{-2} of CIs resulting in a sheet resistance that matches experiments for a compressive strain -0.5%. Transport and strain are along armchair direction.

L_C, therefore Fig. 3.5 shows results for different L_C values. SFs scattering appears too weak to increase resistance to values comparable to experiments, and its influence on mobility and resistance decreases by increasing L_C. This is because, by increasing L_C, the $S_{\Delta\varepsilon}(q)$ decays more steeply at large q, such that SFs scattering cannot effectively relax electron momentum in the wavevectors range that is the most relevant for mobility, namely close to the thermal $k_{th} = \sqrt{2\pi m_d KT}/2\hbar = 0.5 \times 10^7\ cm^{-1}$ (see Fig. 3.7) [135].

Moreover, by including SFs scattering, the sensitivity of resistance to strain is reduced and tends to become much weaker than in experiments. This is due to the long-range nature of SFs scattering (i.e. scattering with small q), in virtue of which SF enhances intra-valley scattering (thus reducing the mobility difference in the two valleys), but it has negligible influence on inter-valley scattering because of the large distance $\Delta k \approx 7$ nm^{-1} between K and Q valleys in reciprocal space. In other words, SFs scattering tends to weaken the sensitivity of mobility to the strain due to valley re population as illustrated in Fig. 3.4.b,c.

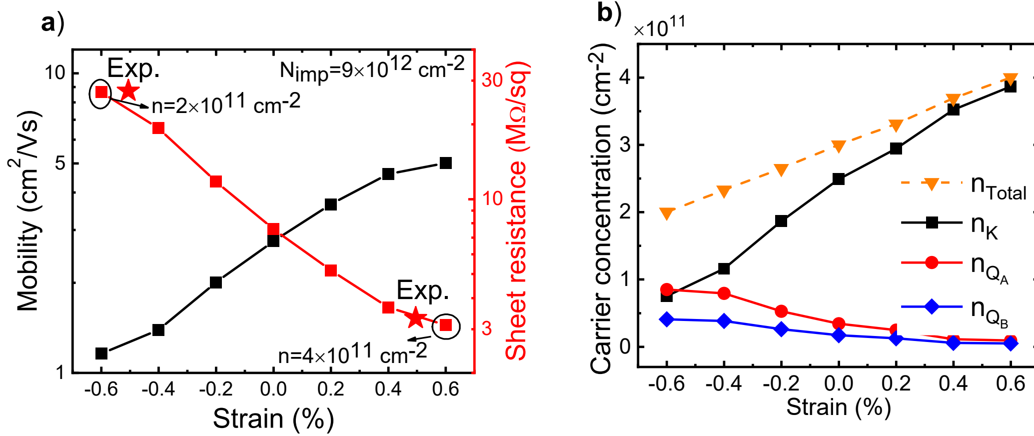

Figure 3.6: Simulated intrinsic electron piezoresistance and strain-induced valley re-population. (a), intrinsic phonon-limited electron mobility (black lines, left y-axis) and sheet resistance (red lines, right y-axis) versus uniaxial strain for a carrier density $n = 2 \times 10^{11}$ cm^{-2}. Transport and strain direction are either armchair (solid lines) or zigzag (dashed lines); red stars are experimental sheet resistance values (b), the first BZ for the single-layer MoS_2. The 6 K valleys are degenerate in all the strain conditions considered in this work, while the 6 Q-valleys split into 4 Q_A- and 2 Q_B-valleys with different effective masses and energy minima when a uniaxial strain is introduced. (c), K-, Q_A- and Q_B-valley minimum energy for MoS_2 versus strain obtained from *ab-initio* DFT calculations [135]. (d), calculated carrier density n_K, n_{Q_A}, n_{Q_B} in the K and $Q_{A/B}$-valley for an overall carrier density (i.e. K- plus $Q_{A/B}$-valley density) of $n = 2 \times 10^{11}$ cm^{-2}, which is the estimated value in experiments.

The next source of scattering we evaluated is neutral point defects (NDs). Monolayer TMDs can have a fairly large density of NDs, and S and Mo vacancies in monolayer MoS_2 have been previously analyzed [142, 143]. Here, we have used the model discussed in Sec.3.2.2.4. An S vacancy in MoS_2 has an estimated effective scattering potential of $\Delta U = 0.7$ eV. Figure. 3.5.b shows the calculated sheet resistance including phonons and NDs scattering up to a very large density of defects (10%). Similar to SFs scattering, ND also appears too weak to justify the experimental resistance and, moreover, tends to reduce the sensitivity to strain.

We finally consider scattering due to charged impurities (CIs) located at $(r, z) = (0, a_z/2)$, whose models have been discussed in detail(Sec.3.2.2.3). Experimentally, the origin of these charged impurities can include ionized dopants in the MoS_2, processing residue, and the substrate [160]. Figure. 3.7 shows that scattering matrix elements are much larger for CI than for ND for same density (i.e. $N_{imp} = N_D$), because of the long range (i.e. small q) part of the potential produced by a point charge. Figure. 3.5.c shows that with a CI density (N_{imp}) of $\sim 9 \times 10^{12}$ cm^{-2}, the simulated sheet resistance

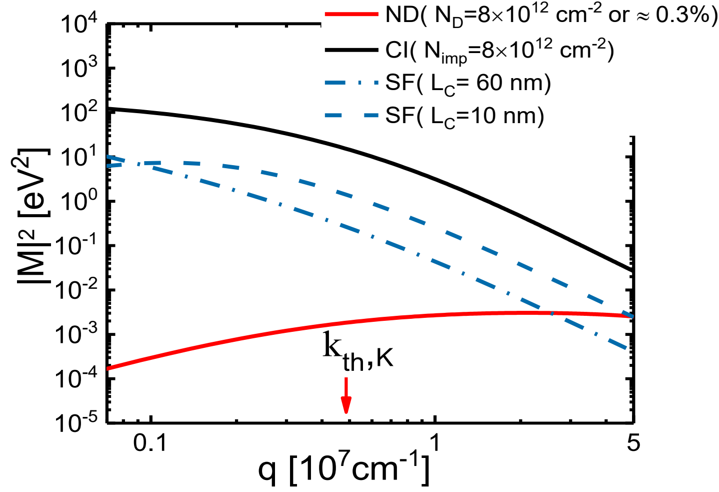

Figure 3.7: Squared matrix element wavevector redirection for SFs scattering ($\Delta\varepsilon = 1\%$ and different L_C), NDs and CIs scattering. The thermal value $k_{th} = \sqrt{2\pi m_d KT}/2\hbar$ of the electron wavevector in K-valley is indicated. Carrier density $n = 2 \times 10^{11}$ cm^{-2}, so the effect of carrier screening is minimum.

approaches the experimental value for the as-fabricated (compressed) TLM in Fig. 3.3a,b. However, this large N_{imp} also suppresses the piezoresistive effect. This is due to the long-range nature of CIs, which is not mitigated by free carrier screening due to the low carrier density n $\approx 9 \times 10^{12}$ cm^{-2}. In fact the long-range CI scattering enhances intra-valley scattering, thus reducing the mobility difference between in K- and Q-valley, which largely contributes to the strain-sensitivity of mobility, and gives negligible contributions to K-Q inter-valley scattering.

We find that our models match well with our experimental sheet resistances of Fig. 3.3.a, both compressive and tensile, when the Fermi level moderately tracks with the K-valley minima. This relationship between carrier density and strain is shown in Fig. 3.6.a. Here, the Fermi level is neither perfectly pinned (i.e., independent of strain) nor perfectly following the energy of the K-valley minima (as implicitly assumed in all previous simulation results). As such, in addition to strain modulation of inter-valley phonon scattering, there is a slight increase in carrier density and subsequently enhanced screening of CIs (see Fig. 3.6.b). One experimental explanation for this is that there is a component of the carrier density that is pinned, possibly arising from the as-grown doping that renders the MoS_2 n-type. The possible role of doping and CIs can indicate some moderate extrinsic contribution to our piezoresistance extraction.

3.4 Temperature Sensors

Fast thermal sensing requires a large temperature coefficient of resistance (TCR) as well as low thermal capacitance [59], which can be obtained by thinning the sensor [51, 58]. However, when thinned below $\sim$ 10 nm, the TCR of metals drops sharply due to strong surface scattering and possible electron localization, limiting their use as fast thermal sensors [50, 51, 60]. In contrast, in a collaborative paper with Stanford we have provided evidence that atomically thin 2D semiconductors such as MoS_2 and $MoTe_2$ maintain large TCRs, up to $\sim$ 0.3 % at 300 K^{-1} and $\sim$ 0.6 % K^{-1} at 100 K, from sub-nanometer to few-nanometer thickness. This is significantly higher than the TCR of metals at sub-10

nm thickness (e.g., 0.08 % for 3.7 nm Pt [161], and 0.02 % for 4.5 nm TiN [162], at 300 K) and higher than the TCR of 95 nm thick Cu ($\sim$ 0.25% K^{-1} at 300 K or 0.52% at 100 K) [163]. Fundamentally, and unlike in ultra-thin metals, phonon-limited transport in high-quality atomically thin 2D semiconductors maintains a large TCR, potentially enabling applications for fast temperature sensing.

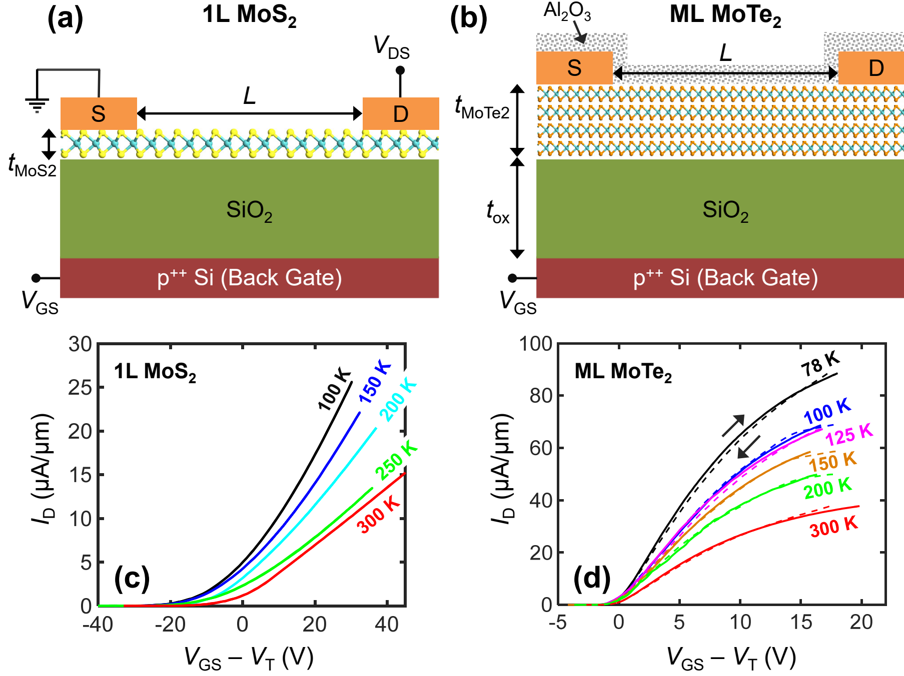

Figure 3.8: (a) Schematic of the measured monolayer (1L) MoS_2 device, with Ag/Au contacts. (b) Schematic of the measured multilayer (ML) MoTe2 device, encapsulated by Al_2O_3, with Ag contacts. Film thicknesses are $t_{MoS_2} \approx 0.615$ nm (single layer) and $t_{MoTe_2} \approx 9.4$ nm (13-layer), and both materials are in the 2H semiconducting phase. (c) Measured I_D normalized by width versus V_{GS} - V_T at several temperatures for MoS_2 and (d) for $MoTe_2$. The MoS_2 device has negligible hysteresis. The $MoTe_2$ device has small hysteresis, with arrows indicating the sweep direction of solid and dashed lines. All measurements are in vacuum. $V_{DS} = 0.1$ V and 1 V for Figs.3.8.c and 3.8.d, respectively.

We focus on measurements of monolayer MoS_2 (three atoms, or 0.615 nm thick) and $\sim$ 13 layer ($\sim$ 9.4 nm thick) $MoTe_2$ devices. These are selected as representative devices among numerous others fabricated and described elsewhere [155, 164, 165], with the focus here being on TCR measurements and simulations. Figures.3.8.a and 3.8.b display schematics of the MoS_2 and $MoTe_2$ devices (L = 3.6 μm and 1.02 μm, respectively) on SiO_2 (thickness t_{ox} = 30 nm). The highly doped Si substrates serve as back-gates to test the dependence on charge carrier density. These devices are sufficiently long to have minimal contact resistance contribution, i.e., the measured contact resistance for the monolayer MoS_2 and multilayer $MoTe_2$ devices was $\sim$ 1.3 k$\Omega\mu$m and $\sim$ 2 k$\Omega\mu$m, respectively [164, 165], at room temperature and $\sim 10^{13} cm^{-2}$ carrier density, accounting for $\sim$ 5% ($\sim$ 20%) of the total device resistance at 300 K (80 K). The complete temperature dependence of contact resistance was reported in [164, 165]. All electrical measurements were in vacuum ($\sim 10^{-5}$ Torr) after an *in situ* annealing at 250° C.

Figs.3.8.c and 3.8.d display measured drain current (I_D) versus back-gate voltage adjusted by threshold voltage (V_{GS} – V_T), from 100 K to 300 K, revealing negligible

hysteresis under forward and backward sweeps for the MoS_2 device, and a small amount of hysteresis for the $MoTe_2$ device. The drain bias (V_{DS}) was kept low to avoid self-heating. The resistance (R) was obtained for all temperatures at the same carrier density, $n \approx C_{ox}(V_{GS}-V_T)/e$, where $C_{ox} \approx 115$ nF/cm^2 is the measured capacitance of the 30 nm SiO_2 [155], and e is the elementary charge. TCR estimates are performed at relatively high n, from $\sim 7.2\times10^{12}$ cm^{-2} to $\sim 2.15\times10^{13}$ cm^{-2}, to ensure band-like transport and improve Coulomb or charged impurity (CI) screening. Figures.3.9.a and 3.9.b depict the measured R versus temperature (T) for MoS_2 and $MoTe_2$, respectively, at several carrier densities, n. Error bars arise from the combined uncertainty of threshold voltage (V_T) estimates with three different methods (linear extrapolation, Y-function and second derivative [166]), and that of the minimal hysteresis seen in Fig. 3.8.d. TCRs were obtained by fitting lines to the experimental data, with $R = R_0[1 + \alpha(T - T_0)]$, where α is the TCR, T_0 is the initial T and R_0 is the average R at T_0, across all carrier densities tested. We note that $\alpha = (1/R_0)(dR/dT)$; thus by definition the TCR itself could be a function of temperature, depending on the reference temperature (T_0) at which the TCR is evaluated. Across the considered carrier densities, we find an average TCR (at $T_0 = 300\ K$) of $\alpha = 0.27 \pm 0.01\%$ K^{-1} for monolayer MoS_2, and $\alpha = 0.28 \pm 0.02\%$ K^{-1} for 13-layer $MoTe_2$. With the reference temperature $T_0 = 100\ K$, the estimated average TCRs are $\alpha = 0.53 \pm 0.04\%$ K^{-1} and $\alpha = 0.63 \pm 0.01\%$ K^{-1} for monolayer MoS_2 and 13-layer $MoTe_2$, respectively.

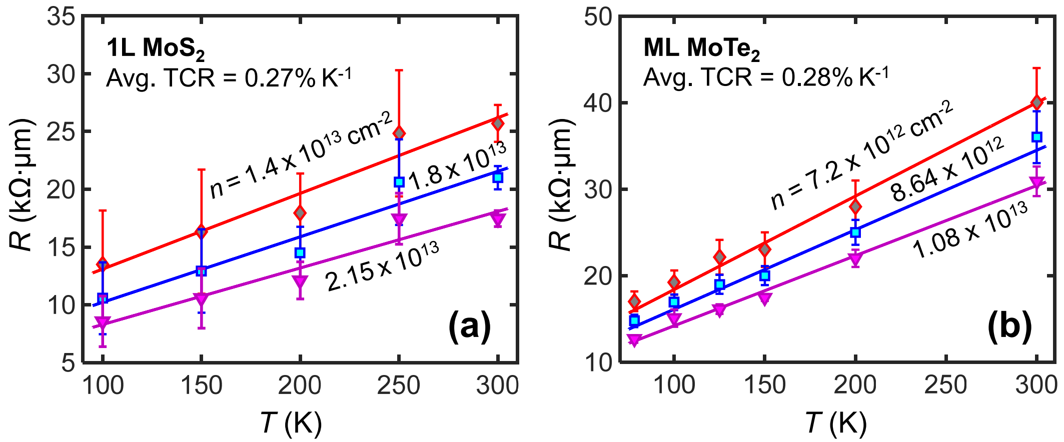

Figure 3.9: Extracting the temperature coefficient of resistance (TCR) at several carrier densities n for (a) monolayer MoS_2 and (b) 13-layer $MoTe_2$. Symbols are measured resistance adjusted by the device width. Solid lines are fits versus temperature (T), whose slope indicates the TCR.

The change of resistance with temperature in these 2D devices is attributed to their temperature-dependent mobility. The mobility is limited by scattering with intrinsic phonons (iPh), with surface optical phonons (SO Ph) of the substrate, and with CIs, as further discussed below. The slightly higher TCR in the multi-layer $MoTe_2$ device (particularly at 100 K) can be attributed to the current flow being distributed further from the interface and CIs, enabling iPh to be more dominant compared to monolayer devices [167,168]. In Fig. 3.10.a, we re-plot the measured R at three temperatures versus carrier density n, and then we display the TCR versus n in Fig. 3.10.b at $T_0 = 300\ K$. TCR increases with n because CIs are more effectively screened by larger carrier densities, enabling a more phonon-dominated mobility. Based on Fig. 3.10.b, the maximum TCRs (at $T_0 = 300\ K$) measured in this work were 0.28% K^{-1} for monolayer MoS_2 and 0.3%

K^{-1} for 13-layer $MoTe_2$. At 100 K, the maximum TCRs measured were 0.57% K^{-1} and 0.64% K^{-1}, respectively. To interpret the temperature dependence of resistance in

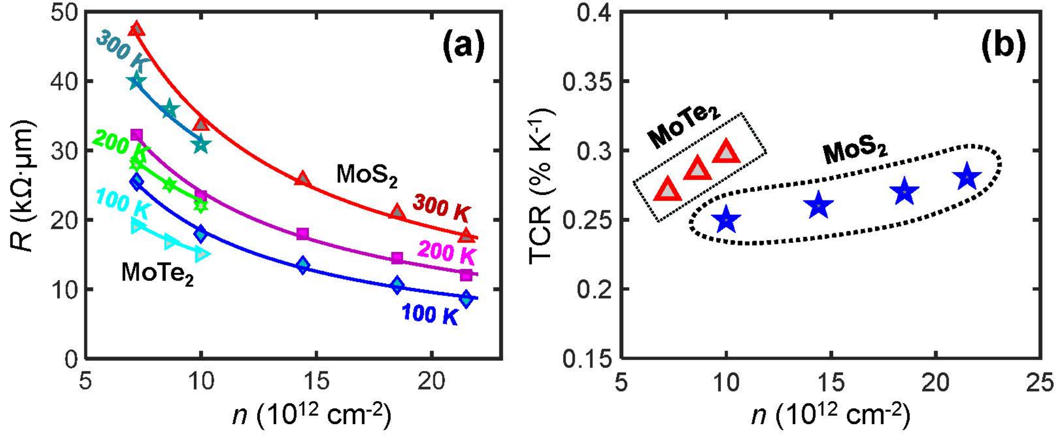

Figure 3.10: (a) Measured resistance (adjusted by width) versus estimated carrier density n at different temperatures for MoS_2 and $MoTe_2$ devices. (b) Extracted TCR (at T_0 = 300 K) versus carrier density for our 2D material devices, here monolayer MoS_2 and 13-layer MoTe2. The TCR of these 2D materials is as high as $\sim 0.6\%$ K^{-1} at $T_0 = 100$ K.

the monolayer limit (MoS_2), we performed numerical simulations using the Linearized Boltzmann Transport Equation (LBTE) discussed in Sec.3.2.1. We included both the K and Q conduction band valleys of MoS_2 [137], and electron scattering with acoustic and optical phonons intrinsic to the MoS_2 (iPh), as well as remote SO phonons and CIs of the SiO_2 substrate, the latter two mechanisms describing the extrinsic effect of the substrate. Some scattering mechanisms involved were anisotropic (e.g., SO Ph. and CIs); thus, we did not introduce any of the isotropic simplifications often employed for the LBTE, but instead performed a direct, numerical solution with the approach discussed earlier in Sec.3.2.1. The effective masses (m_t and m_l), band non-parabolicity factors (α), and K to Q valley offset (ΔE_{KQ}) were obtained from *ab -initio* calculations [137], and the MoS_2 is assumed to be un-strained. SO Ph and CI scattering account for extrinsic effects of the SiO_2 substrate. For SO phonons, we consider only the SiO_2 transverse optical (TO) mode with the lowest energy $\hbar\omega_{TO} \approx 55.6$ meV, assuming semi-infinite SiO_2 and vacuum, respectively, below and above MoS_2, and neglecting the possible coupling between SiO_2 phonons and MoS_2 plasmons [140]. This allows us to write the secular equation $[\epsilon^{int}_{SiO_2} + (\epsilon^0_{SiO_2} - \epsilon^{int}_{SiO_2})/(1 - \omega^2/\omega^2_{TO}) = \epsilon_0$ solving for $\omega = \omega_{SO}$ [137]. For a static $\epsilon^0_{SiO_2} = 3.9\epsilon_0$ and an intermediate frequency SiO_2 dielectric constant $\epsilon^{int}_{SiO_2} = 3.05\epsilon_0$ (ϵ_0 being the permittivity of vacuum), we obtain $\hbar\omega_{SO} = 61$ meV. Fig. 3.11.a reports the simulated mobility versus temperature showing the expected power law dependence ($\mu \propto T^{-\gamma}$) with an exponent varying between $\gamma = 1$ and 1.9 depending on the scattering mechanism included in the analysis. Figure. 3.11.b shows the calculated resistance $R = L/(en\mu)$ with $L = 3.6$ μm (the length of measured MoS_2 sample) as a function of temperature. By neglecting CIs (bottom two curves), the simulations predict TCR as large as 0.45% K^{-1} at 300 K ($\sim 2.5\%$ K^{-1} at $T_0 = 100$ K). In particular, green circles were obtained for iPh only; hence they correspond to a suspended MoS_2 with no scattering sources related to the SiO_2 substrate. By including an equivalent CI density $N_{imp} = 1.3 \times 10^{12}$ cm^{-2} (top three curves), the calculated room temperature resistance is in good agreement with experiments, the temperature dependence becomes weaker, and the TCR drops to $\sim 0.34\%$ K^{-1} at 300 K. Here, N_{imp} may be low compared to the measured sample, because

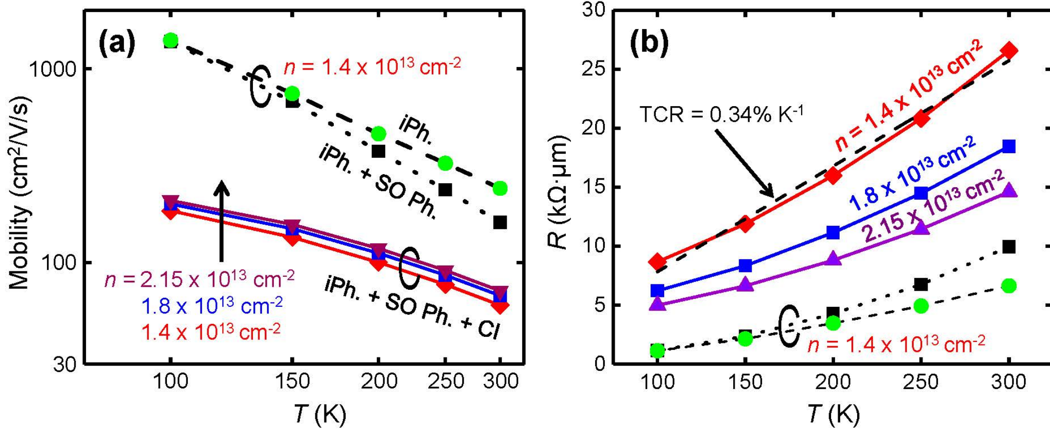

Figure 3.11: Numerical simulations. (a) Monolayer MoS_2 mobility versus temperature for different carrier densities. Simulations are for different scattering mechanisms: intrinsic MoS_2 phonons (iPh), surface optical phonons of the SiO_2 substrate (SO Ph), and Coulomb impurities (CI). (b) Calculated resistance (adjusted by width) versus temperature for scattering mechanisms in (a) and $L = 3.6$ μm, like the measured sample. CI density is $N_{imp} = 1.3 \times 10^{12}$ cm^{-2} for the top three simulations and $N_{imp} = 0$ for the bottom two. Dashes with TCR= 0.34% K^{-1} are a linear fit to the calculated resistance, which most closely matches the experiments at $T_0 = 300$ K.

in simulations it is an equivalent density of CIs in the middle of MoS_2, where the matrix element for Coulomb scattering is the largest [20, 137].

The simulated TCR is slightly larger than the experimental value, which is mainly due to an overestimation of simulated mobility (i.e., underestimate of resistance) at $T = 100$ K. Uncertainty regarding the actual position and density of CIs can also explain the difference between simulations and experiments. Importantly, simulations suggest that the TCR of 2D materials could be improved by reducing the density of CIs. The TCRs obtained here for ultra-thin 2D devices are significantly higher than those of ultra-thin metals, as shown in Fig. 3.12. For all TCR extractions here, we take $T_0 = 300$ K to make a consistent comparison. Although the TCRs measured for ultra-thin 2D devices are slightly lower than the TCR of bulk metals, the TCR for sub-nanometer thin monolayer MoS_2 is higher than that for 95 nm thick Cu lines ($\sim$ 0.25% K^{-1}) [163] and significantly higher than the TCR of metals at comparable (i.e., sub-10 nm) thicknesses. We also note that metal TCRs decrease with film thickness and can even become negative in TiN films thinner than $\sim$ 3 nm [162]. The trends observed for thin metals are due to increased scattering by surface roughness and grain boundaries [179, 180]. Few-nanometer thin metal films could even be discontinuous or oxidized, displaying negative TCR due to hopping-like transport between separated metal islands [162, 181]. On the other hand, the large positive TCR of ultra thin 2D devices illustrates that it is strongly influenced by phonon scattering, even in such atomically thin films. Moreover, our simulations suggest that 2D TCR could be further increased by reducing the density of Coulomb impurities.

While an in-depth discussion of potential applications is beyond the scope of this work, we point out that the large TCR of ultra-thin 2D devices could enable fast yet simple thermal sensors by overcoming the limitation of a low TCR in thin metal lines. These would be thin bridge-like sensors, with the 2D material supported by a few-nanometer thin insulator (e.g., SiO_2 or Si_3N_4) and capped by few-nanometer thin suboxides for doping (e.g., AlO_x, TiO_x, or MoO_x) [182–184]. Proper chemical doping eliminates the need for

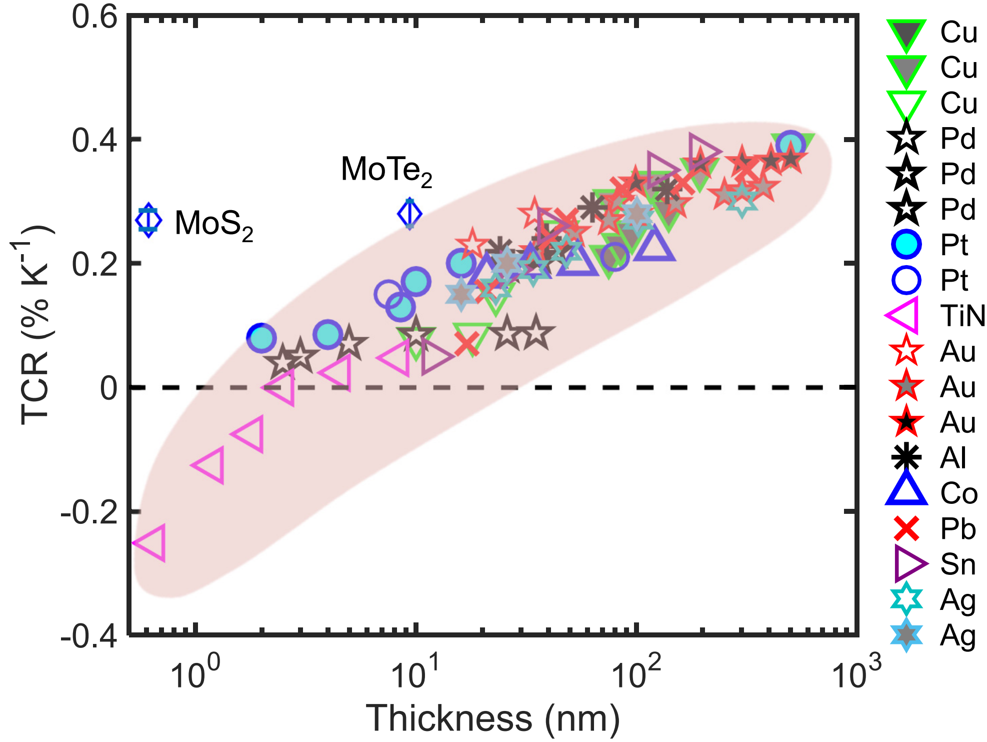

Figure 3.12: Measured TCR versus material thickness. Our measured TCR values at 300 K for monolayer MoS_2 (0.615 nm thick) and multi-layer $MoTe_2$ (9.4 nm thick) are shown with blue diamonds. TCR data at 300 K for various metals (symbols in shaded region) have been extracted from the literature for Cu [163, 169, 170], Pd [171–173], Pt [161, 174], TiN [162], Au [175–177], Al [171], Co, Ag [170, 171], Sn, and Pb [178].

a back-gate, which was used here to test the carrier density dependence. The charge transfer doping separates the dopants (in the suboxide) from the mobile carriers (in the 2D material), thus preserving their mobility [182–184], which could even be enhanced by dielectric or carrier screening.

Regarding the time response of such 2D sensors, molecular dynamics simulations have shown that the thermal time constant of a 2D material on a nanometer-thin oxide is only $\sim$ 0.1–0.4 ns [185], significantly faster than the simulated response times of diode sensors ($\sim$ 165 ns) in complementary metal-oxide-semiconductor (CMOS) silicon on insulator (SOI) technology [55]. While PIN diodes hold an advantage from the point of view of CMOS integration, this comes at the expense of a lower TCR ($\sim$ 0.2% K^{-1}at 300 K) [186] and larger area [55]. Outside of CMOS, ultrathin 2D temperature sensors could be integrated into thermal interface materials (TIMs), where they would introduce a thermal interface resistance of only 10^{-4} cm^2K/W [187], significantly lower than that of conventional TIMs, $\sim$ 0.1 cm^2K/W [188].

3.5 Gas Sensors

3.5.1 Titanium Carbide MXene as NH_3 Sensor

The development of novel gas sensors, with rapid and efficient gas concentration detection capabilities, has been a major research focus for applications including air pollution monitoring [61], medical diagnostics [62], food and beverage quality control [63], and explosives detection [64]. Various materials, such as conductive polymer composites [65], carbon nanotubes [66, 67], metal oxide semiconductors [189], graphene [68], and metal-organic frameworks [69] have been used for the fabrication of gas sensors. Two-dimensional (2D) layered materials consist of atomic sheets with strongly bonded atoms, which are held together by weak interlayer vdW forces. 2D layered materials have attracted growing interest in the development of room-temperature gas sensors with high sensitivity, due to their high surface-to-volume ratios [70, 146].

MXenes are a new family of 2D materials that have received significant attention for various applications, such as gas sensing [72], biosensing [73], catalysis [74, 75], energy storage [76, 77], hydrogen generation [78], and water purification [79]. MXenes have layered structures and are typically formulated as $M_{n+1}X_nT_x$ (n = 1, 2, or 3), where M represents an early transition metal (e.g., Sc, Ti, V, Cr, Zr, Nb, Mo, Hf, Ta), X is carbon and/or nitrogen, with each X layer placed between two M layers, and T_x refers to surface terminations, such as fluorine (-F), oxygen (-O), or hydroxyl (-OH) groups. Naguib et al. have synthesized the first MXene, titanium carbide ($Ti_3C_2T_x$), by selective etching of aluminum (Al) from Ti_3AlC_2 layered precursor [190]. Surface terminations can significantly affect the gas sensing properties of MXenes [191]. The mechanism of gas sensing is primarily dependent on the Charge Transfer (CT) between gas molecules and MXene, leading to conductivity modulation of these materials [191].

Measurement of breath NH_3 has attracted considerable research interest in the biomedical field, since it can be used to predict the kidney or liver malfunction or halitosis [192]. Considerable levels of NH_3 will be found in the human blood if a liver function disorder limits the conversion of NH_3 to urea. NH_3 gas is also present, at high concentrations, in the breath of uremic patients [193]. Measurement of breath NH_3 levels can provide a fast and non-invasive method for the diagnosis of urea balance disturbance, which can be caused by kidney disorder [194] or helicobacter pylori bacterial infection [195]. It is estimated that 5% of the worldwide population are affected by chronic kidney disease [196]. Thus, the development of sensitive, low-cost, and portable devices for monitoring breath NH_3 levels at home, is of high importance.

The use of $Ti_3C_2T_x$ MXene (Fig. 3.13) as a room-temperature flexible NH_3 sensor has been recently demonstrated [197]. Yu et al. have employed DFT to analyze monolayer Ti_2CO_2 for gas sensing [198]. It was concluded that Ti_2CO_2 is more sensitive to NH_3 when compared to other gases assessed in their work. Xiao et al. investigated the adsorption behavior of NH_3 on different oxygen-terminated M_2C MXenes (M = Sc, Ti, Zr, and Hf), by using DFT calculations [199]. They have predicted that the injection of a small number of electrons can alter the adsorption behavior of NH_3 on Ti_2CO_2 from chemisorption to physisorption, much larger than those reported for other M_2CO_2 MXenes (M = Sc, Zr, and Hf), implying that oxygen-terminated Ti_2CT_x is the most suitable candidate among M_2CO_2 materials for NH_3 sensing.

Moreover, $Ti_3C_2T_x$ has been demonstrated as a base material for room-temperature NH_3 sensing [197]. Therefore, optimizing the surface properties of the $Ti_3C_2T_x$ MXene, as a sensing layer is essential for improving the sensitivity and selectivity of the breath NH_3 measurement systems, which is addressed in this work. Even though $Ti_3C_2T_x$ MXenes

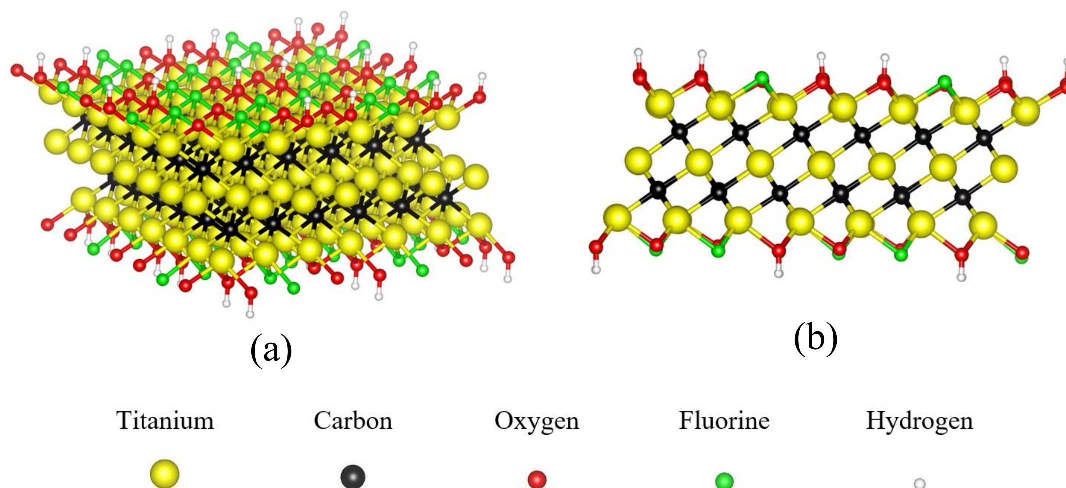

Figure 3.13: The schematic representation (a) and side view illustration (b) of $Ti_3C_2T_x$ with various surface terminations analyzed in this study (S_1).

have been successfully realized for NH_3 sensing [197,200], a comprehensive DFT study for the analysis and optimization of MXene's NH_3 sensing is required. Previous DFT studies have focused on Ti_2CT_x substrate and assumed only a single functional group for surface termination [199, 201]. However, synthesized $Ti_3C_2T_x$ MXene materials usually have a combination of -F, -O and -OH as surface termination groups with ratios that highly depend on the synthesis method. For example, samples prepared by using 50 wt% hydrofluoric acid for the etching process have almost four times more -F termination groups compared to samples prepared by using a solution of lithium fluoride dissolved in 6 M hydrochloric acid for the etching process [202]. As reported in recent literature, changing surface termination groups of titanium carbide MXene by controlling its synthesis method can significantly change gas sensing properties of the MXene [129].

In the activities I contributed to during the PhD course, electrostatic surface potential (ESP), projected density of states (PDOS) and thermal analysis were employed to further investigate the effect of different surface termination groups on NH_3 sensing of the $Ti_3C_2T_x$ from different aspects. Also, the effect of water molecules inherently present on the MXene substrate is taken into consideration in analyzing the gas sensing of the $Ti_3C_2T_x$. This study provides practical insights on tuning the NH_3 sensing of $Ti_3C_2T_x$ by using three configurations representing MXene samples that could result from different synthesis approaches [203]: (a) $Ti_3C_2(OH)_{0.44}F_{0.88}O_{0.66}$ (S_1) with a relatively high -F surface functional groups; (b) $Ti_3C_2(OH)_{0.66}F_{0.22}O_{1.11}$ (S_2) with a relatively low -F surface groups; and (c) $Ti_3C_2(OH)_{0.44}F_{0.88}O_{0.66}(H_2O)_{0.44}$ (S_3) with a relatively high -F surface functional groups as well as water molecules.

3.5.1.1 Computational methods

First-principle calculations were performed by DFT as it is implemented in the Vienna *Ab-initio* Simulation Package (VASP) [204,205]. Projector augmented-wave (PAW) pseudopotentials were employed to describe electron-ion interactions [206]. The Perdew-Burke-Ernzerhof (PBE) version of the generalized gradient approximation (GGA) was applied for the exchange and correlation functional [207]. A plane-wave energy cut-off of 700 eV and an energy convergence criterion of 10^{-6} eV was used for all calculations. Three 3×3 supercells of $Ti_3C_2T_x$ (S_1, S_2, and S_3) were analyzed. Initially, various gases in-

cluding NH_3, NO, NO_2, N_2O, CO, CO_2, CH_4, and H_2S were placed on S_1, considering several directions and different possible sites for the adsorption of the gas molecule on the substrate. Based on the calculated energy of the system, the most stable positions were eventually selected for the gas molecules. The Brillouin zone was sampled by a $3 \times 3 \times 1$ Monkhorst-Pack k-point grid for the relaxation calculations and a $4 \times 4 \times 1$ grid for the self-consistent procedures. The unit cell vectors and atom coordinates were relaxed until the forces on each atom became smaller than 0.01 eV/Å. The vdW interactions were considered using Grimme's semi-empirical dispersion correction method (DFT-D3) [208,209]. A vacuum thickness larger than 25 Å was placed between the $Ti_3C_2T_x$ sheets to ensure the approximation of monolayer $Ti_3C_2T_x$. To analyze interactions between gas molecules and the substrates, the CT between gas molecules and the substrate was evaluated using Bader charge calculations, by differentiating the total charge of gas molecules before and after adsorption on the substrates [118, 198, 210, 211]. Chemical bonding analyses were performed by means of the crystal orbital Hamilton population (COHP) method as implemented in the local-orbital basis suite towards electronic-structure reconstruction (LOBSTER) code [212]. The adsorption energy (E_{ads}) is given by [213]:

$$E_{ads} = E_{\text{Ti}_3\text{C}_2\text{T}_x+\text{Gas}} - E_{\text{Ti}_3\text{C}_2\text{T}_x} - E_{\text{Gas}} \tag{3.54}$$

where $E_{\text{Ti}_3\text{C}_2\text{T}_x+\text{Gas}}$ is the total energy of the monolayer $Ti_3C_2T_x$ and the adsorbed gas molecule, E_{Gas} is the energy of an isolated gas molecule, and $E_{\text{Ti}_3\text{C}_2\text{T}_x}$ is the energy of an isolated monolayer $Ti_3C_2T_x$. The recovery time (τ) is an important figure of merit for gas sensors that will be analyzed in the next sections. The recovery time has an exponential relation with the adsorption energy as:

$$\tau = \nu_0^{-1} e^{E_{\text{ads}}/k_{\text{B}}T} \tag{3.55}$$

where ν_0 is the attempt frequency, k_{B} is the Boltzmann's constant, and T is the temperature. It is assumed that NH_3 gas molecule has an attempt frequency equal to that of NO_2 ($\nu_0 = 10^{12} s^{-1}$) [214].

In order to investigate the effect of the fluorine presence on hydrogen abstraction by NO_2, the Gibbs free energy should be calculated [215]:

$$\Delta G^{\text{H}} = G_{\text{Ti}_3\text{C}_2\text{T}_x-\text{H}} + G_{\text{HNO}_2} - G_{\text{Ti}_3\text{C}_2\text{T}_x} - G_{\text{NO}_2} \tag{3.56}$$

By assuming an ideal gas model, one can write:

$$\Delta G^{\text{H}}(T) = \Delta E^{\text{H}} + \Delta E^{\text{H}}_{\text{ZPE}} + \int_0^T \Delta C^{\text{H}}_{\text{vib}} dT - T\Delta S^{\text{H}}_{\text{vib,rot}}(T) \tag{3.57}$$

where T is the temperature, and ΔE^{H}, $\Delta E^{\text{H}}_{\text{ZPE}}$, $\Delta C^{\text{H}}_{\text{vib}}$, and $\Delta S^{\text{H}}_{\text{vib,rot}}$ are the changes in the reaction chemisorption energy, the zero-point energy, vibrational heat capacity, and vibrational/rotational entropy, respectively. The rotational entropy is zero in solids implying that only vibrational entropy should be considered. In addition to static calculations, *ab-initio* molecular dynamics (AIMD) simulations were performed to address the influence of thermal effects. The total energy convergence criterion is set to 10^{-4} eV for the AIMD simulations. The temperature of the systems during MD simulation is controlled by the Nose-Hoover thermostat [216].

3.5.1.2 Gas adsorption of Ti_3C_2Tx

The most stable structures for the adsorption of NH_3, NO, NO_2, N_2O, CO, CO_2, CH_4, and H_2S gas molecules on S_1 and the energy levels of their highest occupied molecular orbital (HOMO) and lowest unoccupied molecular orbital (LUMO) are illustrated in Fig. 3.14 and Fig. 3.15, respectively. To determine the most stable gas orientation and adsorption site on the substrates, various initial structures for the gas molecule-substrate were considered and the system with the minimum energy was selected. The calculated E_{ads}, CT, and the nearest distances between the S_1 and gas molecules ($D_{\text{gas-substrate}}$) are listed in Table 3.4. A positive CT value indicates electron transfer from the gas molecule to the substrate, while a negative CT value represents the reverse process [217].

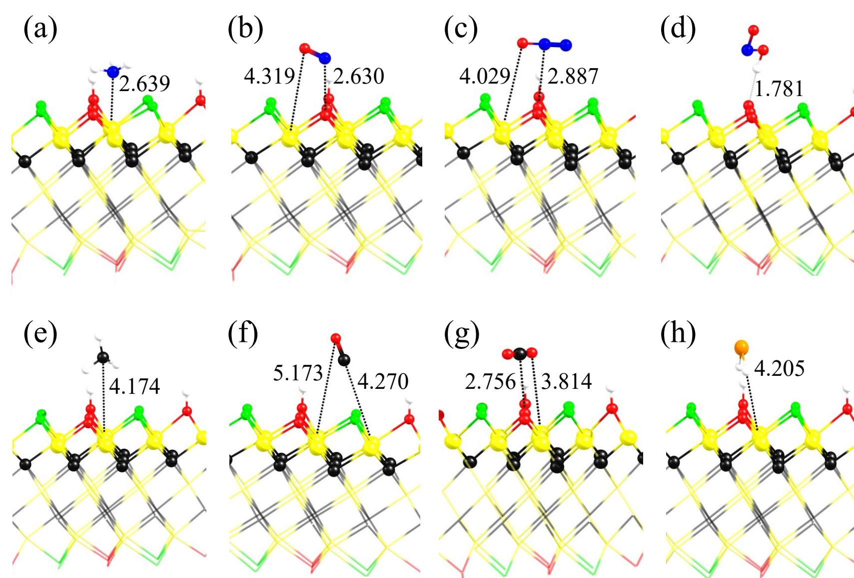

Figure 3.14: The most stable structures for the adsorption of various gas molecules on the S_1: (a) NH_3, (b) NO, (c) N_2O, (d) NO_2, (e) CH_4, (f) CO, (g) CO_2 and (h) H_2S adsorption. Binding distances are in Å.

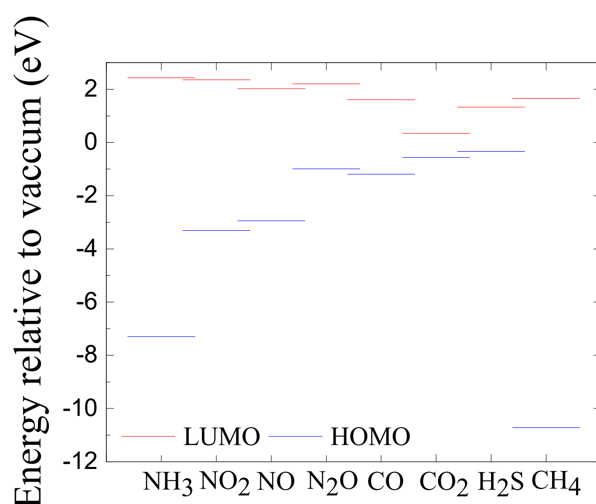

Figure 3.15: The energy levels of the highest occupied molecular orbital (HOMO) and the lowest unoccupied molecular orbital (LUMO) for the adsorption of gases on S_1.

Table 3.4: Adsorption energies, charge transfers, and the nearest distances between S_1 and various gas molecules.

Gas	E_{ads} (eV)	CT (e)	$D_{gas-substrate}$ (Å)
NH_3	−0.36	0.098	2.54
NO	−0.16	0.068	2.32
N_2O	−0.23	−0.006	2.89
CO	−0.20	0.003	3.16
CO_2	−0.08	−0.011	2.75
CH_4	−0.16	0.000	3.17
H_2S	−0.16	−0.010	2.18

In the picture of a covalent Lewis base-acid interaction, a higher HOMO energy level of the gas molecules (Lewis base) means strong adsorption energy with the surface (Lewis acid), which occurs when the HOMO gets closer to the unoccupied part of the surface and lower its energy [218–221]. Lowering energy state leads to an effective charge transfer from the Lewis base to Lewis acid. Based on our calculations, the class of molecules with lone-pair interactions discussed here, preferably bind to the empty d orbitals of Ti atoms on the surface. For instance, CH_4 is not a member of the class of molecules with covalent Lewis acid-base interaction. As shown in Table 3.4 the NO, N_2O, CO, CO_2, CH_4, and H_2S molecules are all physically adsorbed on the S_1 with quite small adsorption energies and charge transfers, but NH_3 molecule with lowest adsorption energy ($E_{ads} = -0.36$ eV) and the highest CT (0.098 e) is the only gas molecule chemically adsorbed on the S_1.

The isosurface representations of the total charge density for the adsorption of NH_3, H_2S, and CO_2 on S_1 were investigated to visualize the interactions between $Ti_3C_2T_x$ and gas molecules (Fig. 3.16). For a reference charge density of 0.018 e/Å^3 , it was observed that a connection was established between the charge density isosurfaces of NH_3 and S_1, while no connection was observed between the charge density isosurfaces of other gases and S_1 that demonstrated a higher sensitivity of S_1 to NH_3 compared to other studied gas molecules.

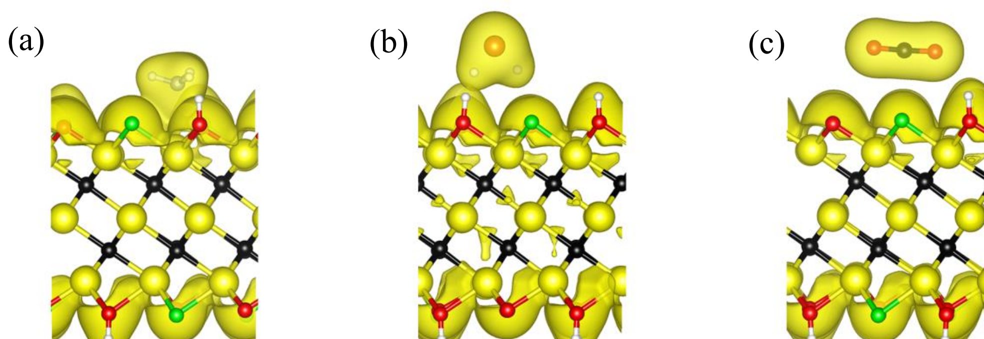

Figure 3.16: Isosurface representations for total charge density of (a) NH_3 , (b) H_2S, and (c) CO_2 on S_1.

Remarkably, the addition of NO_2 to the S_1 results in the formation of nitrous acid (HNO_2), where the oxygen atoms of NO_2 abstract hydrogen atoms from the S_1. The presence of fluorine atoms in S_1 reduces the electronegativity of oxygen atoms. Therefore, the O-H covalent bonds become relatively weak, so that oxygen atoms of NO_2 can abstract hydrogen atoms from the S_1, and new covalent bonds between hydrogen atoms and NO_2 molecules will form HNO_2. The Gibbs free energy (ΔG^{H}) of hydrogen adsorption is

Table 3.5: Thermodynamic quantities for NO_2, HNO_2, $Ti_3C_2T_x$, and $Ti_3C_2T_x$−H (S_1 and S_2) species at $T = 298.15$ K.

Species	E_{ZPE} (eV)	$-TS_{\mathrm{vib}}$ (eV)	$-TS_{\mathrm{rot}}$ (eV)
NO_2	0.23	−0.003	−0.23
HNO_2	0.52	−0.01	−0.26
$Ti_3C_2T_x(S_1)$	5.98	0.00	−2.82
$Ti_3C_2T_x-H(S_1)$	5.69	0.00	−2.79
$Ti_3C_2T_x(S_2)$	6.51	0.00	−2.89
$Ti_3C_2T_x-H(S_2)$	6.35	0.00	−2.77

considered to be an effective indicator of hydrogen-abstraction by the NO_2 molecule. Table 3.5 shows the thermodynamic quantities of this reaction. The calculated ΔG^{H} for a hydrogen atom abstraction by NO_2 molecules from S_1 and S_2 are −1.10 eV and −0.69 eV respectively. This supports the fact that fluorine surface termination groups have a lower ΔG^{H}, which can lead to a higher hydrogen-abstraction by NO_2 molecules and finally formation of more nitrous acid molecules on the $Ti_3C_2T_x$ substrate.

3.5.1.3 Surface functional groups

The NH_3 sensing characteristics of $Ti_3C_2T_x$ can be tuned by modifying the combination ratio of surface termination groups. The effect of surface termination groups and the presence of water molecules on the adsorption of NH_3 molecules on $Ti_3C_2T_x$ MXene are investigated by analyzing three different substrates (S_1, S_2, and S_3). Energy band diagrams for S_1, S_2, and S_3 are shown in Fig. 3.17. The density of states at the Fermi level, $N(E_{\mathrm{F}})$, can be a representative of the material's conductivity [215]. Since the Fermi level is located at lower energies for S_1 and S_2, energy bands intersect the Fermi level at all high-symmetry directions of the Brillouin zone. For S_2, however, energy bands intersect the Fermi level mostly along the $\Gamma - \mathrm{X}$ and $\mathrm{M} - \Gamma$ directions, which results in a slight increase in $N(E_{\mathrm{F}})$ compared to that of S_1, whereas energy bands intersect the Fermi level along the $\mathrm{X} - \mathrm{M} - \Gamma$ directions for S_3 that results in the reduction of $N(E_{\mathrm{F}})$ compared to that of S_1.

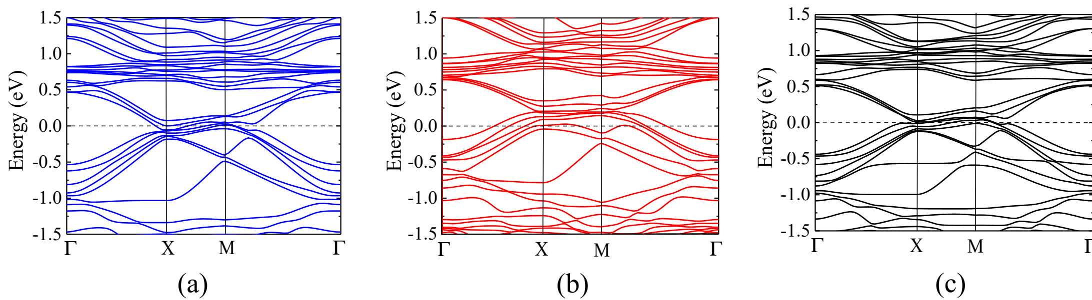

Figure 3.17: The electronic band structures of (a) S_1, (b) S_2, and (c) S_3.

The calculated adsorption parameters of the NH_3 on the three kinds of surfaces are shown in Table 3.6. The adsorption energies between the NH_3 gas molecule and S_1, S_2 and S_3 are calculated as −0.36 eV, −0.49 eV, and −0.19 eV, respectively, which shows stronger adsorption of NH_3 on S_2. For the adsorption energies of NH_3 on S_1, S_2, the recovery times of the sensor at $T = 298.15$ K are 1.21 μs and 0.19 ms, respectively, which shows that

Table 3.6: Adsorption energies, charge transfers, and the nearest distances between NH_3 and S_1, S_2 and S_3.

Species	E_{ads} (eV)	CT (e)	$D_{gas-substrate}$ (Å)
NH_3/S_1	−0.36	0.098	2.37
NH_3/S_2	−0.49	0.099	2.27
NH_3/S_3	−0.19	0.012	2.69

$Ti_3C_2T_x$ MXene is a suitable base material for reusable NH_3 gas sensors. Evidently, the relatively short recovery time reveals the rapid response of the S_1 to NH_3 gas.

Fig. 3.18 elucidates the importance of geometry and composition of surface functional groups and their effect on the adsorption of the NH_3 gas molecule on $Ti_3C_2T_x$ substrates. The NH_3 adsorption causes local structural deformation of both NH_3 molecules and the substrate. Titanium atom closest to the nitrogen atom is pulled outward from the layer, with its neighboring titanium-carbon (Ti-C) bonding length increasing from 2.06 Å to 2.23 Å for S_1, and from 2.10 Å to 2.34 Å for S_2. However, for S_3, the titanium atom closest to the nitrogen atom is pushed inward to the layer, with its neighboring titanium-carbon (Ti-C) bonding length decreasing from 2.059 Å to 2.044 Å. For S_1 and S_2, there is a strong

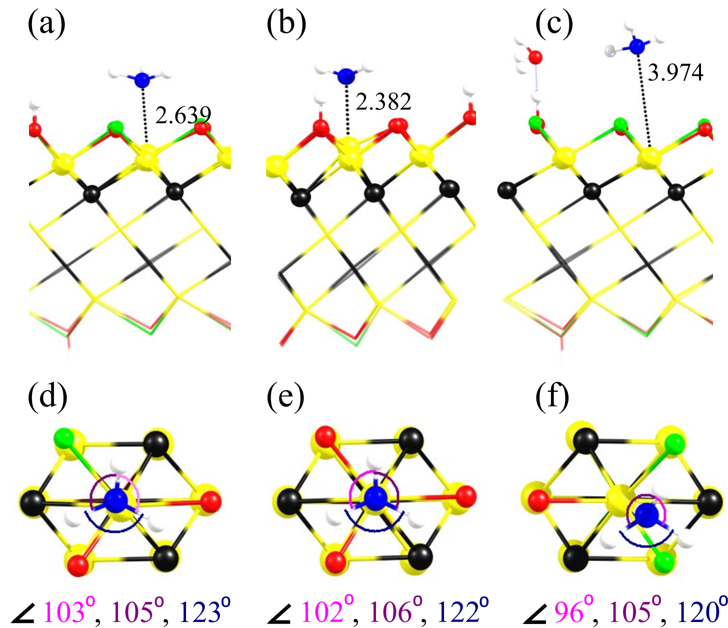

Figure 3.18: The side view of the adsorption structures of the NH_3 gas molecule on the surface: (a) S_1, (b) S_2 and (c) S_3. Binding distances are in Å. The top view of the adsorption structures of the NH_3 gas molecule on the surface: (d) S_1, (e) S_2 and (f) S_3. The bond angles are shown by curves.

electrostatic attraction between the lone pair of oxygen atom on the substrate and the exposed positive parts of hydrogen atoms of NH_3 molecules, thus the created hydrogen bonds change the location of titanium atoms and configuration of NH_3 molecules, which results in the enhancement of CT between NH_3 and titanium. For S_3, the oxygen atom of the H_2O molecule adsorbs the hydrogen atoms of NH_3 by hydrogen bonding. H_2O molecules stabilize NH_3 molecules on S_3, but it could decrease the interaction strength between nitrogen and titanium atoms. It is worth mentioning that the bonding angles of NH_3 on S_1 and S_2 are larger than those of S_3, which implies the repulsion of bond pair of NH_3 on S_1 and S_2 are smaller than that of single NH_3 molecule. As a result, the partially

positive charge of hydrogen atoms and the electronegativity of the nitrogen atom of NH_3 molecule on S_1 and S_2 increase that might affect the CT from nitrogen to titanium.

The electrostatic surface potential (ESP) for the S_1, S_2, and S_3 substrates and NH_3 gas are illustrated in Fig. 3.19. The origin of the ESP is a strong local electrostatic potential on positive centers (titanium atoms) surrounded by negative centers (oxygen and fluorine atoms) of surfaces. The ESP can polarize the lone pair of NH_3 which in turn induces a dipole moment in the $Ti_3C_2T_x$ MXene substrate. The induced dipole moment further polarizes NH_3 and leads to an electrostatic bonding between the substrate's surface and the adsorbed NH_3 molecule [222–224]. The strength of this interaction depends on the depth of the ESP well. As a result, for S_1 and S_2, there is a strong local ESP which stabilizes the occupied states of NH_3 and leads to forming of electrostatic bonds between nitrogen $2p$ lone pair and titanium $3d$ orbitals. For S_2, the interaction and polarization of the NH_3 HOMO in the ESP well were enhanced by the outward movement of Ti from the layer. The results show the importance of electrostatic effects in addition to the covalent picture in determining the bonding mechanism, adsorption energies and CT trends.

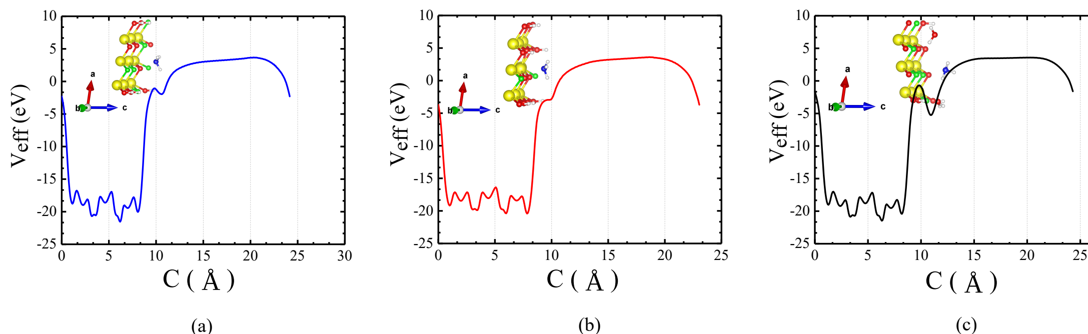

Figure 3.19: The electrostatic surface potential (ESP) for the NH_3 gas molecule adsorption on (a) S_1, (b) S_2 and (c) S_3.

The contribution of surface functional groups to charge transfer is studied by charge difference calculations . The isosurface representations of charge differences for NH_3 adsorption on S_1, S_2, and S_3 for a reference charge density of 0.0028 e/Å^3 are shown in Fig. 3.20.

The accumulation or depletion of electrons between nitrogen and titanium atom sites is an indication of interaction strength between these atoms. Titanium atoms become partially negative due to the gain of electrons from NH_3 gas adsorption. According to Fig. 3.20(d), the fluorine atom has a smaller contribution to CT than the oxygen atom. However, in the case of S_2, due to the presence of more oxygen atoms and fewer fluorine atoms, the CT is larger than that of S_1, as shown in Fig. 3.20(e). The difference in Bader charge of the nearest oxygen and fluorine atoms to NH_3 (before and after adsorption) for S_1 and S_2 were 0.005 e for fluorine atom and between 0.008 e to 0.014 e for different oxygen atoms. The results support the fact that oxygen surface functional groups have a higher contribution in CT between the $Ti_3C_2T_x$ substrate and the NH_3 gas molecule compared to fluorine surface functional groups. In the case of S_3, most of the charge from NH_3 is transferred to the $Ti_3C_2T_x$ substrate and only a small portion is distributed over the water molecules. More precisely, the charge increments in water molecules are 0.0032 e and 0.0008 e, respectively, that shows 33.61% of the CT was transferred to water molecules and the rest (66.39%) is transferred to the substrate.

To investigate the electronic properties of the three substrates, the projected density of states (PDoS) of valence electrons for different substrates are calculated and illustrated in Fig. 3.21. The Fermi energy (E_F) is set to zero as a reference. The PDoS near the Fermi

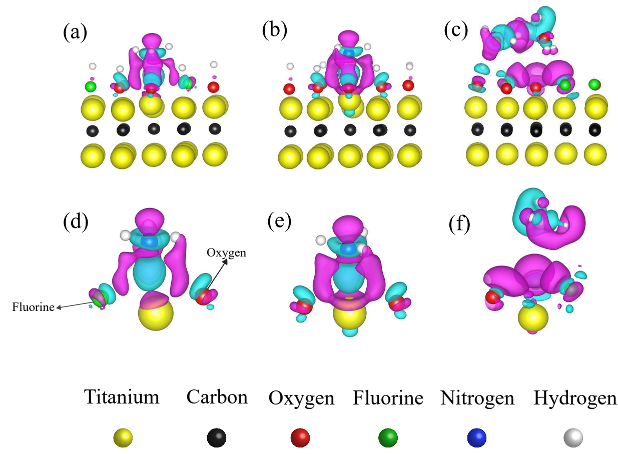

Figure 3.20: Isosurface representations of charge difference for the adsorption of NH_3 on (a) S_1, (b) S_2, and (c) S_3 and isosurfaces of charge difference for the oxygen (red), fluorine (green) and titanium (yellow) atoms nearest to NH_3 molecule, for (d) S_1, (e) S_2, and (f) S_3. The accumulation and depletion of electrons are represented by the cyan and purple regions, respectively.

level is dominated by titanium 3*d* orbitals. For all the three $Ti_3C_2T_x$ substrates, there is no energy gap at the Fermi level, which identifies the metallic nature of these materials. Figure. 3.21(a) shows the total PDoS of a bare Ti_3C_2 for 3*d* orbitals of the titanium atom and 2*p* orbitals of the carbon atom. The valence and conduction bands near the Fermi level are mainly contributed by non-bonding titanium 3*d* orbitals of the surface (dangling bonds). In addition, there is a band at positive energies, which is originated from repellent interactions between titanium atoms.

The strong bond of titanium 3*d* orbitals weakens after termination with -O, -F, and -OH surface functional groups. The titanium band at positive energies changes slightly, due to the interaction of non-bonding orbitals with surface termination groups. The Ti_3C_2 structure becomes stabilized by the saturation of non-bonding orbitals of valence electrons of titanium atoms at the surface by -O, -F, and -OH groups. Due to these bonding interactions, the PDoS curves shift toward more negative energies and pseudo-gaps around Fermi level are induced as shown in Fig. 3.21(b), (c), and (d). The pseudo-gap appears between the bonding orbitals at negative energies and non-bonding orbitals at positive energies. It is worth mentioning that, for metallic structures, the width of the pseudo-gap represents the strength of the covalent bonding, which in turn, determines the stability of the structure [225, 226]. Therefore, it can be considered as a criterion for comparing the stability of substrates with various surface termination groups. For the S_1, as shown in Fig. 3.21(b), valence states below the Fermi level can be divided into two maximum bands which are formed by hybridized titanium 3*d*-carbon 2*p* and titanium 3*d*-oxygen 2*p* orbitals between 0 eV and -5.3 eV (band A), and titanium 3*d*-fluorine 2*p* orbitals between -5.3 eV and -7 eV (band B). In addition, band C is formed below band B corresponding to the hybridization between titanium and functional groups. For the S_2, which has fewer fluorine surface groups, after the surface groups are added to Ti_3C_2, the Fermi level shifts toward lower energies and the DOS at the Fermi level decreases (a pseudo-gap occurs as shown in Fig. 3.21(c)) due to the new induced energy states. The DOS related to bands A are increased by titanium 3*d*-oxygen 2*p* orbitals, whereas that of bands B are decreased. The DOS increases from 19.32 to 30.96 for oxygen atoms and decreases from 35.90 to 13.37 for fluorine atoms. For the S_3, as shown in Fig. 3.21(d), after the addition of surface groups of -OH, -O and -F, the Fermi level shifts downwards

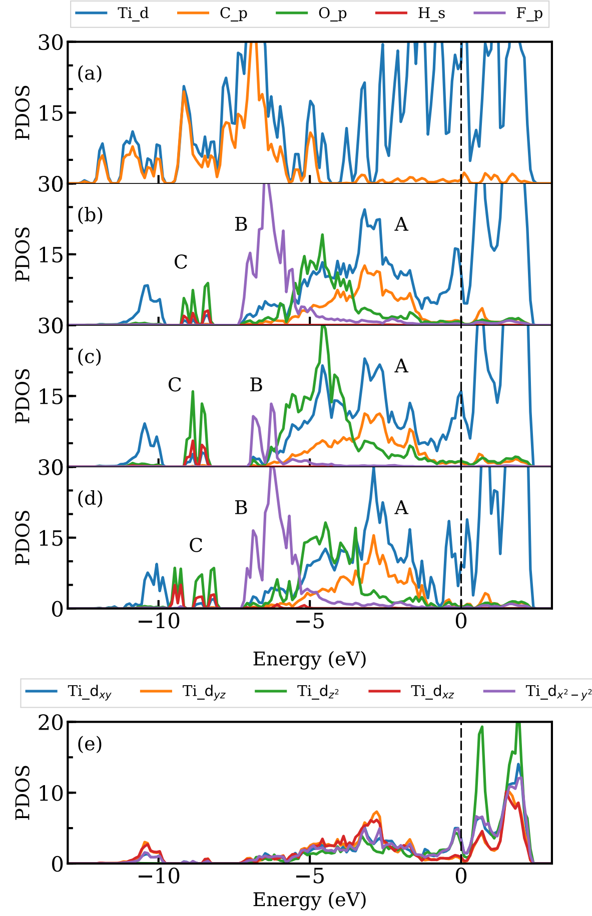

Figure 3.21: The projected density of states (PDoS) of (a) Ti_3C_2, (b) S_1, (c) S_2, (d) S_3, and Ti atoms of the (e) S_1. The PDoS of Ti atoms of the S_1 are projected onto d_{xy}, d_{yz}, $d_{x^2-y^2}$, and d_{z^2} orbitals.

in energy, and in the presence of H_2O molecules a pseudo-gap appears. Figure. 3.21(e) shows the PDoS for titanium atoms of the S_1, which are projected onto d_{xy}, d_{yz}, $d_{x^2-y^2}$, and d_{z^2} orbitals. Five titanium 3d orbitals split into three groups: i) d_{xy} and $d_{x^2-y^2}$, ii) d_{yz}, d_{zx}, and iii) d_{z^2}. The DOS at the Fermi level is dominated by the in plane d_{xy} and $d_{x^2-y^2}$ orbitals, and the d_{z^2} orbitals perpendicular to the substrate's plane.

Fig. 3.22 shows PDoS for the adsorption of NH_3 molecule on S_1, S_2, and S_3. It is worth mentioning that, the conduction states of substrates are mainly contributed from titanium 3d orbitals. This implies that when an extra electron is introduced to the substrates, the electron will fill the titanium 3d unoccupied orbitals. Therefore, the adsorption of NH_3 has a substantial effect near the Fermi level. NH_3 molecules induce several distinct states at the carbon band in the energy range around −7.9 eV and −8.3 eV for S_1 (Fig. 3.22(a)) and S_2 (Fig. 3.22(b)) respectively. However, for S_3, some states are induced around −6.2 eV and around −1.2 eV (near the Fermi level), as shown in Fig. 3.22(c). The results indicate that the orbital mixing in S_2 is stronger when compared to S_1 and S_3, which leads to higher adsorption energy. Figure. 3.23 shows the PDoS of nitrogen and titanium atoms when the NH_3 molecule is adsorbed on the S_1, S_2, and S_3. In Fig. 3.23(a) and 3.23(b), the broadening of the adsorbed NH_3 occupied states and an increased intermixing of nitrogen and titanium states can be observed, which shows a larger covalent contribution to the adsorption energy and CT. A gradual energy downshift of the center of the NH_3 HOMO can be observed at PDoS plots in Fig. 3.23(a)-(b) that reveals a HOMO in NH_3 can be

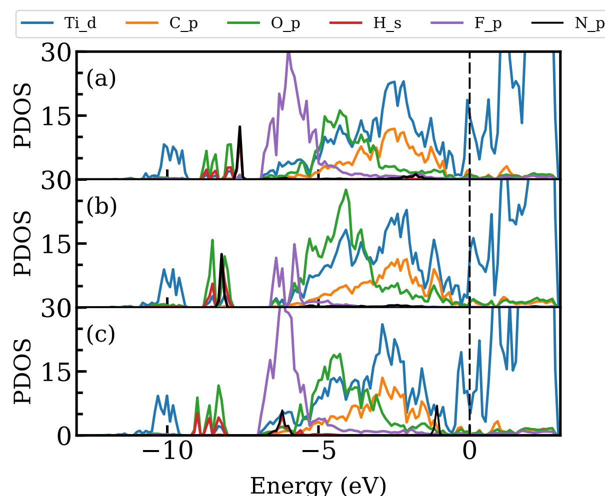

Figure 3.22: The PDoS of (a) S_1/NH_3, (b) S_2/NH_3, and (c) S_3/NH_3.

polarized more easily and responds better to the surface ESP well. The results indicate the importance of surface intrinsic electrostatic potential in the ligand to metal CT. The weak physical nature of NH_3 adsorption on S_3 is illustrated in Fig. 3.23(c).

To evaluate the N-Ti interaction at the surface, crystal orbital Hamilton population (COHP) [227] calculations were performed. When an adsorbate binds to a solid surface, the overlap of their electronic states leads to the formation of bonding and anti-bonding states. The bonding states are positioned below the Fermi-energy and are fully occupied and the anti-bonding states are mostly positioned above the Fermi-level. The delocalized molecular orbitals of NH_3 adsorbed on S_1 and S_2 interact with the titanium bands in about -6 to -2 eV energy zone and the anti-bonding surface-adsorbate states are partially filled. Compared to the case of NH_3 adsorption on S_1, the overlap region is wide in S_2 and the anti-bonding occupancy is reduced. In addition, the bonding and anti-bonding interactions are getting smaller in S_3 and the localized molecular orbitals of NH_3 adsorbed on S_3 weakly interact with the Ti bands at -1.2 eV. The results of the orbital analysis are consistent with the computed CT and adsorption energies of the three NH_3-Mxene systems.

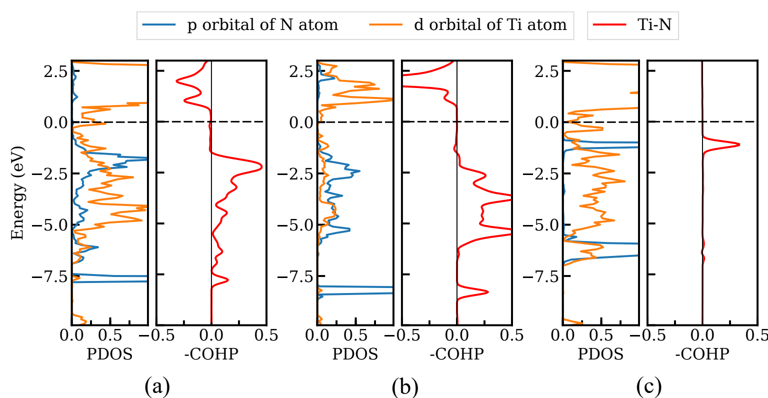

Figure 3.23: The PDoS for the adsorbed N atom and its directly bonded surface Ti atom, and −COHPs averaged over the Ti-N bond for the (a) S_1, (b) S_2, and (c) S_3.

3.5.1.4 Thermal stability of NH_3 adsorption on Ti_3C_2Tx

The thermal stability and NH_3 adsorption on the surface were analyzed by performing AIMD. AIMDs up to 6 ps (1 ps equilibration) are simulated for three surfaces starting from the most stable structures obtained with static calculations. Figure. 3.24 demonstrates that $Ti_3C_2T_x$ substrates are stable systems in the presence of NH_3 gas molecules at room-temperature. Here, the total energy fluctuation is minimal for all the cases. Interestingly, NH_3 gas molecule is dissociated from the S_1 and S_2 at the early stage of the simulation, whereas for S_3, the NH_3 moves over the surface without more separation. These results show that cooperative hydrogen bond interactions and cooperative adsorption are key factors for determining the degree of dissociation of NH_3 over the surface. From a computational point of view, considering the formation of a hydrogen bond between NH_3 molecule and the nearest under-coordinated atom at the surface, as well as water-NH_3 intrinsic interaction are of high importance for the fabrication of the $Ti_3C_2T_x$-based NH_3 sensor.

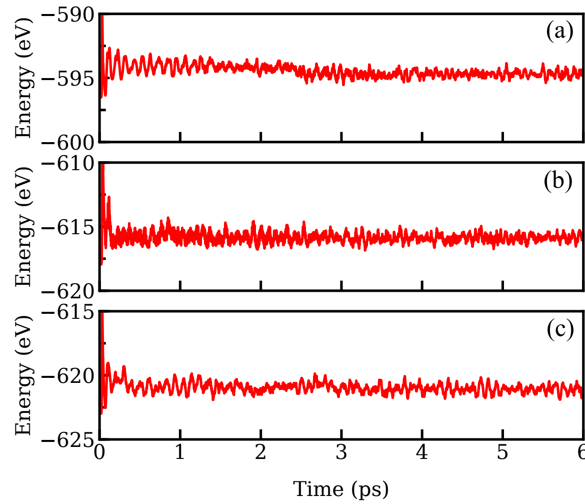

Figure 3.24: The AIMD free energy of $Ti_3C_2T_x$ substrates in the presence of NH_3 gas molecules.

3.5.1.5 The comparison with other 2D materials

Phosphorene, MoS_2, and boron-doped SWCNT have been proposed as promising materials for NH_3 sensing [201,228]. Adsorption energies and CTs related to the interaction between NH_3 and these materials are compared in Fig. 3.25. As illustrated in Fig. 3.25, the CT from NH_3 to MoS_2 and phosphorene is much smaller than that of $Ti_3C_2T_x$ MXenes.

Although boron-doped SWCNT has a higher CT, its relatively high adsorption energy (−0.7 eV) suggests this material as an NH_3 capturer which has a relatively long recovery time. Zr_2CO_2 and V_2CO_2 are MXene substrates that have higher CT compared to $Ti_3C_2T_x$ MXenes [199, 201], however, similar to boron-doped SWCNT, their relatively high adsorption energy (−0.81 eV for both) leads to long recovery time. $Ti_3C_2T_x$ MXenes have a higher CT with NH_3 compared to phosphorene and MoS_2 and more appropriate adsorption energy which leads to a better sensor recovery time. Compared to the ref 201, the configurations studied for $Ti_3C_2T_x$ MXenes are much similar to the reported synthesized samples [202, 203], by choosing surface termination groups ratios closer to those of real samples, instead of using just one type of surface termination groups. The presented re-

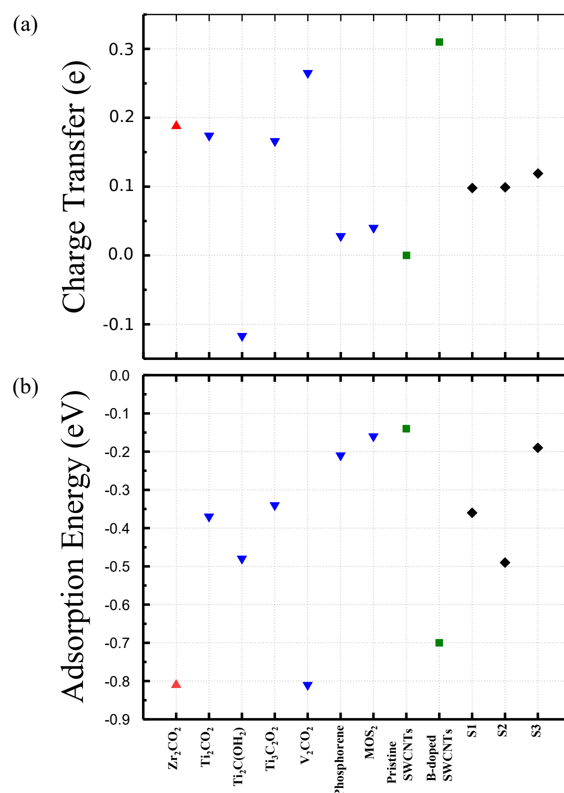

Figure 3.25: (a) The charge transfer and (b) adsorption energies of the interaction between NH_3 and a variety of 2D materials. The data are extracted from [199] (red triangle), [201] (blue triangle), [228] (green square), and, this work (black diamond).

sults in this study provide insights for understanding and performing optimization studies on $Ti_3C_2T_x$ for NH_3 sensing, by controlling the synthesis process.

3.5.2 Fluorinated Graphene-based resistive humidity sensor

Monitoring of humidity is of high importance for various applications, such as food packaging, agriculture, and the development of electronic skin [229–231]. Recently, various types of humidity sensors have been developed for monitoring relative humidity (RH) levels, utilizing different humidity sensing materials and fabrication processes [232–235]. This has stimulated growing research interest for the development of novel nanomaterials that are sensitive to humidity. In addition, the rapid development of wearable electronics technology has increased the demand for flexible humidity sensors. The development of flexible sensors for physical and chemical sensing applications has attracted a fast-growing research interest [236–242]. Carbon nanomaterials have been investigated for the development of flexible sensors [66, 243–246]. Graphene, which is a two-dimensional layered carbon nanomaterial, has proved to be a promising material for the development of flexible sensors, owing to its high surface area and inherent flexibility [247–249]. The functionalization of graphene can be used to modify its properties and develop sensors with improved properties, such as sensitivity, flexibility, dynamic range, response time, and recovery time [250].

Graphene oxide (GO), which is a functionalized graphene, has been used for humidity sensing applications, due to its hydrophilicity [251]. GO has surface functional groups that can form hydrogen bonding with water (H_2O) molecules. The humidity sensing be-

Figure 3.26: Dispersion of fluorinated graphene powder in IPA.

havior of GO is significantly improved when compared to the graphene, because hydrogen bonding between GO and water molecules is much stronger than vdW forces between graphene and water molecules [252]. One disadvantage of GO is its poor stability in various alkali solutions at moderate temperatures [253]. To address the stability problem, fluorinated graphene (FG), which possesses good chemical and thermal stability and can form hydrogen bonding with water molecules, can be a potential candidate for humidity sensing applications [254].

FG has been investigated as an ammonia sensing material. Zhang et al. developed an FG-based ammonia sensor, using SF6 plasma treatment process. The fabricated sensor exhibited a sensitivity of $\sim$ 3.8 % for 100 ppm of ammonia at room temperature and detected ammonia at concentrations as low as 2 ppm [255] . In addition, FG has been used to develop an ammonium ion sensor. The fabricated sensor showed a detection limit of $\sim$ 0.44 pM and a linear response over concentrations of 1 pM - 0.1 μM [256]. Due to the high electronegativity of the fluorine, fluorine atoms of FG can form hydrogen bonding with H_2O molecules. Hence, FG can be a potential humidity sensing material. However, a comprehensive investigation of humidity sensing behavior of FG has not been reported.

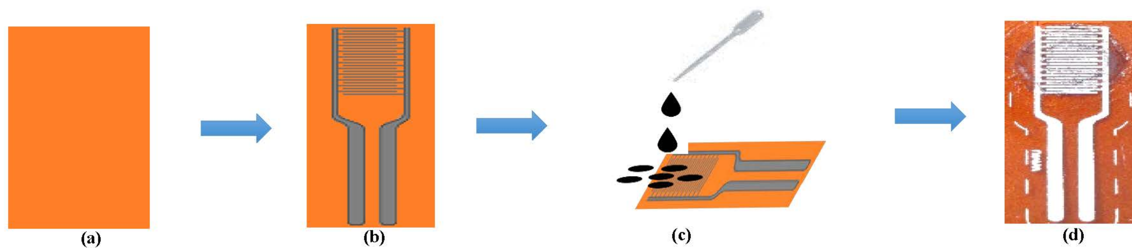

Figure 3.27: Illustration of the humidity sensor fabrication (a) polyimide substrate, (b) screen printed Ag IDEs on polyimide, (c) drop casting of fluorinated graphene on IDEs and (d) fabricated humidity sensor.

3.5.2.1 Materials and fabrication methods

The FG (fluorine to graphene – 2.57 mol%) was synthesized by Blair Research Group at the University of Central Florida. The FG has $\sim$4 mass % fluorine, and carbon atoms, where fluorine and carbon forms semi-ionic bonding (the sp^2-hybridized carbon atoms connected to the fluorine atoms). Flexible polyimide film (Kapton 500HN) from DuPont

Teijin Films was used as the substrate. Conductive silver ink (AG-800) from Applied Ink Solutions was used for printing IDEs. IPA, from Sigma-Aldrich Chemical Company, was used as the solvent for the dispersion of the FG. Dimethyl glycol acetate, from Sigma-Aldrich Chemical Company, was used as the cleaning solvent for the silver ink. A flat flexible connector (Model No. 65801-002LF) from Amphenol ICC, was used to make electrical connections to the humidity sensor.

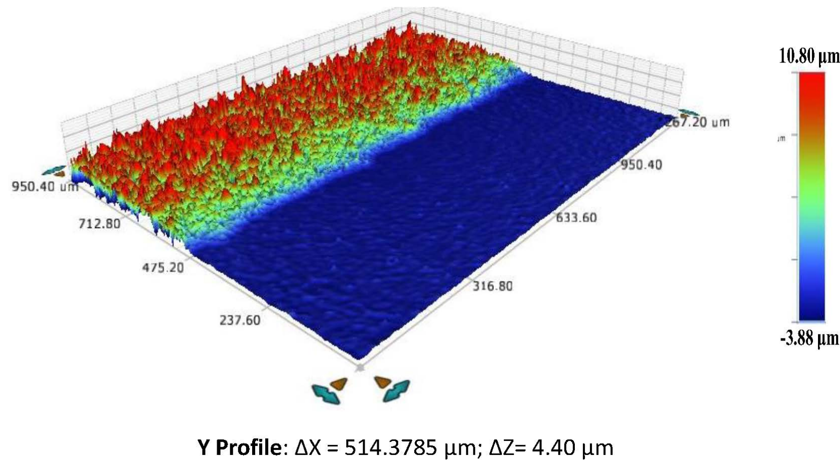

Figure 3.28: 3D output of vertical scanning interferometry of printed Ag on polyimide illustrating a thickness (ΔZ) of 4.40 μm.

The FG was synthesized using the method reported by Siddhanti et al. [257]. Briefly, 1.6 mg of FG was added to 4 mL of IPA. Then the FG suspension was placed in a 130 W bath ultra-sonicator (Model FS30, Fisher Scientific Company) for 6 hours to improve the dispersion [258]. After ultra-sonication, uniform dispersion of FG in IPA was achieved, with no visible sediments (see Fig. 3.26).

The sensor fabrication steps are shown in Fig. 3.27. The silverbased IDEs were deposited on the flexible polyimide substrate using an HMI 485 screen printer and thermally cured at 135 °C for 5 minutes in a VWR 1320 temperature-controlled oven. An average thickness and surface roughness of 4.45 ± 0.21 μm and 0.95 ± 0.04 μm were measured for the printed silver IDEs, using a Bruker Contour GT-K vertical scanning interferometer (Fig. 3.28). The printed IDE was placed on a VWR Signature 810 hot plate, with a surface temperature of 90°C, and 280 μL of the FG suspension was drop cast onto the IDEs to form the humidity sensing layer. The experiment setup to investigate the resistive response of the humidity sensor is shown in Fig. 3.29. A Thermotron SE 3000 environmental chamber was used to simultaneously test the resistive response of three humidity sensors towards varying RH levels ranging from 20% RH to 80% RH, in steps of 10% RH, at a constant temperature of 24°C. Electrical connections to the humidity sensors were made using the flat flexible connectors and connected to a Keithley 7700 multiplexer, integrated into a Keithley 2700 mainframe. The Keithley 7700 multiplexer's output was connected to an Agilent E4980A precision LCR meter to measure the resistive response of the humidity sensor, at an operating frequency of 1 kHz and an applied voltage of 1 V. The LCR meter was connected to a PC installed with a custom-built MATLAB^{TM} program, to record the resistive response of the three humidity sensors.

The relative resistance change (ΔR/R$_b$) of humidity sensors was calculated using:

$$\Delta R/R_b = 100 \times (R - R_b)/R_b, \tag{3.58}$$

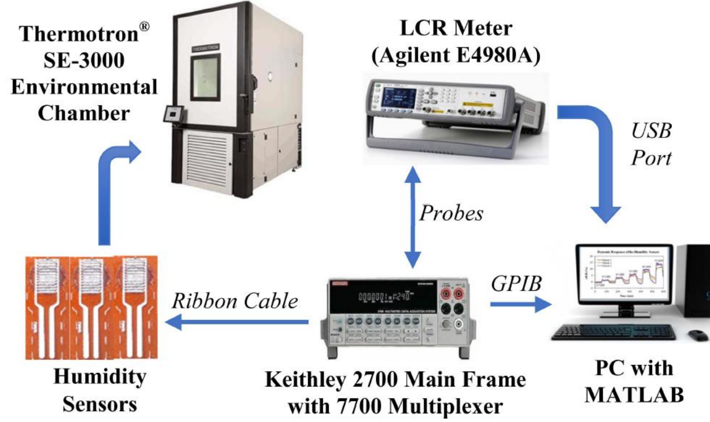

Figure 3.29: Experiment setup for humidity sensor measurements.

where R is the measured resistance, and R_b is the base resistance. In this work, the resistance at 20% RH is considered as the base resistance. The sensitivity of the humidity sensor is calculated using:

$$S = (\Delta R/R_b)\Delta RH, \tag{3.59}$$

where ΔRH is the difference between initial and final RH levels.

The response time of the humidity sensor is defined as the time taken by the sensor to reach 90% of the transition between the initial value and the final value, when the RH level is increased. Also, the recovery time is defined as the time taken by the humidity sensor to go back to its initial state after decreasing the RH to its initial level. The response time and the recovery time of the environmental chamber were also measured and subtracted from the resistance values of the humidity sensor, to eliminate the effect of the environmental chamber's delay in reaching the next RH level.

The temperature coefficient of resistance (TCR) of the tested sensors was also calculated using:

$$TCR = (\Delta R/R_b)(T - T_b), \tag{3.60}$$

where T is the measured temperature, and T_b is the base temperature, which is 30°C for the performed TCR measurements. A first-principles study, employing DFT calculations, was performed to investigate interactions between the fluorine atom and graphene substrate, as well as humidity sensing behavior of the FG. The FG-based humidity sensor was fabricated on a flexible polyimide substrate, using the screen printing process, and its resistive response towards varying RH levels was reported. The DFT calculations were performed along with generalized gradient approximation (GGA) as implemented in the SIESTA code [259]. A 15 $\AA$ vacuum was used to isolate the materials' layers and ensure no interactions between layers, making the simulations effectively illustrative of a monolayer. A cut-off energy of 150 Ry and an energy convergence criterion of 1×10^{-5} eV were used for the calculations. The reciprocal space Brillouin zone (BZ) was sampled by using a Monkhorstpack grid of $3 \times 3 \times 1$ k-points. Calculations began with the determination of the optimized geometry, which is the structure in which the residual Hellmann–Feynman forces acting on atoms are smaller than 0.1 eV/$\AA$. These optimizations were performed for different adsorption sites of molecules on the graphene, in order to achieve the most stable configuration. The analyzed FG supercells comprised of 24 carbon atoms and one

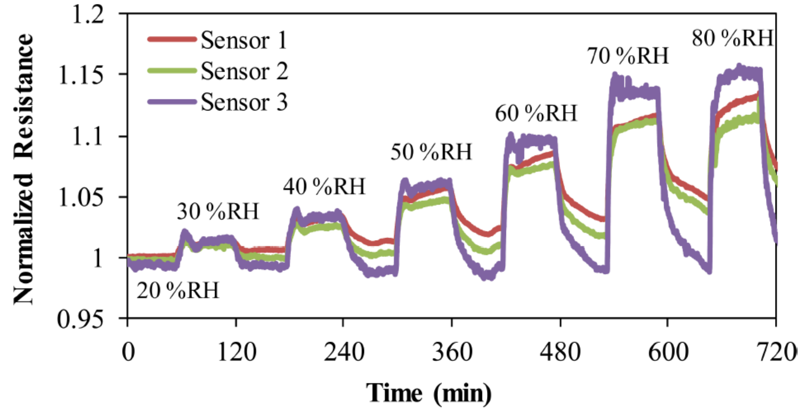

Figure 3.30: Dynamic resistive response of humidity sensors.

fluorine atoms. First, the fluorine group was added to the graphene supercell with 24 carbon atoms to find the stable state of the FG material. Next, water (H_2O) molecules were added to the system to obtain the stable state of the adsorption of the water molecule on the FG supercell. To analyze interactions between the water molecule and the FG, the adsorption energy (E_{ads}) was calculated using:

$$E_{ads} = E_{FG+\mathrm{H_2O}} - E_{FG} - E_{\mathrm{H_2O}}, \tag{3.61}$$

where $E_{FG+\mathrm{H_2O}}$ is the total energy of the FG supercell and the adsorbed water molecule, $E_{\mathrm{H_2O}}$ is the energy of an isolated water molecule, and E_{FG} is the energy of an isolated FG supercell.

In this work, in a collaborative paper with Western Michigan University, the humidity sensing performance of the FG-based sensor was investigated under varying RH levels. The author of this thesis has contributed to the research work illustrated in this section by carrying out the *ab-initio* calculations. The dynamic resistive response of humidity sensors towards varying RH levels was investigated. Since the fabricated humidity sensors have different base resistance values, the normalized resistances of the fabricated sensors for different RH levels were found, as shown in Fig. 3.30. It was observed that the resistance of humidity sensors increased as the chamber's RH level was increased. The obtained results showed the linear response of the humidity sensors towards the variations of RH. The sensor's resistance curve followed the chamber's RH curve effectively.

The FG includes fluorine atoms, possessing the highest electronegativity among all elements. It provides active sites for the adsorption of water molecules and forms hydrogen bonding with the hydrogen atoms of the water molecules. Upon the adsorption of water molecules, their electrons transfer to the FG. This electron transfer reduces the concentration of the major charge carriers (holes) of FG and increases the sensor resistance. When RH increases, more water molecules will be adsorbed on the FG resulting in further increase of resistance of the humidity sensor and vice versa [260].

The $\Delta R/R_b$ of humidity sensors for varying RH levels is shown in Fig. 3.31, which further supports the linearity of the resistive response of humidity sensors. The relative resistance changes ($\Delta R/R_b$ (%)) of humidity sensors were measured as $1.3 \pm 0.3\%$, $3.1 \pm 0.5\%$, $5.5 \pm 0.7\%$, $8.5 \pm 1.0\%$, $12.1 \pm 1.3\%$ and $13.3 \pm 1.8\%$ for the RH of 30%, 40%, 50%, 60%, 70%, and 80%, respectively when compared to 20% RH. The response of the humidity sensors demonstrated a linear relation against the RH levels, with a sensitivity and correlation coefficient of 0.22% RH and 0.98, respectively. The performance of the

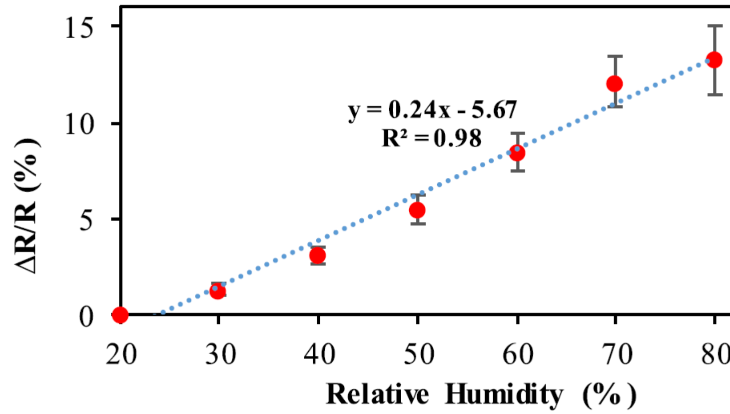

Figure 3.31: Relative resistance change of humidity sensors.

fabricated humidity sensor is compared to various resistive humidity sensors reported in the literature and, as shown in Table I, our fabricated humidity sensor exhibited high sensitivity [261–265].

Table 3.7: Performance of resistive humidity sensors reported in the literature and the humidity sensor presented in this work.

Sensing material	Measurement range	Sensitivity (%/%RH)	Ref.
Multi-layer graphene	15% – 80%RH	S= 0.1 – 0.17	[261]
PI/MWCNT (2.0 wt%)	20% – 90%RH	S= 0.18	[262]
CNTs/Al_2O_3	30% – 80%RH	S= 0.034	[263]
Graphene	1% – 96%RH	S= 0.31	[264]
rGO/MoS_2	10% – 90%RH	S= 0.19	[265]
Fluorinated graphene	20% – 80%RH	S= 0.22	This work

The response time and recovery time are important parameters for evaluating the performance of any sensor. The response and recovery time of humidity sensors were measured for transitions between 45% RH and 70% RH. The response and recovery characteristic curves of the sensor are shown in Fig. 3.32. The response time of the humidity sensor and chamber were measured as 232 ± 19 s and 150 s, respectively. This results in a sensor response time of 82 ± 19 s. Similarly, a recovery time of the 527 ± 23 s and 402 s was measured for the humidity sensor and the chamber, respectively, resulting in a sensor's recovery time of 125 ± 23 s.

The response of the fabricated humidity sensors toward the varying temperature levels was also investigated at 43% RH. The temperature was increased from 20°C to 90°C, in steps of 10°C. Figure. 3.33 shows the normalized response of three sensors toward the varying temperature levels. It was observed that the normalized resistance decrease of the humidity sensors was linearly proportional to the temperature, with a slope of −0.0032/°C and a correlation coefficient of 0.9948. The TCR of −0.25±0.03, −0.26±0.02, −0.28±0.02, -0.30 ± 0.02, -0.29 ± 0.02, -0.30 ± 0.02, and -0.32 ± 0.02 were calculated at 30°C, 40°C, 50°C, 60°C, 70°C, 80°C, and 90°C, respectively, for the humidity sensors (Fig. 3.33.b), with an average TCR of $-0.29 \pm 0.02\%°C$ for the temperature range of 30°C to 90°C.

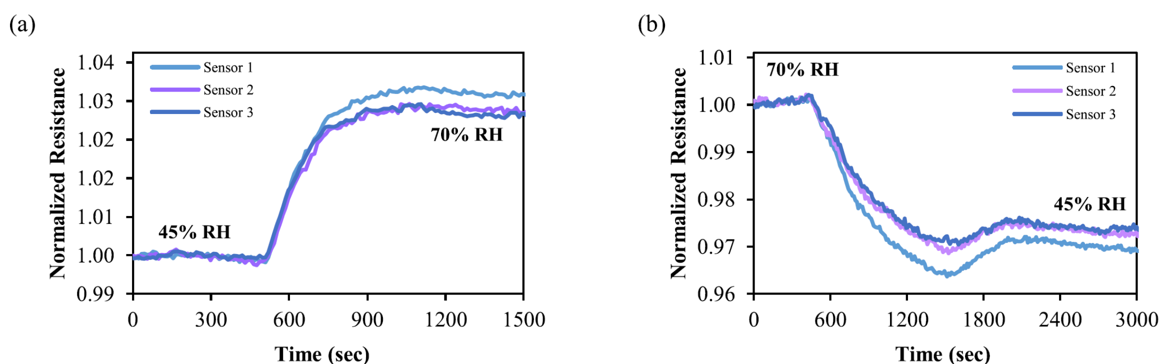

Figure 3.32: Response (a) and recovery (b) curves of the fabricated humidity sensors, for transitions between 45% and 70% RH.

3.5.2.2 First-principles calculations

First-principles study, employing DFT calculations, was performed to investigate interactions between the fluorine atom and graphene substrate, as well as humidity sensing behaviour of the FG. The FG supercell designed for the DFT calculations included 24 carbon atoms and one fluorine atoms. This model represents FG with low fluorination rate, which was used in this work for the fabrication of humidity sensors. In the first step, in order to fluorinate the graphene, the fluorine atom was placed on top of the graphene sheet and structural relaxation of the system was performed. After the structure relaxation, the fluorine atom bonded with the underlying carbon atom. The top view and side view of the most stable structure of FG is shown in Fig. 3.34. The carbon–fluorine bond length was 1.5 $\AA$. It was observed that the F-adsorbed carbon atom was pulled outward from the graphene layer, with its bond length with the closest carbon atom increasing from 1.4 $\AA$ to 1.5 $\AA$ (see Fig. 3.34.d). The local structure deformation indicates the strong adsorption of F atom on the graphene monolayer. The most stable structure of FG was used to investigate the adsorption of water molecules on the FG.

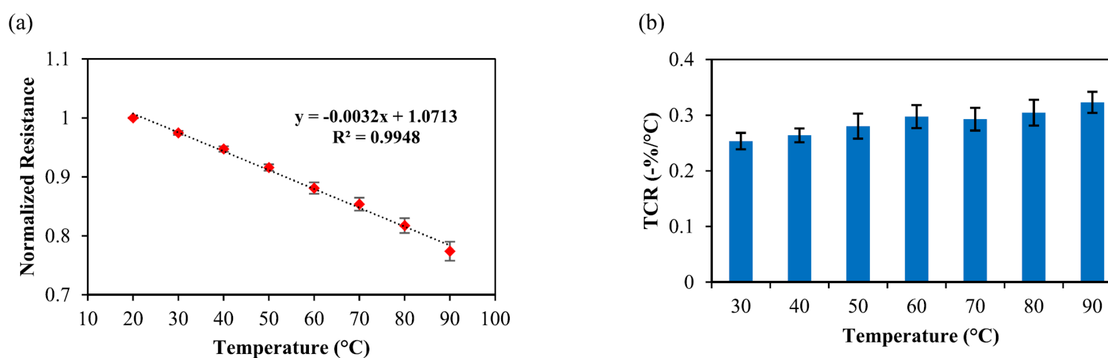

Figure 3.33: Normalized resistance (a) and TCR (b) of the fabricated sensors for different temperature levels.

The interactions between the FG substrate and water molecules were then investigated, using DFT calculations, by adding water molecules to the FG substrate. Several initial structures for the H_2O molecule with respect to the FG substrate were considered. The most stable structures for the adsorption of water molecules on the FG, found by comparing the total energy of relaxed systems, are shown in Fig. 3.35. By comparing

the water molecule's position before and after the relaxation procedure, it was observed that hydrogen atoms of the water molecule moved towards the fluorine atom of the FG substrate. After the relaxation process was completed for the system 5, which had the minimum energy, the distance of the F atom from the closest hydrogen atom was 1.91 Å. It is also worth mentioning that the H-O-H angle of water molecule decreased from 104.5° to 100.5° during the adsorption of the water molecule on the FG substrate. Also, the carbon–fluorine bond length increased slightly, from 1.5 Å to 1.52 Å. The E_{ads} was calculated for the most stable structures, which is shown in Fig. 3.35. As shown in Fig. 3.35, the system 5 has the minimum E_{ads}, so it is the most stable structure for the adsorption of water molecules on the FG substrate. The E_{ads} of -0.5 eV was calculated for the system 5, which supports the strong adsorption of water molecules on the humidity sensing FG.

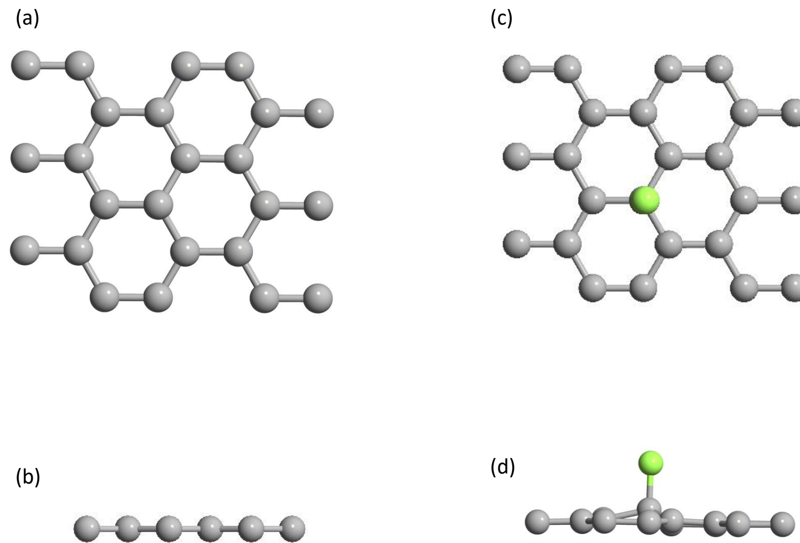

Figure 3.34: Top view (a) and side view (b) illustration of graphene supercell used in this study. The top view (c) and side view (d) illustration of fluorinated graphene supercell used in this study. Carbon and fluorine atoms are shown with gray and green colors, respectively.

The interactions between the FG and water molecules were then investigated, using DFT calculations, by adding water molecules to the FG. Several initial structures for the H_2O molecule with respect to the FG were considered. The most stable structures for the adsorption of water molecules on the FG, found by comparing the total energy of relaxed systems, are shown in Fig. 3.35. By comparing the water molecule's position before and after the relaxation procedure, it was observed that hydrogen atoms of the water molecule moved towards the fluorine atom of the FG. After the relaxation process was completed for the system 5, which had the minimum energy, the distance of the F atom from the closest hydrogen atom was 1.91 $\AA$. It is also worth mentioning that the H-O-H angle of water molecule decreased from 104.5 Å to 100.5 Å during the adsorption of the water molecule on the FG. Also, the carbon–fluorine bond length increased slightly, from 1.5 Å to 1.52 Å. The E_{ads} was calculated for the most stable structures, which is shown in Fig. 3.35. As shown in Fig. 3.35, the system 5 has the minimum E_{ads}, so it is the most stable structure for the adsorption of water molecules on the FG. The E_{ads} of -0.5 eV was calculated for the system 5, which supports the strong adsorption of water molecules on the humidity sensing FG.

The obtained results demonstrated that FG, a highly stable derivative of graphene, is a

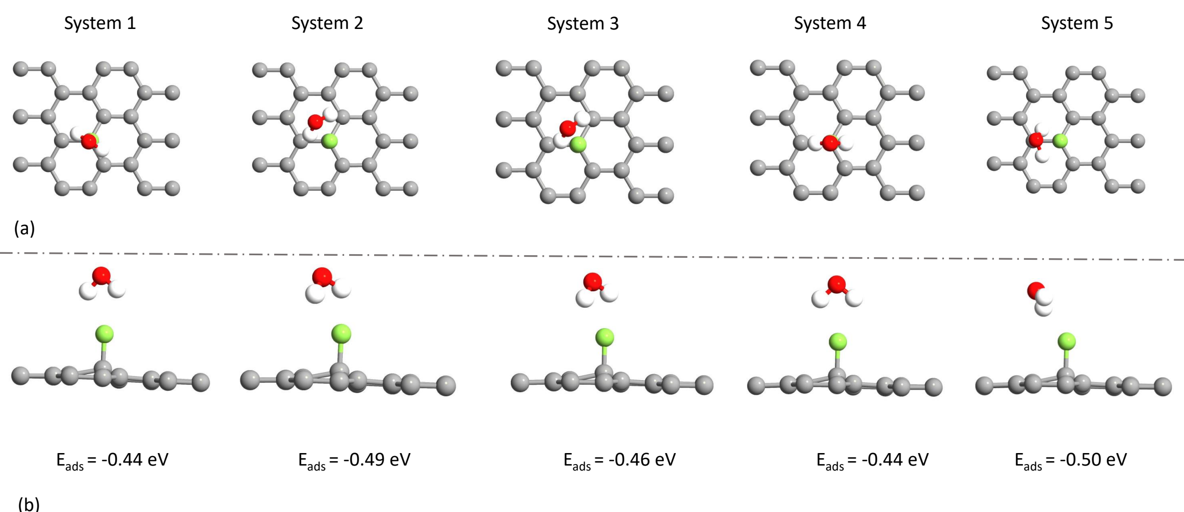

Figure 3.35: Top view (a) and side view (b) illustrations of the most stable structures for the adsorption of water molecule on the fluorinated graphene. Carbon, fluorine, oxygen, and hydrogen atoms are shown with gray, green, red, and white colors, respectively.

promising 2D material for the development of humidity sensors. Like FG, recent advances in the synthesis of 2D materials has led to the development of novel sensors for numerous applications. For example, 2D materials such as stannic sulfide and MXenes have shown selectivity to gases such as nitrogen dioxide and ammonia through physisorption process similar to FG [128, 266]. Other 2D materials such as bismuth (III) oxide have shown sensitivity to UV rays and demonstrated its suitability to be employed as UV photodetector [267]. These 2D materials possess excellent sensitivity and reversibility due to its physisorption property when compared to chemisorptive and ion conductive materials. These 2D materials are compatible with flexible substrates and when employed in the development of flexible and printed sensors similar to this process can result in promising low-cost devices for various fields including biomedical, automotive and wearable electronics.

3.6 Conclusion

It was shown that monolayer MoS_2 exhibits a giant intrinsic piezoresistance of ~ 724, which is driven by the uniquely strain-tunable band structure that is shared among MX_2 ($M = Mo$, W, $X = S$, Se) TMDs. The experimental piezoresistance is calculated using careful extractions of sheet resistance, from TLMs under vacuum, and large-area maps of strain using optical techniques of Raman and PL. The origins of this piezoresistive effect are explained through a detailed analysis of several scattering models, including intervalley phonon scattering and short-range strain vari-ation. This giant intrinsic piezoresistive can enable emerging applications in tactile sensing, like soft robotics, as well as improving the mobility (and understanding variation) in TMD electronics.

We have also demonstrated a large TCR in atomically thin 2D materials ($\sim 0.3\%\ K^{-1}$ at 300 K and $\sim 0.6\%\ K^{-1}$ at 100 K), significantly higher than that of metals in the sub-10 nm-thickness range. Simulations show that even larger TCRs (up to 0.45 % K^{-1} at 300 K and 2.5 % K^{-1} at 100 K) in monolayer 2D devices could be obtained by further reducing the density of charged impurities. These could enable fast temperature sensors

with low thermal resistance and thermal capacitance at the atomically thin limit.

Then we investigated $Ti_3C_2T_x$ as an ammonia sensor by means of a first-principles study. Since synthesized sample of $Ti_3C_2T_x$ have a combination of various surface termination groups, as well as water molecules, the impacts of different ratios of surface termination groups were analyzed, as well as the presence of water molecules on ammonia gas sensing behavior of $Ti_3C_2T_x$. DFT calculations for E_{ads} and CT between various gases and S_1 show a relatively high sensitivity of the substrate to NH_3 gas molecules compared to other gases with the highest CT (0.098 e) and the lowest E_{ads} (−0.36 eV). The calculated NH_3 adsorption energy for S_2 was −0.49 eV, which is larger than those of S_1 and S_3. Isosurface representations of charge difference showed a smaller CT between fluorine atoms and NH_3 molecules compared to the CT between oxygen atoms and NH_3 molecules. At NH_3 adsorption sites, the Bader charge difference of nearest oxygen atoms was 60% to 180% larger than that of the nearest fluorine atoms, demonstrating a stronger interaction of NH_3 with the $Ti_3C_2T_x$-based sensor with a lower ratio of fluorine surface terminations. PDoS curves shift toward energies that are more negative, and a pseudogap around the Fermi level appear, as surface termination groups are added to the Ti_3C_2 substrate. It shows that the orbital mixing of S_3/NH_3 is weaker compared to S_1/NH_3 and S_2/NH_3, which will lead to a smaller CT. Moreover, ESP and PDoS analyses for NH_3 adsorption showed that the surface properties can dictate the strength and nature of bonding through a combination of covalent and electrostatic effects. The findings are related to the general Lewis acid-base interactions in the matter of molecular chemistry. AIMD simulations were also performed to confirm that all the structures in the presence of the NH_3 gas molecule are thermally stable at room-temperature.

Finaly we have shown that a novel fluorinated graphene (FG)-based resistive humidity sensor was successfully fabricated by drop-casting FG suspension on Ag-based IDEs. The FG was uniformly dispersed in IPA, using the ultra-sonication process, and the resulted suspension was drop cast on silver-based IDEs screen printed on a flexible polyimide substrate. The resistive response of humidity sensors towards varying RH levels ranging from 20% to 80% was investigated at 24°C, which showed good repeatability for the fabricated sensors. The response of the humidity sensors demonstrated a linear relation towards varying RH levels from 20% RH to 80 % RH, with a sensitivity and correlation coefficient of 0.22%/% RH and 0.98, respectively. The response and recovery time of the sensor for transitions between 45% RH and 70% RH were calculated as 82 and 125 s, respectively. The humidity sensors showed a linear response towards varying temperatures from 20 °C to 90 °C, with a slope of −0.0032/°C and a correlation coefficient of 0.9948. The average TCR calculated for the sensors was approximately −0.3%/°C. DFT calculations confirmed the hydrogen bonding between FG and water molecules and demonstrated the strong humidity sensing property of the FG. The obtained results suggest that FG, a highly stable derivative of graphene, is a potential material for humidity sensing applications.

Chapter 4

Non linear transport based on MoS_2

4.1 Introduction

Promising features of Molybdenum Disulfide (MoS_2) such as the sub-nanometer thickness, large piezo-resistance [20], and extreme flexibility qualify MoS_2 as a candidate baseline material for many applications. While linear transport (used to interpret the experimental low field mobility) has been addressed in several contributions [137, 138], high field transport and velocity saturation have received a more limited scrutiny [164, 268, 269].

The velocity versus field curves are relevant for many experimentally characterized transistors (which are not at all nanoscale) and, moreover, for sensor applications that do not require aggressively scaled devices. On the other hand, the high field saturation velocity is not the most appropriate figure of merit for the performance of nanoscale FETs [135], where carrier transport depends on scattering mechanisms that govern how close to the ballistic regime the device can operate, and then on the thermal velocity at the source that sets an upper limit to carrier velocity even in the fully ballistic transport limit.

As a result of a collaboration with Dr. Alessandro Pilotto, in this chapter we document the development of a Monte Carlo (MC) solver for the multi-valley Boltzmann Transport Equation (BTE) in MoS_2, that is employed to investigate transport under uniform electric field as well as quasi-ballistic transport in FETs. For the work illustrated in this chapter we have leveraged on a previously developed MC solver described in [270], then we have extended the solver to the electronic structure of 2D MoS_2 and also updated the formulation of the scattering mechanisms. This Chapter proceeds as follows. Sec. 4.2 summarizes the model employed for the description of the conduction band of monolayer MoS_2, while Sec. 4.3, provides details on the multi-valley Monte Carlo technique. In Sec. 4.4, firstly the MoS_2 electron mobility calculated from MC simulations including different scattering mechanisms is compared with the results of the linearized-BTE (LBTE) solver described in Sec. 3.2, then the velocity versus field curves obtained with the MC solver are reported and discussed. In Section 4.4.6, we report self-consistent simulations of a 100 nm FET showing the impact of velocity saturation on the I-V curves of short channel devices in the presence of different scattering mechanisms. Section 4.5 offers some concluding remarks.

4.2 Description of the conduction band of monolayer MoS_2

A sketch of the hexagonal First Brillouin Zone (FBZ) of monolayer MoS_2 is shown in Fig. 4.1.a, where the two Cartesian directions are denoted as Armchair (A) and Zigzag (Z). As already mentioned in Sec. 3.3, the conduction band structure of MoS_2 presents two sets of minima: in Fig. 4.1.a we can identify circular K valleys at the edge of the FBZ (for each corner, only one third of a K valley falls inside the FBZ), and six elliptical Q valleys with orientation $\theta_v = -2\pi/3, -\pi/3, 0, \pi/3, 2\pi/3$ with respect to the Z direction in the reciprocal space. It is worth noting that the A and Z directions in the real space translate into the Z and A directions in the reciprocal space, respectively. As shown in Fig. 4.1.b, the K valleys set the absolute minimum of the conduction band, while the Q valleys are the second lowest valleys.

We have employed a non-parabolic description of the band structure based on the Effective Mass Approximation (EMA) close to the K and Q conduction band minima (Eq. 3.18). The longitudinal and transverse effective masses, m_l and m_t respectively, and the non parabolic factors α were extracted by comparing to DFT calculations obtained with QUANTUM ESPRESSO [108] (see Fig. 4.1.b); the corresponding values of the EMA parameters are reported in Tab. 4.1. Analytical bands seem a defendable approximation

Valley	m_l $[m_0]$	m_t $[m_0]$	α $[eV^{-1}]$	ΔE $[eV]$
K	0.47	0.47	0.94	–
Q	1.14	0.54	1.16	0.16

Table 4.1: EMA parameters for the K and Q valleys in monolayer MoS_2 extracted by fitting DFT calculations [108].

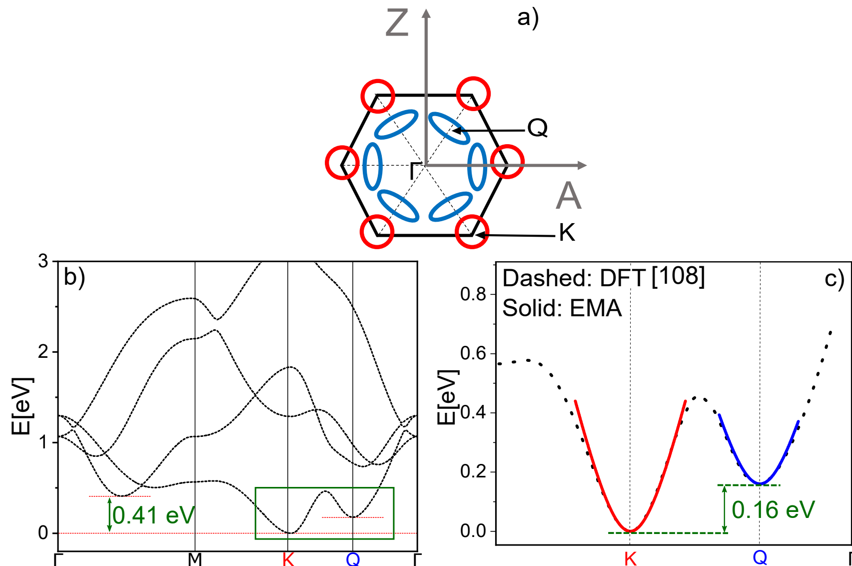

Figure 4.1: (a) Sketch of the First Brillouin Zone: A and Z denote the armchair and zigzag directions, respectively. b) MoS_2 energy dispersion computed by DFT simulations. c) MoS_2 energy dispersion close to the K (red) and Q (blue) conduction band minima as calculated with DFT simulations [108] (dashed), and then fitted with the non-parabolic EMA model of Eq. 3.18 (solid). The minimum in Q is plotted along the K-Γ (transverse) direction.

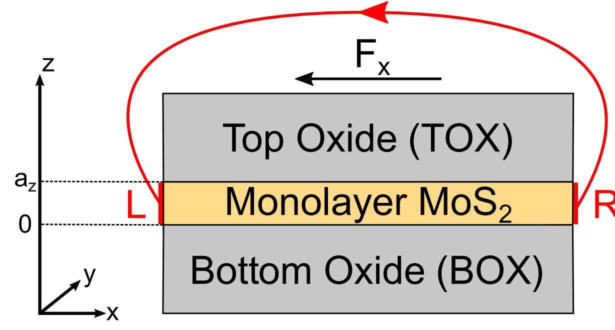

Figure 4.2: Sketch of the simulated structure. F_x is the electric field along the x direction, while L and R are the left and right contacts, respectively.a$_z$ is the thickness of the monolayer MoS_2.

for the monolayer MoS_2 because the K and Q conduction band minima are well separated in energy from the next lowest conduction band extrema [138, 271], and in fact they have been employed in several previous references [138, 272–274]. Monte Carlo simulations with a full band descriptions have been reported for mobility and uniform high field transport in phosphorene [275], and also for a 10 nm long MoS_2 based FET [276]. The use of analytical bands, however, is particularly suitable for Monte Carlo simulations of transistors with channel lengths up to hundreds nanometers, where the computational burden of a full band Monte Carlo approach may become prohibitive.

4.3 The multi-valley Monte carlo transport simulator

The sketch of the physical system simulated with the multi-valley Monte Carlo simulator is reported in Fig. 4.2. Uniform transport (i.e. an infinitely long device) is considered. Monolayer MoS_2 is sandwiched between the top and bottom oxides, an electric field F_x is imposed in the MoS_2 monolayer and *looping* boundary conditions are used [135], namely the electrons collected at a contact are injected at the opposite contact with the same energy, momentum and velocity. The total number of particles in the simulation is thus kept fixed and set by the electron density per unit area $N_s = \frac{\text{number of electrons}}{S}$.

Our simulator takes as input the geometrical parameters of the structure in Fig. 4.2 and the EMA parameters (Tab. 4.1) of the K and Q valleys. The scattering rates are described according to Eqs. 3.28, 3.29, 3.44, 3.36 already discussed in chapter. 3. In the case of isotropic mechanisms like intrinsic phonons (iPh), the scattering rates are stored as a function of the initial valley and the carrier energy, while for anisotropic mechanisms due to the Neutral Defects (NDs), Coulomb Impurities (CIs), and Surface Optical phonons (SO ph), they are stored as a function of the initial valley, the carrier's energy, the angle θ_i that sets the direction of the initial state in the $\vec{k}$-space, and the angle θ_s between the initial and the final states.

For isotropic scattering mechanisms (i. e. intrinsic acoustic and optical phonons), Vogt-Herring transformations are used to determine the state after scattering $\vec{k'}$ [277]. Firstly, an effective wave vector $\vec{k'}_{eff}$ is determined in the valley of the final state by using

$$E(1 + \alpha E) = \frac{\hbar^2}{2}\left(\frac{k_l^2}{m_l} + \frac{k_t^2}{m_t}\right) = \frac{\hbar^2 k'^2_{eff}}{2m_{eff}}, \tag{4.1}$$

where $m_{eff} = \sqrt{m_l m_t}$. Then, a random number r with uniform distribution in $[0, 1]$ is

generated and k'_l and k'_t are obtained as

$$k'_l = k_{eff}\sqrt{\frac{m_l}{m_{eff}}}cos(2\pi r) \tag{4.2}$$

$$k'_t = k_{eff}\sqrt{\frac{m_t}{m_{eff}}}sin(2\pi r). \tag{4.3}$$

On the other hand, for anisotropic scattering mechanisms (i. e. neutral defects, coulomb impurities, and SO phonons), $\vec{k'}$ and its components along the longitudinal and transverse directions are given by [135]

$$k' = \frac{\sqrt{2m_\theta E(1+\alpha E)}}{\hbar} \tag{4.4a}$$

$$k'_l = k' cos(\theta) \tag{4.4b}$$

$$k'_t = k' sin(\theta), \tag{4.4c}$$

where $\theta = \theta_i + \theta_s$ represents the direction of the final state and it is chosen according to the relative weight (w. r. t. the total scattering rate) of the scattering rate that corresponds to a deflection θ_s, and m_θ is the angle-dependent effective mass defined as

$$m_\theta = \left[\frac{cos^2(\theta)}{m_l} + \frac{sin^2(\theta)}{m_t}\right]^{-1}. \tag{4.5}$$

An ensemble MC technique is finally used to compute average quantities, such as the average velocity v_x along the x direction

$$v_x = v_l cos(\theta_w) - v_t sin(\theta_w), \tag{4.6}$$

as well as the energy and momentum distribution functions $f(E)$ and $f_v(\vec{k})$, respectively. θ_w is the angle describing the Q valley orientation with respect to the zigzag direction in k-space.

Treatment of carrier degeneracy, i.e. accounting for Pauli's exclusion principle, as been implemented as described in [278].

4.4 Results

4.4.1 Mobility calculation: MC versus LBTE

As a first validation of the multi-valley MC simulator, in Fig. 4.3 we compare the MoS_2 electron mobility extracted as v_x/F_x at low field with the mobility provided by the LBTE solver in [20]. Mobility is analyzed at room temperature, for different values of the electron density N_s and considering different combinations of scattering mechanisms (iPh, iPh and ND, iPh and CI, iPh and SO Ph). The defect concentrations for ND scattering is $N_D = 2.4{\times}10^{13}$ cm^{-2} (that corresponds to the 1% of of the sulfur atoms areal density), and the concentration of Coulomb centers for CI scattering is $N_{imp} = 3 \times 10^{12}$ cm^{-2} (a reasonable value, similar to what reported in [20, 269]). The agreement between the two modeling approaches is very good for all the considered cases. Fig. 4.3. Table 4.2 compares the mobility computed with our Monte Carlo solver with results reported in the literature, obtained for different values of the free electron's concentration N_s and by including different scattering mechanisms. Even if a quite large spread in the values of the phonon

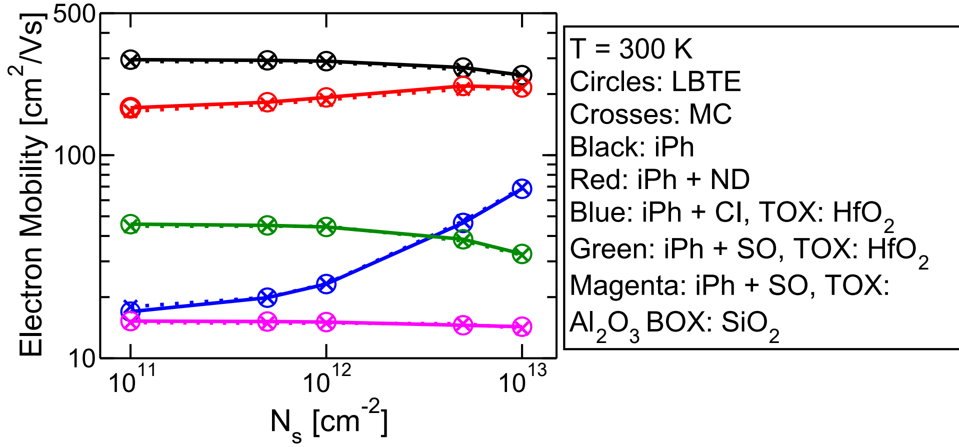

Figure 4.3: Comparison between the MoS_2 electron mobility at $T = 300$ K as a function of N_s computed by using either the LBTE (circles) or the MC simulations (crosses). Phonon scattering and scattering with ND ($N_D = 2.4 \times 10^{13}$ cm^{-2}), CI ($N_{imp} = 3 \times 10^{12}$ cm^{-2}) or with SO phonons were included in different combinations.

limited mobility can be observed [138,268,279,280], our approach is fairly consistent with the results in [268,280]. On the other hand, regarding the simulations with the inclusion of scattering with Coulomb centers, our MC solver agrees quite well with the mobility value reported in [281] (TOX: HfO_2, BOX: SiO_2, $N_{imp} = 4 \times 10^{12}$ cm^{-2}).

N_s [cm^{-2}]	TOX/BOX	Scattering	[REF] [cm^2/(Vs)]	This Work [cm^2/(Vs)]
10^{13}	-	iPh	420 [138]	244
10^{13}	-	iPh (Intravalley)	400 [279]	308
-	-	iPh	193 [268]	$290 \geq \mu \geq 122$[1]
5×10^{13}	-	iPh	144 [280]	122
10^{13}	HfO_2/SiO_2	iPh + CI ($N_{imp} = 4 \times 10^{12}$ cm^{-2})	49 [281]	56

Table 4.2: Comparison of the electron mobility (μ) computed with our Monte Carlo solver with the results reported in [138], [279], [268], [280], and [281].

4.4.2 Velocity-field curves in the presence of intrinsic phonons

To check the correctness of our implementation and assess the adequacy of the analytical band description as the electric field increases, we compare our MC solver against previous literature [139,268]. The results in [268] are helpful to validate the analytical band model on a more accurate full-band description, while in [139] we find results over an extended temperature range. The comparison is reported in Fig. 4.4.

To verify that phonon scattering captures the temperature dependence of mobility and saturation velocity, we first compare our results at different temperature (solid lines) to the results in [139] for a MC with analytical bands. For the purposes of this comparison, in our simulator we used the EMA parameters reported in [139] (instead of those in Tab. 4.1), and included only the scattering with MoS_2 intrinsic phonons. The electron density is $N_s = 10^{12}$ cm^{-2}. We notice that our MC simulator and the one in [139] are in good mutual agreement at all temperatures.

[1] In [268], the value of N_s is not specified, therefore we report the results of our Monte Carlo simulations for 10^{11} cm$^{-2} \leq N_s \leq 5 \times 10^{13}$ cm^{-2}.

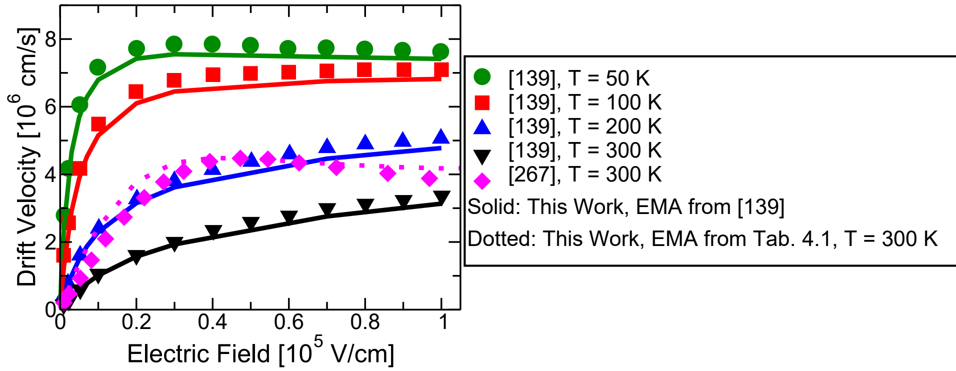

Figure 4.4: Comparison between the $v_x(F_x)$ curves from [139], and the results of this study by using the phonon scattering parameters and the EMA parameters as in [139], and between the $v_x(F_x)$ curve at room temperature from [268] and the results of this study obtained by using the phonon scattering parameters from [139], but the EMA parameters in Tab. 4.1.

However, the EMA parameters in [139] are not consistent with DFT calculations reported in Fig. 4.1. In order to investigate the influence of the bandstructure description, the dotted line in Fig. 4.4 reports the results of our MC simulations at room temperature by using the EMA parameters of Tab. 4.1, and those are compared with the full band MC simulations in [268]. A closer agreement over the whole range of applied electric fields is observed with simulations from [268] (note that we used the same phonon energies and deformation potentials as in [139], that, together with the EMA parameters in Tab 4.1, appear to be a good choice also to reproduce the results in [268]). To further corroborate the limited relevance of full-band effects, we plot in Fig. 4.5 the average energy and the valley occupation as a function of the electric field in the different cases: we see that the average energy, w.r.t. the valley's minimum, in the range of electric fields considered here is no larger than 150 meV for the K valleys and 75 meV for the Q valleys, so that the non-parabolic band model is quite adequate in reproducing the full band structure as seen in Fig. 4.1. Concerning the difference between our model with the parameters in Tab. 4.1 (that reproduce the curves in [268] and will be used in the rest of this paper) and the velocity versus field curves of [139] (compare magenta dotted-line and blue triangles up), it is mainly due to the energy separation between the K and Q valleys, which is 160 meV in our case (Tab. 4.1) and 70 meV in [139]. This inconsistency is mainly due to the usage of different exchange-and-correlation functional in DFT calculations. We have observed a certain spread (starting from 60 meV to 300 meV) in the literature about the energy distance between the K and Q valleys [148, 282, 283].

4.4.3 Velocity-field curves including scattering with neutral defects and coulomb centers

In Fig. 4.5 we report the $v_x(F_x)$ curves computed with MC simulations when only intrinsic phonon scattering is considered (black line), compared with the results obtained by including also scattering with ND ($N_D = 2.4{\times}10^{13}$ cm^{-2}) or CI ($N_{imp} = 3{\times}10^{12}$ cm^{-2}). We notice that the scattering with impurities has a strong effect on the mobility, which degrades from values above 200 cm^2/(Vs) down to about 9 cm^2/(Vs) when CI is included. The drastic mobility reduction also increases the electric field required to reach velocity saturation above 10^5 V/cm, which is the maximum field that has been experimentally explored in MoS_2 devices [268]. Figure 4.6 also shows that, however, the saturation velocity

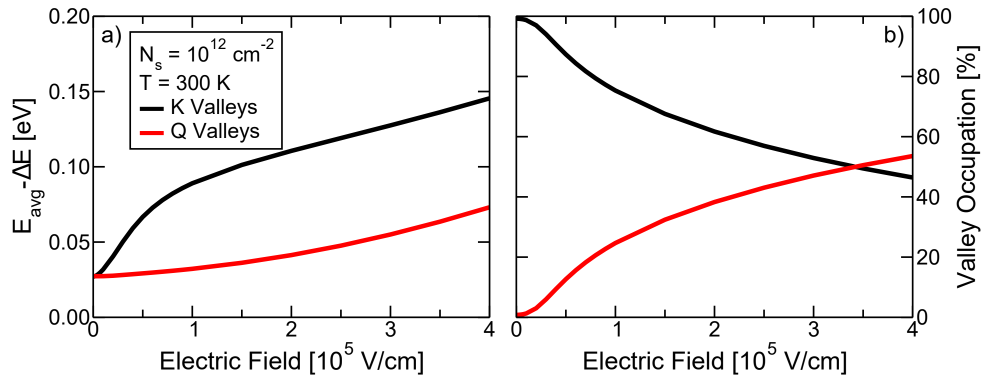

Figure 4.5: a) Average energy with respect to the valley minimum versus electric field. b) Valleys' occupation versus electric field. Results are reported in black for K valleys and in red for Q valleys.

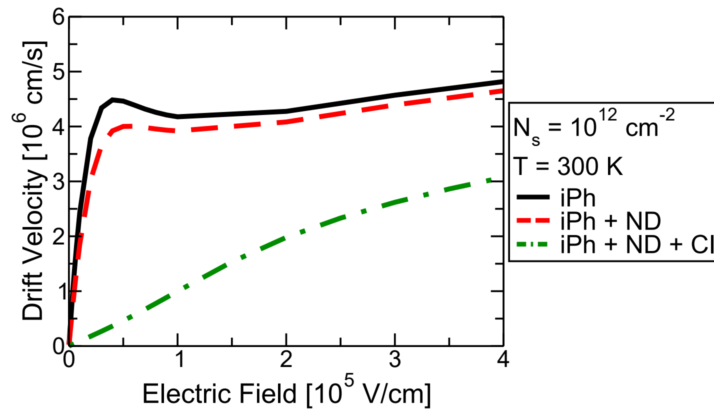

Figure 4.6: Comparison between the room temperature $v_x(F_x)$ curves computed with the MC simulator for electric fields up to $4{\times}10^5$ V/cm, with the EMA parameters of Fig. 4.1a and for $N_s = 10^{12}$ cm^{-2}. Results are shown for intrinsic phonon scattering only (solid black), then by adding the scattering by neutral defects (dashed red), and finally also Coulomb centers (dashed-dotted green). TOX is vacuum, BOX is SiO_2.

value that is eventually reached at high fields is essentially the same for the different sets of scattering mechanisms.

4.4.4 Velocity-field curves including SO phonons

Figure 4.7 compares the velocity versus electric field curves obtained with the MC simulator either including only scattering with intrinsic phonons or considering also scattering with SO phonons originating in the top and bottom oxides. We notice that, in the latter case, the mobility is reduced, as previously observed in Fig. 4.3, but v_{sat} is larger than the counterpart obtained neglecting the SO phonons (see also Fig. 4.6). The velocity saturation in Fig. 4.7, however, is reached only for an electric field that is larger than 10^5 V/cm, namely a field range that has been so far impossible to probe in actual experiments [268]. In order to better understand the counter intuitive influence of the SO scattering on the saturation velocity, we compare in Fig. 4.8 the valleys' occupation as a function of the applied electric field obtained from the MC simulations when scattering with SO phonons is neglected or instead accounted for, and by considering vacuum as TOX. Figure 4.8 shows that in the presence of SO phonons, and for longitudinal electric fields up to 4×10^5 V/cm, the electron population in the six Q valleys is below 15%,

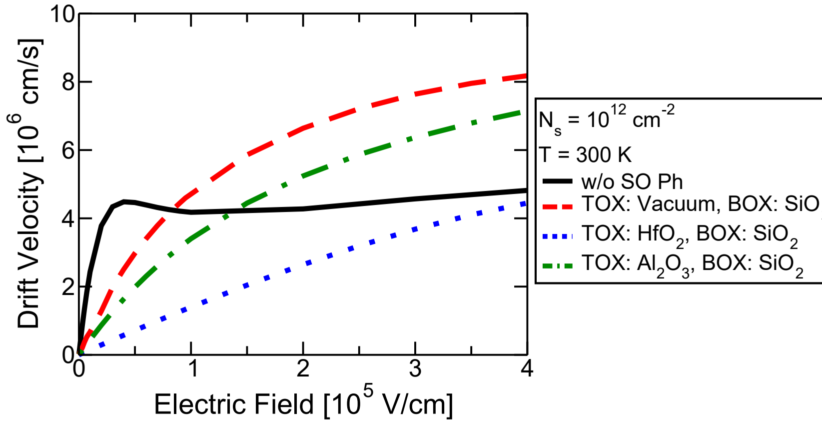

Figure 4.7: Comparison between the room temperature $v_x(F_x)$ curves computed with the MC simulator when scattering with SO phonons from TOX and BOX is neglected (solid black) or is instead accounted for. Vacuum (dashed red), HfO_2 (dotted blue) and Al_2O_3 (dashed-dotted green) are the dielectric options here considered for the TOX. The BOX is always SiO_2. The electron density is $N_s = 10^{12}$ cm^{-2}.

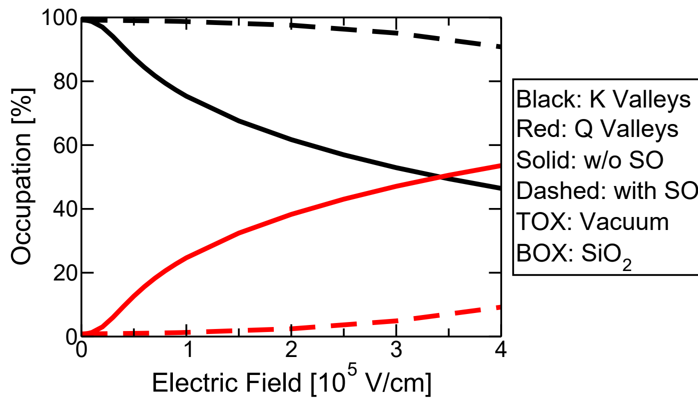

Figure 4.8: Comparison between valleys' occupation vs. electric field when scattering with SO phonons is either neglected (solid) or considered (dashed): TOX is vacuum and BOX is SiO_2.

so that carriers mostly occupy the K valleys. When SO phonon scattering is neglected, instead, a large fraction of electrons ($52 \div 58\%$) resides in the Q valleys, that feature a much lower mobility. This is confirmed also by the energy distribution functions at $F_x = 3{\times}10^5$ V/cm reported in Fig. 4.9, where we notice that the presence of scattering with SO phonons results in a more peaked $f(E)$ at low energies. The reason of the increase in the saturation velocity observed by including SO phonons is thus due to the anisotropic and inelastic nature of the SO scattering mechanism. In fact, as it can be inferred from the occupation functions in the reciprocal space reported in Fig. 4.10, the presence of SO phonons tends to reduce the energy of the electrons that populate a valley (see Fig. 4.9) without excessively randomizing their momentum. Therefore, for a given electric field, the $f(\vec{k})$ is more elongated in the direction of the electric field when SO phonons are active. In other words, SO phonons tend to induce an energy relaxation that prevents electrons from occupying the Q valleys, whereas it produces only a small $\vec{k}$ randomization.

It is worth noting that the effects of SO phonons on v_{sat} shown in Fig. 4.7 are quite different from those obtained from MC simulations in [269] that, instead, reported a $v_{sat} = 5.8 \times 10^6$ cm/s at $F_x \geq 5 \times 10^4$ V/cm when a SiO_2 substrate is considered and CI is active (with $N_c = 10^{12}$ cm^{-2} and $N_s = 5 \times 10^{11}$ cm^{-2}). This discrepancy may be ascribed to a difference in the electron mobility, that originates from different scattering rates

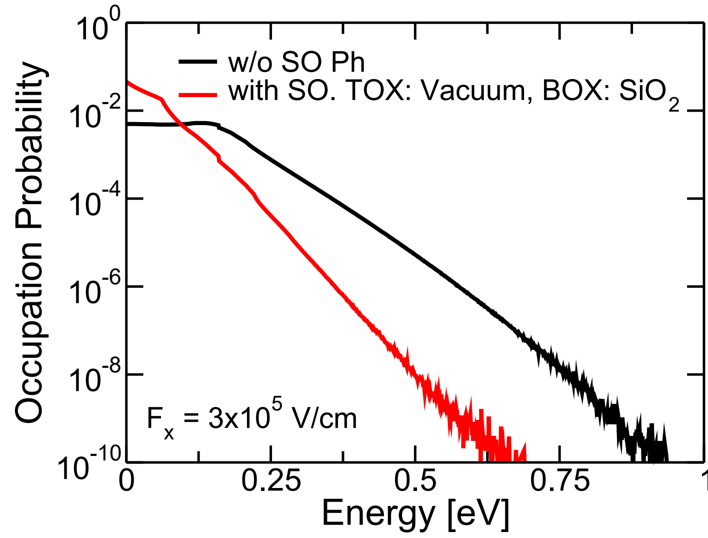

Figure 4.9: Comparison between the energy distribution functions extracted from MC simulations at $F_x = 3{\times}10^5$ V/cm when scattering with SO phonons is either neglected (black) or included: TOX is vacuum and BOX is SiO_2 (red).

with intrinsic phonons. In fact, the authors in [269] reported a phonon-limited mobility for monolayer MoS_2 in the order of 2000 cm^2/Vs, while in this work we found about 300 cm^2/Vs (see Fig. 4.3). Moreover, Fig. 4.4.a of [269] shows that, for all the simulated electric fields, intrinsic phonons are the dominant scattering mechanism, whereas in our MC model, the scattering rate of SO phonons largely exceeds the rate of acoustic and optical intrinsic phonons (see Fig. 4.11).

4.4.5 Effect of screening of SO phonons

Finally, in this work we have assumed that scattering with SO phonons is not screened by the free electrons. This leads to an overestimation of the scattering rate. More accurate results may be obtained by employing a dynamic screening approach [135] that, on the other hand, would dramatically increase the computational burden of MC simulations. Preliminary results with static screening suggest that the inclusion of screening in the treatment of the scattering with SO phonons may be important for an accurate evaluation of the value of v_{sat} in MoS_2. In fact, From Fig. 4.12 we can notice that, as the value of N_s increases, when static screening is considered the $v_x(F_x)$ curves rapidly converge toward the case when scattering with SO phonons is neglected in our MC simulations.

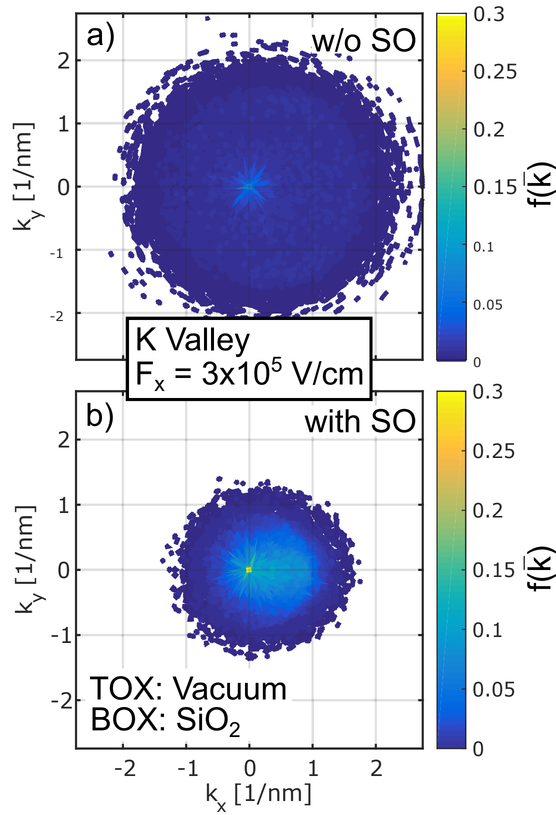

Figure 4.10: Occupation functions in the $\vec{k}$-space for the K valleys of MoS_2 at $F_x = 3 \times 10^5$ V/cm when (a) scattering with SO phonons is turned off and when (b) scattering with SO phonons is considered, TOX is vacuum and BOX is SiO_2.

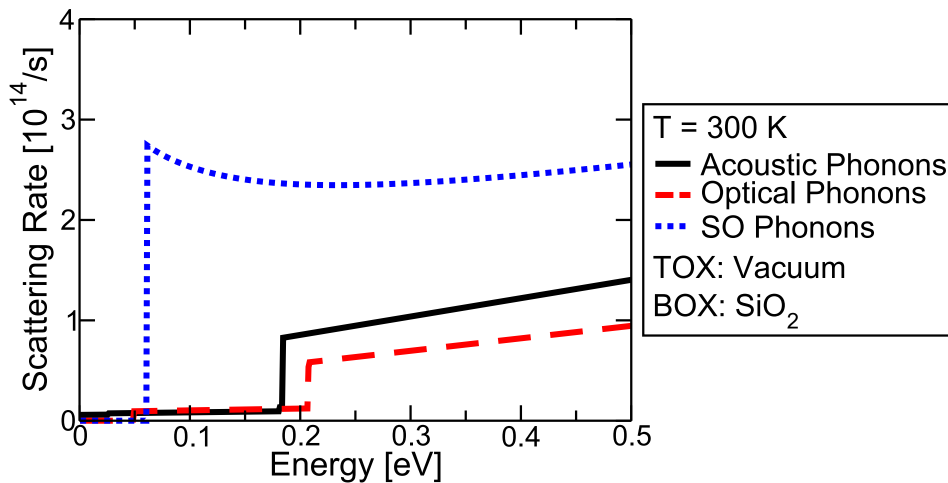

Figure 4.11: Total scattering rate for emission of acoustic (solid black), optical (dashed red) and SO phonons (dotted blue) as a function of energy for electrons in K valleys. The curve for acoustic phonons includes both elastic and inelastic transitions.

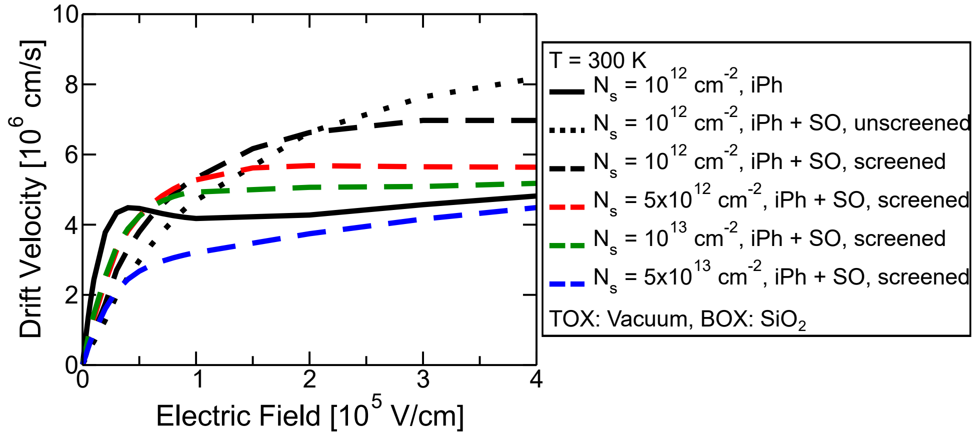

Figure 4.12: Comparison between the room temperature $v_x(F_x)$ curves for electrons in MoS_2 computed with MC simulations by considering only iPh (black solid line) or iPh and SO scattering for different values of N_s. Static screening is either neglected (black dotted line) or included (dashed lines).

4.4.6 I-V curves of a short channel FET

The Monte Carlo transport procedure described in the previous sections has been coupled with the 2D Poisson equation to perform simulations of a short channel FET (see Fig. 4.13), analyze the impact of different scattering mechanisms on the current-voltage $(I-V)$ characteristics and inspect the electron velocity profiles in the transistor channel. We remark that, to focus only on how the performance of MoS_2-based FETs are affected by scattering mechanisms, in the following, we neglect the effects on the $I-V$ curves of the series resistances that, notably, are quite large at contacts between metals and 2D semiconductors.

The Poisson equation and the Monte Carlo transport are coupled using the non-linear scheme [284]. Compared to the simulations in the previous section, where periodic boundary conditions were applied to mimic an infinitely long device, here the boundary conditions described in [285] have been employed: electrons trying to exit the domain are removed, while other electrons are regularly injected from the source and drain according to Fermi-Dirac distributions whose Fermi levels are split by V_{DS}. As in [285], the derivative of the electrostatic potential is set to zero at the source and drain contacts.

Figure 4.14 shows the drain current versus gate-to-source voltage characteristics considering the scattering due to either only phonons or to phonons and Coulomb centers. Since the work-function of the metal gate is assumed to be equal to the MoS_2 affinity, the threshold voltage is very close to $V_T = 0V$. We see that when only phonons are included, the curve is essentially a straight line, that is consistent with textbook formulas for FETs under velocity saturation (i.e. $I_D = W v_{sat} C_{OX}(V_{GS} - V_T)$). In other words, the saturation drain voltage is very low and just above threshold we observe a linear relation between I_D and V_{GS}. We have indeed verified that the velocity along the channel is fairly constant and close to the saturation velocity displayed in Fig. 4.6 for uniform field simulations accounting only for phonon scattering. When including Coulomb centers, instead, the mobility is so low (see again Fig. 4.6) that the electron average velocity does not reach a saturation value. As a result, we have the expected parabolic behavior of the current for gate-source voltages in between V_T and $V_T + V_{DS}$, that becomes linear only when the device enters the triode region.

Figure 4.15 shows the output characteristics for the same cases as in Fig. 4.14. The

slope at low V_{DS} is related to the mobility and it is thus much larger when only phonons are included. Then the current saturates at high V_{DS}. This is due to velocity saturation when only phonons are included and, whereas it is due to the formation of a pinched-off region close to the drain in the case including the scattering due to phonons and Coulomb centers.

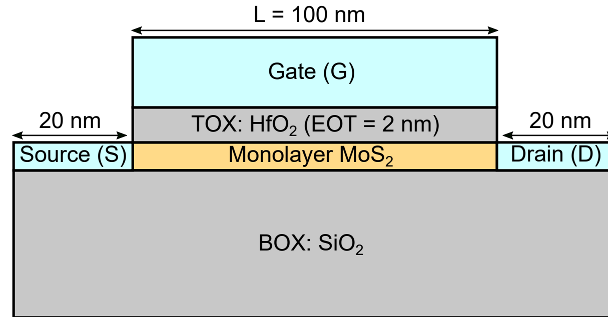

Figure 4.13: Sketch of the simulated FET device. A 100 nm long monolayer MoS_2 channel is sandwiched between a thick SiO_2 BOX and HfO_2 (EOT = 2 nm) TOX. The Source (S) and Drain (D) regions are 20 nm long. A doping $D_p = 8 \times 10^{13}$ cm^{-2} has been assumed.

4.5 Conclusions

We have developed a multi-valley Monte Carlo Transport simulator that has been used to study uniform field transport in monolayer MoS_2, but can be naturally extended to other two-dimensional semiconductors.

At low electric field our simulator has been validated against the results of a solver of the Linearized Boltzmann Transport Equation, showing good mutual agreement.

Monte Carlo simulations of high field transport in monolayer MoS_2 have shown that a multi-valley non-parabolic description of the band structure is accurate and that our results well match the outcomes of more complex models, such as Full Band Monte Carlo transport simulations. Moreover, we have found that the electron's saturation velocity in monolayer MoS_2 is only slightly affected by scattering with Coulomb centers and neutral defects, while the effect of SO phonons is more subtle. Our results also indicate that

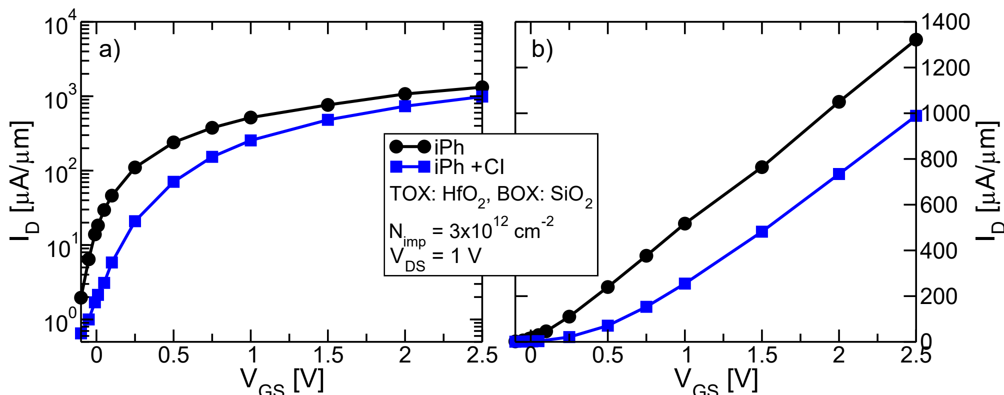

Figure 4.14: I_D versus V_{GS} characteristics of the device of Fig. 4.13 in a) logarithmic and b) linear scales simulated at $V_{DS} = 1$ V. Results obtained by including only scattering with intrinsic phonons (black circles) are compared to the ones obtained by considering also scattering with Coulomb centers (blue squares), when $N_{imp} = 3 \times 10^{12}$ cm^{-2}.

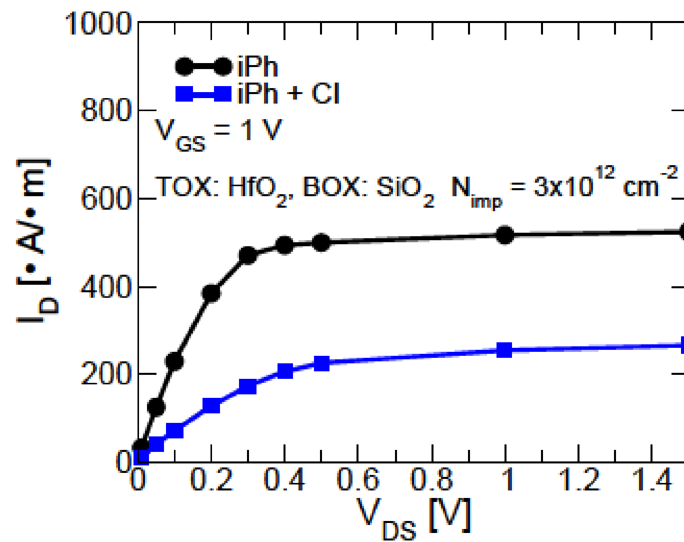

Figure 4.15: I_D versus V_{DS} characteristics of the device of Fig. 4.13 simulated at $V_{GS} = 1$ V. Results obtained by including only scattering with intrinsic phonons (black circles) are compared to the ones obtained by considering also scattering with Coulomb centers (blue squares), when $N_{imp} = 3 \times 10^{12}$ cm^{-2}.

accurate description of the screening of scattering with SO phonons is of great importance for the correct determination of the velocity vs. field curve of monolayer MoS_2.

Preliminary results for a short channel FET with MoS_2 as channel material have been obtained by coupling the Monte Carlo transport with the 2D Poisson equation. Due to the low mobility of MoS_2, a 100 nm FET behaves as a long channel device following the textbook theory of FET with velocity saturation.

Chapter 5

Conclusions

Although a number of different device concepts have been discussed in this thesis, the red thread linking the different topics of this thesis is given by the 2D materials. In chapter 2, we have studied the contact properties of graphene and monolayer MoS_2 with different metals. We have shown that Ni and Cu dope graphene significantly at minimum energy distance, but not at larger distances. In this respect, the experiments for Ni-G and Cu-G contacts report a large R_C (especially at $V_{BG} = 0$), thus suggesting $d > 0.5$ nm. This may be the result of wrinkles, roughness and/or impurities impacting the quality of the M-G interface. For the Au-G contact, a longer range interaction and considerable G doping are predicted for d up to 1 nm, explaining the lower experimental R_C compared to Ni-G and Cu-G.

Simulation results predicted a large R_C dependence on V_{BG} at $d > 0.4$ nm that seems in agreement with the experimental behavior, thus supporting the picture of a M-G with larger distance than the minimum one.

We have also showed that for a defect-free MoS_2 layer, the control of the metal-MoS_2 distance d is crucial in order to enable a modulation of the SBH, that can be further adjusted by an effective back-gating of the structure. This may be achieved by introducing a proper buffer layer such as graphene or h-BN between the metal and MoS_2. Moreover, by employing an in-house developed *ab-initio* transport methodology, several options for a metal contact to monolayer MoS_2 have been discussed. We have quantitatively analyzed the trade-off between SBH and TB in contacts with a buffer layer and confirmed by simulations the superior performance of the bismuth-MoS_2 n-type contact. We also showed that the Au-NbS_2-MoS_2 system provides a pathway to an Ohmic p-type contact. These results can be naturally extended to TMDs other than MoS_2.

In chapter 3, applications of 2D materials in various sensors have been discussed. First we have analyzed the sensing properties of monolayer MoS_2 for strain and temperature sensors. It was shown that monolayer MoS_2 exhibits a giant intrinsic Gauge factor of ~ 724. The origins of this piezoresistive effect are explained through a detailed analysis of several scattering models. This giant intrinsic piezoresistive can enable emerging applications in tactile sensing, like soft robotics, as well as improving the mobility (and electronic transport) in TMD electronics.

We have also demonstrated a large Temperature Coefficient of Resistance (TCR) in atomically thin 2D materials ($\sim 0.3\%$ K^{-1} at 300 K and $\sim 0.6\%$ K^{-1} at 100 K), significantly higher than that of metals in the sub-10 nm-thickness range. Simulations demonstrate that even larger TCRs (up to 0.45 % K^{-1} at 300 K and 2.5 % K^{-1} at 100 K) in monolayer 2D devices could be obtained by further reducing the density of charged impurities. These could enable fast temperature sensors with low thermal resistance and

thermal capacitance at the atomically thin limit.

We also investigated $Ti_3C_2T_x$ as an ammonia sensor by means of a first-principles study. The impacts of different ratios of surface termination groups were analyzed, as well as the presence of water molecules on ammonia gas sensing behavior of $Ti_3C_2T_x$. DFT calculations showed that at NH_3 adsorption sites, the Bader charge difference of nearest oxygen atoms was 60% to 180% larger than that of the nearest fluorine atoms, demonstrating a stronger interaction of NH_3 with the $Ti_3C_2T_x$-based sensor with a lower ratio of fluorine surface terminations.

In chapter 3 we have showed that the response of the humidity sensors demonstrated a linear relation towards varying Relative Humidity (RH) levels from 20% RH to 80 % RH, with a sensitivity and correlation coefficient of 0.22%/% RH and 0.98, respectively. The humidity sensors also showed a linear response towards varying temperatures from 20 °C to 90 °C, with a slope of -0.0032/°C and a correlation coefficient of 0.9948. The average TCR calculated for the sensors was approximately -0.3%/°C. Density functional theory calculations confirmed the hydrogen bonding between Fluorinate Graphene (FG) and water molecules and demonstrated the strong humidity sensing property of the FG. The obtained results suggest that FG, a highly stable derivative of graphene, is a potential material for humidity sensing applications.

Finally in chapter 4, by means of multi-valley Monte Carlo Transport simulator, uniform field transport in monolayer MoS_2 has been studied. We showed that at low electric field, our simulator has a good mutual agreement with the solver of the lineraized Boltzmann transport equation (discussed in Sec. 3.2). Monte Carlo simulations for high field transport in monolayer MoS_2 have also shown that a multi-valley non-parabolic description of the band structure is accurate and that our results match well the outcomes of more complex models, such as full band Monte Carlo transport simulations. Moreover, we have found that the electron's saturation velocity in monolayer MoS_2 is only slightly affected by scattering with Coulomb centers and neutral defects, while the effect of surface optical (SO) phonons is more subtle. Our results also indicate that accurate description of the screening of scattering with SO phonons is of great importance for the correct determination of the velocity versus field curve of monolayer MoS_2. These findings pave the way towards the development of a Monte Carlo simulator for MOSFETs using MoS_2 as a channel material.

The variety of prospective applications for 2D materials explored along this Ph.D. project shows that in coming years more research efforts will be able to harness new fruits from these materials, for new exciting opportunities in the nanoelectronic field.

Bibliography

[1] "International technology roadmap for semiconductor," http://www.itrs2.net/.

[2] A. K. Geim and K. S. Novoselov, "The rise of graphene," in *Nanoscience and technology: a collection of reviews from nature journals*. World Scientific, 2010, pp. 11–19.

[3] N. D. Mermin, "Crystalline order in two dimensions," *Physical Review*, vol. 176, no. 1, p. 250, 1968.

[4] K. S. Novoselov, D. Jiang, F. Schedin, T. Booth, V. Khotkevich, S. Morozov, and A. K. Geim, "Two-dimensional atomic crystals," *Proceedings of the National Academy of Sciences*, vol. 102, no. 30, pp. 10 451–10 453, 2005.

[5] J. Kang, W. Cao, X. Xie, D. Sarkar, W. Liu, and K. Banerjee, "Graphene and beyond-graphene 2D crystals for next-generation green electronics," in *Micro-and Nanotechnology Sensors, Systems, and Applications VI*, vol. 9083. International Society for Optics and Photonics, 2014, p. 908305.

[6] K. S. Novoselov, A. K. Geim, S. V. Morozov, D.-e. Jiang, Y. Zhang, S. V. Dubonos, I. V. Grigorieva, and A. A. Firsov, "Electric field effect in atomically thin carbon films," *science*, vol. 306, no. 5696, pp. 666–669, 2004.

[7] K. S. Novoselov, A. K. Geim, S. V. Morozov, D. Jiang, M. I. Katsnelson, I. Grigorieva, S. Dubonos, Firsov, and A. A, "Two-dimensional gas of massless Dirac fermions in graphene," *nature*, vol. 438, no. 7065, pp. 197–200, 2005.

[8] M. G. Ancona, "Electron transport in graphene from a diffusion-drift perspective," *IEEE Transactions on Electron Devices*, vol. 57, no. 3, pp. 681–689, 2010.

[9] S. Chen, A. L. Moore, W. Cai, J. W. Suk, J. An, C. Mishra, C. Amos, C. W. Magnuson, J. Kang, L. Shi *et al.*, "Raman measurements of thermal transport in suspended monolayer graphene of variable sizes in vacuum and gaseous environments," *ACS nano*, vol. 5, no. 1, pp. 321–328, 2011.

[10] K. I. Bolotin, K. J. Sikes, Z. Jiang, M. Klima, G. Fudenberg, J. Hone, P. Kim, and H. Stormer, "Ultrahigh electron mobility in suspended graphene," *Solid state communications*, vol. 146, no. 9-10, pp. 351–355, 2008.

[11] J.-H. Chen, C. Jang, S. Xiao, M. Ishigami, and M. S. Fuhrer, "Intrinsic and extrinsic performance limits of graphene devices on SiO_2," *Nature nanotechnology*, vol. 3, no. 4, pp. 206–209, 2008.

[12] S. Fratini and F. Guinea, "Substrate-limited electron dynamics in graphene," *Physical Review B*, vol. 77, no. 19, p. 195415, 2008.

[13] M. Bresciani, A. Paussa, P. Palestri, D. Esseni, and L. Selmi, "Low-field mobility and high-field drift velocity in graphene nanoribbons and graphene bilayers," in *2010 International Electron Devices Meeting*. IEEE, 2010, pp. 32–1.

[14] A. Konar, T. Fang, and D. Jena, "Effect of high-κ gate dielectrics on charge transport in graphene-based field effect transistors," *Physical Review B*, vol. 82, no. 11, p. 115452, 2010.

[15] R. Frindt, "Single crystals of MoS_2 several molecular layers thick," *Journal of Applied Physics*, vol. 37, no. 4, pp. 1928–1929, 1966.

[16] G. Fiori, F. Bonaccorso, G. Iannaccone, T. Palacios, D. Neumaier, A. Seabaugh, S. K. Banerjee, and L. Colombo, "Electronics based on two-dimensional materials," *Nature nanotechnology*, vol. 9, no. 10, pp. 768–779, 2014.

[17] R. Roldán, J. A. Silva-Guillén, M. P. López-Sancho, F. Guinea, E. Cappelluti, and P. Ordejón, "Electronic properties of single-layer and multilayer transition metal dichalcogenides MX2 (M= Mo, W and X= S, Se)," *Annalen der Physik*, vol. 526, no. 9-10, pp. 347–357, 2014.

[18] W. S. Yun, S. Han, S. C. Hong, I. G. Kim, and J. Lee, "Thickness and strain effects on electronic structures of transition metal dichalcogenides: 2H-M X 2 semiconductors (M= Mo, W; X= S, Se, Te)," *Physical Review B*, vol. 85, no. 3, p. 033305, 2012.

[19] A. I. Khan, P. Khakbaz, K. A. Brenner, K. K. Smithe, M. J. Mleczko, D. Esseni, and E. Pop, "Large temperature coefficient of resistance in atomically thin two-dimensional semiconductors," *Applied Physics Letters*, vol. 116, no. 20, p. 203105, 2020.

[20] M. Hosseini, M. Elahi, M. Pourfath, and D. Esseni, "Strain-Induced Modulation of Electron Mobility in Single-Layer Transition Metal Dichalcogenides MX2," *IEEE Transactions on Electron Devices*, vol. 62, no. 10, pp. 3192–3198, 2015.

[21] Anna Demming, "Can 2D materials contribute to consumer electronics?" https://physicsworld.com/a/can-2d-materials-contribute-to-consumer-electronics/.

[22] S. L. Wong, H. Liu, and D. Chi, "Recent progress in chemical vapor deposition growth of two-dimensional transition metal dichalcogenides," *Progress in Crystal Growth and Characterization of Materials*, vol. 62, no. 3, pp. 9–28, 2016.

[23] K. Novoselov, "Nobel lecture: Graphene: Materials in the flatland," *Reviews of modern physics*, vol. 83, no. 3, p. 837, 2011.

[24] A. Vanarse, A. Osseiran, and A. Rassau, "A review of current neuromorphic approaches for vision, auditory, and olfactory sensors," *Frontiers in neuroscience*, vol. 10, p. 115, 2016.

[25] Y. Omura, A. Mallik, and N. Matsuo, *MOS Devices for Low-voltage and Low-energy Applications*. John Wiley & Sons, 2017.

[26] J. Bardeen and W. Shockley, "Deformation potentials and mobilities in non-polar crystals," *Physical review*, vol. 80, no. 1, p. 72, 1950.

[27] C. S. Smith, "Piezoresistance effect in germanium and silicon," *Physical review*, vol. 94, no. 1, p. 42, 1954.

[28] S. E. Thompson, M. Armstrong, C. Auth, M. Alavi, M. Buehler, R. Chau, S. Cea, T. Ghani, G. Glass, T. Hoffman *et al.*, "A 90-nm logic technology featuring strained-silicon," *IEEE Transactions on electron devices*, vol. 51, no. 11, pp. 1790–1797, 2004.

[29] W. Mason and R. Thurston, "Use of piezoresistive materials in the measurement of displacement, force, and torque," *The Journal of the Acoustical Society of America*, vol. 29, no. 10, pp. 1096–1101, 1957.

[30] D. Rus and M. T. Tolley, "Design, fabrication and control of soft robots," *Nature*, vol. 521, no. 7553, pp. 467–475, 2015.

[31] A. Chortos, J. Liu, and Z. Bao, "Pursuing prosthetic electronic skin," *Nature materials*, vol. 15, no. 9, pp. 937–950, 2016.

[32] R. F. Potter, "Piezoresistance of Indium Antimonide," *Physical Review*, vol. 108, no. 3, p. 652, 1957.

[33] J. Hinckley and J. Singh, "Theoretical investigation of hole transport in strained III-V semiconductors: Application to GaAs," *Applied physics letters*, vol. 53, no. 9, pp. 785–787, 1988.

[34] S. D. Poisson, *TRAITÉ DE MÉCANIQUE.: TOME PREMIER.* Chez Mme veuve Courcier, Imprimeur-Libraire pour les Mathématiques, quai des ..., 1811, vol. 1.

[35] H. Rolnick, "Tension coefficient of resistance of metals," *Physical review*, vol. 36, no. 3, p. 506, 1930.

[36] D. J. Cohen, D. Mitra, K. Peterson, and M. M. Maharbiz, "A highly elastic, capacitive strain gauge based on percolating nanotube networks," *Nano letters*, vol. 12, no. 4, pp. 1821–1825, 2012.

[37] X. Li, R. Zhang, W. Yu, K. Wang, J. Wei, D. Wu, A. Cao, Z. Li, Y. Cheng, Q. Zheng *et al.*, "Stretchable and highly sensitive graphene-on-polymer strain sensors," *Scientific reports*, vol. 2, no. 1, pp. 1–6, 2012.

[38] R. He and P. Yang, "Giant piezoresistance effect in silicon nanowires," *Nature nanotechnology*, vol. 1, no. 1, pp. 42–46, 2006.

[39] Z. Shan, G. Adesso, A. Cabot, M. Sherburne, S. S. Asif, O. Warren, D. Chrzan, A. Minor, and A. Alivisatos, "Ultrahigh stress and strain in hierarchically structured hollow nanoparticles," *Nature materials*, vol. 7, no. 12, pp. 947–952, 2008.

[40] T. Yamada, Y. Hayamizu, Y. Yamamoto, Y. Yomogida, A. Izadi-Najafabadi, D. N. Futaba, and K. Hata, "A stretchable carbon nanotube strain sensor for human-motion detection," *Nature nanotechnology*, vol. 6, no. 5, pp. 296–301, 2011.

[41] D. Akinwande, N. Petrone, and J. Hone, "Two-dimensional flexible nanoelectronics," *Nature communications*, vol. 5, no. 1, pp. 1–12, 2014.

[42] M. K. Blees, A. W. Barnard, P. A. Rose, S. P. Roberts, K. L. McGill, P. Y. Huang, A. R. Ruyack, J. W. Kevek, B. Kobrin, D. A. Muller *et al.*, "Graphene kirigami," *Nature*, vol. 524, no. 7564, pp. 204–207, 2015.

[43] Z. Liu, M. Amani, S. Najmaei, Q. Xu, X. Zou, W. Zhou, T. Yu, C. Qiu, A. G. Birdwell, F. J. Crowne *et al.*, "Strain and structure heterogeneity in MoS_2 atomic layers grown by chemical vapour deposition," *Nature communications*, vol. 5, no. 1, pp. 1–9, 2014.

[44] X. Hu, P. Yasaei, J. Jokisaari, S. Öğüt, A. Salehi-Khojin, and R. F. Klie, "Mapping thermal expansion coefficients in freestanding 2D materials at the nanometer scale," *Physical review letters*, vol. 120, no. 5, p. 055902, 2018.

[45] A. Grifiith, "The phenomena of rupture and flow in solids," *Philosophical Transactions of the Royal Society of London*, vol. 221, pp. 163–198, 1921.

[46] C. Lee, X. Wei, J. W. Kysar, and J. Hone, "Measurement of the elastic properties and intrinsic strength of monolayer graphene," *science*, vol. 321, no. 5887, pp. 385–388, 2008.

[47] S. Bertolazzi, J. Brivio, and A. Kis, "Stretching and breaking of ultrathin MoS_2," *ACS nano*, vol. 5, no. 12, pp. 9703–9709, 2011.

[48] C. D. Brites, P. P. Lima, N. J. Silva, A. Millán, V. S. Amaral, F. Palacio, and L. D. Carlos, "Thermometry at the nanoscale," *Nanoscale*, vol. 4, no. 16, pp. 4799–4829, 2012.

[49] D. Estrada, Z. Li, G.-M. Choi, S. N. Dunham, A. Serov, J. Lee, Y. Meng, F. Lian, N. C. Wang, A. Perez *et al.*, "Thermal transport in layer-by-layer assembled polycrystalline graphene films," *npj 2D Materials and Applications*, vol. 3, no. 1, pp. 1–7, 2019.

[50] C. L. Everhart, K. E. Kaplan, M. M. Winterkorn, H. Kwon, J. Provine, M. Asheghi, K. E. Goodson, F. B. Prinz, and T. W. Kenny, "High stability thermal accelerometer based on ultrathin platinum ALD nanostructures," in *2018 IEEE Micro Electro Mechanical Systems (MEMS).* IEEE, 2018, pp. 976–979.

[51] F. Mailly, A. Giani, A. Martinez, R. Bonnot, P. Temple-Boyer, and A. Boyer, "Micromachined thermal accelerometer," *Sensors and Actuators A: Physical*, vol. 103, no. 3, pp. 359–363, 2003.

[52] F. Purkl, T. S. English, G. Yama, J. Provine, A. K. Samarao, A. Feyh, B. Kim, G. O'Brien, O. Ambacher, R. T. Howe *et al.*, "Serpentine geometry for enhanced performance of nanometer-thin platinum bolometers," in *2013 Transducers & Eurosensors XXVII: The 17th International Conference on Solid-State Sensors, Actuators and Microsystems (TRANSDUCERS & EUROSENSORS XXVII).* IEEE, 2013, pp. 1507–1510.

[53] A. Vassighi and M. Sachdev, "Thermal runaway in integrated circuits," *IEEE Transactions on Device and Materials Reliability*, vol. 6, no. 2, pp. 300–305, 2006.

[54] B. Zhang, Y. Ding, Z. Chen, and C. Lin, "Random optical bipolar pulses," *Applied Physics Letters*, vol. 104, no. 19, p. 194105, 2014.

[55] M. Malits, I. Brouk, and Y. Nemirovsky, "Study of CMOS-SOI integrated temperature sensing circuits for on-chip temperature monitoring," *Sensors*, vol. 18, no. 5, p. 1629, 2018.

[56] G. Meijer, *Smart sensor systems.* John Wiley & Sons, 2008.

[57] R. Mukherjee, J. Basu, P. Mandal, and P. K. Guha, "A review of micromachined thermal accelerometers," *Journal of Micromechanics and Microengineering*, vol. 27, no. 12, p. 123002, 2017.

[58] S.-K. Nam, J.-K. Kim, S.-C. Cho, and S.-K. Lee, "Design and characterization of a high resolution microfluidic heat flux sensor with thermal modulation," *Sensors*, vol. 10, no. 7, pp. 6594–6611, 2010.

[59] R. C. Webb, A. P. Bonifas, A. Behnaz, Y. Zhang, K. J. Yu, H. Cheng, M. Shi, Z. Bian, Z. Liu, Y.-S. Kim *et al.*, "Ultrathin conformal devices for precise and continuous thermal characterization of human skin," *Nature materials*, vol. 12, no. 10, pp. 938–944, 2013.

[60] C. H. Sharma, A. P. Surendran, A. Varghese, and M. Thalakulam, "Stable and scalable 1t MoS_2 with low temperature-coefficient of resistance," *Scientific reports*, vol. 8, no. 1, pp. 1–9, 2018.

[61] W. Tsujita, A. Yoshino, H. Ishida, and T. Moriizumi, "Gas sensor network for air-pollution monitoring," *Sensors and Actuators B: Chemical*, vol. 110, no. 2, pp. 304–311, 2005.

[62] S. Ryabtsev, A. Shaposhnick, A. Lukin, and E. Domashevskaya, "Application of semiconductor gas sensors for medical diagnostics," *Sensors and Actuators B: Chemical*, vol. 59, no. 1, pp. 26–29, 1999.

[63] N. Funazaki, A. Hemmi, S. Ito, Y. Asano, Y. Yano, N. Miura, and N. Yamazoe, "Application of semiconductor gas sensor to quality control of meat freshness in food industry," *Sensors and Actuators B: Chemical*, vol. 25, no. 1-3, pp. 797–800, 1995.

[64] S. Emamian, A. Eshkeiti, B. B. Narakathu, S. G. R. Avuthu, and M. Z. Atashbar, "Gravure printed flexible surface enhanced Raman spectroscopy (SERS) substrate for detection of 2, 4-dinitrotoluene (DNT) vapor," *Sensors and Actuators B: Chemical*, vol. 217, pp. 129–135, 2015.

[65] R. Gangopadhyay and A. De, "Conducting polymer composites: novel materials for gas sensing," *Sensors and Actuators B: Chemical*, vol. 77, no. 1-2, pp. 326–329, 2001.

[66] M. Z. Atashbar, B. E. Bejcek, and S. Singamaneni, "Carbon nanotube network-based biomolecule detection," *IEEE Sensors Journal*, vol. 6, no. 3, pp. 524–528, 2006.

[67] M. Z. Atashbar, B. Bejcek, S. Singamaneni, and S. Santucci, "Carbon nanotube based biosensors," in *SENSORS, 2004 IEEE.* IEEE, 2004, pp. 1048–1051.

[68] F. Schedin, A. K. Geim, S. V. Morozov, E. Hill, P. Blake, M. Katsnelson, and K. S. Novoselov, "Detection of individual gas molecules adsorbed on graphene," *Nature materials*, vol. 6, no. 9, pp. 652–655, 2007.

[69] S. Achmann, G. Hagen, J. Kita, I. M. Malkowsky, C. Kiener, and R. Moos, "Metal-organic frameworks for sensing applications in the gas phase," *Sensors*, vol. 9, no. 3, pp. 1574–1589, 2009.

[70] W. Yang, L. Gan, H. Li, and T. Zhai, "Two-dimensional layered nanomaterials for gas-sensing applications," *Inorganic Chemistry Frontiers*, vol. 3, no. 4, pp. 433–451, 2016.

[71] L. Zhang, K. Khan, J. Zou, H. Zhang, and Y. Li, "Recent advances in emerging 2D material-based gas sensors: Potential in disease diagnosis," *Advanced Materials Interfaces*, vol. 6, no. 22, p. 1901329, 2019.

[72] J. Chen, K. Chen, D. Tong, Y. Huang, J. Zhang, J. Xue, Q. Huang, and T. Chen, "CO_2 and temperature dual responsive "Smart" MXene phases," *Chemical Communications*, vol. 51, no. 2, pp. 314–317, 2015.

[73] B. Xu, M. Zhu, W. Zhang, X. Zhen, Z. Pei, Q. Xue, C. Zhi, and P. Shi, "Ultra-thin MXene-micropattern-based field-effect transistor for probing neural activity," *Advanced Materials*, vol. 28, no. 17, pp. 3333–3339, 2016.

[74] N. Li, X. Chen, W.-J. Ong, D. R. MacFarlane, X. Zhao, A. K. Cheetham, and C. Sun, "Understanding of electrochemical mechanisms for CO_2 capture and conversion into hydrocarbon fuels in transition-metal carbides (MXenes)," *Acs Nano*, vol. 11, no. 11, pp. 10 825–10 833, 2017.

[75] L. M. Azofra, N. Li, D. R. MacFarlane, and C. Sun, "Promising prospects for 2D d^2-$d^4M_3C_2$ transition metal carbides (MXenes) in N_2 capture and conversion into ammonia," *Energy & Environmental Science*, vol. 9, no. 8, pp. 2545–2549, 2016.

[76] C. E. Ren, M.-Q. Zhao, T. Makaryan, J. Halim, M. Boota, S. Kota, B. Anasori, M. W. Barsoum, and Y. Gogotsi, "Porous two-dimensional transition metal carbide (MXene) flakes for high-performance Li-ion storage," *ChemElectroChem*, vol. 3, no. 5, pp. 689–693, 2016.

[77] B. Anasori, M. R. Lukatskaya, and Y. Gogotsi, "2D metal carbides and nitrides (MXenes) for energy storage," *Nature Reviews Materials*, vol. 2, no. 2, pp. 1–17, 2017.

[78] Z. W. Seh, K. D. Fredrickson, B. Anasori, J. Kibsgaard, A. L. Strickler, M. R. Lukatskaya, Y. Gogotsi, T. F. Jaramillo, and A. Vojvodic, "Two-dimensional molybdenum carbide (MXene) as an efficient electrocatalyst for hydrogen evolution," *ACS Energy Letters*, vol. 1, no. 3, pp. 589–594, 2016.

[79] Q. Zhang, J. Teng, G. Zou, Q. Peng, Q. Du, T. Jiao, and J. Xiang, "Efficient phosphate sequestration for water purification by unique sandwich-like mxene/magnetic iron oxide nanocomposites," *Nanoscale*, vol. 8, no. 13, pp. 7085–7093, 2016.

[80] W. Yuan and G. Shi, "Graphene-based gas sensors," *Journal of Materials Chemistry A*, vol. 1, no. 35, pp. 10 078–10 091, 2013.

[81] A. Allain, J. Kang, K. Banerjee, and A. Kis, "Electrical contacts to two-dimensional semiconductors," *Nature materials*, vol. 14, no. 12, pp. 1195–1205, 2015.

[82] S. Das, H.-Y. Chen, A. V. Penumatcha, and J. Appenzeller, "High performance multilayer MoS_2 transistors with scandium contacts," *Nano letters*, vol. 13, no. 1, pp. 100–105, 2013.

[83] H. Liu, A. T. Neal, and P. D. Ye, "Channel length scaling of MoS_2 MOSFETs," *ACS nano*, vol. 6, no. 10, pp. 8563–8569, 2012.

[84] P. Khakbaz, F. Driussi, P. Giannozzi, A. Gambi, and D. Esseni, "Simulation study of Fermi level depinning in metal-MoS_2 contacts," *Solid-State Electronics*, p. 108039, 2021.

[85] P.-C. Shen, C. Su, Y. Lin, A.-S. Chou, C.-C. Cheng, J.-H. Park, M.-H. Chiu, A.-Y. Lu, H.-L. Tang, M. M. Tavakoli *et al.*, "Ultralow contact resistance between semimetal and monolayer semiconductors," *Nature*, vol. 593, no. 7858, pp. 211–217, 2021.

[86] R. T. Tung, "The physics and chemistry of the Schottky barrier height," *Applied Physics Reviews*, vol. 1, no. 1, p. 011304, 2014.

[87] S. M. Sze, Y. Li, and K. K. Ng, *Physics of semiconductor devices.* John wiley & sons, 2021.

[88] R. L. Anderson, "Experiments on ge-GaAs heterojunctions," in *Electronic Structure of Semiconductor Heterojunctions.* Springer, 1988, pp. 35–48.

[89] J. Waldrop, "Schottky-barrier height of ideal metal contacts to GaAs," *Applied physics letters*, vol. 44, no. 10, pp. 1002–1004, 1984.

[90] C. Kim, I. Moon, D. Lee, M. S. Choi, F. Ahmed, S. Nam, Y. Cho, H.-J. Shin, S. Park, and W. J. Yoo, "Fermi level pinning at electrical metal contacts of monolayer molybdenum dichalcogenides," *ACS nano*, vol. 11, no. 2, pp. 1588–1596, 2017.

[91] M. Farmanbar and G. Brocks, "First-principles study of van der Waals interactions and lattice mismatch at MoS_2/metal interfaces," *Physical Review B*, vol. 93, no. 8, p. 085304, 2016.

[92] J. Kang, W. Liu, D. Sarkar, D. Jena, and K. Banerjee, "Computational study of metal contacts to monolayer transition-metal dichalcogenide semiconductors," *Physical Review X*, vol. 4, no. 3, p. 031005, 2014.

[93] J. Robertson, "Band offsets, Schottky barrier heights, and their effects on electronic devices," *Journal of Vacuum Science & Technology A: Vacuum, Surfaces, and Films*, vol. 31, no. 5, p. 050821, 2013.

[94] R.-S. Chen, G.-L. Ding, Y. Zhou, and S.-T. Han, "Fermi Level Depinning of 2D Transition Metal Dichalcogenides Transistors," *Journal of Materials Chemistry C*, 2021.

[95] V. Heine, "Theory of surface states," *Physical Review*, vol. 138, no. 6A, p. A1689, 1965.

[96] W. Mönch, "Metal-semiconductor contacts: electronic properties," *Surface science*, vol. 299, pp. 928–944, 1994.

[97] K. Sotthewes, R. Van Bremen, E. Dollekamp, T. Boulogne, K. Nowakowski, D. Kas, H. J. Zandvliet, and P. Bampoulis, "Universal Fermi-level pinning in transition-metal dichalcogenides," *The Journal of Physical Chemistry C*, vol. 123, no. 9, pp. 5411–5420, 2019.

[98] P. Bampoulis, R. van Bremen, Q. Yao, B. Poelsema, H. J. Zandvliet, and K. Sotthewes, "Defect dominated charge transport and Fermi-level pinning in MoS_2/metal contacts," *ACS applied materials & interfaces*, vol. 9, no. 22, pp. 19 278–19 286, 2017.

[99] J. R. D. Retamal, D. Periyanagounder, J.-J. Ke, M.-L. Tsai, and J.-H. He, "Charge carrier injection and transport engineering in two-dimensional transition metal dichalcogenides," *Chemical science*, vol. 9, no. 40, pp. 7727–7745, 2018.

[100] P. Hohenberg and W. Kohn, "Inhomogeneous electron gas," *Physical review*, vol. 136, no. 3B, p. B864, 1964.

[101] W. Kohn and L. J. Sham, "Self-consistent equations including exchange and correlation effects," *Physical review*, vol. 140, no. 4A, p. A1133, 1965.

[102] H.-P. Komsa and A. V. Krasheninnikov, "Electronic structures and optical properties of realistic transition metal dichalcogenide heterostructures from first principles," *Physical Review B*, vol. 88, no. 8, p. 085318, 2013.

[103] M. Bokdam, G. Brocks, M. I. Katsnelson, and P. J. Kelly, "Schottky barriers at hexagonal boron nitride/metal interfaces: A first-principles study," *Physical Review B*, vol. 90, no. 8, p. 085415, 2014.

[104] W. Ku, T. Berlijn, C.-C. Lee *et al.*, "Unfolding first-principles band structures," *Physical review letters*, vol. 104, no. 21, p. 216401, 2010.

[105] M. Pala, P. Giannozzi, and D. Esseni, "Unit cell restricted Bloch functions basis for first-principle transport models: Theory and application," *Physical Review B*, vol. 102, no. 4, p. 045410, 2020.

[106] M. G. Pala and D. Esseni, "Full-band quantum simulation of electron devices with the pseudopotential method: Theory, implementation, and applications," *Physical Review B*, vol. 97, no. 12, p. 125310, 2018.

[107] P. Khomyakov, G. Giovannetti, P. Rusu, G. v. Brocks, J. Van den Brink, and P. J. Kelly, "First-principles study of the interaction and charge transfer between graphene and metals," *Physical Review B*, vol. 79, no. 19, p. 195425, 2009.

[108] P. Giannozzi, O. Andreussi, T. Brumme, O. Bunau, M. B. Nardelli, M. Calandra, R. Car, C. Cavazzoni, D. Ceresoli, M. Cococcioni *et al.*, "Advanced capabilities for materials modelling with Quantum ESPRESSO," *Journal of physics: Condensed matter*, vol. 29, no. 46, p. 465901, 2017.

[109] F. Driussi, S. Venica, A. Gahoi, A. Gambi, P. Giannozzi, S. Kataria, M. Lemme, P. Palestri, and D. Esseni, "Improved understanding of metal–graphene contacts," *Microelectronic Engineering*, vol. 216, p. 111035, 2019.

[110] P. Khakbaz, F. Driussi, A. Gambi, P. Giannozzi, S. Venica, D. Esseni, A. Gaho, S. Kataria, and M. Lemme, “DFT study of graphene doping due to metal contacts,” in *2019 International Conference on Simulation of Semiconductor Processes and Devices (SISPAD)*. IEEE, 2019, pp. 1–4.

[111] T. Brumme, M. Calandra, and F. Mauri, “Electrochemical doping of few-layer ZrNCl from first principles: Electronic and structural properties in field-effect configuration,” *Physical Review B*, vol. 89, no. 24, p. 245406, 2014.

[112] H. Zhong, R. Quhe, Y. Wang, Z. Ni, M. Ye, Z. Song, Y. Pan, J. Yang, L. Yang, M. Lei *et al.*, “Interfacial properties of monolayer and bilayer MoS_2 contacts with metals: beyond the energy band calculations,” *Scientific reports*, vol. 6, no. 1, pp. 1–16, 2016.

[113] S. Venica, F. Driussi, A. Gahoi, S. Kataria, P. Palestri, M. C. Lemme, and L. Selmi, “Reliability analysis of the metal–graphene contact resistance extracted by the Transfer Length Method,” *Proceedings of ICMTS*, pp. 57–62, 2018.

[114] A. Gahoi, S. Wagner, A. Bablich, S. Kataria, V. Passi, and M. C. Lemme, “Contact resistance study of various metal electrodes with CVD graphene,” *Solid-State Electronics*, vol. 125, pp. 234–239, 2016.

[115] S. Venica, F. Driussi, A. Gahoi, V. Passi, P. Palestri, M. C. Lemme, and L. Selmi, “Detailed characterization and critical discussion of series resistance in graphene–metal contacts,” *Proceedings of ICMTS*, pp. 27–31, 2017.

[116] S. Venica, F. Driussi, A. Gahoi, P. Palestri, M. C. Lemme, and L. Selmi, “On the adequacy of the Transmission Line Model to describe the graphene–metal contact resistance,” *IEEE Transactions on Electron Devices*, vol. 65, no. 4, pp. 1589–1596, 2018.

[117] J. Gebhardt, F. Viñes, and A. Görling, “Influence of the surface dipole layer and pauli repulsion on band energies and doping in graphene adsorbed on metal surfaces,” *Physical Review B*, vol. 86, no. 19, p. 195431, 2012.

[118] G. Henkelman, A. Arnaldsson, and H. Jónsson, “A fast and robust algorithm for Bader decomposition of charge density,” *Computational Materials Science*, vol. 36, no. 3, pp. 354–360, 2006.

[119] R. F. Bader, “Atoms in molecules,” *Accounts of Chemical Research*, vol. 18, no. 1, pp. 9–15, 1985.

[120] B. Radisavljevic, A. Radenovic, J. Brivio, V. Giacometti, and A. Kis, “Single-layer MoS_2 transistors,” *Nature nanotechnology*, vol. 6, no. 3, pp. 147–150, 2011.

[121] J. Choukroun, M. Pala, S. Fang, E. Kaxiras, and P. Dollfus, “High performance tunnel field effect transistors based on in-plane transition metal dichalcogenide heterojunctions,” *Nanotechnology*, vol. 30, no. 2, p. 025201, 2018.

[122] D. Logoteta, M. G. Pala, J. Choukroun, P. Dollfus, and G. Iannaccone, “A steep-slope mos 2-nanoribbon mosfet based on an intrinsic cold-contact effect,” *IEEE Electron Device Letters*, vol. 40, no. 9, pp. 1550–1553, 2019.

[123] G. Iannaccone, F. Bonaccorso, L. Colombo, and G. Fiori, "Quantum engineering of transistors based on 2D materials heterostructures," *Nature nanotechnology*, vol. 13, no. 3, pp. 183–191, 2018.

[124] "International Roadmap for Devices and Systems," https://irds.ieee.org/.

[125] M. Farmanbar and G. Brocks, "Ohmic contacts to 2D semiconductors through van der Waals bonding," *Advanced electronic materials*, vol. 2, no. 4, p. 1500405, 2016.

[126] G.-S. Kim, S.-H. Kim, J. Park, K. H. Han, J. Kim, and H.-Y. Yu, "Schottky barrier height engineering for electrical contacts of multilayered MoS_2 transistors with reduction of metal-induced gap states," *ACS nano*, vol. 12, no. 6, pp. 6292–6300, 2018.

[127] N. Kaushik, D. Karmakar, A. Nipane, S. Karande, and S. Lodha, "Interfacial n-doping using an ultrathin TiO_2 layer for contact resistance reduction in MoS_2," *ACS applied materials & interfaces*, vol. 8, no. 1, pp. 256–263, 2016.

[128] P. Khakbaz, M. Moshayedi, S. Hajian, M. Soleimani, B. B. Narakathu, B. J. Bazuin, M. Pourfath, and M. Z. Atashbar, "Titanium carbide MXene as NH_3 sensor: realistic first-principles study," *The Journal of Physical Chemistry C*, vol. 123, no. 49, pp. 29 794–29 803, 2019.

[129] S. Hajian, P. Khakbaz, M. Moshayedi, D. Maddipatla, B. B. Narakathu, V. S. Turkani, B. J. Bazuin, M. Pourfath, and M. Z. Atashbar, "Impact of different ratios of fluorine, oxygen, and hydroxyl surface terminations on $Ti_3C_2T_x$ mxene as ammonia sensor: A first-principles study," in *2018 IEEE SENSORS*. IEEE, 2018, pp. 1–4.

[130] S. Hajian, X. Zhang, D. Maddipatla, B. Narakathu, A. Hanson, R. Blair, and M. Atashbar, "Development of a fluorinated graphene-based flexible humidity sensor," in *2019 IEEE International Conference on Flexible and Printable Sensors and Systems (FLEPS)*. IEEE, 2019, pp. 1–3.

[131] G. Comparone, P. Palestri, D. Esseni, L. Lucci, and L. Selmi, "A better understanding of the requirements for predictive modeling of strain engineering in nMOS transistors," *Journal of Computational and Theoretical Nanoscience*, vol. 5, no. 6, pp. 1106–1114, 2008.

[132] C. Jungemann, N. Subba, J.-S. Goo, C. Riccobene, Q. Xiang, and B. Meinerzhagen, "Investigation of strained Si/SiGe devices by MC simulation," *Solid-State Electronics*, vol. 48, no. 8, pp. 1417–1422, 2004.

[133] Q. Xiang, J.-S. Goo, J. Pan, B. Yu, S. Ahmed, J. Zhang, and M.-R. Lin, "Strained silicon NMOS with nickel-silicide metal gate," in *2003 Symposium on VLSI Technology. Digest of Technical Papers (IEEE Cat. No. 03CH37407)*. IEEE, 2003, pp. 101–102.

[134] A. Paussa, "Numerical simulation of advanced CMOS and beyond CMOS nanoscale transistors," 2013.

[135] D. Esseni, P. Palestri, and L. Selmi, *Nanoscale MOS transistors: semi-classical transport and applications*. Cambridge University Press, 2011.

[136] A. Paussa and D. Esseni, "An exact solution of the linearized Boltzmann transport equation and its application to mobility calculations in graphene bilayers," *Journal of Applied Physics*, vol. 113, no. 9, p. 093702, 2013.

[137] M. Hosseini, M. Elahi, M. Pourfath, and D. Esseni, "Strain induced mobility modulation in single-layer MoS_2," *Journal of Physics D: Applied Physics*, vol. 48, no. 37, p. 375104, 2015.

[138] K. Kaasbjerg, K. S. Thygesen, and K. W. Jacobsen, "Phonon-limited mobility in n-type single-layer MoS_2 from first principles," *Physical Review B*, vol. 85, no. 11, p. 115317, 2012.

[139] X. Li, J. T. Mullen, Z. Jin, K. M. Borysenko, M. B. Nardelli, and K. W. Kim, "Intrinsic electrical transport properties of monolayer silicene and MoS_2 from first principles," *Physical Review B*, vol. 87, no. 11, p. 115418, 2013.

[140] Z.-Y. Ong and M. V. Fischetti, "Theory of remote phonon scattering in top-gated single-layer graphene," *Physical Review B*, vol. 88, no. 4, p. 045405, 2013.

[141] M. V. Fischetti, D. A. Neumayer, and E. A. Cartier, "Effective electron mobility in Si inversion layers in metal-oxide-semiconductor systems with a high-k insulator: The role of remote phonon scattering," *Journal of Applied Physics*, vol. 90, no. 9, pp. 4587–4608, 2001.

[142] W. Zhou, X. Zou, S. Najmaei, Z. Liu, Y. Shi, J. Kong, J. Lou, P. M. Ajayan, B. I. Yakobson, and J.-C. Idrobo, "Intrinsic structural defects in monolayer molybdenum disulfide," *Nano letters*, vol. 13, no. 6, pp. 2615–2622, 2013.

[143] C. González, B. Biel, and Y. J. Dappe, "Theoretical characterisation of point defects on a MoS_2 monolayer by scanning tunnelling microscopy," *Nanotechnology*, vol. 27, no. 10, p. 105702, 2016.

[144] J. Harrison and J. Hauser, "Alloy scattering in ternary iii-v compounds," *Physical Review B*, vol. 13, no. 12, p. 5347, 1976.

[145] N. J. Couto, D. Costanzo, S. Engels, D.-K. Ki, K. Watanabe, T. Taniguchi, C. Stampfer, F. Guinea, and A. F. Morpurgo, "Random strain fluctuations as dominant disorder source for high-quality on-substrate graphene devices," *Physical Review X*, vol. 4, no. 4, p. 041019, 2014.

[146] M. Hosseini, M. Elahi, M. Pourfath, and D. Esseni, "Very large strain gauges based on single layer $MoSe_2$ and WSe_2 for sensing applications," *Applied Physics Letters*, vol. 107, no. 25, p. 253503, 2015.

[147] M. Chhowalla, H. S. Shin, G. Eda, L.-J. Li, K. P. Loh, and H. Zhang, "The chemistry of two-dimensional layered transition metal dichalcogenide nanosheets," *Nature chemistry*, vol. 5, no. 4, pp. 263–275, 2013.

[148] Z. Jin, X. Li, J. T. Mullen, and K. W. Kim, "Intrinsic transport properties of electrons and holes in monolayer transition-metal dichalcogenides," *Physical Review B*, vol. 90, no. 4, p. 045422, 2014.

[149] P. Johari and V. B. Shenoy, "Tuning the electronic properties of semiconducting transition metal dichalcogenides by applying mechanical strains," *ACS nano*, vol. 6, no. 6, pp. 5449–5456, 2012.

[150] H. J. Conley, B. Wang, J. I. Ziegler, R. F. Haglund Jr, S. T. Pantelides, and K. I. Bolotin, "Bandgap engineering of strained monolayer and bilayer MoS_2," *Nano letters*, vol. 13, no. 8, pp. 3626–3630, 2013.

[151] S. Manzeli, A. Allain, A. Ghadimi, and A. Kis, "Piezoresistivity and strain-induced band gap tuning in atomically thin MoS_2," *Nano letters*, vol. 15, no. 8, pp. 5330–5335, 2015.

[152] C. Stampfer, A. Jungen, R. Linderman, D. Obergfell, S. Roth, and C. Hierold, "Nano-electromechanical displacement sensing based on single-walled carbon nanotubes," *Nano letters*, vol. 6, no. 7, pp. 1449–1453, 2006.

[153] M. Park, Y. J. Park, X. Chen, Y.-K. Park, M.-S. Kim, and J.-H. Ahn, "MoS_2-based tactile sensor for electronic skin applications," *Advanced Materials*, vol. 28, no. 13, pp. 2556–2562, 2016.

[154] H. Berger, "Models for contacts to planar devices," *Solid-state electronics*, vol. 15, no. 2, pp. 145–158, 1972.

[155] K. K. Smithe, S. V. Suryavanshi, M. Munnoz Rojo, A. D. Tedjarati, and E. Pop, "Low variability in synthetic monolayer MoS_2 devices," *ACS nano*, vol. 11, no. 8, pp. 8456–8463, 2017.

[156] J. Verble and T. Wieting, "Lattice mode degeneracy in MoS_2 and other layer compounds," *Physical review letters*, vol. 25, no. 6, p. 362, 1970.

[157] C. Lee, H. Yan, L. E. Brus, T. F. Heinz, J. Hone, and S. Ryu, "Anomalous lattice vibrations of single-and few-layer MoS_2," *ACS nano*, vol. 4, no. 5, pp. 2695–2700, 2010.

[158] C. Rice, R. Young, R. Zan, U. Bangert, D. Wolverson, T. Georgiou, R. Jalil, and K. Novoselov, "Raman-scattering measurements and first-principles calculations of strain-induced phonon shifts in monolayer MoS_2," *Physical Review B*, vol. 87, no. 8, p. 081307, 2013.

[159] C. Neumann, S. Reichardt, P. Venezuela, M. Drögeler, L. Banszerus, M. Schmitz, K. Watanabe, T. Taniguchi, F. Mauri, B. Beschoten *et al.*, "Raman spectroscopy as probe of nanometre-scale strain variations in graphene," *Nature communications*, vol. 6, no. 1, pp. 1–7, 2015.

[160] J.-H. Chen, C. Jang, S. Adam, M. Fuhrer, E. D. Williams, and M. Ishigami, "Charged-impurity scattering in graphene," *Nature physics*, vol. 4, no. 5, pp. 377–381, 2008.

[161] H. J. K. Kim, K. E. Kaplan, P. Schindler, S. Xu, M. M. Winterkorn, D. B. Heinz, T. S. English, J. Provine, F. B. Prinz, and T. W. Kenny, "Electrical properties of ultrathin platinum films by plasma-enhanced atomic layer deposition," *ACS applied materials & interfaces*, vol. 11, no. 9, pp. 9594–9599, 2019.

[162] H. Van Bui, A. Y. Kovalgin, J. Schmitz, and R. A. Wolters, "Conduction and electric field effect in ultra-thin TiN films," *Applied physics letters*, vol. 103, no. 5, p. 051904, 2013.

[163] J. Plombon, E. Andideh, V. M. Dubin, and J. Maiz, "Influence of phonon, geometry, impurity, and grain size on copper line resistivity," *Applied physics letters*, vol. 89, no. 11, p. 113124, 2006.

[164] K. K. Smithe, C. D. English, S. V. Suryavanshi, and E. Pop, "High-field transport and velocity saturation in synthetic monolayer MoS_2," *Nano letters*, vol. 18, no. 7, pp. 4516–4522, 2018.

[165] M. J. Mleczko, A. C. Yu, C. M. Smyth, V. Chen, Y. C. Shin, S. Chatterjee, Y.-C. Tsai, Y. Nishi, R. M. Wallace, and E. Pop, "Contact engineering high-performance n-type $MoTe_2$ transistors," *Nano letters*, vol. 19, no. 9, pp. 6352–6362, 2019.

[166] A. Ortiz-Conde, F. G. Sánchez, J. J. Liou, A. Cerdeira, M. Estrada, and Y. Yue, "A review of recent MOSFET threshold voltage extraction methods," *Microelectronics reliability*, vol. 42, no. 4-5, pp. 583–596, 2002.

[167] B. Chamlagain, Q. Li, N. J. Ghimire, H.-J. Chuang, M. M. Perera, H. Tu, Y. Xu, M. Pan, D. Xaio, J. Yan *et al.*, "Mobility improvement and temperature dependence in $MoSe_2$ field-effect transistors on parylene-C substrate," *ACS nano*, vol. 8, no. 5, pp. 5079–5088, 2014.

[168] H. Ji, G. Lee, M.-K. Joo, Y. Yun, H. Yi, J.-H. Park, D. Suh, and S. C. Lim, "Thickness-dependent carrier mobility of ambipolar mote2: Interplay between interface trap and Coulomb scattering," *Applied Physics Letters*, vol. 110, no. 18, p. 183501, 2017.

[169] R. Suri, A. Thakoor, and K. Chopra, "Electron transport properties of thin copper films. i." *Journal of Applied Physics*, vol. 46, no. 6, pp. 2574–2582, 1975.

[170] W. F. Leonard and R. Ramey, "Temperature coefficient of resistance in thin metal films," *Journal of Applied Physics*, vol. 37, no. 9, pp. 3634–3635, 1966.

[171] J. De Vries, "Temperature and thickness dependence of the resistivity of thin polycrystalline aluminium, cobalt, nickel, palladium, silver and gold films," *Thin Solid Films*, vol. 167, no. 1-2, pp. 25–32, 1988.

[172] S. Shivaprasad and M. Angadi, "Temperature coefficient of resistance of thin palladium films," *Journal of Physics D: Applied Physics*, vol. 13, no. 9, p. L171, 1980.

[173] M. M. Rojo, Z. Li, C. Sievers, A. C. Bornstein, E. Yalon, S. Deshmukh, S. Vaziri, M.-H. Bae, F. Xiong, D. Donadio *et al.*, "Thermal transport across graphene step junctions," *2D Materials*, vol. 6, no. 1, p. 011005, 2018.

[174] R. B. Belser and W. H. Hicklin, "Temperature coefficients of resistance of metallic films in the temperature range 25 to 600 c," *Journal of Applied Physics*, vol. 30, no. 3, pp. 313–322, 1959.

[175] H. Marom and M. Eizenberg, "The temperature dependence of resistivity in thin metal films," *Journal of applied physics*, vol. 96, no. 6, pp. 3319–3323, 2004.

[176] F. Warkusz, “The size effect and the temperature coefficient of resistance in thin films,” *Journal of Physics D: Applied Physics*, vol. 11, no. 5, p. 689, 1978.

[177] K. Choprat and L. Bobb, “Electrical resistivity studies on polycrystalline and epitaxially grown gold films,” *Acta Metallurgica*, vol. 12, no. 7, pp. 807–811, 1964.

[178] A. Kumar, G. Chandra, and O. Katyal, “The study of temperature coefficient of resistivity of polycrystalline metal films,” *Journal of materials science*, vol. 23, no. 7, pp. 2361–2364, 1988.

[179] A. Singh, “Film thickness and grain size diameter dependence on temperature coefficient of resistance of thin metal films,” *Journal of Applied Physics*, vol. 45, no. 4, pp. 1908–1909, 1974.

[180] Y. Namba, “Resistivity and temperature coefficient of thin metal films with rough surface,” *Japanese Journal of Applied Physics*, vol. 9, no. 11, p. 1326, 1970.

[181] D. Campbell and A. Morley, “Electrical conduction in thin metallic, dielectric and metallic-dielectric films,” *Reports on Progress in Physics*, vol. 34, no. 1, p. 283, 1971.

[182] C. J. McClellan, E. Yalon, K. K. Smithe, S. V. Suryavanshi, and E. Pop, “Effective n-type doping of monolayer MoS_2 by AlOx,” in *2017 75th Annual Device Research Conference (DRC)*. IEEE, 2017, pp. 1–2.

[183] L. Cai, C. J. McClellan, A. L. Koh, H. Li, E. Yalon, E. Pop, and X. Zheng, “Rapid flame synthesis of atomically thin MoO_3 down to monolayer thickness for effective hole doping of WSe_2,” *Nano letters*, vol. 17, no. 6, pp. 3854–3861, 2017.

[184] A. Rai, A. Valsaraj, H. C. Movva, A. Roy, R. Ghosh, S. Sonde, S. Kang, J. Chang, T. Trivedi, R. Dey *et al.*, “Air stable doping and intrinsic mobility enhancement in monolayer molybdenum disulfide by amorphous titanium suboxide encapsulation,” *Nano letters*, vol. 15, no. 7, pp. 4329–4336, 2015.

[185] S. V. Suryavanshi, A. J. Gabourie, A. Barati Farimani, and E. Pop, “Thermal boundary conductance of two-dimensional MoS_2 interfaces,” *Journal of Applied Physics*, vol. 126, no. 5, p. 055107, 2019.

[186] R. Caverly, G. Hiller, D. Rancour, J. Bukowski, and Z.-W. Tang, “Temperature effects on PIN diode forward bias resistance,” *Solid-State Electronics*, vol. 38, no. 11, pp. 1879–1885, 1995.

[187] E. Yalon, O. B. Aslan, K. K. Smithe, C. J. McClellan, S. V. Suryavanshi, F. Xiong, A. Sood, C. M. Neumann, X. Xu, K. E. Goodson *et al.*, “Temperature-dependent thermal boundary conductance of monolayer MoS_2 by raman thermometry,” *ACS applied materials & interfaces*, vol. 9, no. 49, pp. 43 013–43 020, 2017.

[188] K. M. Razeeb, E. Dalton, G. L. W. Cross, and A. J. Robinson, “Present and future thermal interface materials for electronic devices,” *International Materials Reviews*, vol. 63, no. 1, pp. 1–21, 2018.

[189] C. Wang, L. Yin, L. Zhang, D. Xiang, and R. Gao, “Metal oxide gas sensors: sensitivity and influencing factors,” *sensors*, vol. 10, no. 3, pp. 2088–2106, 2010.

[190] M. Naguib, M. Kurtoglu, V. Presser, J. Lu, J. Niu, M. Heon, L. Hultman, Y. Gogotsi, and M. W. Barsoum, "Two-dimensional nanocrystals produced by exfoliation of Ti_3AlC_2," *Advanced Materials*, vol. 23, no. 37, pp. 4248–4253, aug 2011.

[191] K. Huang, Z. Li, J. Lin, G. Han, and P. Huang, "Correction: Two-dimensional transition metal carbides and nitrides (MXenes) for biomedical applications," *Chemical Society Reviews*, vol. 47, no. 17, pp. 6889–6889, 2018.

[192] K. Toda, J. Li, and P. K. Dasgupta, "Measurement of ammonia in human breath with a liquid-film conductivity sensor," *Analytical Chemistry*, vol. 78, no. 20, pp. 7284–7291, oct 2006.

[193] S. Davies, P. Spanel, and D. Smith, "Quantitative analysis of ammonia on the breath of patients in end-stage renal failure," *Kidney International*, vol. 52, no. 1, pp. 223–228, jul 1997.

[194] L. R. Narasimhan, W. Goodman, and C. K. N. Patel, "Correlation of breath ammonia with blood urea nitrogen and creatinine during hemodialysis," *Proceedings of the National Academy of Sciences*, vol. 98, no. 8, pp. 4617–4621, apr 2001.

[195] D. J. Kearney, T. Hubbard, and D. Putnam, "Breath ammonia measurement in Helicobacter pylori infection," *Digestive diseases and sciences*, vol. 47, no. 11, pp. 2523–2530, 2002.

[196] P. L. Maout, J.-L. Wojkiewicz, N. Redon, C. Lahuec, F. Seguin, L. Dupont, S. Mikhaylov, Y. Noskov, N. Ogurtsov, and A. Pud, "Polyaniline nanocomposites based sensor array for breath ammonia analysis. portable e-nose approach to non-invasive diagnosis of chronic kidney disease," *Sensors and Actuators B: Chemical*, vol. 274, pp. 616–626, nov 2018. [Online]. Available: https://doi.org/10.1016%2Fj.snb.2018.07.178

[197] E. Lee, A. VahidMohammadi, B. C. Prorok, Y. S. Yoon, M. Beidaghi, and D.-J. Kim, "Room temperature gas sensing of two-dimensional titanium carbide (MXene)," *ACS Applied Materials & Interfaces*, vol. 9, no. 42, pp. 37 184–37 190, oct 2017. [Online]. Available: https://doi.org/10.1021%2Facsami.7b11055

[198] M. Yu and D. R. Trinkle, "Accurate and efficient algorithm for Bader charge integration," *The Journal of Chemical Physics*, vol. 134, no. 6, p. 064111, feb 2011. [Online]. Available: https://doi.org/10.1063%2F1.3553716

[199] B. Xiao, Y. chun Li, X. fang Yu, and J. bo Cheng, "MXenes: Reusable materials for NH_3 sensor or capturer by controlling the charge injection," *Sensors and Actuators B: Chemical*, vol. 235, pp. 103–109, nov 2016. [Online]. Available: https://doi.org/10.1016%2Fj.snb.2016.05.062

[200] S. J. Kim, H.-J. Koh, C. E. Ren, O. Kwon, K. Maleski, S.-Y. Cho, B. Anasori, C.-K. Kim, Y.-K. Choi, J. Kim, Y. Gogotsi, and H.-T. Jung, "Metallic $Ti_3C_2T_x$ MXene gas sensors with ultrahigh signal-to-noise ratio," *ACS Nano*, vol. 12, no. 2, pp. 986–993, jan 2018. [Online]. Available: https://doi.org/10.1021%2Facsnano.7b07460

[201] X. fang Yu, Y. chun Li, J. bo Cheng, Z. bo Liu, Q. zhong Li, W. zuo Li, X. Yang, and B. Xiao, “Monolayer Ti_2CO_2: A promising candidate for NH_3 sensor or capturer with high sensitivity and selectivity,” *ACS Applied Materials & Interfaces*, vol. 7, no. 24, pp. 13 707–13 713, jun 2015.

[202] M. A. Hope, A. C. Forse, K. J. Griffith, M. R. Lukatskaya, M. Ghidiu, Y. Gogotsi, and C. P. Grey, “NMR reveals the surface functionalisation of Ti_3C_2 MXene,” *Physical Chemistry Chemical Physics*, vol. 18, no. 7, pp. 5099–5102, 2016. [Online]. Available: https://doi.org/10.1039%2Fc6cp00330c

[203] J. Halim, K. M. Cook, M. Naguib, P. Eklund, Y. Gogotsi, J. Rosen, and M. W. Barsoum, “X-ray photoelectron spectroscopy of select multi-layered transition metal carbides (MXenes),” *Applied Surface Science*, vol. 362, pp. 406–417, jan 2016. [Online]. Available: https://doi.org/10.1016%2Fj.apsusc.2015.11.089

[204] G. Kresse and J. FurthmÃ¼ller, “Efficiency of *ab-initio* total energy calculations for metals and semiconductors using a plane-wave basis set,” *Computational Materials Science*, vol. 6, no. 1, pp. 15–50, jul 1996. [Online]. Available: https://doi.org/10.1016%2F0927-0256%2896%2900008-0

[205] G. Kresse and J. FurthmÃ¼ller, “Efficient iterative schemes forab initiototal-energy calculations using a plane-wave basis set,” *Physical Review B*, vol. 54, no. 16, pp. 11 169–11 186, oct 1996. [Online]. Available: https://doi.org/10.1103%2Fphysrevb.54.11169

[206] G. Kresse and D. Joubert, “From ultrasoft pseudopotentials to the projector augmented-wave method,” *Physical Review B*, vol. 59, no. 3, pp. 1758–1775, jan 1999. [Online]. Available: https://doi.org/10.1103%2Fphysrevb.59.1758

[207] Y. Wang and J. P. Perdew, “Correlation hole of the spin-polarized electron gas, with exact small-wave-vector and high-density scaling,” *Physical Review B*, vol. 44, no. 24, pp. 13 298–13 307, dec 1991. [Online]. Available: https://doi.org/10.1103%2Fphysrevb.44.13298

[208] S. Grimme, J. Antony, S. Ehrlich, and H. Krieg, “A consistent and accurate *ab initio* parametrization of density functional dispersion correction (DFT-d) for the 94 elements H-Pu,” *The Journal of Chemical Physics*, vol. 132, no. 15, p. 154104, apr 2010. [Online]. Available: https://doi.org/10.1063%2F1.3382344

[209] S. Grimme, S. Ehrlich, and L. Goerigk, “Effect of the damping function in dispersion corrected density functional theory,” *Journal of Computational Chemistry*, vol. 32, no. 7, pp. 1456–1465, mar 2011. [Online]. Available: https://doi.org/10.1002%2Fjcc.21759

[210] W. Tang, E. Sanville, and G. Henkelman, “A grid-based Bader analysis algorithm without lattice bias,” *Journal of Physics: Condensed Matter*, vol. 21, no. 8, p. 084204, jan 2009. [Online]. Available: https://doi.org/10.1088%2F0953-8984%2F21%2F8%2F084204

[211] E. Sanville, S. D. Kenny, R. Smith, and G. Henkelman, “Improved grid-based algorithm for Bader charge allocation,” *Journal of Computational Chemistry*, vol. 28, no. 5, pp. 899–908, 2007. [Online]. Available: https://doi.org/10.1002%2Fjcc.20575

[212] V. L. Deringer, A. L. Tchougréeff, and R. Dronskowski, "Crystal orbital Hamilton population (COHP) analysis as projected from plane-wave basis sets," *The journal of physical chemistry A*, vol. 115, no. 21, pp. 5461–5466, 2011.

[213] M. Asad, M. Fathipour, M. H. Sheikhi, and M. Pourfath, "High-performance infrared photo-transistor based on SWCNT decorated with PbS nanoparticles," *Sensors and Actuators A: Physical*, vol. 220, pp. 213–220, dec 2014. [Online]. Available: https://doi.org/10.1016%2Fj.sna.2014.10.017

[214] S. Peng, K. Cho, P. Qi, and H. Dai, "*Ab initio* study of CNT NO_2 gas sensor," *Chemical Physics Letters*, vol. 387, no. 4-6, pp. 271–276, 2004.

[215] L. M. Azofra, C. Sun, L. Cavallo, and D. R. MacFarlane, "Feasibility of N_2 binding and reduction to ammonia on fe-deposited MoS_2 2D sheets: A DFT study," *Chemistry - A European Journal*, vol. 23, no. 34, pp. 8275–8279, may 2017. [Online]. Available: https://doi.org/10.1002%2Fchem.201701113

[216] S. Nosé, "A unified formulation of the constant temperature molecular dynamics methods," *The Journal of chemical physics*, vol. 81, no. 1, pp. 511–519, 1984.

[217] T. Ouyang, Z. Qian, X. Hao, R. Ahuja, and X. Liu, "Effect of defects on adsorption characteristics of AlN monolayer towards SO_2 and NO_2: *Ab-initio* exposure," *Applied Surface Science*, vol. 462, pp. 615–622, dec 2018. [Online]. Available: https://doi.org/10.1016%2Fj.apsusc.2018.08.073

[218] S. Satoh, H. Fujimoto, and H. Kobayashi, "Theoretical study of NH_3 adsorption on Fe (110) and Fe (111) surfaces," *The Journal of Physical Chemistry B*, vol. 110, no. 10, pp. 4846–4852, 2006.

[219] C.-C. Wang, S. S. Siao, and J.-C. Jiang, "Density Functional Theory Study of NHx (x= 0- 3) and N_2 Adsorption on IrO_2 (110) Surfaces," *The Journal of Physical Chemistry C*, vol. 114, no. 43, pp. 18 588–18 593, 2010.

[220] J. Beheshtian, A. A. Peyghan, and Z. Bagheri, "Ab initio study of NH_3 and H_2O adsorption on pristine and Na-doped MgO nanotubes," *Structural Chemistry*, vol. 24, no. 1, pp. 165–170, 2013.

[221] A. Kakekhani, L. T. Roling, A. Kulkarni, A. A. Latimer, H. Abroshan, J. Schumann, H. AlJama, S. Siahrostami, S. Ismail-Beigi, F. Abild-Pedersen, and J. K. Nørskov, "Nature of lone-pair–surface bonds and their scaling relations," *Inorganic chemistry*, vol. 57, no. 12, pp. 7222–7238, 2018.

[222] M. S. Christian, A. O. de-la Roza, and E. R. Johnson, "Surface adsorption from the exchange-hole dipole moment dispersion model," *Journal of Chemical Theory and Computation*, vol. 12, no. 7, pp. 3305–3315, jun 2016. [Online]. Available: https://doi.org/10.1021%2Facs.jctc.6b00222

[223] S.-B. Zhu and M. R. Philpott, "Interaction of water with metal surfaces," *The Journal of Chemical Physics*, vol. 100, no. 9, pp. 6961–6968, may 1994. [Online]. Available: https://doi.org/10.1063%2F1.467012

[224] E. A. Leed, J. O. Sofo, and C. G. Pantano, "Electronic structure calculations of physisorption and chemisorption on oxide glass surfaces,"

Physical Review B, vol. 72, no. 15, oct 2005. [Online]. Available: https://doi.org/10.1103%2Fphysrevb.72.155427

[225] C.-M. Li, Q.-M. Hu, R. Yang, B. Johansson, and L. Vitos, "Theoretical investigation of the magnetic and structural transitions of Ni-Co-Mn-Sn metamagnetic shape-memory alloys," *Physical Review B*, vol. 92, no. 2, jul 2015. [Online]. Available: https://doi.org/10.1103%2Fphysrevb.92.024105

[226] G. Miessler, P. Fischer, and D. Tarr, "Inorganic chemistry fifith edition," 2014.

[227] W. V. Glassey, G. A. Papoian, and R. Hoffmann, "Total energy partitioning within a one-electron formalism: A Hamilton population study of surface–CO interaction in the c (2× 2)-CO/Ni (100) chemisorption system," *The Journal of chemical physics*, vol. 111, no. 3, pp. 893–910, 1999.

[228] L. Bai and Z. Zhou, "Computational study of B- or N-doped single-walled carbon nanotubes as NH_3 and NO_2 sensors," *Carbon*, vol. 45, no. 10, pp. 2105–2110, sep 2007. [Online]. Available: https://doi.org/10.1016%2Fj.carbon.2007.05.019

[229] F. Bibi, C. Guillaume, A. Vena, N. Gontard, and B. Sorli, "Wheat gluten, a bio-polymer layer to monitor relative humidity in food packaging: Electric and dielectric characterization," *Sensors and Actuators A: Physical*, vol. 247, pp. 355–367, 2016.

[230] M. Srbinovska, C. Gavrovski, V. Dimcev, A. Krkoleva, and V. Borozan, "Environmental parameters monitoring in precision agriculture using wireless sensor networks," *Journal of cleaner production*, vol. 88, pp. 297–307, 2015.

[231] H. Guo, C. Lan, Z. Zhou, P. Sun, D. Wei, and C. Li, "Transparent, flexible, and stretchable WS_2 based humidity sensors for electronic skin," *Nanoscale*, vol. 9, no. 19, pp. 6246–6253, 2017.

[232] A. Reddy, B. Narakathu, M. Atashbar, M. Rebros, E. Rebrosova, B. Bazuin, M. Joyce, P. Fleming, and A. Pekarovicova, "Printed capacitive based humidity sensors on flexible substrates," *Sensor Letters*, vol. 9, no. 2, pp. 869–871, 2011.

[233] H. Taghinejad, M. Taghinejad, M. Abdolahad, A. Saeidi, and S. Mohajerzadeh, "Fabrication and modeling of high sensitivity humidity sensors based on doped silicon nanowires," *Sensors and Actuators B: Chemical*, vol. 176, pp. 413–419, 2013.

[234] A. Lokman, H. Arof, S. W. Harun, Z. Harith, H. A. Rafaie, and R. M. Nor, "Optical fiber relative humidity sensor based on inline Mach–Zehnder interferometer with ZnO nanowires coating," *IEEE Sensors Journal*, vol. 16, no. 2, pp. 312–316, 2015.

[235] V. S. Turkani, D. Maddipatla, B. B. Narakathu, T. S. Saeed, S. O. Obare, B. J. Bazuin, and M. Z. Atashbar, "A highly sensitive printed humidity sensor based on a functionalized MWCNT/HEC composite for flexible electronics application," *Nanoscale Advances*, vol. 1, no. 6, pp. 2311–2322, 2019.

[236] A. Reddy, B. Narakathu, M. Atashbar, M. Rebros, E. Rebrosova, and M. Joyce, "Gravure printed electrochemical biosensor," *Procedia Engineering*, vol. 25, pp. 956–959, 2011.

[237] A. Nag, S. C. Mukhopadhyay, and J. Kosel, "Wearable flexible sensors: A review," *IEEE Sensors Journal*, vol. 17, no. 13, pp. 3949–3960, 2017.

[238] D. B. Go, M. Z. Atashbar, Z. Ramshani, and H.-C. Chang, "Surface acoustic wave devices for chemical sensing and microfluidics: a review and perspective," *Analytical methods*, vol. 9, no. 28, pp. 4112–4134, 2017.

[239] B. B. Narakathu, M. S. Devadas, A. S. G. Reddy, A. Eshkeiti, A. Moorthi, I. R. Fernando, B. P. Miller, G. Ramakrishna, E. Sinn, M. Joyce *et al.*, "Novel fully screen printed flexible electrochemical sensor for the investigation of electron transfer between thiol functionalized viologen and gold clusters," *Sensors and Actuators B: Chemical*, vol. 176, pp. 768–774, 2013.

[240] M. Atashbar, B. Bazuin, M. Simpeh, and S. Krishnamurthy, "3-D finite-element simulation model of SAW palladium thin film hydrogen sensor," in *Proceedings of the 2004 IEEE International Frequency Control Symposium and Exposition, 2004.* IEEE, 2004, pp. 549–553.

[241] S. Khan, S. Tinku, L. Lorenzelli, and R. S. Dahiya, "Flexible tactile sensors using screen-printed P (VDF-TrFE) and MWCNT/PDMS composites," *IEEE sensors Journal*, vol. 15, no. 6, pp. 3146–3155, 2014.

[242] Z. Ramshani, A. S. Reddy, B. B. Narakathu, J. T. Wabeke, S. O. Obare, and M. Z. Atashbar, "SH-SAW sensor based microfluidic system for the detection of heavy metal compounds in liquid environments," *Sensors and Actuators B: Chemical*, vol. 217, pp. 72–77, 2015.

[243] V. Bliznyuk, S. Singamaneni, R. Kattumenu, and M. Atashbar, "Surface electrical conductivity in ultrathin single-wall carbon nanotube/polymer nanocomposite films," *Applied physics letters*, vol. 88, no. 16, p. 164101, 2006.

[244] M. Z. Atashbar and S. Singamaneni, "Comparative studies of temperature dependence of G-band peak in single walled carbon nanotube and highly oriented pyrolytic graphite," *Applied physics Letters*, vol. 86, no. 12, p. 123112, 2005.

[245] V. S. Turkani, D. Maddipatla, B. B. Narakathu, B. J. Bazuin, and M. Z. Atashbar, "A carbon nanotube based NTC thermistor using additive print manufacturing processes," *Sensors and Actuators A: Physical*, vol. 279, pp. 1–9, 2018.

[246] B. B. Narakathu, W. Guo, S. O. Obare, and M. Atashbar, "Novel approach for detection of toxic organophosphorus compounds," *Sensors and Actuators B: Chemical*, vol. 158, no. 1, pp. 69–74, 2011.

[247] Y. Seekaew, S. Lokavee, D. Phokharatkul, A. Wisitsoraat, T. Kerdcharoen, and C. Wongchoosuk, "Low-cost and flexible printed graphene–PEDOT: PSS gas sensor for ammonia detection," *Organic Electronics*, vol. 15, no. 11, pp. 2971–2981, 2014.

[248] M. Pumera, "Electrochemistry of graphene: new horizons for sensing and energy storage," *The Chemical Record*, vol. 9, no. 4, pp. 211–223, 2009.

[249] M. Pumera, A. Ambrosi, A. Bonanni, E. L. K. Chng, and H. L. Poh, "Graphene for electrochemical sensing and biosensing," *TrAC Trends in Analytical Chemistry*, vol. 29, no. 9, pp. 954–965, 2010.

[250] Y. Shao, J. Wang, H. Wu, J. Liu, I. A. Aksay, and Y. Lin, "Graphene based electrochemical sensors and biosensors: a review," *Electroanalysis: An International*

Journal Devoted to Fundamental and Practical Aspects of Electroanalysis, vol. 22, no. 10, pp. 1027–1036, 2010.

[251] T. Q. Trung, L. T. Duy, S. Ramasundaram, and N.-E. Lee, "Transparent, stretchable, and rapid-response humidity sensor for body-attachable wearable electronics," *Nano Research*, vol. 10, no. 6, pp. 2021–2033, 2017.

[252] L. Guo, H.-B. Jiang, R.-Q. Shao, Y.-L. Zhang, S.-Y. Xie, J.-N. Wang, X.-B. Li, F. Jiang, Q.-D. Chen, T. Zhang *et al.*, "Two-beam-laser interference mediated reduction, patterning and nanostructuring of graphene oxide for the production of a flexible humidity sensing device," *Carbon*, vol. 50, no. 4, pp. 1667–1673, 2012.

[253] X. Fan, W. Peng, Y. Li, X. Li, S. Wang, G. Zhang, and F. Zhang, "Deoxygenation of exfoliated graphite oxide under alkaline conditions: a green route to graphene preparation," *Advanced Materials*, vol. 20, no. 23, pp. 4490–4493, 2008.

[254] W. Feng, P. Long, Y. Feng, and Y. Li, "Two-dimensional fluorinated graphene: synthesis, structures, properties and applications," *Advanced Science*, vol. 3, no. 7, p. 1500413, 2016.

[255] H. Zhang, L. Fan, H. Dong, P. Zhang, K. Nie, J. Zhong, Y. Li, J. Guo, and X. Sun, "Spectroscopic investigation of plasma-fluorinated monolayer graphene and application for gas sensing," *ACS applied materials & interfaces*, vol. 8, no. 13, pp. 8652–8661, 2016.

[256] K. K. Tadi, S. Pal, and T. N. Narayanan, "Fluorographene based ultrasensitive ammonia sensor," *Scientific reports*, vol. 6, no. 1, pp. 1–9, 2016.

[257] D. A. Siddhanti, D. J. Nash, M. A. Navarro, D. M. Mills, A. Khaniya, B. Dhar, W. E. Kaden, K. Y. Chumbimuni-Torres, and R. G. Blair, "The safer and scalable mechanochemical synthesis of edge-chlorinated and fluorinated few-layer graphenes," *Journal of Materials Science*, vol. 52, no. 20, pp. 11 977–11 987, 2017.

[258] A. O'Neill, U. Khan, P. N. Nirmalraj, J. Boland, and J. N. Coleman, "Graphene dispersion and exfoliation in low boiling point solvents," *The Journal of Physical Chemistry C*, vol. 115, no. 13, pp. 5422–5428, 2011.

[259] J. M. Soler, E. Artacho, J. D. Gale, A. García, J. Junquera, P. Ordejón, and D. Sánchez-Portal, "The siesta method for ab initio order-n materials simulation," *Journal of Physics: Condensed Matter*, vol. 14, no. 11, p. 2745, 2002.

[260] M. Katkov, V. Sysoev, A. Gusel'Nikov, I. Asanov, L. Bulusheva, and A. Okotrub, "A backside fluorine-functionalized graphene layer for ammonia detection," *Physical Chemistry Chemical Physics*, vol. 17, no. 1, pp. 444–450, 2015.

[261] V. Popov, D. Nikolaev, V. Timofeev, S. Smagulova, and I. Antonova, "Graphene-based humidity sensors: The origin of alternating resistance change," *Nanotechnology*, vol. 28, no. 35, p. 355501, 2017.

[262] Q.-Y. Tang, Y. Chan, and K. Zhang, "Fast response resistive humidity sensitivity of polyimide/multiwall carbon nanotube composite films," *Sensors and Actuators B: Chemical*, vol. 152, no. 1, pp. 99–106, 2011.

[263] C.-Y. Hung, W.-L. Sung, S.-C. Chen, and W. Fang, “Resistance-type humidity sensor using CNTs sensing material with Al_2O_3 conformal coating for enhanced sensitivity,” in *2019 20th International Conference on Solid-State Sensors, Actuators and Microsystems & Eurosensors XXXIII (TRANSDUCERS & EUROSENSORS XXXIII).* IEEE, 2019, pp. 761–764.

[264] A. D. Smith, K. Elgammal, F. Niklaus, A. Delin, A. C. Fischer, S. Vaziri, F. Forsberg, M. Råsander, H. Hugosson, L. Bergqvist *et al.*, “Resistive graphene humidity sensors with rapid and direct electrical readout,” *Nanoscale*, vol. 7, no. 45, pp. 19 099–19 109, 2015.

[265] S. Y. Park, J. E. Lee, Y. H. Kim, J. J. Kim, Y.-S. Shim, S. Y. Kim, M. H. Lee, and H. W. Jang, “Room temperature humidity sensors based on rGO/MoS_2 hybrid composites synthesized by hydrothermal method,” *Sensors and Actuators B: Chemical*, vol. 258, pp. 775–782, 2018.

[266] J. Z. Ou, W. Ge, B. Carey, T. Daeneke, A. Rotbart, W. Shan, Y. Wang, Z. Fu, A. F. Chrimes, W. Wlodarski *et al.*, “Physisorption-based charge transfer in two-dimensional SnS_2 for selective and reversible NO_2 gas sensing,” *ACS nano*, vol. 9, no. 10, pp. 10 313–10 323, 2015.

[267] K. A. Messalea, B. J. Carey, A. Jannat, N. Syed, M. Mohiuddin, B. Y. Zhang, A. Zavabeti, T. Ahmed, N. Mahmood, E. Della Gaspera *et al.*, “Bi_2O_3 monolayers from elemental liquid bismuth,” *Nanoscale*, vol. 10, no. 33, pp. 15 615–15 623, 2018.

[268] C. Zhang, L. Cheng, and Y. Liu, “Understanding high-field electron transport properties and strain effects of monolayer transition metal dichalcogenides,” *Physical Review B*, vol. 102, no. 11, p. 115405, 2020.

[269] D. Ferry, “Electron transport in some transition metal di-chalcogenides: MoS_2 and WS_2,” *Semiconductor Science and Technology*, vol. 32, no. 8, p. 085003, 2017.

[270] A. Paussa, G. Fiori, P. Palestri, M. Geromel, D. Esseni, G. Iannaccone, and L. Selmi, “Simulation of the performance of graphene FETs with a semiclassical model, including band-to-band tunneling,” *IEEE Transactions on Electron Devices*, vol. 61, no. 5, pp. 1567–1574, 2014.

[271] T. Cheiwchanchamnangij and W. R. L. Lambrecht, “Quasiparticle band structure calculation of monolayer, bilayer, and bulk MoS_2,” *Phys. Rev. B*, vol. 85, p. 205302, May 2012.

[272] L. Zeng, Z. Xin, S. Chen, G. Du, J. Kang, and X. Liu, “Remote phonon and impurity screening effect of substrate and gate dielectric on electron dynamics in single layer MoS_2,” *Applied Physics Letters*, vol. 103, no. 11, p. 113505, 2013.

[273] N. Ma and D. Jena, “Charge scattering and mobility in atomically thin semiconductors,” *Phys. Rev. X*, vol. 4, p. 011043, Mar. 2014.

[274] A. Hauber and S. Fahy, “Scattering of carriers by coupled plasmon-phonon modes in bulk polar semiconductors and polar semiconductor heterostructures,” *Phys. Rev. B*, vol. 95, p. 045210, Jan. 2017.

[275] G. Gaddemane, W. G. Vandenberghe, M. L. Van de Put, S. Chen, S. Tiwari, E. Chen, and M. V. Fischetti, "Theoretical studies of electronic transport in monolayer and bilayer phosphorene: A critical overview," *Phys. Rev. B*, vol. 98, p. 115416, Sep. 2018.

[276] M. L. Van de Put, G. Gaddemane, S. Gopalan, and M. V. Fischetti, "Effects of the dielectric environment on electronic transport in monolayer MoS_2: Screening and remote phonon scattering," in *2020 International Conference on Simulation of Semiconductor Processes and Devices (SISPAD)*, 2020, pp. 281–284.

[277] C. Herring and E. Vogt, "Transport and deformation-potential theory for many-valley semiconductors with anisotropic scattering," *Physical review*, vol. 101, no. 3, p. 944, 1956.

[278] P. Borowik and J.-L. Thobel, "Improved Monte Carlo method for the study of electron transport in degenerate semiconductors," *Journal of Applied Physics*, vol. 84, no. 7, pp. 3706–3709, 1998.

[279] T. Gunst, T. Markussen, K. Stokbro, and M. Brandbyge, "First-principles method for electron-phonon coupling and electron mobility: Applications to two-dimensional materials," *Phys. Rev. B*, vol. 93, p. 035414, Jan. 2016.

[280] T. Sohier, D. Campi, N. Marzari, and M. Gibertini, "Mobility of two-dimensional materials from first principles in an accurate and automated framework," *Phys. Rev. Materials*, vol. 2, p. 114010, Nov. 2018.

[281] Z.-Y. Ong and M. V. Fischetti, "Mobility enhancement and temperature dependence in top-gated single-layer MoS_2," *Phys. Rev. B*, vol. 88, p. 165316, Oct. 2013.

[282] A. Kumar and P. Ahluwalia, "Electronic structure of transition metal dichalcogenides monolayers 1H-MX_2 (M= Mo, W; X= S, Se, Te) from *ab-initio* theory: new direct band gap semiconductors," *The European Physical Journal B*, vol. 85, no. 6, pp. 1–7, 2012.

[283] C.-H. Chang, X. Fan, S.-H. Lin, and J.-L. Kuo, "Orbital analysis of electronic structure and phonon dispersion in MoS_2, $MoSe_2$, WS_2, and WSe_2 monolayers under strain," *Phys. Rev. B*, vol. 88, p. 195420, Nov 2013.

[284] P. Palestri, N. Barin, D. Esseni, and C. Fiegna, "Revised stability analysis of the nonlinear Poisson scheme in self-consistent Monte Carlo device simulations," *IEEE Transactions on Electron Devices*, vol. 53, no. 6, pp. 1443–1451, 2006.

[285] P. Palestri, L. Lucci, S. Dei Tos, D. Esseni, and L. Selmi, "An improved empirical approach to introduce quantization effects in the transport direction in multi-subband Monte Carlo simulations," *Semiconductor Science and Technology*, vol. 25, no. 5, p. 055011, Apr. 2010.

List of Publications

International Journals

P. Khakbaz, M. Moshayedi, S. Hajian, M. Soleimani, B. B. Narakathu, B. J. Bazuin, M. Pourfath, and M. Z. Atashbar. "**Titanium carbide MXene as NH_3 sensor: realistic first-principles study**." *The Journal of Physical Chemistry C* 123, no. 49 (2019): 29794-29803.

S. Hajian, X. Zhang, P. Khakbaz, S.M. Tabatabaei, D. Maddipatla, B. B. Narakathu, R. G. Blair, and M. Z. Atashbar. "**Development of a fluorinated graphene-based resistive humidity sensor**." *IEEE Sensors Journal* 20, no. 14 (2020): 7517-7524.

A. Khan, P. Khakbaz, K. A. Brenner, K. KH Smithe, M. J. Mleczko, D. Esseni, and E. Pop. "**Large temperature coefficient of resistance in atomically thin two-dimensional semiconductors**." *Applied Physics Letters* 116, no. 20 (2020): 203105.

P. Khakbaz, F. Driussi,,P. Giannozzi,A. Gambi, and D. Esseni. 2021. "**Simulation study of Fermi level depinning in metal-MoS_2 contacts**." *Solid-State Electronics*(2021), 108039.

International Conferences

S. Hajian, P. Khakbaz, M. Moshayedi, D. Maddipatla, B. B. Narakathu, V. S. Turkani, B. J. Bazuin, M. Pourfath, and M. Z. Atashbar. "**Impact of Different Ratios of Fluorine, Oxygen, and Hydroxyl Surface Terminations on Ti_3C_2Tx MXene as Ammonia Sensor: A First-Principles Study**." *In 2018 IEEE SENSORS*, pp. 1-4. IEEE, 2018.

M. Soleimani, N. Asoudegi, P. Khakbaz, and M. Pourfath. "**Negative Capacitance Field-Effect Transistor Based on a Two-Dimensional Ferroelectric**." *In 2019 International Conference on Simulation of Semiconductor Processes and Devices (SISPAD)*, pp. 1-4. IEEE, 2019.

P. Khakbaz, F. Driussi, A. Gambi, P. Giannozzi, S. Venica, D. Esseni, A. Gaho, S. Kataria, and M. C. Lemme. "**DFT study of graphene doping due to metal contacts**." *In 2019 International Conference on Simulation of Semiconductor Processes and Devices (SISPAD)*, pp. 1-4. IEEE, 2019.

S. Hajian, P. Khakbaz, B. B. Narakathu, S. Masihi, M. Panahi, D. Maddipatla, V. Palaniappan, R. G. Blair, B. J. Bazuin, and M. Z. Atashbar. "**Humidity Sensing Properties of Halogenated Graphene: A Comparison of Fluorinated Graphene and Chlorinated Graphene**." *In 2020 IEEE International Conference on Flexible and Printable Sensors and Systems (FLEPS)*, pp. 1-4. IEEE, 2020.

A. Pilotto, P. Khakbaz, P. Palestri, and D. Esseni. "**Modeling Low and High Field Uniform Transport in Monolayer MoS_2**." *In 2021 Joint International EUROSOI Workshop and International Conference on Ultimate Integration on Silicon (EuroSOI-ULIS)*, pp. 1-4. IEEE, 2021.

Acknowledgements

Countless people supported my effort on this thesis, but I would like to express my deepest gratitude to my advisor, Prof. David Esseni, whose support and encouragement I will never forget. I am proud of, and grateful for, my time working with Prof. Esseni. Also this thesis would not have been possible without Prof. Francesco Driussi, whose guidance from the very outset enabled me to develop an understanding of the subject. Several other professors including Profs. Paolo Giannozi, Alberto Gambi, and Marco Pala provided me with their helpful advice and full support in this path. I especially would like to thank Prof. Pierpaolo Palestri for his very sympathetic support and encouragement in the development of the Monte Carlo simulator. I greatly appreciate my Master's Degree supervisor, Prof. Mahdi Pourfath for his great support, excellent encouragement, and guidance.

I also would like to thank my colleagues at the University of Udine, especially Dr. Alessandro Pilotto and Dr. Julian Mele, who supported me in both my personal and professional life. I am grateful for my family, whose constant love and support keep me motivated and confident, especially my father Dr. Afshin Khakbaz, and my grandfather Mohammad Khakbaz. My accomplishments and success are because they believed in me. Deepest thanks to my mom, Farzam and Setayesh, who keep me grounded, remind me of what is important in life, and are always supportive of my adventures. Thank you all for the strength you gave me. Last but not least, I owe my deepest gratitude to Sahar, I am forever thankful for the unconditional love and support throughout my Ph.D. and every day.

Pedram Khakbaz
University of Udine
January 2022